Dissecting Merging Galaxies Using Integral Field Spectroscopy

A thesis submitted for the degree of Doctor of Philosophy of
The Australian National University

Elise Jasmin Hampton

December, 2017

Disclaimer

I hereby declare that the work in this thesis is that of the candidate alone, except where indicated below.

Chapter 2: This Chapter has been published in the *Monthly Notices of the Royal Astronomical Society*. The paper is co-authored with A.M. Medling, B. Groves, L. Kewley, M. Dopita, R. Davies, I.-T. Ho, M. Kaasinen, S. Leslie, R. Sharp, S.M. Sweet, A.D. Thomas, J. Allen, J. Bland-Hawthorn, S. Brough, J.J. Bryant, S. Croom, M. Goodwin, A. Green, I.S. Konstantantopoulos, J. Lawrence, A.R. Lopez-Sanchez, N.P.F Lorente, R. McElroy, M.S. Owers, S.N. Richards, P. Shastri. The emission line fitting for the SAMI Survey was conducted by I-Ting Ho, a PhD Candidate at the University of Hawaii, as is stated in the chapter. The code for the F-test was provided by Rebecca McElroy, a PhD Candidate at the University of Sydney, and used by the candidate. The minimisation code used as a part of the Machine Learning algorithm, `fmincg` written by Carl Edward Rasmussen, is used by the candidate as stated in the chapter. All other code used in this research is the candidates. The training sample was created with the organisational help of Dr. Anne Medling for the SAMI Galaxy Survey. The work described in this chapter is by the candidate.

Chapter 3: The emission line fitting of the WiGS galaxies was conducted by Dr. Jeff Rich, as stated in the chapter. The emission line fitting of the CALIFA galaxies was conducted by Anshu Gupta, a PhD Candidate at the Research School of Astronomy and Astrophysics (ANU), using the IDL code `LZIFU` written by I-Ting Ho. The classifications of the central emission line excitation mechanisms of the CALIFA galaxies were determined by I-Ting Ho. The work described in this chapter is by the candidate.

Chapter 4 and Chapter 5: These chapters describe the research done in collaboration with Professor David Rupke at Rhodes College, Memphis. The absorption fitting code was written by David Rupke and adjusted by the candidate to work with this research. The work described in these chapters is by the candidate.

Elise Jasmin Hampton

December 2017

Acknowledgements

Firstly, I would like to thank my supervisors and collaborators for their continued support over my PhD Candidature; Professor Lisa Kewley (supervisor), Professor Michael Dopita (panel), Dr. Robert Sharp (panel), Dr. Tian-Tian Yuan (panel), Dr. Jeff Rich (panel), Dr. Ralph Sutherland (panel), Professor David Rupke (collaborator), Dr. Brent Groves (collaborator), Dr. Anne Medling (collaborator); This thesis would not have been possible without all of their support and the support of my fellow PhD Candidates at RSAA and the University of Hawaii.

This research is supported by an Australian Government Research Training Program (RTP) Scholarship. I gratefully acknowledge the financial support of a RSAA top-up scholarship, and the Duffield scholarship as a part of my PhD program. I also acknowledge the financial support of CAASTRO for the ADASS conference in 2015, ASA for the ASA conference in 2016, RSAA for the Alex Rodgers travel scholarship, ANU for the Vice Chancellors research scholarship, and financial support from my supervisor for collaboration trips to work with Professor David Rupke on chapters 4 and 5 of my thesis.

I also gratefully acknowledge the financial support of the Zonta Club of Canberra Breakfast for the Women in Science Scholarship. The members of this club have been an amazing support group for me and my PhD, I thank you all for your encouraging words over the years.

I would very much like to thank my family for their continued support; You have all helped in getting me to the finish line. To Peter (husband), Tracy (Mum), Bruce (Dad), Emma (Sister), Liam (Brother), and Paul (Brother-in-law), I say thank you. Thanks for the listening ears, even when I was not making much sense to you when talking about my research.

I would also like to thank my friends and co-workers for their encouragement and good times.

Finally, I would like to thank those who had supported me in my endeavour of completing a PhD in Astronomy but are unable to see me finish; Ronald Payne, Joy Hampton, and Pauline Martin.

Abstract

Galaxies grow through the accretion of gas, minor mergers and major mergers in the hierarchical picture of galaxy evolution. The merging of two gas-rich galaxies cause gas to be driven towards the centres of the individual galaxies producing intense circum-nuclear star formation and creating a fuel reservoir for the accretion onto the central blackhole. Feedback due to supernova winds or AGN (Active Galactic Nuclei) accretion blows out the surrounding gas through an outflow at later merger stages, that may be large enough to deplete the galaxies of their fuel reservoir and hence shut down star formation and starve the central black hole. It is still uncertain what the impact of outflows is on merging galaxies, and when in the merging process they are most significant. This thesis has used Integral Field Spectroscopy (IFS) observations of merging galaxies to probe the impact of outflows on gas-rich major mergers. Using velocity-resolved absorption and emission lines arising from the interstellar medium of the galaxies, this thesis shows that the occurrence of outflows increases with merger stage and also that these outflows are not caused by the same physical processes, such as star formation or an AGN, in each merger system.

This thesis describes the machine learning algorithm created to expedite the decision making process of multi-component emission line fitting for studies of ionised gas in large IFS surveys. The remainder of the research outlined in this thesis has identified a number of new facts about merging galaxies that are important for further research in this field including the following; Composite galaxies are being incorrectly classed as the same type of galaxy when they can range in excitation mechanisms; Composite galaxies are not the same between different morphologies, including between merging galaxies and isolated galaxies; The outflow from the northern nucleus of the merging system IRAS F10257-4339 can be traced in neutral, ionised, and molecular gas, and is most likely caused by starformation; Outflows of neutral gas from galaxies increases with merger stage.

Contents

List of Figures

List of Tables

Chapter 1

A study of merging galaxies

1.1 Introduction

In the hierarchical picture of galaxy formation and evolution, galaxies grow through the accretion of gas, minor mergers and major mergers. When two gas-rich galaxies merge, gas is driven towards the centres of the individual galaxies causing intense circum-nuclear star formation and creating a fuel reservoir for the accretion onto the central blackhole. This accretion increases the Active Galactic Nuclei (AGN) activity (e.g. Veilleux et al., 1995a; Scoville et al., 2000; Arribas et al., 2004; Springel et al., 2005; Alonso-Herrero et al., 2006; Yuan et al., 2010a; Hopkins et al., 2012; Rich et al., 2015). In later merger stages, the AGN can be obscured in optical observations until feedback from supernova winds or AGN accretion blows out the surrounding gas through an outflow (e.g. Rupke et al., 2005b,c; Sharp & Bland-Hawthorn, 2010). If the impact of these outflows is large enough, the merged galaxy can be depleted of its fuel reservoir, shutting down star formation and starving the central black hole of the merged system. The galaxy will then fade into a quiescent elliptical galaxy. It is still uncertain what impact outflows have on merging galaxies, and when in the merging process they are most significant.

This thesis used Integral Field Spectroscopy (IFS) observations of merging galaxies to determine the power sources of outflows and probe the impact of outflows in gas-rich major mergers. By using velocity-resolved absorption and emission lines arising from the interstellar medium of the galaxies, this thesis demonstrates that outflows are not all caused by the same events in each merger system. The research was undertaken in four

steps:

1. Devising a solution to the big data problem of decomposing spectral emission lines into multiple velocity components,
2. Determining the excitation sources of merging galaxies that are neither star formation dominated or AGN dominated, also known as composite galaxies, in order to identify the excitation mechanisms involved in outflows,
3. Identifying the neutral gas outflow in the merging system IRAS F10257-4339, as a test case in identifying outflows in merging systems,
4. Investigating the association of neutral gas outflows with merger stage.

The research has identified a number of new facts about the merging galaxies that are important for further research in this field:

1. Composite galaxies are being incorrectly classed as the same type of galaxy when they can range in excitation mechanisms; AGNs (LINERs and Seyfert), shocks, star formation (Chapter 3),
2. Composite galaxies do not have the same power sources across morphologies (Chapter 3),
3. The outflow from the northern nucleus of IRAS F10257-4339 can be traced in neutral, ionised, and molecular gas, and is most likely caused by starformation (Chapter 4),
4. The neutral gas outflows from within merging galaxies are not all caused by the same physical mechanism (Chapter 5),
5. There are indications that the commonness of galaxies with neutral gas outflows increases with merger stage (Chapter 5).

1.2 Previous research

Simulations of merging galaxies (e.g. Springel et al., 2005) have provided a theoretical platform linking mergers, increased AGN activity, and increased star formation. Springel et al. (2005) have shown that galaxy mergers can cause large gas inflows (Barnes & Hernquist, 1991, 1996a) which could then trigger nuclear starbursts (Mihos & Hernquist, 1996; Springel et al., 2005) and increase black hole accretion and AGN activity (Di Matteo et al.,

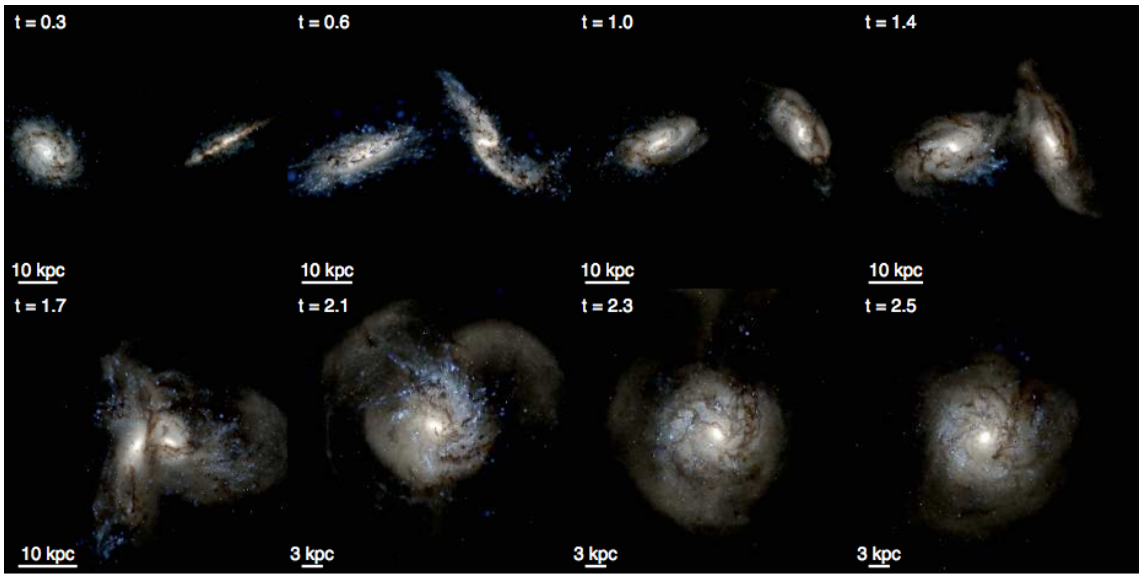

Figure 1.1: Snapshots of galaxy merger simulation courtesy of Hopkins et al. (2012). Each snapshot shows the optical image at different stages of the merger of two Sbc galaxies. The optical image is a false colour ugr composite, with the spectrum of all stars calculated from their age and metallicity, and dust extinction and reddening is accounted for in line-of-sight dust mass. The brightness of the image is on a logarithmic scale.

2005). The nuclear starbursts form stars at a rate which is consistent with the observations of excess light in ongoing mergers (Rothberg & Joseph, 2004, 2006) as well as with the luminosity profiles of old red elliptical galaxies (Mihos & Hernquist, 1994; Kormendy et al., 2009).

More recently Hopkins et al. (2012) have analysed simulations of major mergers and the production of starbursts. A selection of snapshots of a major merger simulation from Hopkins et al. (2012) is reproduced in Figure 1.1. These merger models show that on the first pass of two galaxies the torques exerted on the system drive gas into the centre of the galaxies and produce strong shocks in tidal regions. Feedback from stars blows out powerful super winds of hot X-ray emitting gas, warm ionised gas, and dense molecular material. After the coalescence of the two galaxies a stronger burst of star formation is predicted, driving a more pronounced outflow. Not all of the gas blown out through these outflows is unbound and thus some of the gas falls back onto the galaxy after the merger. In gas-rich galaxies this feedback fuels rapid re-building of rotating disks, while gas poor galaxies will have exhausted their gas reservoir and so the merger remnant relaxes and reddens as it evolves to become an elliptical galaxy.

In a major observational study, Yuan et al. (2010b) investigated the fraction of 500 Infrared selected galaxies classified as starburst, composite, Seyfert AGN, and LINER (Low Ionisation Nuclear Emission Region) as a function of merger stage. The galaxies are derived from three samples;

1. 118 ULIRGs (Ultra-Luminous Infrared Galaxies) from the IRAS 1 Jy sample of ULIRGs (Kim & Sanders, 1998) (Figure 1.2);
2. 104 of the highest luminosity objects from the IRAS Bright Galaxy Survey (Veilleux et al., 1995b);
3. 285 galaxies from the Southern Warm Infrared Galaxies sample (Kewley et al., 2001c).

Yuan et al. (2010b) separated the galaxies by their dominant power sources using standard optical diagnostic diagrams, which are explored in more detail in Chapter 3. The galaxies were then separated by merger stage to analyse the change of power sources with merger progression. Yuan et al. (2010b) found several key features from the 1 Jy sample of ULIRGs. Firstly, the fraction of starburst-AGN composite galaxies peaks at the diffuse merger stage indicating that both a starburst and an AGN contribute to the total energy budget at the diffuse merger stage. Secondly, the fraction of starburst-AGN composites decreases sharply at late stage mergers, where there is a corresponding increase in the fraction of Seyfert galaxies. Yuan et al. (2010b) propose that the starburst-AGN composite galaxies transition into Seyfert galaxies at later merger stages. They also see a possible trend of Seyfert galaxies decreasing to the diffuse merger stage before increasing greatly at even later merger stages. They argue that a larger sample of ULIRGs is needed to verify either of these trends. Yuan et al. (2010b) conducted the same analysis with the other two galaxy samples but found no significant trends across merger stages. They argue that this is due to the classification process not separating diffuse, compact, and old merger stages where the most significant changes were seen in the 1 Jy sample (see following section for details of the merger stage classification).

Rich et al. (2015) investigated the fraction of shocks and HII region emission galaxies as a function of merger stage. The galaxies were separated in the same way as Yuan et al. (2010b) into power source classifications and merger stages. Rich et al. (2015) found that the fraction of star formation decreased with merger stage while shocks increased.

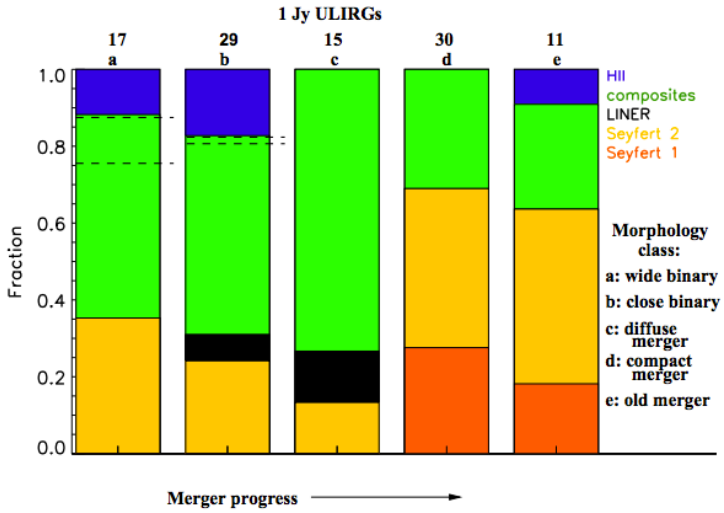

Figure 1.2: 1 Jy ULIRGS (Kim et al., 1998) spectroscopic classification as a function of merger stage (Yuan et al., 2010b). Merger stages evolve from left to right. a - wide binary, b - close binary, c - diffuse merger, d - compact merger, e - old merger, see Section 1.3.1. The number on top of each merger stage indicates the number of galaxies in that stage. The number of composite galaxies peaks at the diffuse merger stage then sharply decreases.

They also found that there is a significant contribution from merger-induced shocks to the optical spectra as well as an interesting increase in shock dominated emission in later stage mergers.

1.3 Studying merging galaxies

1.3.1 Merger stage classification

The merger stage of a system is determined by its morphological classification (Rich et al., 2015; Yuan et al., 2010a) based on that determined by Veilleux et al. (2002). The galaxy morphology classification is related to merger stage by comparing observations with numerical simulations of galaxy mergers, (Barnes & Hernquist, 1992, 1996b). The classification is as follows and is shown graphically in Figure 1.3 reproduced from Yuan et al. (2010b):

1. Wide binary: binary system with projected nuclear separation > 10 kpc (a),
2. Close binary: binary system with projected nuclear separation < 10 kpc (b),
3. Diffuse merger: single system with tidal features and no K-band luminous core (c),

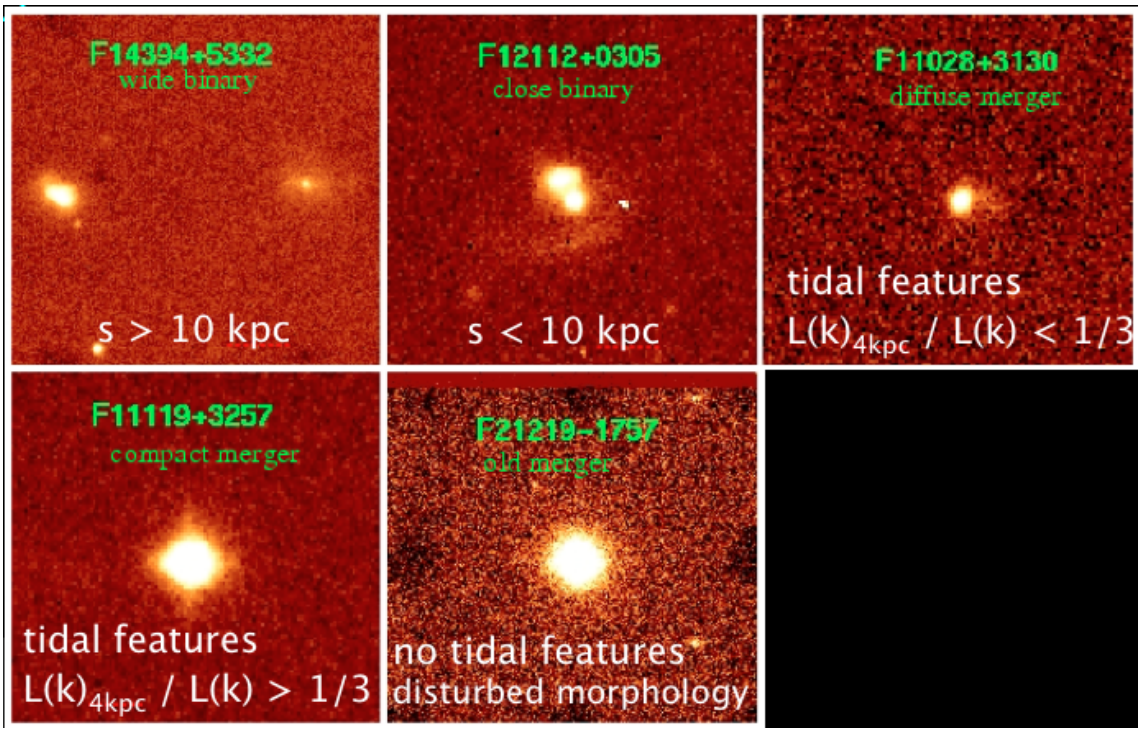

Figure 1.3: Galaxies are classed by merger stage. This figure is courtesy of Yuan et al. (2010a). From left to right: top panels are examples of a wide binary, close binary, and diffuse merger. Bottom panels are examples of a compact merger and an old merger.

4. Compact merger: single system with tidal features and with a K-band luminous core (d),
5. Old merger: single system with no tidal tails but with disturbed central morphologies (e).

1.3.2 Analysis methods

The study of the excitation sources and outflows in merging galaxies relies on three analysis methods; emission line studies, absorption line studies, and IFS. Emission line spectra traces the ionised gas within a galaxy. This method of analysis, described in detail below, is fundamental to the analysis of the excitation sources of composite galaxies, those that are neither dominated by star formation or an AGN. The second analysis method is using NaI D absorption features to trace neutral gas, such as galaxy disks, tidal features of mergers and outflows. IFS studies combine both emission and absorption line studies into spatially resolved processes.

Emission line methods

Emission lines are indicative of hot, ionised gas. By modelling the emission line peaks in the spectra of galaxies we can obtain emission line fluxes, velocities, and velocity dispersions of each emission line of interest. Individually emission line fluxes are not instructive on the excitation processes, however they do indicate the relative quantities of elements within a galaxy. The analysis of multiple emission lines, due to different elements or the same elements in different ionised states, can be used to identify the physical excitation source producing the emission line features in the spectra.

The classification of galaxies by their dominant excitation source began with Baldwin et al. (1981), which separated galaxies into four distinct classes; those excited by star formation, by planetary nebulae, by shocks and by a power-law continuum associated with Active Galactic Nuclei (AGN). The classes are defined by the ratios of the bright optical emission lines; [OIII]λ5007/Hβ, [NII]λ6583/Hα, [OI]λ6300/Hα, and [OII]λ3727/Hα. The ratio [SII]$\lambda\lambda 6716, 6731$/H$\alpha$ was later added to the set of emission line ratios by Keel (1983) and Kennicutt & Keel (1984). The [OIII]/Hβ, [NII]/Hα, [SII]/Hα, and [OI]/Hα emission line ratios, all sensitive to ionising radiation, form a set of optical diagnostic diagrams used to determine the dominant power source of a galaxy.

Different power sources are separated on the diagnostic diagrams by sets of diagnostic lines. The first set of semi-empirical classification curves, to be used with the diagnostic diagrams to separate AGN from star-forming galaxies, was by Osterbrock & De Robertis (1985) and Veilleux & Osterbrock (1987). The first purely theoretical classification diagnostics were developed by Kewley et al. (2001a) using a combination of stellar population synthesis and photoionisation models to define an upper limit to the contribution of star formation to an emission line ratio. Kauffmann et al. (2003) considered only the [NII]/Hα vs. [OIII]/Hβ diagnostic when determining an empirical upper-limit to star formation dominated galaxies in diagnostic diagram space while considering [OIII] luminosity as a tracer of AGN activity. The galaxies which fall between the Kewley et al. (2001a) and Kauffmann et al. (2003) diagnostic curves on the [NII]/Hα vs. [OIII]/Hβ diagnostic diagram are neither dominated by star formation or by an AGN and are classified as composite. Chapter 3 will show that composite emission line ratios are not necessarily a combination of AGN and star formation emission, but may also include shocked gas emission.

Sodium D-line absorption line methods

Absorption lines are used to trace the cold, neutral gas in a galaxy. In this thesis the analysis concentrated on the use of the NaI D$\lambda\lambda$5890, 5896 absorption feature, because of its low ionisation state of 5.4 keV, to trace outflows of neutral gas within a galaxy. NaI D absorption is also observed from the stellar continuum due to old stars as well as the neutral gas outflows. Modelling of the absorption due to stars was performed using stellar populations synthesis and absorption lines that are not contaminated by non-stellar contributions. The NaI D absorption that remains after this process was then assumed to be associated with the neutral gas physics of the galaxy. A blue-shifted absorption component is indicative of an outflow (towards the observer) (e.g. Rupke et al., 2002, 2005b,c). The process to use NaI D absorption to trace the neutral gas in galaxies is explained in further detail in Chapters 4 and 5.

Integral Field Spectroscopy

Single Fibre, or single spectrum, surveys such as Sloan Digital Sky Survey (SDSS) (York et al., 2000) and Galaxy And Mass Assembly (GAMA) (Driver et al., 2011) typically observe a single spectrum of the nuclear region of a galaxy. For low redshift ($z < 0.01$) this single spectrum is on the order of 1 kpc of a total galaxy, where a galaxy can be up to 10 kpc across. This is approximately 10% of the total information that could be obtained from observing a galaxy. This is, for example, like using a single floor of an apartment block to determine its entire structure. If it was possible to observe the whole apartment block including the numbers of floors, numbers of apartments and rooms, and the overall structure of the building, including the intricacies of the floors with no apartments, it would provide a much more accurate picture. To better understand what is happening within a galaxy the Field-of-View (FoV) needs to also include the outskirts of the galaxy.

To achieve this increased FoV an extension of single spectrum observations has been used, namely long slit observations. These types of observations observe the spectra along a line of the galaxy, usually centred on its nucleus. Instead of observing just the nuclear spectra this type of observation observes both sides of a galaxy and the nuclear spectra. This information can be used to obtain the rotation curve of a galaxy from the emission line spectra and the emission line ratios of the nuclear spectra. However, this is still a

single spectrum of a galaxy with maybe 20% of the information of the galaxy. Additional information is still needed to complete the picture of a galaxy in order to fully understand the physical processes within. Long slit spectra in steps across a galaxy can be used to build up this larger picture but complications arise from the inconsistency between each slice observed at a slightly different time. What is required is an observation that can be done all-at-once so that the spatial information is consistent. An observation like this can also be made quicker than stepping long slit spectra, meaning more observations can be made.

Integral Field Spectroscopy (IFS) is capable of obtaining data on the full extent of the galaxy in a single observation. IFS is capable of this type of analysis because it uses multiple fibres, or slits, to build a spatial map of spectra across a galaxy (e.g. Croom et al., 2012; Sánchez et al., 2012; Dopita et al., 2014a; Bundy et al., 2015). It is analogous to overlaying a grid onto a galaxy and observing the spectra from each individual grid point. At each grid point the emission line ratios can be calculated such that a map of the excitation processes can be followed as well as tracing the rotation of the galaxy and follow the spatial extent of outflows or inflows. IFS is a powerful tool in the understanding of galaxies and a statistical study of similar galaxies using IFS can provide better information about the behaviour of galaxies as they evolve.

This thesis shows how IFS surveys can be utilised to dissect galaxies both spatially and spectrally. The research method concentrated on the analysis of galaxies along the merger sequence, but also includes comparison galaxies that are not merging.

1.4 Overview of research and thesis contents

IFS has changed the approach to studying galaxy evolution. Surveys are now creating databases of hundreds to thousands of galaxies, all observed with IFS, that requires expansive data-reduction. Automated continuum and emission line fitting of spectra is common place. However, the assignment of the number of components required to describe certain emission line features is not automated. To overcome the limitations of manually manipulating these observations an Artificial Neural Network (ANN) was developed and is described in Chapter 2. This accelerated the selection of the number of components in emission line fitting. Two different IFS surveys were used to show the compatibility of

the ANN to the emission line fitting code `LZIFU` (Ho et al., 2016b) and the reliability of separating multiple excitation sources.

The reliable separation of excitation sources, either spatially or spectrally, allows studies of galaxies which are not dominated by a single excitation source. Chapter 3 shows that single spectrum analysis of galaxies can result in very different galaxies being classified as similar types. The study concentrates on composite classified merging galaxies in order to determine what they are made up of and also compare the results of merging galaxies with those of isolated spiral composite galaxies and isolated bar composite galaxies.

Chapter 4 continues to dissect one of the composite galaxies analysed in Chapter 3 with the NaI D absorption feature. IRAS F10257-4339 is a close merger with shocks (Rich et al., 2011), a strongly star-forming northern nucleus (Chapter 3), and outflows of ionised, neutral and molecular gas (Lípari et al., 2000, 2004; Heckman et al., 2000; Emonts et al., 2014; Sakamoto et al., 2014). The known northern outflow is traced in the neutral gas with the help of the IFS observation and the disk of the southern galaxy is mapped by the NaI D absorption.

Larger surveys are used to understand galaxies as they evolve. Chapter 5 expands the NaI D study of Chapter 4 to include another 23 galaxies across merger stages with NaI D detections to understand how the numbers of galaxies with outflows changes along the merger sequence. The results show that outflows do increase with merger stage. Merger stages also do not correlate with outflows having the same excitation processes.

Chapter 6 summarises the results of this thesis and describes further research options using new, larger surveys of galaxies to continue dissecting the excitation sources of composite emission line ratios in a statistical sample, now that the studies have shown they are more complicated than first expected. This thesis combined the three last stages of merging for the analysis of outflows with merger stage. However, the separation of the three stages may hold vital keys to understanding why outflows are observed more frequently at later stages.

Chapter 2

Artificial Neural Networks for multi-component emission line fitting classifications

2.1 Introduction

Integral Field Spectroscopy (IFS) is transforming our approach to studying galaxy evolution. Surveys such as CALIFA (Calar Alto Legacy Integral Field Area, Sánchez et al., 2012), SAMI (Sydney-AAO Multi-object Integral field spectrograph, Croom et al., 2012), MaNGA (Mapping Nearby Galaxies at Apache Point Observatory, Bundy et al., 2015), and S7 (Siding Spring Southern Seyfert Spectroscopic Snapshot Survey, Dopita et al., 2014a) are building databases of spatially-resolved spectra of hundreds to thousands of galaxies in order to explore galaxy evolution as a function of morphology, environment, and spectral type. IFS provides a powerful probe into the spatial variation of physical processes across galaxies. For example, single-fibre redshift surveys such as SDSS (Sloan Digital Sky Survey, York et al., 2000) and GAMA (Galaxy And Mass Assembly, Driver et al., 2011) observe only a single spectrum for each galaxy, typically from the galaxy's core. As such, it is often possible to misidentify the global properties of an individual galaxy, (e.g. Fogarty et al., 2012; Ho et al., 2014; Richards et al., 2014, 2016, Chapter 3).

Access to the wealth of information from an IFS survey comes at a price: the necessary computational resources needed to process the large volume of data. Advances in IFS

technology are not only pushing the previous sample size boundaries but each galaxy observation now contains as many individual spectra as an entire early redshift survey. Datacubes of multiple gigabytes, with thousands of spaxels (spatial pixels) for each galaxy, are not uncommon.

Data reduction pipelines (e.g. Husemann et al., 2013; Sharp et al., 2015; Allen et al., 2015a) are efficient ways to convert raw data into a final spectral datacube for analysis, but interpreting these spectra remains a significant challenge. The data volume is too great to allow tailored analysis of each spectrum individually. Some form of automated analysis is required to extract information from the spectra and to target galaxies for further investigation.

Automated continuum and absorption line fitting is routinely used to understand the stellar populations within galaxies. Subsequent emission-line fitting provides insight into the star formation, AGN (active galactic nuclei) activity and the shock properties of galaxies. This type of pre-analysis can be time consuming for IFS surveys and fitting each emission line by hand is no longer a feasible option. There can be multiple processes generating a single emission line such as; emission coming from different regions of a galaxy in the same line-of-sight, multiple kinematic components, and/or different excitation mechanisms causing the emission line shapes being observed. The complexity of emission line profiles requires further steps to be undertaken in the pre-analysis. Automated emission line fitting, including multi-component fitting for situations with multiple physical processes contributing to emission lines, is currently in use, e.g. `LZIFU`; Ho et al. (2016b) and `GANDALF`; Sarzi et al. (2006). Often, a statistic is used to determine where the cut-off is between one or more components, for example χ^2 values or an F-test. However, human input is often still required to decide where to make the cut-off, if one can be made, that separates 1-component fits from higher order fits. When statistics are not usable, humans are required to eye-ball each individual spectral fit to decide the best number of components. Manually classifying the spectra of many galaxies is a time consuming venture but does lead to picking out interesting scientific results that may be missed when using a simple cut-off statistic.

This chapter describes the development and use of an automated machine learning algorithm to remove the time-consuming human input of visually inspecting multi-component emission-line fitting for large surveys by creating an astronomer-like 3-way classifier. Sec-

tion 2.2 describes the spectral properties that can be extracted from datacubes. The architecture of the supervised Artificial Neural Network is described in Section 2.3. The analysis conducted during the research to determine the best architecture for the ANN, `LZComp`, is discussed in detail in Sections 2.4 and 2.5. The results of using an ANN to distinguish between the best fits of emission line spectra are documented in Section 2.6 and a comparison to an F-test is in Section 2.7.The applicability to the two test samples is shown and discussed in Section 2.8. The increase in speed of using an ANN over manual multi-component selections is listed in Section 2.9. Finally, the results and possible future studies using this tool are presented in Section 2.10.

2.2 Spectral properties from datacubes

The analysis of a galaxy datacube requires measurements of key physical properties extracted from the individual spectra of each spaxel. The spectrum at each spaxel typically contains an emission-line spectrum that arises from shock-heated or photoionised gas, superimposed upon continuum light that comes either from the underlying stellar populations or an active galactic nucleus. Accurate modelling and subtraction of the underlying continuum is critical in correcting for stellar absorption which would otherwise lead to the incorrect measurement of coincident emission-lines. For example, in the Hydrogen Balmer series the stellar absorption line can have high equivalent widths which interfere with the emission line extraction if not accounted for correctly.

Each line-of-sight into the galaxy can encompass gas at different velocities and with different excitation mechanisms. For example, Figure 2.1 highlights the effect of the changing physical processes across NGC 5728. Panels (a) and (b) show the nuclear spectra with obvious double-peaked emission-line profiles that can be attributed to gas moving with different velocities relative to the line of sight, e.g. an outflow of gas in the disk of the galaxy. Panels (c) and (d) show the spectra of a different part of NGC 5728 where there are single peaked emission lines. Multiple Gaussians are fit to these resulting emission-line profiles in order to explain the underlying physical processes occurring within a galaxy. However, we do not *a priori* know the number of physical components within a resolution element.

To fit the spectral datacubes, we use the automated fitting package `LZIFU` (Ho et al.,

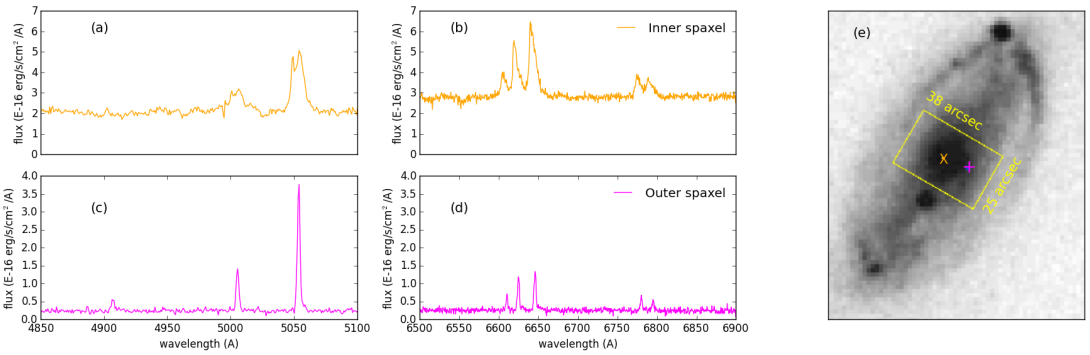

Figure 2.1: NGC5728. (a) Blue and (b) red spectra from a core spaxel. Note the double peak in the emission lines. (c) Blue and (d) red spectra from a spaxel away from the core of the galaxy. Note the difference in the shapes of the emission lines in comparison to the spectra in (a) and (b). (e): DSS image of NGC5728 with WiFeS (Dopita et al., 2007) field of view overlaid as a yellow box. Orange 'X' indicates the core spaxel shown in panels (a) and (b), magenta '+' indicates the outer spaxel shown in panels (c) and (d).

2016b). This program, written in the IDL programming language, fits multiple Gaussian components to each emission-line complex in a spectrum after correcting for the underlying stellar absorption component using `pPXF` (Cappellari & Emsellem, 2004). The emission lines are fit simultaneously, forcing each component to have a single velocity and velocity dispersion across all line transitions. However, the relative fluxes of the emission lines are left free, and the line ratios for each component can vary, Ho et al. (2016b, for a full description).

S7 (The Siding Spring Southern Seyfert Spectroscopic Snapshot Survey; Dopita et al., 2014a) and SAMI (the SAMI Galaxy Survey; Croom et al., 2012; Bryant et al., 2015) are the two example galaxy surveys used to determine the validity of using machine learning in this application. See Section 2.4 for details on the S7 and SAMI surveys. Each galaxy observed is comprised of ∼1000 spaxels, each with an associated high spectral resolution spectrum. Each spectrum is fit in turn with 1, 2, and 3 Gaussian components for the strongest emission lines by `LZIFU`. The significant challenge is in identifying which set of Gaussian components best describes the spectrum for each spaxel. Visual inspection to make the identifications, which is the common approach, can take up to ∼1 hour for a single galaxy. For small surveys this manual classification is feasible, but with surveys the size of SAMI (∼3000 galaxies) the time involved increases to ∼ 125 days of manual classification.

F-tests are used to compare different model fits to a data set. The F-test tests whether the increase in the χ^2 value of a fit with more Gaussian components justifies the addition of extra parameters. The results of using F-tests, as was done in McElroy et al. (2015), in comparison to using astronomers and our machine learning algorithm, see Section 2.7, clearly indicate that an F-test is not as robust in making the decisions of the number of components required as it heavily selects 1-component fits. In complex parameter spaces such as those involving multiple Gaussians, the chi-squared value produced by least-squares minimisation algorithms (such as `mpfit` (Markwardt, 2009), which `LZIFU` uses) may represent a local rather than global minimum. This local minimum can be avoided by implementing algorithms like MCMC (Monte Carlo Markov Chain) or Nested Sampling, which probe a greater proportion of the parameter space. Nested sampling has been tested on SAMI galaxies, and because it samples much of the parameter space as it converges upon a fit, model comparisons come for free as it can be used to calculate the integrated likelihood for use with Bayesian model comparison. Unfortunately, performing the fitting and model comparison for complex spectra takes over a minute per spaxel.

2.3 A supervised Artificial Neural Network

The machine learning algorithm designed as part of this research activity is an artificial neural network (ANN) designed to learn and make classification decisions across an entire survey[1].

The use of machine learning in astronomy is not a new idea. Contemporary examples include the prediction of solar flares (e.g. Bobra & Couvidat, 2015), understanding gamma-ray emission from AGNs (e.g. Hassan et al., 2013; Doert & Errando, 2014), and the classification of galaxy types (e.g. Kuminski et al., 2014). Supervised machine learning covers a wide range of distinct classes of artificial intelligence (AI) such as Artificial Neural Networks (ANNs), Support Vector Machines (SVMs), and Random Forest algorithms, that learn without being explicitly programmed. Each have their benefits and weaknesses but all are based on the same underlying principle, they learn from a training set and create models to be used to predict outcomes. To solve the data management issue, this research uses a supervised Artificial Neural Network (ANN) to build a classification model for

[1]The ANN, called `LZComp` (Lay-Ze-Components), is in a prototype stage and can be found on Github at `https://github.com/EliseHampton/LZComp`.

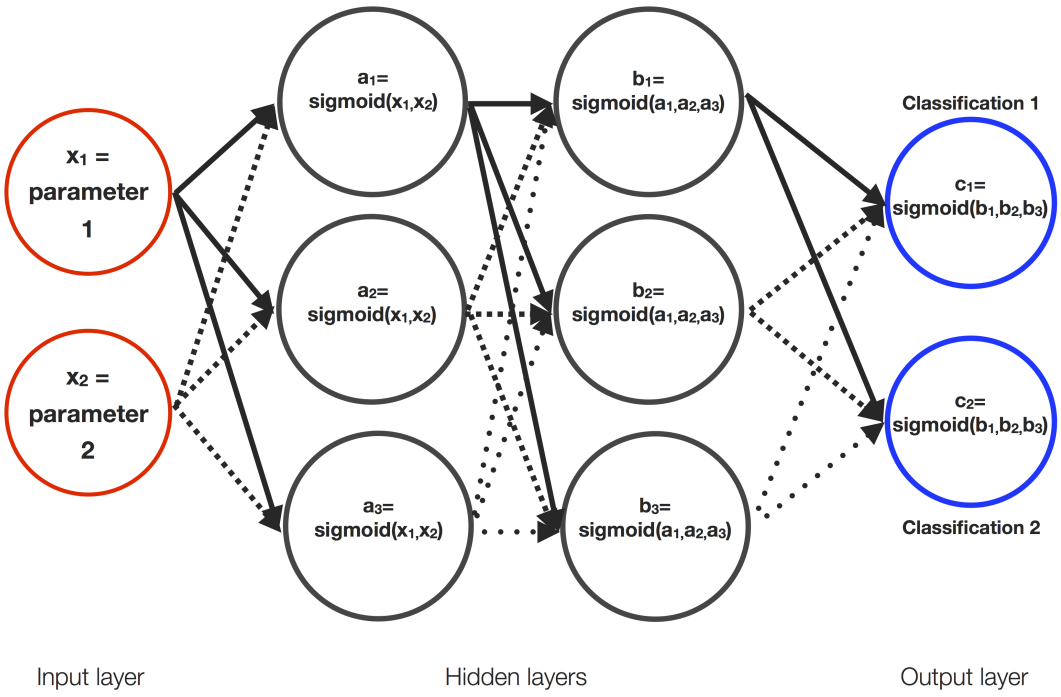

Figure 2.2: An Artificial Neural Network design. The circles indicate the nodes and are grouped into the 3 layer types: Input, hidden and output. This ANN is used to decide if something with the input parameters x_1 and x_2 are of classification 1 or classification 2. At each layer, calculations are done using the values of the previous layer. The final classification is then decided based on which node in the output layer has the largest value. Another simplified explanation of how an ANN works can be found in Appendix A.

multi-component emission line fitting.

An ANN has three types of layers; an input layer, hidden layers, and an output layer. A simplified architecture is presented in Figure 2.2. Each circle is a node with lines indicating the connection between each layer. The nodes in the input layer, represented as x_j in the following equations, are parameter values making up the feature vector. The feature vector is a vector of parameters that describes the example being processed by the ANN.

From the input layer the x_j parameters are sent into the next layer, the first hidden layer of the ANN. The parameter values are put into a sigmoid function with different weights assigned to each parameter. For each node in the first hidden layer the node performs the calculation described in Equation 2.1 where θ_{ij} are the weights for the node i on the input parameters x_j between the input and first hidden layer.

$$a_i = \frac{1}{1 + exp(\sum_{j=1}^{2} \theta_{ij}^1 x_j)} \tag{2.1}$$

Each node in the first layer uses the same parameters x_1 and x_2 but different weights θ_{ij}^1 corresponding to the specific node.

Once the values of the sigmoid functions are calculated for each node in the first hidden layer they are passed on to the second hidden layer. The process is repeated using the values calculated from the previous layer and different weights corresponding to the different nodes in the second hidden layer. Equation 2.2 shows the functional form of the equation calculated in the nodes of the second hidden layer.

$$b_i = \frac{1}{1 + exp(\sum_{j=1}^{3} \theta_{ij}^2 a_j)} \tag{2.2}$$

The final layer is the output layer which determines the classification of the example with feature vector x_j as classification 1 or classification 2. The values b_i from the second hidden layer are sent into the output layer where one last set of sigmoid functions are calculated with a final set of weights. Equation 2.3 shows the equation calculated by the nodes in the output layer.

$$c_i = \frac{1}{1 + exp(\sum_{j=1}^{3} \theta_{ij}^3 b_j)} \tag{2.3}$$

The final classification is determined by which output node has the higher value. During the training phase of the ANN a cost is also calculated. The cost function, Equation 2.4, describes how close the classification from the ANN is to the labels given to the ANN, where m is the number of training examples.

$$J = \frac{1}{m} \sum_i (-y_i log(c_i) - (1 - y_i) log(1 - c_i)) + \frac{\lambda}{2m} (\sum_{ijk} \theta_{ij}^k) \tag{2.4}$$

The cost is summed over all output nodes and all training examples. The second term in the cost function sums the weights from each layer with a regularisation parameter, λ, that helps prevent any particular weight from becoming too large and dominating the cost

function. λ is also known as a tuneable parameter. By changing the value of lambda and comparing the results of the cost function during training the best value, between 0.01 to 10, to minimise the cost function can be determined.

The cost function is minimised in the training phase by iterating over the entire training set using the octave[2] script `fmincg`[3]. The minimisation uses the cost function, Equation 2.4, to alter the weights at each node to return a classification closer to the labels for each training example in the next iteration. Each successive iteration adjusts the weights again to create a decision matrix capable of matching the classifications of the labelled training examples. These iterations are the learning phase of the supervised ANN.

In the case of the example, in Figure 2.2, there are two parameters making up the feature vector but these two values may not be enough to differentiate between the two classifications. For this reason it is necessary to give the ANN enough information to adequately describe the classifications the ANN is to make.

The ANN developed through this research, `LZComp`, has two hidden layers with 15 nodes in each layer. The input layer has 91 (S7) or 94 (SAMI) input parameters making up the feature vector for each example and the output layer has 3 nodes corresponding to the best number of Gaussian components; 1-, 2-, or 3-components.

[2] `https://www.gnu.org/software/octave/`

[3] Originally written by Carl Edward Rasmussen and added to by the Stanford Machine Learning online course. `fmincg` is based on Polack-Ribiere minimisation.

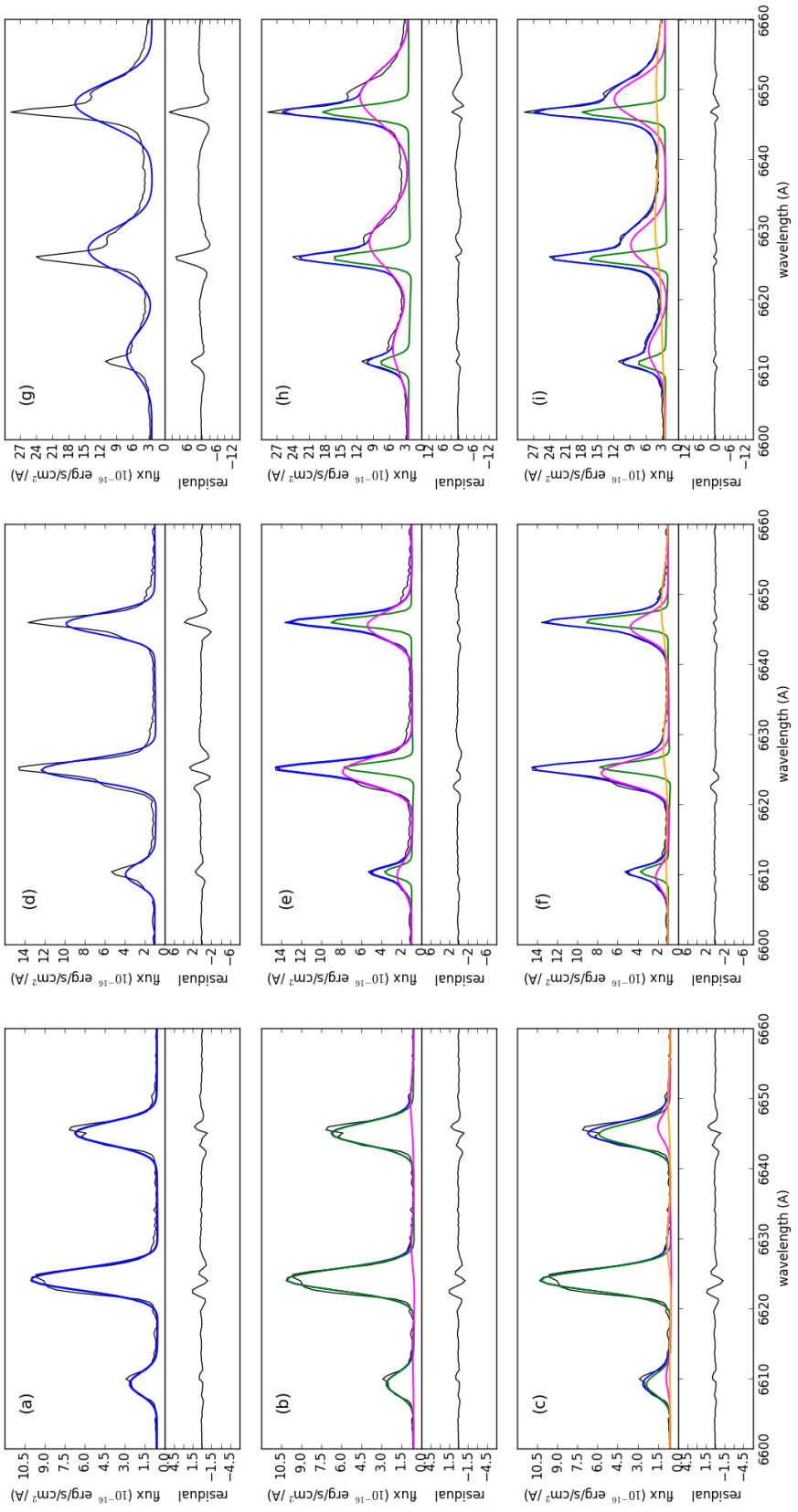

Figure 2.3: Each column is an individual spectrum from a different position within the galaxy NGC5728 highlighting the `LZIFU` fits to [Nii]$\lambda\lambda$6548, 6584 and Hα emission lines where there are high S/N and high spectral resolution spectra from S7. Each row shows the `LZIFU` 1-, 2-, and 3-component fits to these spectra, respectively. Black shows the data, blue the total line fit, green the 1st component fit, magenta the 2nd component, and yellow the 3rd component. The residuals of the total fit are below each individual fit panel in black.

2.4 Testing LZComp on IFS surveys

LZComp is a supervised learning algorithm. The supervision component comes from repeated training using data with labelled examples, i.e. LZComp is provided with the answers for a subset of spectra. LZComp can then use this information to correct itself using the cost function. The following subsections explain the two test cases that were used, the S7 and SAMI Galaxy Surveys, to test, train and run LZComp in order to classify the number of components needed for each spaxel of a galaxy.

During the testing of LZComp it was found that each survey requires its own training set due to differences between the surveys; (a) The signal-to-noise ratios of the most common emission lines; (b) spectral resolution and; (c) the overall galaxy types targeted by each survey. When running LZComp on the SAMI Galaxy Survey after being trained with S7, the results showed no correlation with our SAMI trainers, and vice versa. The SAMI Galaxy Survey has been observing for over a year (2014) and has included studies of galactic winds (Fogarty et al., 2012), studying a unified dynamical scaling relation (Cortese et al., 2014), shocks and outflows within galaxies (Ho et al., 2014), galaxy decomposition (Cecil et al., 2015), star formation and stellar populations (Leslie et al., 2015) and galaxy kinematics (Allen et al., 2015c; Cecil et al., 2016; Ho et al., 2016a; Cortese et al., 2016). S7 has targeted galaxies with very strong AGN-like emission lines to study the physics of the narrow line region in Seyfert galaxies (Dopita et al., 2015; Scharwächter et al., 2016; Davies et al., 2016b,a).

In both galaxy samples, a range of galaxies were used to include spaxels dominated by star formation, galactic winds, Seyfert 1 (Sy1) and Seyfert 2 (Sy2) AGN emission, while making sure there was a range of signal-to-noise ratios that were expected to be seen in the two samples. The inputs into LZComp during training were spaxels from eight galaxies which have been randomly assigned to the training (50%), testing (25%) or cross-validation (25%) sets of examples. After training the test set is aggregated with a completely unseen galaxy for calculations of accuracy. At no point are these spaxels used to train LZComp, only used in comparing results. All inputs into LZComp are based on values from LZIFU and these are not galaxy specific so there is high confidence in using spaxels from the same galaxies in both the training and the testing and cross-validation sets.This statement is explained in detail with a comparison set of three galaxies in Section 2.6.

Using a range of galaxy types with different physical processes to cover the expectations of the entire surveys allows the process of labelling the training data to occur in a short period of time. The expected time to label the 12 galaxies, eight galaxies in the training part of this study, plus a ninth galaxy for calculations of the algorithms accuracy, and three galaxies in a comparison set, manually is around 12 hours for each individual astronomer/trainer. The spaxels are classified as 1-, 2-, or 3-components by the groups of astronomers (hereafter ″the Trainers″). In Section 2.6, we present the number of components selected by the Trainers for both surveys in comparison to how LZComp labels examples after training. In Section 2.8 physically motivated selections made by LZComp are shown.

2.4.1 Siding Spring Southern Seyfert Spectroscopic Snapshot Survey : S7

The Siding Spring Southern Seyfert Spectroscopic Snapshot Survey (S7, Dopita et al., 2015) is a survey of 136 Seyfert galaxies, observed with the Wide Field Spectrograph (WiFeS, Dopita et al., 2007) on the ANU 2.3m telescope at Siding Spring Observatory. These galaxies are at redshifts less than 0.02 and thus use most of the field of view of the WiFeS detector ($25'' \times 38''$) with $1''$ pixels. In many S7 galaxies WiFeS only covers the central region of the galaxy. The spectral resolution of S7 is R = 3000 in the blue and R = 7000 in the red. S7 is intended to explore the narrow and broad line regions in Seyfert galaxies and therefore includes a large number of galaxies with underlying broad emission lines. The S7 set of galaxies used in this research is made up of 12 galaxies for splitting among the training, testing, cross-validation, and the comparison sets all from the initial data release. These galaxies were chosen to cover the full range of activity within the sample; Seyfert 1's, Seyfert 2's, LINERs and star-forming galaxies.

Manual classification of the training set entails the Trainers (three astronomers from S7) looking at every observed spectrum along with the LZIFU fits using each 1-, 2-, and 3-Gaussian components and the resulting residuals. Concentrating on the strong emission lines, the Trainers decide the minimum number of components needed to reproduce the spectrum within the noise. This classification was carried out for every spaxel, resulting in a 2D component mask of the galaxy with values of 1, 2, or 3 for each of the Trainers.

It was found that the Trainers did not agree for $\sim$ 25% of cases. To counteract this

disagreement, `LZComp` was trained using a sample of $\sim$ 2900 examples for which at least two of the three astronomers agreed on the number of components. (See Section 2.6 for a discussion of using a majority rule criteria.) For testing another $\sim$ 2900 examples were split between the cross validation and testing sets. See Section 2.5 for an explanation on the numbers of examples used.

2.4.2 Sydney-AAO Multi-object Integral field: SAMI

The SAMI Galaxy Survey (Croom et al., 2012) is a survey of $\sim$ 3400 nearby ($z < 0.1$) galaxies observed with the SAMI instrument on the 3.9-metre Anglo-Australian Telescope at Siding Spring Observatory. The survey is made up of four volume-limited galaxy samples with the aim of covering a broad range in stellar mass and environment (Bryant et al., 2015). The survey uses SAMI fibre 'hexabundles' (Bland-Hawthorn et al., 2011; Bryant et al., 2011, 2014) to map these galaxies out to < 1 effective radius. The SAMI hexabundles have 61 fibres and a chosen binning scale of $0.5''$ (see Sharp et al., 2015, for details). Each SAMI observation is $15''$ in diameter and thus each has fewer spaxels than the S7 galaxies. The spectral resolution of SAMI is R = 1730 in the blue and R = 4500 in the red.

The set consists of 12 galaxies, covering both strong and weak emission line galaxies and Seyfert and star-forming galaxies. The first testing set includes one galaxy not seen during training and the second training set consists of three galaxies not seen during training (Section 2.6). Each spaxel in these 12 galaxies was manually classified by the Trainers (five astronomers from SAMI) in the same manner as with S7. As the galaxies did not always have emission lines towards their outer edges, pixels with no signal were left unclassified.

For the five trainers labels were created for `LZComp` by calculating the most common classification between the five astronomers. This aggregation of labels from all trainers provided a clean sample of $\sim$ 2500 spaxels to train and test `LZComp`. (See Section 2.6 for a discussion on the use of the majority rule.) The increased number of trainers corresponds to a lower ($\sim$ 50%) percentage of agreement in example labels, compared to our S7 trainers, but is not a factor in the training as the requirement is that the majority of the Trainers agree on an example for it to be entered into the samples.

2.5 Identifying the correct model

The objective of `LZComp` is to create a reliable, fast, self-consistent and easy to use method of determining the most likely number of components needed to describe a given emission line. As with all supervised machine learning algorithms, the first step is to train the algorithm before applying it to the survey data. To create the target labels, astronomers make the decisions for a test set of galaxies (Section 2.4), labelling each spaxel with the number of components that most likely describe the emission. `LZComp` is trained with these examples and tested to confirm that the tuneable parameters, e.g. λ, the number of iterations, and the number of training examples obtain the best possible results.

The training and use of `LZComp` is as follows:

1. Label two sets of galaxies by the Trainers for each survey to create labelled examples. One will be used for training, cross-validation, and initial testing. The second set will be used as a final test set for confirmation of the results.
2. Create feature vectors, a numerical set of parameters, associated with each example from `LZIFU` fitting.
3. Use half of these examples to train `LZComp` to build a model, using the labels to correct the weights. These examples will be the training set.
4. Use a quarter of the labelled examples not used in training as a subset to optimise the tuneable parameters of `LZComp`. These examples will be the cross-validation set.
5. Compare results of `LZComp` to the remaining quarter of labelled examples, also unseen in training. These examples are the first test set.
6. Compare results of `LZComp` to the aggregation of the CV, test and 1 extra galaxy to calculate the accuracy of the algorithm.

The test set provides an understanding of how many more examples may be required for training; this is calculated during the training. The cross-validation set tunes the regularisation parameter, λ, to best suit the problem. The test and cross-validation sets also enable an understanding of how many nodes each layer should have to optimise the algorithm and how many layers `LZComp` needs to give the outcomes that best match the human trainers. This process is completed using the eight galaxies sent to `LZComp` as the training, test, and CV example sets.

Each example spectrum has 91 (S7) or 94 (SAMI) parameters that describe the emission-line fits. These parameters are the parameters related to a fit of multiple Gaussians that we believe to be important for determining if a particular fit is better than another. The parameters include the total signal-to-noise ratio, $\mathrm{Flux_T/Flux_T\_err}$, of each of the strongest emission lines (Hα, Hβ, [NII]λ6583, [SII]$\lambda\lambda$6716, 6731, and [OIII]λ5007), the relative contribution of each individual component to the total flux of an emission-line, e.g. $\mathrm{Flux_1/Flux_T}$. The relative fluxes are important in determining if a particular component is not contributing substantially to the total flux or if it is contributing a large part of the total flux. A component that contributes little to the total flux may not be significant enough to be a real physical component of the emission line. The input parameters also include the velocity dispersion, σ, in the form of $\sigma/\sigma_{\mathrm{err}}$. By using the ratio of the velocity dispersion with the error in the velocity dispersion the certainty of the parameter is input instead of a galaxy specific value of just σ. Also included are parameters associated with the calculation of the stellar absorption fitting on the underlying stellar continuum; Stellar $\mathrm{EBV^{S7}}$, Hα_$\mathrm{EBV^{SAMI}}$, and Hβ_$\mathrm{E(B-V)^{SAMI}}$. The parameter vectors also include the goodness of fit parameters as returned by `LZIFU`; χ^2, χ^2/DOF, χ^2_{cont}. All input parameters of the input feature vector are listed in Table 2.1.

All parameters in the vector input play some role in determining the final result out of the neural network. During the training of `LZComp`, the weights assigned to each parameter in the nodes determine how much each parameter contributes to the final result. It has not been tested as to which particular parameters, if any, in the feature vectors play the largest roles in determining which label an example produces. However, the weights are designed to make redundant parameters negligible in the final determination of the labels negating the need to go through each parameter and determine if it affects the result during this prototype study of using an ANN.

Part of the testing of `LZComp` has been to identify the best configuration of nodes and layers within `LZComp`. The number of layers is selected by choosing the minimum number that still successfully minimises the cost function. Another method to determine how the number of layers changes the results of training is to look at how different layers work alongside each other, while also looking for an adequate number of nodes. Figure 2.4 presents the cost function, J (Equation 2.4), resulting from training using two hidden layers (left side)

	components fit		
Value	1	2	3
$\mathrm{Flux_T}/\mathrm{Flux_T}$_err	x	x	x
$\mathrm{Flux_1}/\mathrm{Flux_1}$_err		x	x
$\mathrm{Flux_2}/\mathrm{Flux_2}$_err		x	x
$\mathrm{Flux_3}/\mathrm{Flux_3}$_err			x
$\mathrm{Flux_1}/\mathrm{Flux_T}$	x	x	x
$\mathrm{Flux_2}/\mathrm{Flux_T}$		x	x
$\mathrm{Flux_3}/\mathrm{Flux_T}$			x
χ^2	x	x	x
χ^2/DOF	x	x	x
χ^2_{cont}	x	x	x
$\mathrm{V_1}/\mathrm{V_1}$_err	x	x	x
$\mathrm{V_2}/\mathrm{V_2}$_err		x	x
$\mathrm{V_3}/\mathrm{V_3}$_err			x
σ_1/σ_1_err	x	x	x
σ_2/σ_2_err		x	x
σ_3/σ_3_err			x
Stellar $\mathrm{EBV}^{\mathrm{S7}}$	x	x	x
Hα_$\mathrm{EBV}^{\mathrm{SAMI}}$	x	x	x
Hβ_$\mathrm{EBV}^{\mathrm{SAMI}}$	x	x	x

Table 2.1: This table indicates each input parameter given to `LZComp` as the input vector. Each flux value is calculated for the following six emission lines: Hα, Hβ, [NII]λ6583, [SII]$\lambda\lambda$6716, 6731, and [OIII]λ5007. Also included for each of the six emission lines is the ratio of the total flux from 1 component fitting to the total flux from 2 and 3 component fitting separately. `LZComp` is given 91 parameters for the S7 galaxies and is given 94 parameters for SAMI. The difference is in the information given in the fitted cubes before processing through `LZComp`. The S7 fitting extracts the stellar EBV from the continuum fitting, while SAMI extracts Hα_EBV and Hβ_EBV values from the continuum fit.

and three hidden layers (right side) with a different number of nodes in the layers. The testing was constrained to have the same number of nodes in the two or three hidden layers for each configuration. Each panel shows the results of training using different values of the regularisation parameter λ. By comparing the different ANN configurations it can be determined which configuration minimises the cost function. Figure 2.4 presents the average cost functions calculated for the training set of examples (blue), the testing set of examples with a regularisation parameter matching the training (green), and the cross-validation (CV) set of examples using a regularisation parameter of $\lambda = 0$ (red) for comparison. The values are averaged between three randomised sets of the training, CV, and testing examples from the SAMI survey. The results of each set are presented in Figures 2.5, 2.6, and 2.7. The results from S7 are very similar and thus not presented in this chapter. Similarly, once the number of layers and nodes have been determined, it is possible to determine the regularisation parameter, λ, that minimises the cost function in both training and testing examples.

As is clear from Figure 2.4, the two hidden layer ANN gives better results than the three layer architecture, independent of the number of nodes in each layer. Using a two hidden layer configuration, it was found that 15 nodes gave the lowest training cost functions with different parameters. Once this configuration was set the testing results were narrowed to a range of regularisation parameters, $\lambda = 0.3, 1, 3$. At these regularisation parameters the cost function is at a minimum consistently, where a more detailed analysis of the training results for each component could be investigated.

In addition to the cost functions presented in Figure 2.4, the configuration of `LZComp` was based on the success in training of 1-, 2-, and 3-components. `LZComp` must distinguish between different components in the testing and cross validation sets of examples to its best ability. The cost function can easily be taken over by the influence of the accuracy `LZComp` has in selecting 1-components, which dominate the spaxels in the testing sets in each survey (as explained in Section 2.4). Figure 2.8 presents the recall and precision values (described in detail in Section 2.6) of `LZComp` in selecting the numbers of components in comparison to the Trainers for the SAMI survey with different values of λ. For `LZComp` it is necessary to maximise the recall and precision for each number of components without losing the ability of `LZComp` to select a specific number of components. For example, a $\lambda = 0.3$ has a high precision for 3-components, but it is lower in precision in selecting

both 1 and 2 components with $\lambda = 3$. The red line presented in Figure 2.8 presents the precision and recall of using a regularisation parameter of $\lambda = 3$, the value that allows `LZComp` to best make its selections.

By combining the results in Figure 2.4 with the success of `LZComp` for a two hidden layer, 15 node configuration with a regularisation parameter of $\lambda = 3$ for both SAMI (Figure 2.8) and S7 samples results in an ANN that can select the number of Gaussian components as well as the Trainers if not above the lower limit of the Trainers (Section 2.6.

Not only is the configuration of `LZComp` important, but also the number of examples used in training. An investigation was performed to determined how many examples would not under fit or over fit the parameter space. Figure 2.9 presents the comparison of the cost function of the training set (blue) and cross validation set (green) as a function of the number of examples used to train. The training cost function is calculated using the regularisation parameter assigned to the survey undergoing testing, while the cross-validation cost function is calculated with a regularisation parameter $\lambda = 0$. There are two scenarios for determining the number of examples. A high variance system does not converge the two lines, indicating the need for more examples. A high bias system is where the two lines converge to almost the same value, indicating too many examples or the need for more features or hidden layers. The system being defined needs to be between the high variance and high bias scenarios so as to avoid under or over fitting the training examples. It must also incorporate enough examples of each 1-, 2-, and 3-component fits in order to give `LZComp` enough examples of each. Figure 2.9 presents a system that is in between a high bias and high variance system, showing that the number of examples being used is adequate for this study. The same analysis and testing was completed with the S7 survey with similar results. Section 2.6 presents the results of accuracy for both survey samples for comparison.

2.6 Accuracy of the model

The accuracy of `LZComp` was assessed after training using the subset of trainer-classified input examples set aside for testing, cross-validation, and the ninth unseen galaxy. The accuracy (how well `LZComp` can match the labels agreed upon by the Trainers labels) of `LZComp` was defined by its ability to recall the same classifications as the Trainers and the

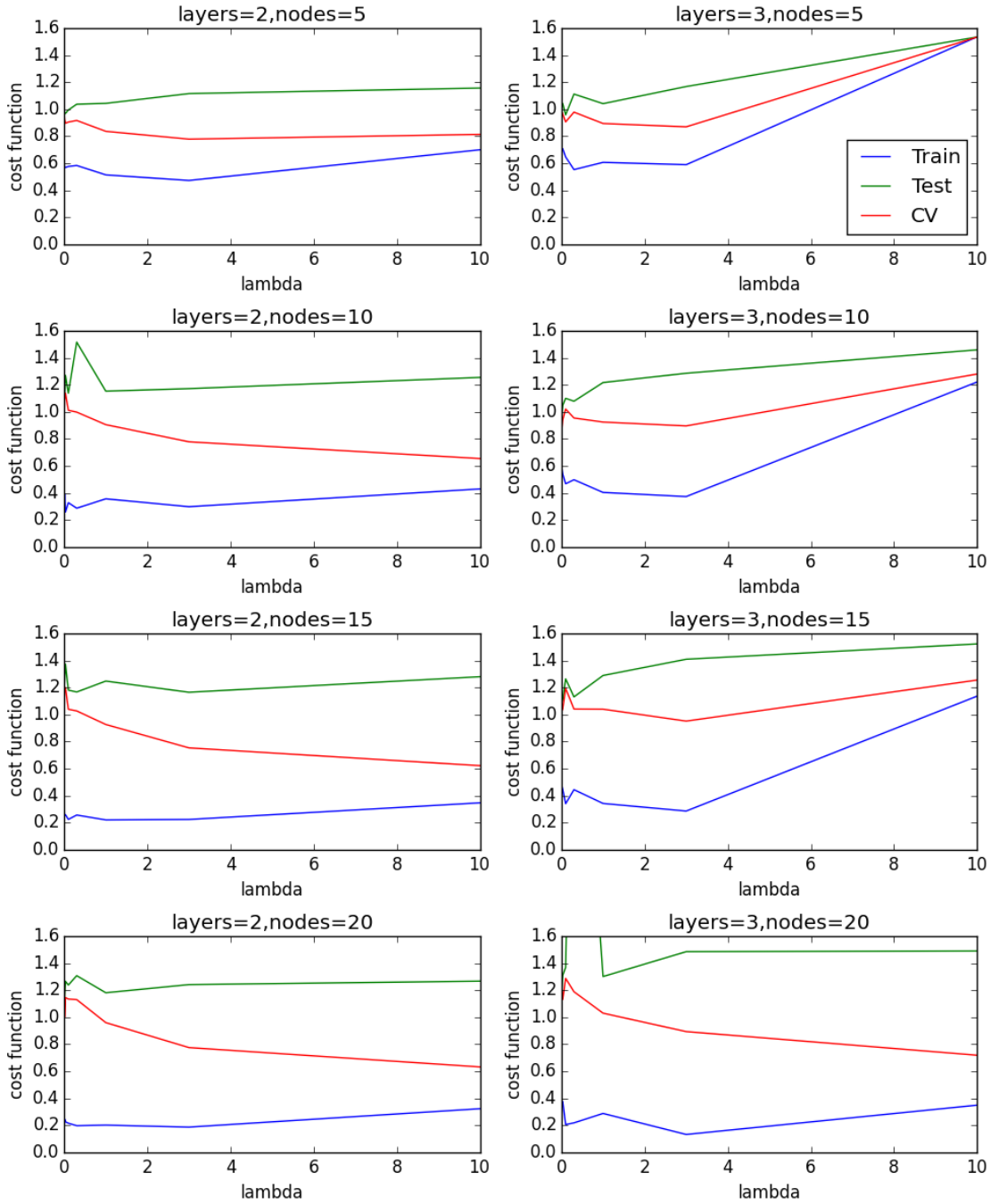

Figure 2.4: Average cost functions of different configurations of `LZComp` to determine the best configuration for our study. The results presented here are from the testing of the SAMI Survey. The left side shows the results of a two hidden layer configurations. The right side presents the results of a three hidden layer configuration. The plots present the cost function of the training, testing and cross-validation sets as a function of the regularisation parameter λ of 0.1, 0.3, 1, 3, and 10.

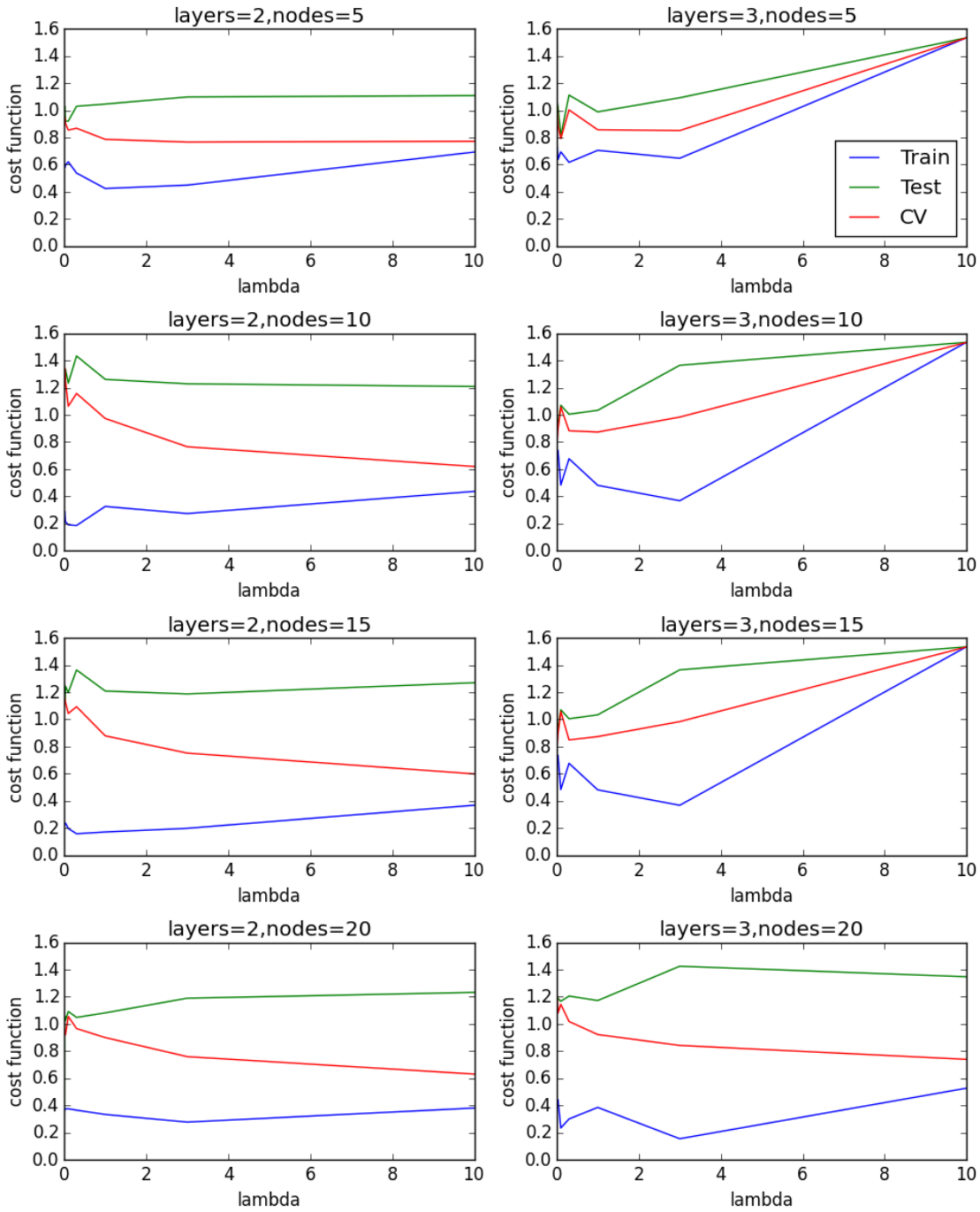

Figure 2.5: Randomised sample 1: Cost functions of different configurations of `LZComp` to determine the best configuration for our study. The left side shows the results of a two hidden layer configurations. The right side presents the results of a three hidden layer configuration. The plots present the cost function of the training, testing and cross-validation sets as a function of the regularisation parameter λ.

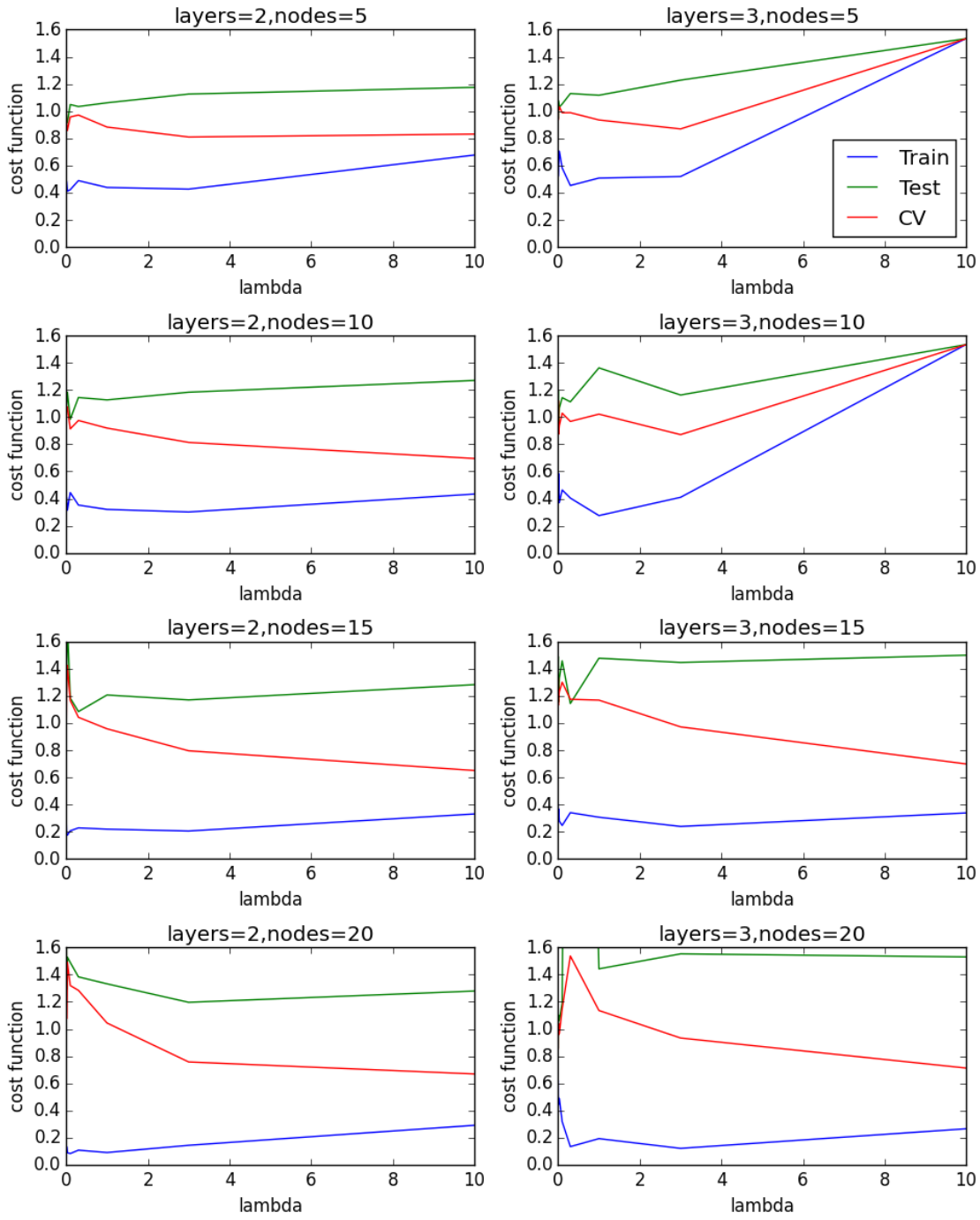

Figure 2.6: Randomised sample 2: Cost functions of different configurations of `LZComp` to determine the best configuration for our study. The left side shows the results of a two hidden layer configurations. The right side presents the results of a three hidden layer configuration. The plots present the cost function of the training, testing and cross-validation sets as a function of the regularisation parameter λ.

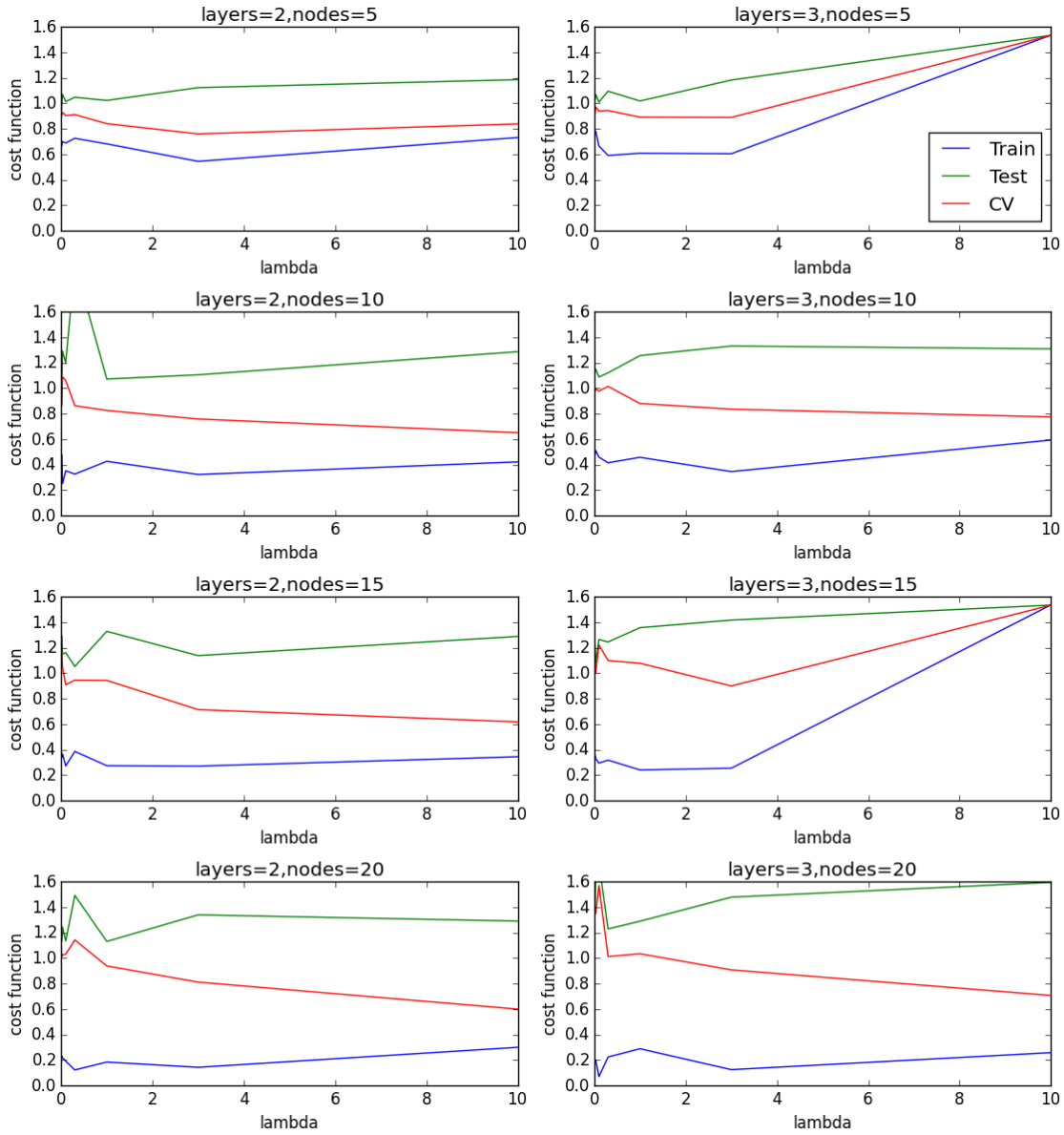

Figure 2.7: Randomised sample 3: Cost functions of different configurations of `LZComp` to determine the best configuration for our study. The left side shows the results of a two hidden layer configurations. The right side presents the results of a three hidden layer configuration. The plots present the cost function of the training, testing and cross-validation sets as a function of the regularisation parameter λ.

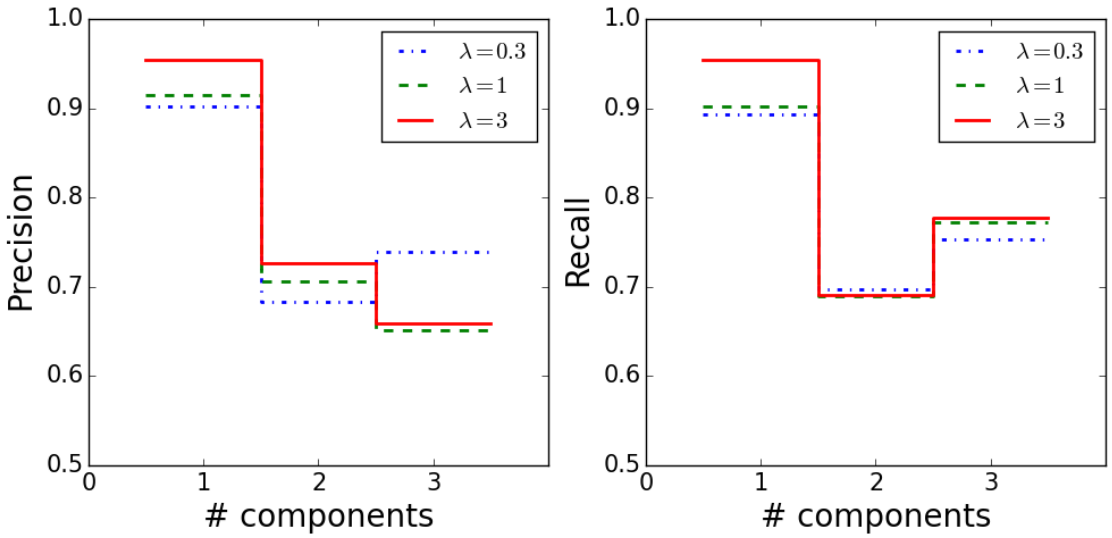

Figure 2.8: Left: The precision of `LZComp` using different values of the regularisation parameter λ. Right: The recall of `LZComp` using different values of the regularisation parameter λ. See section 2.6 for a detailed explanation of precision (precision measures how often `LZComp` will misclassify an example as a particular number of components) and recall (the recall measures the consistency `LZComp` has for each classification related to how often it misclassifies an example of that component number).

precision in making its decisions.

Equations 2.5 and 2.6 show how the recall (R) and precision (P) values are calculated for each number of components. N is the number of examples which LZ (`LZComp`) and T (the Trainers) classify with the conditions for LZ and T as stated in the equations. Together these describe how well `LZComp` can classify examples in comparison to the Trainers. These values are calculated for each component classification,

$$R_{LZ} = \frac{N_{LZ=T}}{\sum N_{LZ,T=1,2,3}} \tag{2.5}$$

$$P_{LZ} = \frac{N_{LZ=T}}{\sum N_{LZ=1,2,3,T}} \tag{2.6}$$

More completely, the recall R_{LZ} measures the consistency `LZComp` has for each classification related to how often it misclassifies an example of that component number. For example, if `LZComp` correctly classifies 200 examples as 1-components but misclassifies 50 1-component examples as 2- or 3-components, it has a recall of $R_1 = 200/250 = 80\%$ for

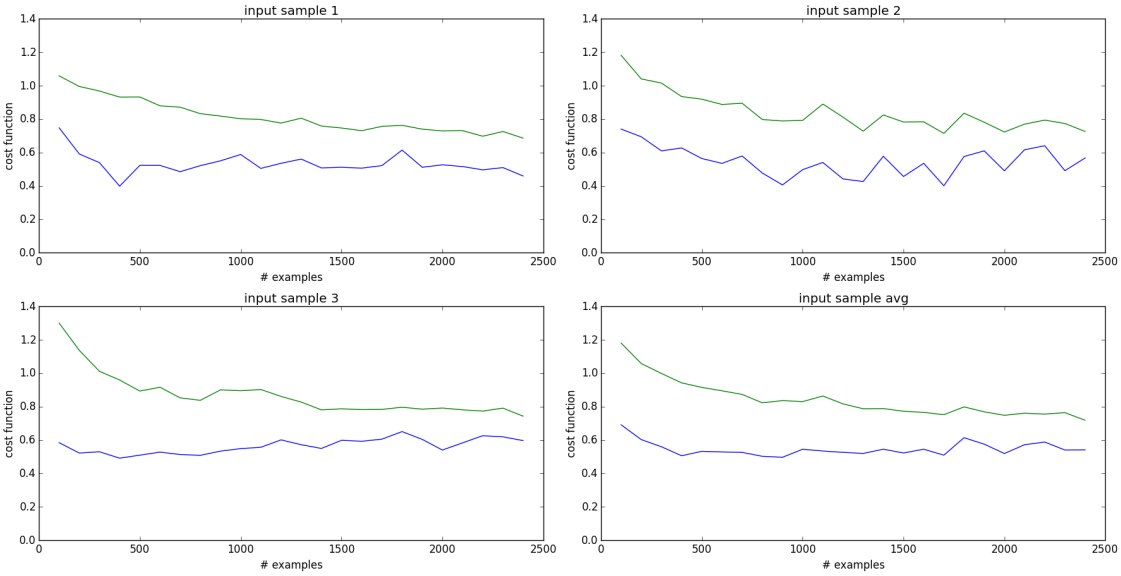

Figure 2.9: The blue line indicates the cost function of the training set as we increase the number of examples used to train with. The green line indicates the cross-validation cost function. The three input samples are derived from different subsets of the labelled examples assigned to either the training, testing, or cross validation sets. The bottom right plot shows the average cost functions calculated from all three differing sets of examples. The survey testing presented here is the SAMI Survey. Results form the S7 Survey are similar.

1-component classifications. A recall value is calculated for each classification. The precision P_{LZ} measures how often `LZComp` will misclassify an example as a particular number of components. For example, if `LZComp` correctly classifies 200 examples as 1-components but also incorrectly classifies 25 examples (of 2- and 3-components) as 1-component, then `LZComp` has a precision of $P_1 = 200/225 = 89\%$ for 1-component classifications. Precision values are, like recall values, calculated for each classification.

This same comparison of precision and recall can be repeated using the individual trainers to show how `LZComp`s performance compares to an astronomer's visual inspections. Taking the spaxels from the training galaxies that were not used in the training of `LZComp` and including a completely unseen galaxy, new component maps were formed from N-1 trainer classification maps. For each trainer a new combined classification map was created using the remaining four trainers for SAMI. For S7, the combined maps used two of the three trainers. There was a large spread in the agreement of classifications through the recall and precision values, as is shown in Figure 2.10 by the solid lines. The dashed lines in Figure 2.10 present the resulting recall and precision values for each of the two surveys using `LZComp`. The largest spread in the ability of people agreeing with each other is between 2- and 3-components, while agreement is very good over 1-component fits. It was also shown that `LZComp` does as well at making the classification decisions for spectra as using individual people.

In addition to the histograms presenting the recall and precision limits of the Trainers and `LZComp`, the matrices in Figure 2.11 graphically represent the numbers of examples with each possible label. Each element of the matrices has been normalised by the total number of trainer-labelled examples for that particular label in order to be able to see the smaller numbers of 2- and 3-components on the same plot as the 1-components. The top panel presents the matrix for the SAMI sample and the bottom presents the matrix for the S7 sample. The figure shows that `LZComp` is making the same decisions as the Trainers for the majority of examples, even including a galaxy in both surveys that was not included in the training set of `LZComp`.

Using the models learned during training, `LZComp` is able to successfully classify new spectra. To show this result explicitly, Figures 2.12 and 2.13 present the component maps defined by `LZComp` and the Trainers for the S7 galaxy and the SAMI galaxy not seen during training, respectively. `LZComp` defines a component map that is between all of the Trainers

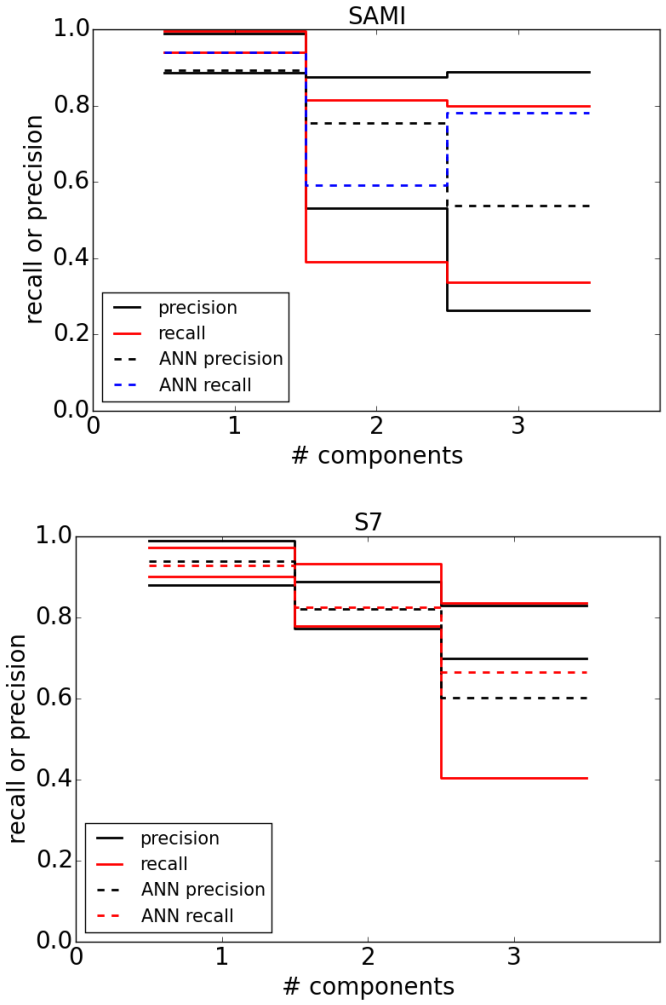

Figure 2.10: The minimum and maximum values of the precision and recall of the sets of trainers to the precision and recall of `LZComp` for the SAMI (top) and S7 (bottom) samples. The solid black lines show the min and max values of precision for each component number, the solid red lines indicate the minimum and maximum values of the recall for each component number from the Trainers in comparison to each other. The dashed lines show results from training using `LZComp`.

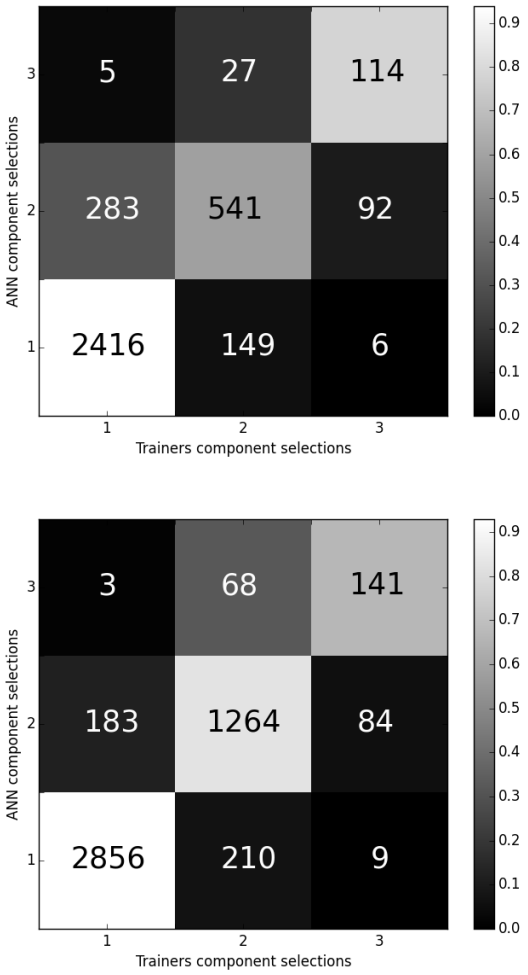

Figure 2.11: Top: Matrix presenting the fractions of examples `LZComp` selects the same label as the combined trainers for the SAMI examples. Bottom: The same but for the S7 sample. The fractions are calculated in the same way as the recall value, measuring the fraction of each example selected by `LZComp` divided by the total number of the same example labels as chosen by the Trainers. An ANN that selects exactly as the combined Trainers would show white along the diagonal and black in the rest. The Trainers do not agree 100% of the time and therefore it is not a requirement that `LZComp` exactly match the combined Trainers.

maps in both the SAMI and S7 galaxies.

The recall and precision of `LZComp` is as good as the human trainers. On the full training sets for SAMI and S7, each trainer selected classifications based on what they are seeing. By using the spaxels for which a majority of trainers agreed it avoids any individual favouritism towards a particular number of components from a trainer. Figure 2.14 presents the number of spaxels that each trainer classifies as each number of components for the testing and CV example sets and the unseen galaxy for SAMI and S7. In both SAMI and S7, `LZComp` classifies the components in a similar manner to the Trainers, following the average favouritism of the Trainers as a whole. `LZComp` favours 1- and 2-components, but we can see that two of the three trainers also favour 2-components over 1-components. The case may be that the S7 galaxies do have more 2-component spectra than 1-component spectra. S7 is selected to sample very interesting Seyfert galaxies that are expected to require multi-component fits to express the data.

This study also compares the results, including precision and recall, of `LZComp` on a completely unseen set of three galaxies to the labels made by the Trainers. The results include the number of components `LZComp` selects, and the precision and recall, all compared to the results of the Trainers with the same set of three galaxies.

The requirement of a final comparison set is because the initial accuracy is calculated over labelled examples that are parts of the same galaxies that are used in training. This study assumed, and maintains, that the input parameters that make up the feature vectors of each example are mostly galaxy independent.

The number of components, precision and recall, and confusion matrix are presented in Figures 2.15 and 2.16 for SAMI and S7, respectively. In comparison to the results of the previous testing `LZComp` still performs as well as our Trainers in making the component selections. Except in the instance of 3-component selections for both SAMI and S7 where `LZComp` has a lower precision score than the set of three Trainers. This lower precision for S7 is seen in the previous results, which found a lower precision score but still higher than that of the SAMI Trainers of the SAMI sample. Thus for S7 this lower precision score is expected from the comparison set of three galaxies. The lower precision score was not seen in SAMI previously, however unlike S7 the precision is marginally below the lower limit set by the SAMI Trainers, and thus also allowed for the purpose of this study.

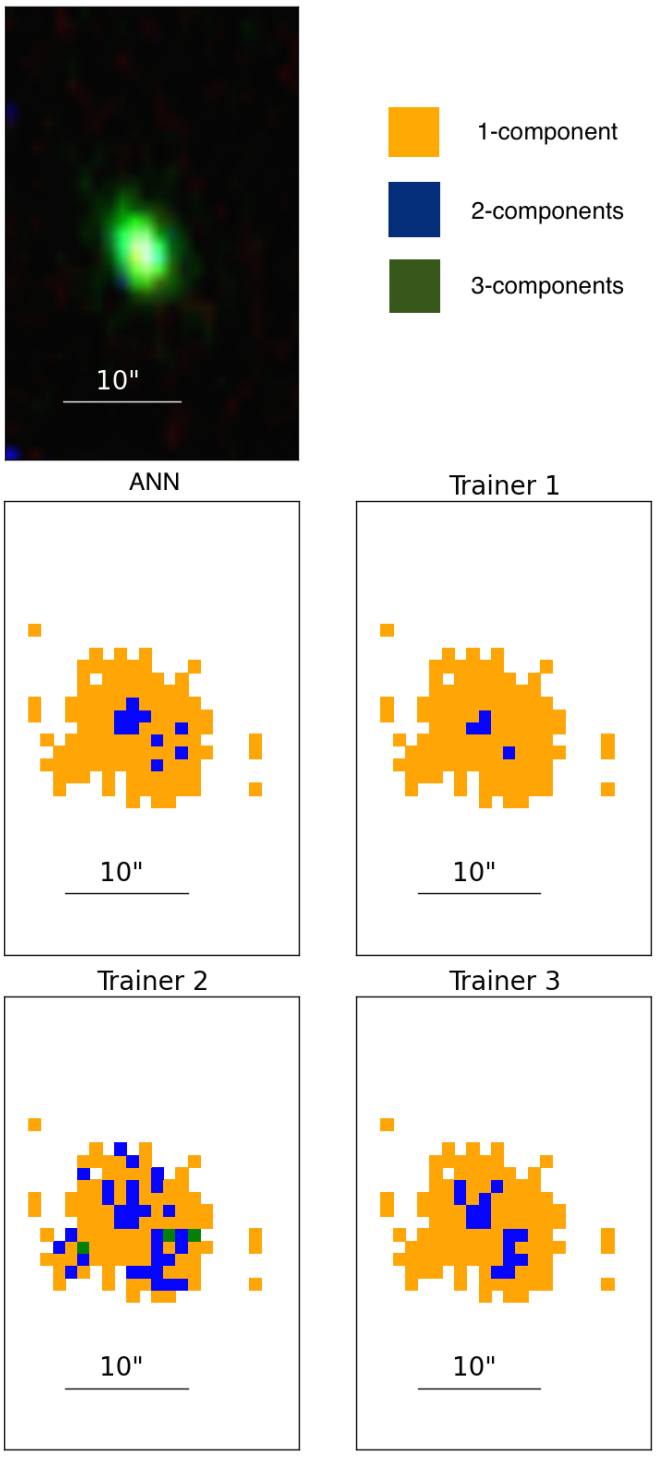

Figure 2.12: Component maps defined by `LZComp` and the three S7 trainers for NGC4044 in S7. Green for a 3-component fit, blue for a 2-component fit and yellow for a 1-component fit. Top left image is a three-colour image created from WiFeS observation; blue [OIII], green [NII], red Hα emission.

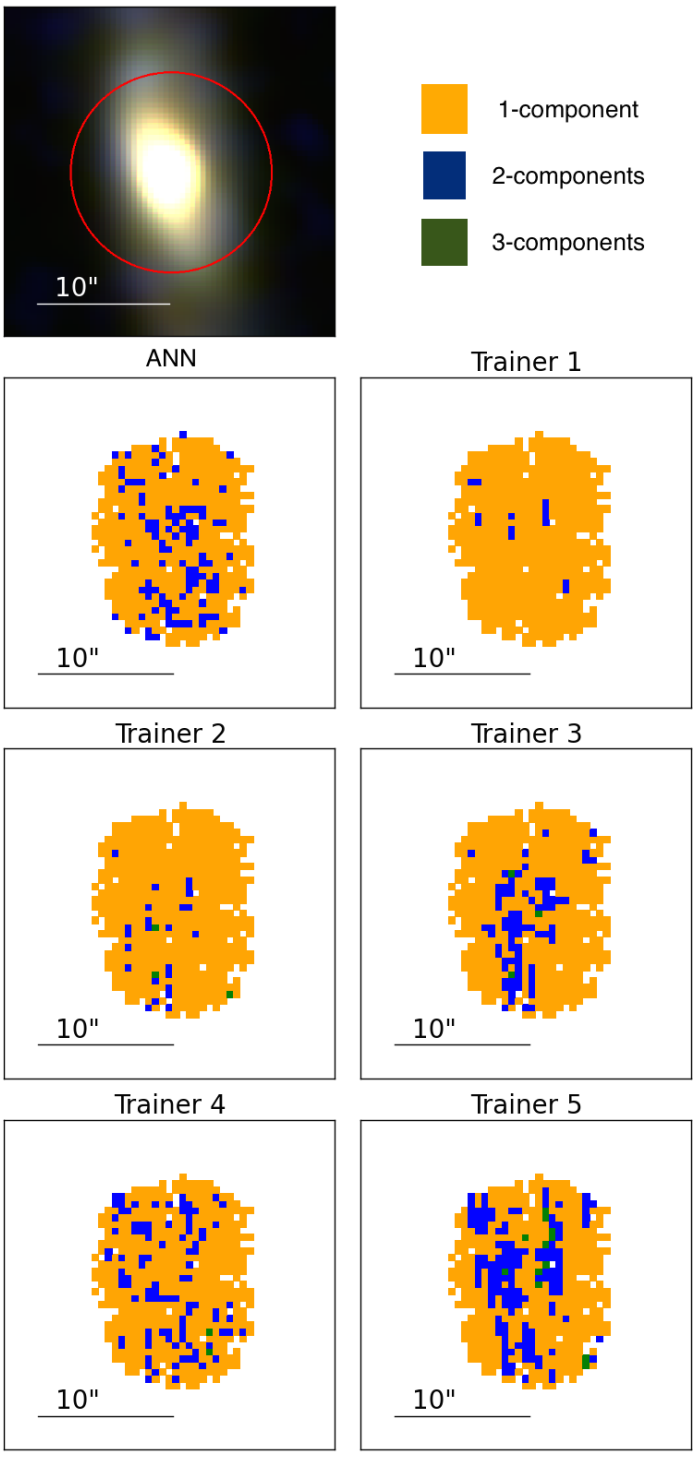

Figure 2.13: Component maps defined by `LZComp` and the five SAMI trainers for ID: 9011900367 in the SAMI Galaxy Survey. Green for a 3-component fit, blue for a 2-component fit and yellow for a 1-component fit. Top left image is an SDSS 3-colour image of this galaxy. Red r-band, green g-band, blue u-band. The red circle indicates the SAMI aperture.

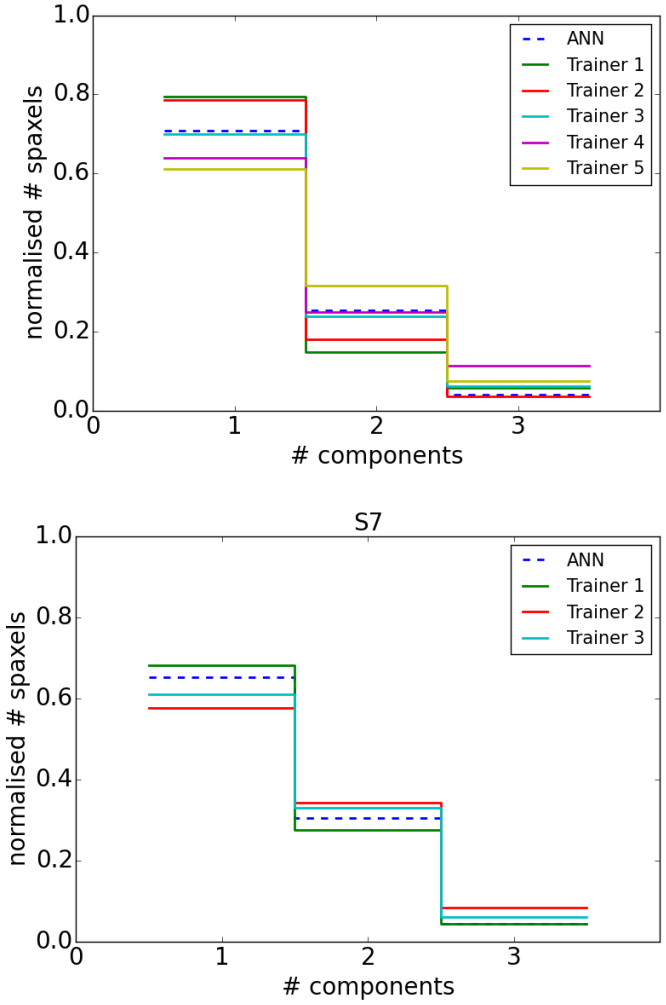

Figure 2.14: Top: A representation of how many 1-, 2-, or 3-component classifications made by each trainer (-) and ANN (- -) for the SAMI training set of galaxies. Bottom: A representation of how many 1-, 2-, or 3-component classifications made by each trainer (-) and ANN (- -) for the S7 training set of galaxies. In both training sets `LZComp` predicts similar numbers of 1-, 2-, or 3-components for the training sets.

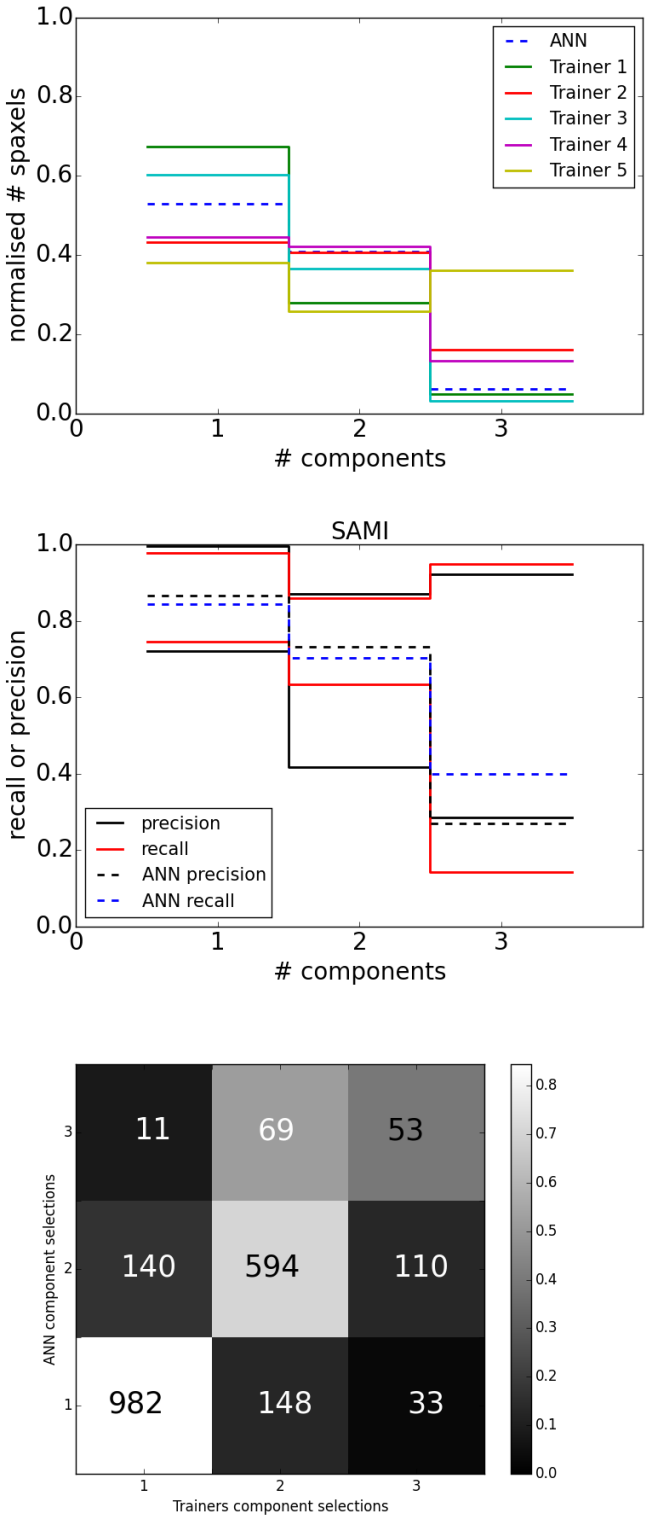

Figure 2.15: Top: number of components selected by `LZComp` and the five SAMI Trainers. Middle: Precision and recall values calculated on the comparison set of three unseen galaxies. Bottom: The relevant confusion matrix.

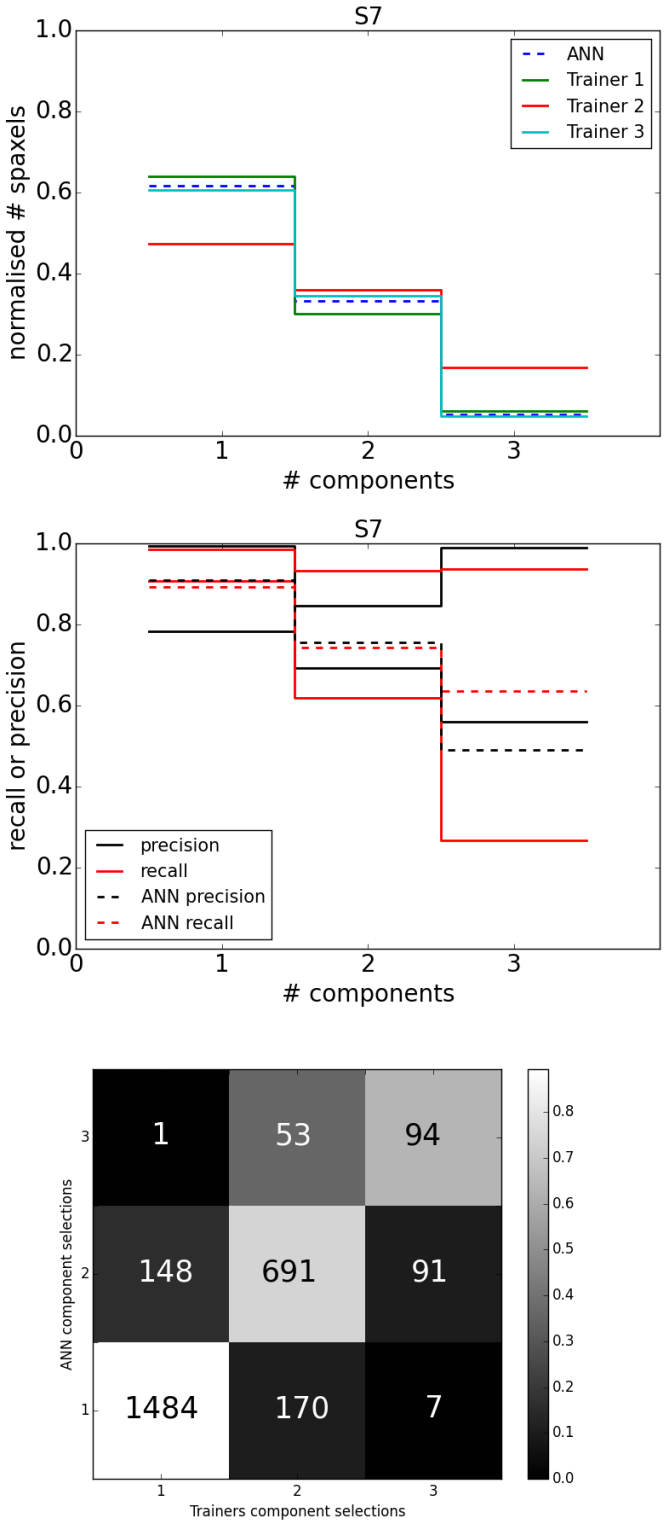

Figure 2.16: Top: number of components selected by `LZComp` and the three S7 Trainers. Middle: Precision and recall values calculated on the comparison set of three unseen galaxies. Bottom: The relevant confusion matrix.

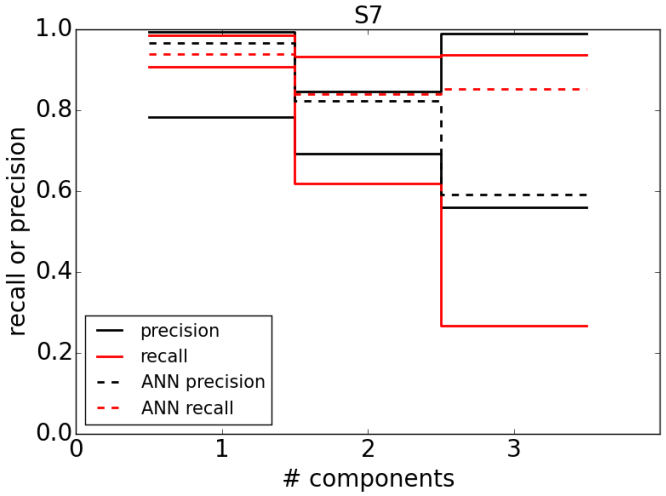

Figure 2.17: Precision and recall values calculated using a training set where all three S7 trainers must agree.

`LZComp` requires labelled training examples in order to learn how to make the different classifications on the number of Gaussian components that best fit each spaxel. In this study a majority rule was applied to examples that are given to `LZComp` to learn from. Another strategy for making the labelled examples could have been to require that all Trainers agree, which gives a higher degree of assurance that this is the best number of components but also decreases the number of examples available for learning and testing.

Tests were conducted on the precision and recall of `LZComp` if the agreement on the labels were to be increased. For S7 this meant requiring all three Trainers to agree on the labels that were then used for training and testing. For SAMI this meant that at least four or all five Trainers had to agree, in two separate tests.

The results of requiring all three S7 Trainers to agree are presented in Figure 2.17. The results of precision and recall from `LZComp` show promise in the top panel of this figure. However, what is not shown is the number of examples that were available for training in this instance. For example, there were $\sim$ 2000 1-component, $\sim$ 1000 2-component, and $\sim$ 100 3-component examples available for training. The skew in the numbers of examples is predominant throughout this study, but the significantly decreased number of 3-component examples available means the precision and recall of `LZComp` are calculated with low numbers.

Similar results are seen using the SAMI sample. In Figure 2.18 the precision and recall

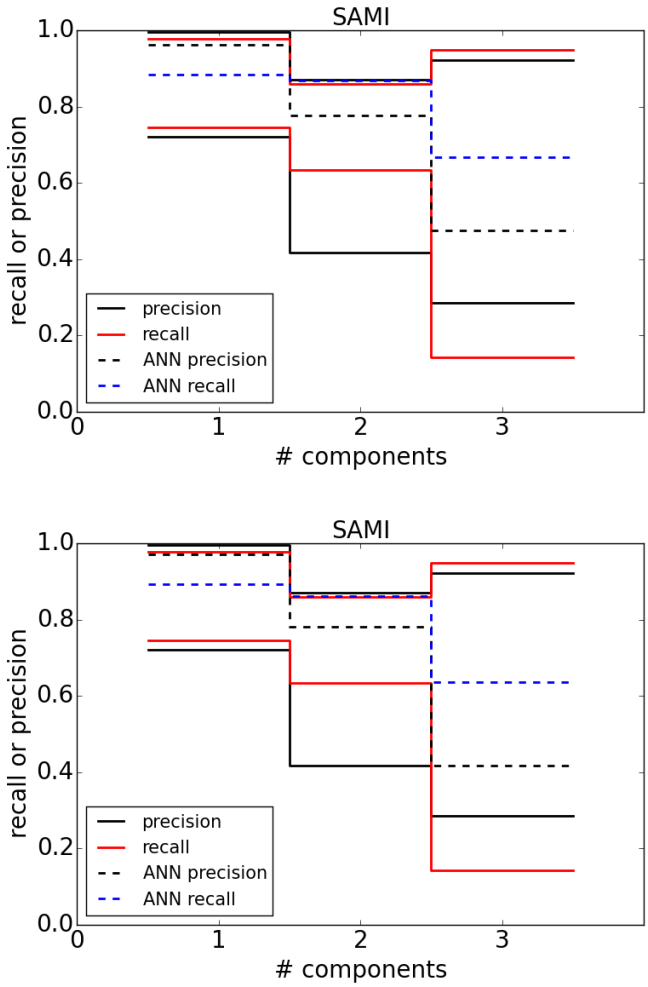

Figure 2.18: Top: Precision and recall values calculated using a training set where at least four SAMI trainers must agree on the example labels. Bottom: Precision and recall values calculated using a training set where all five SAMI trainers must agree on the example labels.

values are presented for the two situations; 1) when at least four Trainers must agree, and 2) when all five Trainers must agree, left and right respectively. Again, as with S7, the precision and recall seems to be good. However, requiring more Trainers to agree decreases the numbers of examples that can be used in training `LZComp`.

A solution to the lower numbers of examples for each type of component could be to increase the number of galaxies in the training set. However, this brings the discussion back to why an ANN solution was introduced in the first place; the time required to make the component selections needed to be decreased to allow astronomers a quicker step into studying the results of multicomponent emission line fits over manual classification. On top of this, the higher agreement will also begin to pick out only the spaxels where there

is a clean spectrum and clear fitting result. This is not always the case with spectral fitting and the majority rule allows spaxels which are more ambiguous to be trained on by `LZComp`.

2.7 Comparison to the F-test

In addition to comparing `LZComp` results to the Trainers, a comparison of the results of using an F-test to the Trainers was also made. Figure 2.19 presents the results of using an F-test on the training set of galaxies by comparing the recall and precision values obtained by the F-test. The F-test selects 1-components more often than our SAMI trainers. The precision obtained by using an F-test is comparable to people, but the recall is much lower, pointing to the fact that only $\sim 20\%$ of the spaxels the F-test classifies as 1-component agree with the Trainers. Due to the discrepancies among the Trainers in selecting 2- and 3-components, the F-test is comparable in both recall and precision for 2- and 3-components. In comparison to `LZComp`, however, the F-test is not as capable at representing an astronomer and their decisions. This result indicates that a selection via an F-test may not identify spaxels with multiple emission line components as well as humans or `LZComp`, missing some more interesting galaxies.

2.8 Application to S7 and SAMI

As presented in the previous sections, the `LZIFU` code (Ho et al., 2016b), in combination with an ANN, can be used to provide a reliable decomposition of the different emission-line components present in galaxies observed with integral field spectroscopy[4]. With the availability of a reliable decomposition analysis for multiple emission-lines spanning the full optical spectrum for each of the survey sources, it then becomes practical to undertake an in-depth analysis of the wide range of physical processes driving emissions with complex composite sources. Early examples of such analysis from the SAMI Galaxy Survey include phenomena such as; binary black-holes (Allen et al., 2015c), metallicity measurements of isolated HII regions in dwarf galaxies (Richards et al., 2014), and the identification of shocks and outflows in modest luminosity star-forming galaxies (Ho et al., 2014, 2016a).

[4]Note that this study uses the output of `LZIFU`, however, there is no reason the same application could not be made to emission line fitting by a code other than `LZIFU`.

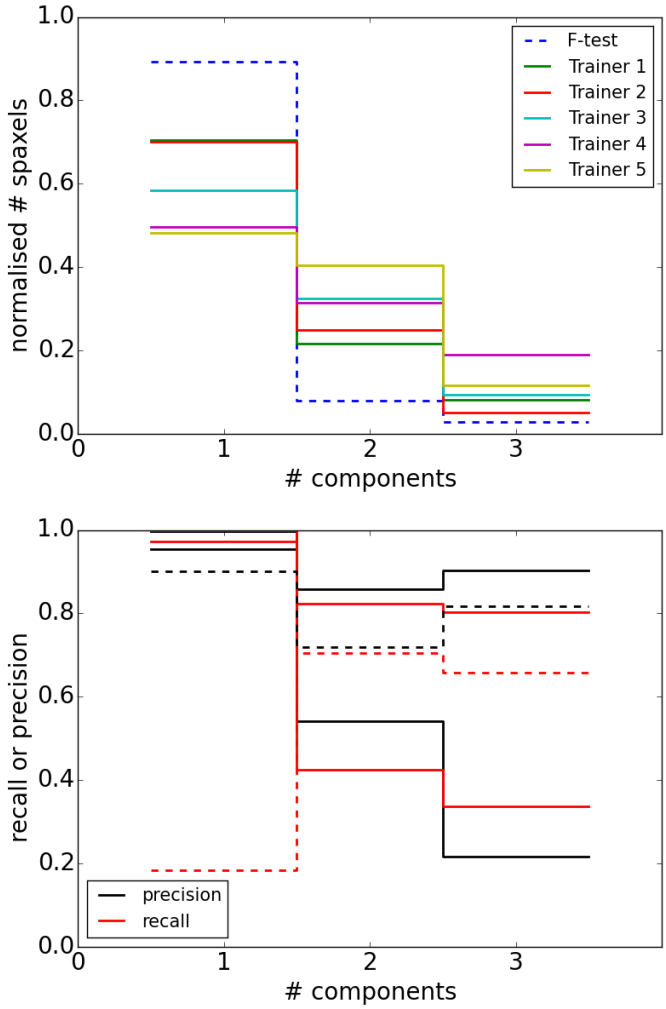

Figure 2.19: Top: A comparison of the number of 1-, 2-, and 3-components classified by the SAMI trainers (-) and using an F-test (- -). Bottom: A comparison of the recall and precision obtained by using an F-test on the SAMI training set of galaxies in comparison to our trainers against each other.

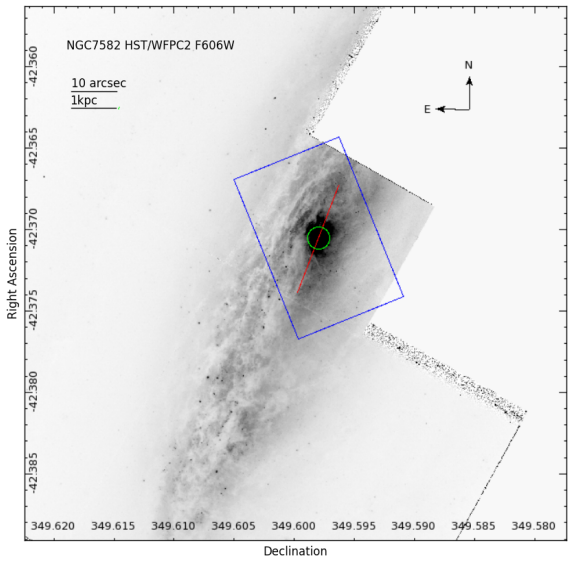

Figure 2.20: HST image of NGC5782. Blue box indicates the S7 FoV and the red line shows the major axis of the galaxy we have used in our analysis of the WiFeS data. The green circle indicates the centre of the galaxy.

The Hubble Space Telescope (HST) image of the Seyfert galaxy NGC7582 (PI:Michael Regan) is presented in Figure 2.20. The central region has been observed with WiFeS as part of S7 (blue rectangle in Figure 2.20). This galaxy has a large star-forming disk, visible in the image. Perpendicular to this disk is an ionisation cone with an opening angle of 110° that is excited by the central AGN, highlighted in Figure 2.21 and described in Dopita et al. (2015). The gas within this cone is highly ionised and extends to 15 kpc. The counter-cone is also visible through the optical observation, but is partly obscured by the dust of the star-forming disk. The red line on Figure 2.20 indicates the major axis and the circle indicates the centre where the AGN is located. The S7 observation of NGC7582 has been fit with 1-, 2-, and 3-components using `LZIFU` and then run through `LZComp`, to obtain the component maps. The decomposition obtained for NGC 7582 with `LZIFU` and `LZComp` is shown in Figure 2.21.

The decomposition of emission lines into different components enables the separation of the different excitation processes occurring within a galaxy. In NGC7582, the decomposition of the emission lines separates the galactic disk from the ionisation cone and counter-cone. In Figure 2.21, panels (a), (b), and (c) show the continuum map, 3-colour emission-line total flux map ([OIII], [NII] and Hα), and the [NII]/Hα total flux ratio map of NGC5782, respectively. Multi-component emission line fitting was necessary because

these lines are not always well described by a single Gaussian. The emission-line decomposition of NGC7582 is presented in Figure 2.21 panels (d), (e), and (f) by the velocities assigned to each component for each spaxel. Component one (d) contains the narrowest emission line components and traces the disk of the galaxy. The rotation curve of this disk gas is shown in panel (g) tracing the major axis along the galaxy. There is no turnover observed in the rotation curve because the S7 observations are looking at only the central regions of the galaxy. The second component, shown in panel (e), consists of the broadest emission line components and traces the ionisation cone. Verification of the cause of the broadest emission lines can be made by looking at the velocity of the second component as a function of distance from the centre in the area of the cones. Panel (h) shows that the counter-cone is partly obscured by the galactic disk. The cone and counter-cone are both moving material at a projected velocity of +/- 100km/s. The velocity plateaus in panel (h) suggest the front cone is outflowing. A possible counter-cone is observed, outlined by blue dashed lines. The remainder of the points in panel (h) are most likely due to the disk of the galaxy broadened due to beam smearing in the line of sight.

The third component is a secondary narrow component of emission. In the histograms of velocity dispersions for each component (Figure 2.21 panel g), these third components are located between the first and second and are labelled in red. These spaxels have separated narrow peaks with a broader underlying component. These components may be due to the ionisation of matter around or at the edge of the cone. To determine what causes this third component, the ionisation hardness of each component of each spaxel was examined using the [NII]/Hα diagnostic diagram (Baldwin et al., 1981). Each component is displayed (panel k) in a separate colour, this third component (red) shows high ionisation, above the Kewley et al. (2001b) diagnostic line. This result suggests that the emission may be shock-induced (Ho et al., 2014; Rich et al., 2015).

Although this research does not go into further detail on NGC7582, it has been shown that the decomposition of emission lines is important in understanding the detailed kinematics within a galaxy. McElroy et al. (2015) found it beneficial to fit each galaxy with `LZIFU` then use an F-test with harsh cut-offs to determine the component decompositions. In Section 2.7, however, it is demonstrated that `LZComp` is able to more effectively classify complex emission profiles and produces classifications which are more consistent with those of human astronomers.

Surveys are now creating more data than before, meaning that it is not always feasible to fit emission lines by hand, nor to make the component decisions by eye. This is where using an ANN is most advantageous. `LZComp` is able to process thousands of galaxies and assign the best representation of emission line fits as well as an astronomer in very little time. The quick processing of multicomponent emission line fitting then allows the deeper analysis of galaxies such as NGC7582 through multi-component emission-line fits.

Figure 2.22 presents the results of running the SAMI Galaxy Survey DR1 data (Allen et al., 2015b) through `LZComp`. The top panel shows a histogram of the number of Gaussian components classified by `LZComp` for all spectra. The total number of spaxels fit and classified for SAMI is 348,023, with the majority being one component fits. The bottom panel presents the histograms of fractions of each galaxy that are described by 1-, 2-, or 3-Gaussian components. The histogram helps to pin-point galaxies that show mostly star formation (mostly 1-component fits) and those galaxies that have multiple physical processes ongoing (greater than zero percentage of 2 or 3 component fits).

In a future study it is proposed to explore the prevalence of multicomponent emission lines in the SAMI Galaxy Survey. This study will consist of comparing the number of emission line components to the galaxy's mass, AGN activity, star formation history and other parameters, to search for correlations that may help in identifying certain types of galaxies or to help understand which types of galaxies contain combinations of certain physical processes. A study of galaxy type and component fitting is only possible with hundreds or thousands of galaxies all fit with multiple components. Using an ANN to make the classifications of the emission line fits has made it possible to do this study on a short timescale with `LZIFU` and `LZComp`, opening the possibility of statistical studies of multi-component emission processes for a large range of galaxies.

2.9 Timing breakdown

`LZComp` is faster than using astronomers in making the decisions about the best number of Gaussian components needed to adequately describe emission lines. For an astronomer, it can take up to an hour per galaxy to make the visual classifications. For small surveys this is a quick process; however, with increased survey sizes the time taken to visually classify every galaxy becomes increasingly long. For example, the time for the final SAMI survey of

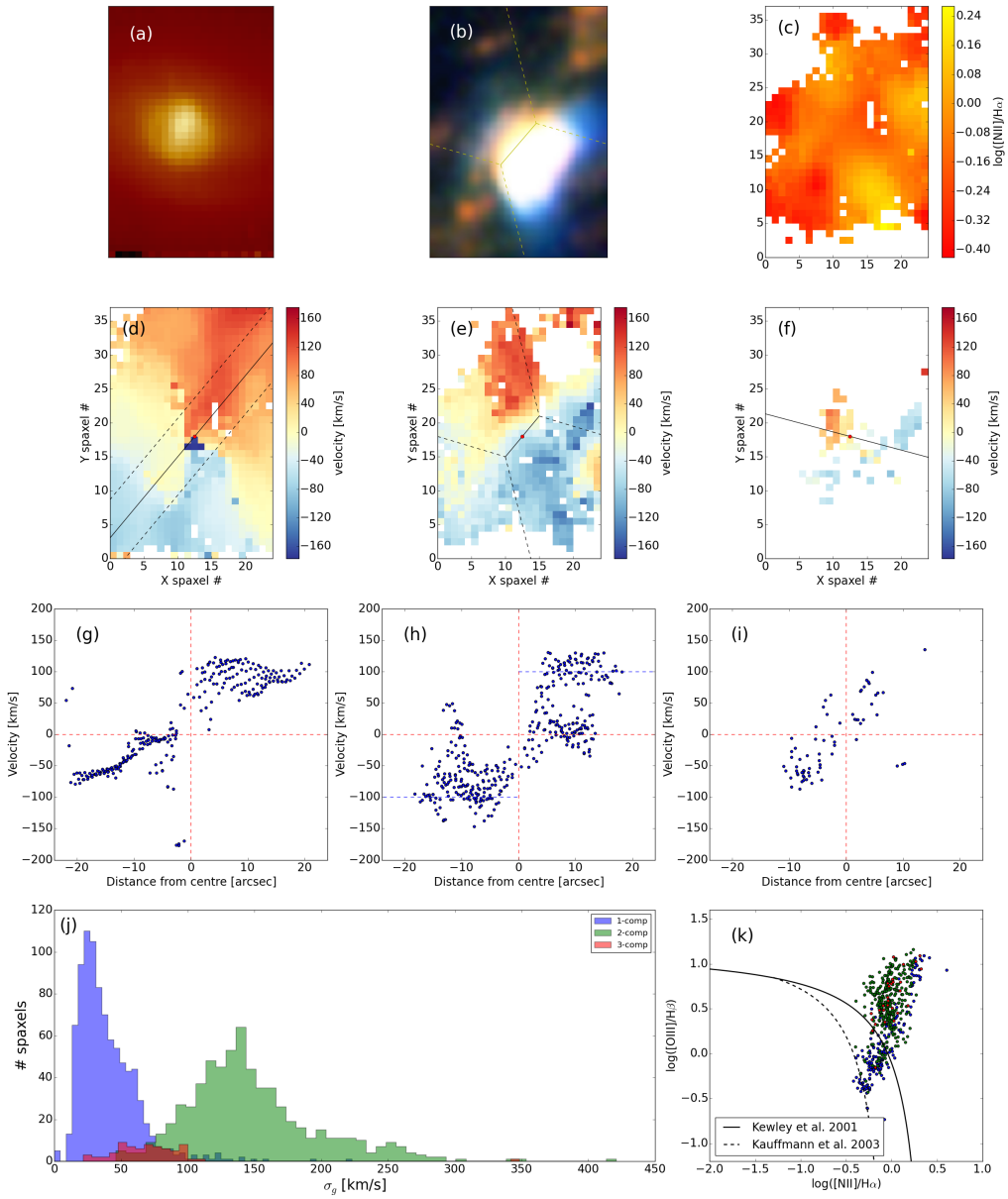

Figure 2.21: S7 data for Seyfert galaxy NGC7582. (a) Continuum image. (b) 3-colour image of emission lines: [OIII] - blue, [NII] - green, Hα - red. (c) Total [NII]/Hα flux map. (d) Velocity field of the first component, related to the disk. (e) Velocity field of the second component, related to the ionisation cone and counter-cone. (f) Velocity field of the 3rd component, related to the interaction at the edge of the ionisation cone. (g) Rotation curve of the gas disk, points taken from 1st component velocity within dashed lines of (d). (h) Rotation of gas due to the ionisation cones. The plateau at +/- 100 km/s is indicative of outflowing gas. (i) Rotation of 3rd component. (j) Histogram of velocity dispersions of each component. (k) [NII]/Hα diagnostic diagram with components colour-coded to show that the 3rd component has high ionisation, as is expected from being caused by the interaction of the ionisation cone.

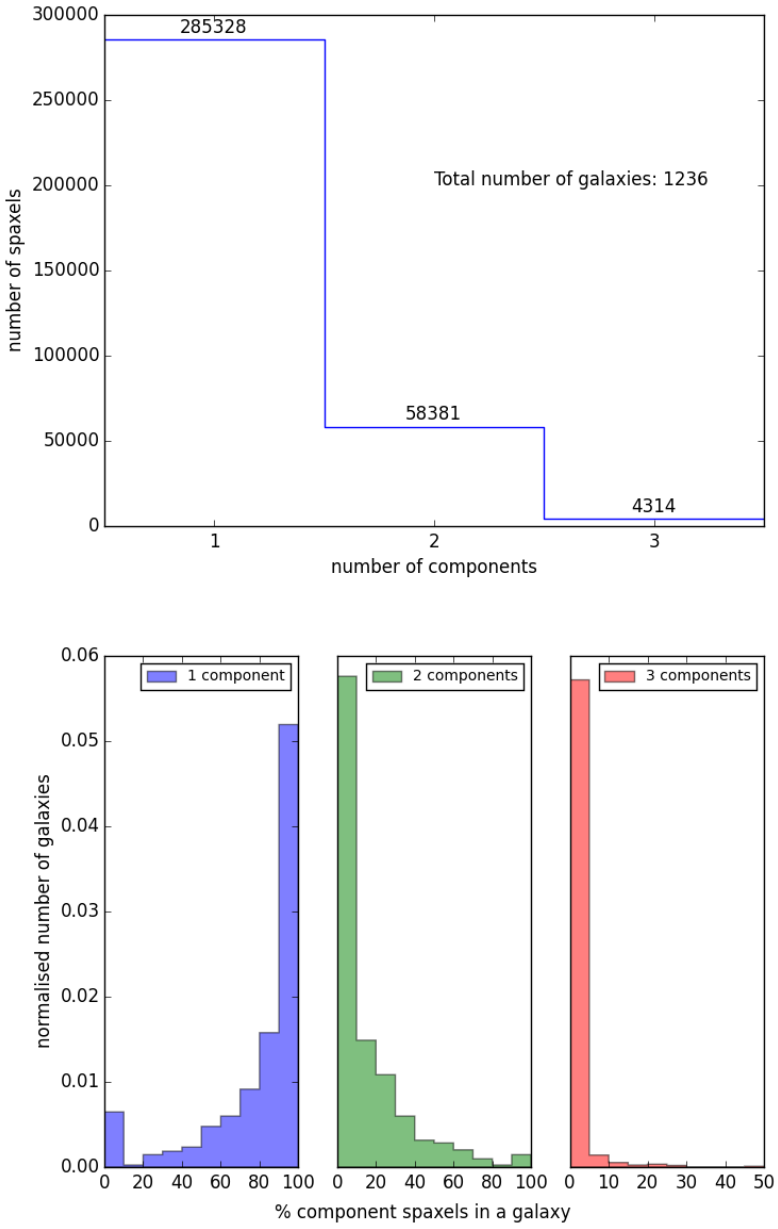

Figure 2.22: The top histogram presents the number of components classified for the 1236 current SAMI galaxies. The bottom presents the number of galaxies (normalised by the total number of galaxies) with different percentages of 1-, 2- or 3-component spaxels. Although a significant fraction of SAMI galaxies reveal a second component in many of their spaxels, very few galaxies have any spaxels with a third component.

3400 galaxies could take 3400 hours to visually inspect. Figures 2.10, 2.12, and 2.13 show that astronomers don't agree with each other all the time so using multiple astronomers is not necessarily a suitable solution. The time involved in using an ANN greatly decreases the amount of time required to reach the step of scientific analysis. The creation of the training set takes 8-9 hours with multiple astronomers creating labels for the same set of galaxies. The training of `LZComp` and devising of the configuration/regularisation parameter is on the order of a few hours of computation with overheads for decisions. To run a survey through `LZComp`, the majority of the time is taken by reading the information into `LZComp` and is on the order of minutes. This research has been used to decrease the amount of time required to make the decision on each spaxel of the best number of Gaussian components, by using an ANN instead of astronomers to make the majority of the decisions.

Two surveys were used where the information of each spaxel is put into a text file for easy reading and small file size instead of using a larger file like the original fits files. There is time (on the order of hours) required to put the information from the individual fitting of LZIFU fits files into a final merged fits files with the corresponding information to each number of components selected. For example, the current SAMI Survey of 1236 galaxies takes 16 hours on 8 CPUs to be put into their final form. This time to make the final cubes is still required if we were to use visual classification of every galaxy.

2.10 Conclusions

With the larger IFS surveys now in progress, automated complex emission line fitting is a must. `LZIFU` has automated the fitting process for up to 3 Gaussian components, but does not have the capacity to determine the best number of components for a particular spaxel. `LZComp` provides this capability. The complexities of differentiating between multi-component fits can be solved reliably and rapidly.

`LZComp` is a supervised ANN used to take in information produced by `LZIFU` and output the best fit classification for each individual spaxel in each galaxy of a survey. The breakdown of the accuracy into recall and precision of `LZComp's` results shows that its classifications are indistinguishable from the human trainers. The recall of `LZComp` for 1-component classifications is 94.2% for S7 and 92.3% for SAMI, while the precision of `LZComp` for 1-

component classifications is 95.3% for S7 and 94.7% for SAMI. The trend of recall and precision for the SAMI test sample continues with 2- and 3- component classifications. For the S7 test sample we see `LZComp` is capable of matching the Trainers in recall but not precision of 3-component classifications. Comparing the precision of the S7 3-component selections to the precision of the SAMI 3-component selections, the results are very similar between the surveys and so it is considered adequate to accept the lower value of 3-component precision. The comparison of an ANN with the human trainers, and analysing NGC7582 with the multi-component fitting results, shows that `LZComp` approach returns realistic numbers of components.

The training and testing of `LZComp` can be achieved in a matter of days. The final datacubes can then be created with the results of the `LZComp` decisions in hours. As mentioned earlier, manually making the decisions on the number of components is a time consuming process that is no longer suitable for large surveys using IFS observations. `LZComp` and `LZIFU` can be used together to negate this time consuming process to speed-up the pre-analysis of datacubes, so they are ready for scientific analysis quickly.

The use of an ANN is not limited to classifying the numbers of Gaussian components fit by `LZIFU` or to the SAMI and S7 surveys. It is clear that an ANN is capable of this classification process and thus could also be used on large IFU surveys to come, where the spectral resolution is high enough to fit multiple Gaussian components.

Chapter 3

The nature of composite classifications of merging and non-merging galaxies

3.1 Introduction

A composite galaxy is a galaxy with nuclear emission that is not clearly classified as being excited by a specific heating mechanism (e.g. an Active Galactic Nuclei (AGN) or star formation). This type of galaxy is classified by nuclear emission line ratios that lie between the Kewley et al. (2001b) and Kauffmann et al. (2003) diagnostic curves on the [NII]/Hα vs. [OIII]/Hβ diagnostic diagram (Baldwin et al., 1981). As described in Chapter 1, Section 1.3.2; the two diagnostic curves are used to separate the dominant excitation sources of star formation (below the Kauffmann et al. (2003) curve) and AGN excitation (above the Kewley et al. (2001b) curve). Galaxies that lie in the overlap composite region between these two curves are ambiguous in excitation source and cannot be easily classified.

The nature of these composite classified galaxies remains unclear. The composite region of the [NII]/Hα vs. [OIII]/Hβ diagnostic diagram (hereon after the [NII]/Hα diagnostic diagram) is neither dominated by star formation nor AGN excitation, but is possibly a combination of both (e.g. Panessa et al., 2005; Kewley et al., 2006; Yuan et al., 2010a; Scharwächter et al., 2011; Dopita et al., 2014b; Davies et al., 2014, 2016b). Shock excited gas also results in similar emission line ratios to that of AGN/LINER (Low Ionisation

Emission Region) excitation on the [NII]/Hα diagnostic diagram (e.g. Shull & McKee, 1979). Thus, the emission line ratios of composite galaxies on the [NII]/Hα diagnostic diagram may be due to a combination of shocks, AGN and star formation (e.g. Rich et al., 2014, 2015; Ho et al., 2015). Not only that, the Kewley et al. (2001b) diagnostic curve is a maximum starburst limit and thus composite galaxies may consist of evolved starburst galaxies, with no contribution from any other excitation source such as an AGN or shocks.

The study conducted by Belfiore et al. (2016), using IFS observation from the MaNGA survey, determined that post-AGB stars and weak AGNs can have similar emission line ratios. Post-AGB stars here include all stellar evolution stages subsequent to giant branch stars (Stanghellini & Renzini, 2000). This chapter does not look into the possibility of post-AGB stars contributing to the composite emission line ratios. However, there are several candidate LINER AGNs that may turn out to be post-AGB emission after further analysis.

Galaxy mergers are a scenario where such composite galaxies could arise. When two gas-rich galaxies interact or collide, material is driven towards the centres of the galaxies (e.g. Rupke et al., 2005a; Kewley & Kobulnicky, 2007). This in-falling material (gas and dust) can feed the massive black hole at the galaxies' centres, resulting in emission line ratios that are AGN-like (Sanders & Mirabel, 1996). A centralised star burst is also likely given the increase in gas density caused by the same infall of material. Finally, these large scale gas flows will also result in shocks (e.g. Rich et al., 2011). The combined emission from each of these scenarios would result in an aggregated composite-like emission line ratio on the [NII]/Hα diagnostic diagram (e.g. Veilleux et al., 1995a; Scoville et al., 2000; Arribas et al., 2004; Springel et al., 2005; Alonso-Herrero et al., 2006; Yuan et al., 2010a; Hopkins et al., 2012; Rich et al., 2015). All three scenarios could occur at the same stage to produce composite emission line ratios. The combination of any of these scenarios is most likely between the close and diffuse merger stages (see Chapter 1 for definition of merger stages), before galactic-scale winds clear the gas and dust to reveal AGNs within the central region (Hopkins et al., 2012).

Yuan et al. (2010a) studied the changes in excitation source of galaxies as a function of merger stage. Their composite galaxies were assumed to all be starburst-AGN combination galaxies. Yuan et al. (2010a) discovered that in one of their samples of galaxies (the 1 Jy Ultra Luminous InfraRed Galaxy sample) composites were most common in the

diffuse merger stage. This result led to their conclusion that the starburst-AGN composite galaxies were a bridging classification between the merger stages of separated star forming galaxies and coalesced Seyfert AGN host galaxies. However, the presence of shocks caused by the in-falling gas or a central starburst, which could be misconstrued as AGN emission, was not investigated, and no investigation was made into confirming AGNs.

A caveat of Yuan et al. (2010a) is the use of the metric d_AGN as a measure of the relative fraction of AGN excitation in an emission line ratio for their composite galaxies. The value of d_AGN is calculated using the [OI]/Hα vs. [OIII]/Hβ diagnostic diagram (hereon after the [OI]/Hα diagnostic diagrams) and associated diagnostic curve. On the [OI]/Hα diagnostic digrams the emission line ratios can be separated into AGN types of LINER and Seyfert. However the separation of shocked and LINER caused emission line ratios is still difficult with the [OI]/Hα diagnostic diagrams without complementary analysis.

Panessa et al. (2005) examined six composite barred spiral galaxies from the survey conducted by Moran et al. (1996). These objects have X-ray luminosities typical of broad-line AGNs, ranging from 1.5×10^{42} to 5×10^{43}erg s^{-1} in the ROSAT energy band (0.1-2 keV) and are optically classified as composite galaxies. The results of their study determined that three galaxies could possibly host AGNs, while the remaining three were more likely to be starburst galaxies. This study also did not investigate the presence of shocks in their galaxies as a possible cause of the composite classification, but these results hint that composites do not necessarily host AGNs

Rich et al. (2010) investigated NGC 839 for the presence of galactic scale shock excited super wind. In their identification of the shock-excited gas they determined that the shock excitation was pushing the optical emission line ratios observed from the galaxy into the composite region of the [NII]/Hα diagnostic diagram. This is a strong indication that shocks could be a contributing factor to composite classified galaxies.

If shocks and AGNs have both been used to explain the composite nature of merging galaxies, it may also be the case for composite galaxies not undergoing a merge, e.g. the isolated bar spiral galaxies studied in Panessa et al. (2005).

These previous studies of optically composite galaxies have determined that not all composite galaxies host an AGN but it is unclear whether different composite classes correlate

with different galaxy types. This chapter will show that composite galaxies, although having an AGN-like emission line component in the [NII]/Hα diagnostic diagram, are also not always hosts to AGNs, except in the case of isolated spiral galaxies. For this morphological type the use of d_AGN as a measure of the AGN relative fraction can be accurate. However, for isolated bar galaxies and merging galaxies more caution is needed. The possibility of shock excited gas also needs to be accounted for in composite galaxies.

A distinction can be made between shocks and AGNs using X-Ray emission and Infrared (IR) observations. This chapter uses Chandra X-ray observations to determine if AGN-like optical emission is caused by an AGN or shocks. As well as using the results of a previous IR study into the excitation sources of a subset of the galaxies investigated here.

The nature of composite galaxies, and hence interpretation of composite emission line ratios, is explored in this chapter. Integral Field Spectroscopic (IFS) observations are used in this chapter to investigate the spatial and spectral separation of different excitation sources. Resolved spectroscopy is essential for decomposing the complex nature of composite galaxies. In order to disentangle the various spatial components of the ionised gas, and to disentangle the kinematics, IFS is required. IFS observations provide an efficient method for gathering resolved spectroscopic information. IFUs have the advantage of being able to observe targets over a wide spectral range with decent spatial sampling ($< 1\,$kpc on average). The spatial resolution of IFS observations can be used to resolve and better understand the composite nature of the sample of merging and non merging composite galaxies.

The morphology of a composite galaxy is also important in understanding their composite natures. Previous studies have not specifically studied composite galaxies of different morphologies. This chapter explicitly separates and compares galaxies by morphology (isolated spiral galaxies, isolated bar galaxies, and mergers) in order to identify the excitation sources that are a function of galaxy morphology.

The sample of composite galaxies used in this study is described in Section 3.2. Section 3.3 describes the derived quantities obtained through the optical IFS observations of each galaxy and the X-ray observations of 10 of the composite galaxies. A discussion of the previous IR study into the excitation sources of the WiGS (Rich et al., 2015) galaxies is in Section 3.4. Each possible excitation source is investigated separately in Sections 3.5, 3.6, 3.7, and 3.8 for AGNs (optical and X-ray analysis), shocks and star formation respectively.

The results of identifying the excitation sources of each composite galaxy are discussed in Section 3.9. This chapter concludes in Section 3.10.

3.2 Sample

The composite galaxy sample used in this chapter is derived from two Integral Field Spectroscopic (IFS) surveys of nearby galaxies. The two samples are complementary in the types of galaxies they have observed. The main survey of galaxies (WiGS, Rich et al., 2015) are merging galaxies, while the secondary survey (CALIFA, Sánchez et al., 2012) includes many more isolated galaxies as a control group of composite galaxies. The use of two surveys allows the comparison of the composite nature due to mergers, to that of isolated galaxies where the same physical processes such as massive in-falls of material are not necessarily occurring.

WiGS

The WiFeS GOALS Survey (Rich et al., 2015) is a subset of 27 galaxy systems from the GOALS (Great Observatory All-Sky LIRG Survey; Armus et al., 2009) sample, chosen to be observable by the WiFeS (Wide Field Spectrograph, a dual-beam, image-slicing integral field unit, Dopita et al., 2007) instrument on the ANU 2.3m telescope, with redshifts $z < 0.05$.

A single pointing of the WiFeS instrument provides a $25'' \times 38''$ field of view with $1''$ spatial binning. The setup used for these observations produced a spectral coverage of $3700 - 5700$ Å for the blue spectra, at a resolution of R ~ 3000 (100 km/s) and $5700 - 7000$ Å for the red spectra at a resolution of R ~ 7000 (45 km/s). A full description of the individual observations is in Rich et al. (2015).

The WiGS sample contains 27 galaxy systems at different stages of merging. (See Section 1.3.1 for detail of merging stages.)

CALIFA

The Calar Alto Legacy Integral Field Area Survey (Sánchez et al., 2012) is a statistically significant sample of nearly 600 galaxies within the redshift range of $0.005 < z < 0.03$. The sample used in this chapter is a subset of the main survey comprising the first 100 publicly released IFS observations (Husemann et al., 2013).

Catalogue	blue			red			spatial size
	λ range		resolution	λ range		resolution	
WiGS	$3700\text{Å} < \lambda < 5700\text{Å}$	R3000	100 km/s	$5700\text{Å} < \lambda < 7000\text{Å}$	R7000	45 km/s	$25'' \times 38''$ with $1''$ spaxels
CALIFA	$3650\text{Å} < \lambda < 4840\text{Å}$	R1650	60-80 km/s	$3745\text{Å} < \lambda < 7400\text{Å}$	R850	110-210 km/s	$74'' \times 64''$ with $1''$ spaxels

Table 3.1: Comparison of WiGS and CALIFA datacube attributes. WiGS is a survey of merging galaxies. CALIFA covers a range of galaxy morphologies.

The CALIFA Survey uses the PPAK IFU of the PMAS instrument (Roth et al., 2005) with a $1.3'$ field of view. Two overlapping gratings were used (V500 and V1200) with wavelength coverages of $3745 - 7500$Å and $3650 - 4840$Å, respectively. The velocity resolutions for the two gratings are $100 - 210$km/s and $60 - 80$km/s, which is a lower resolution than required for the identification of shocks using velocity dispersions (discussed in Section 3.3). A comparison between the two surveys is made in Table 3.1.

3.2.1 Defining a composite galaxy

In single fibre studies of galaxies such as the Sloan Digital Sky Survey (York et al., 2000), the central emission line ratios on the [NII]/Hα diagnostic diagram are used to determine the excitation classification of the galaxy. In IFS studies there is a choice of aperture size that can be used to mimic the single fibre observations. In this chapter a 1 kpc physical circular aperture on the nucleus of each galaxy was chosen to be used in determining the excitation classification. This aperture was chosen because (a) it is comparable to the angular projected size of an SDSS $3''$ fibre on a galaxy at redshift 0.016 and (b) a physical size has been used to ensure that the region of a galaxy extracted is physically the same in each case, independent of redshift.

The central emission line ratios of each galaxy in WiGS and CALIFA are presented in Figure 3.1. The figure is of the [NII]/Hα diagnostic diagram with points coded as follows: WiGS galaxies are represented by circles and the CALIFA galaxies are represented by crosses. The galaxies which fall into the composite region of the [NII]/Hα diagnostic diagram, between the Kewley et al. (2001b) and Kauffmann et al. (2003) diagnostic curves, are blue (WiGS) and orange (CALIFA).

There are a total of 32 composite galaxies in this sample. However, a signal-to-noise cut

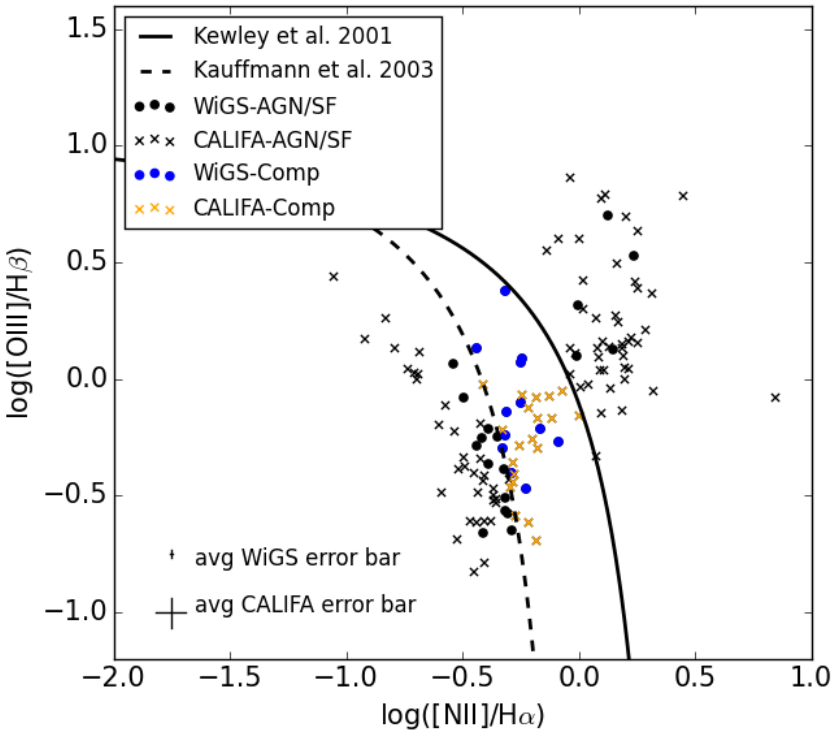

Figure 3.1: Emission line ratios of the central 1kpc for all WiGS and CALIFA galaxies. The Kewley et al. (2001a) diagnostic curve, indicating the lower boundary of AGN emission line ratios, is shown in solid black and the Kauffmann et al. (2003) diagnostic curve, indicating the upper bound on star-forming emission line ratios, is shown by the dashed black line. The CALIFA galaxies are shown by the orange or black crosses and WiGS galaxies by the blue or black circles. The orange and blue coloured points are the galaxies classified as composite from this diagram and make up the 30 composite galaxies in this chapter.

of 3 is made on the strong emission lines, Hα, [NII]λ6583, Hβ, and [OIII]λ5007, which reduces the sample to 30 composite galaxies; 12 from WIGS and 18 from CALIFA. The morphology make-up of the sample is 13 merging galaxies (10 from WiGS and three from CALIFA), six isolated spiral galaxies (one from WiGS and five from CALIFA), and ten isolated bar galaxies (one from WiGS and nine from CALIFA). The IDs, morphology types, and redshifts for each of these 30 composite galaxies are listed in Tables 3.2 (WiGS) and 3.3 (CALIFA). The galaxy morphologies are extracted from previous studies (Rich et al., 2015; Sánchez et al., 2012).

Identifier/ID	Morphological Class	z
(1)	(2)	(3)
WiGS		
IRAS F02072-1025	S0	0.0129
IRAS F06076-2139	pec/merger	0.0374
IRAS 08355-4944	pec/merger	0.0259
IRAS F10038-3338	pec/merger	0.0341
IRAS F10257-4339	pec/merger	0.0094
IRAS F13373+0105 West	pec/merger	0.0226
IRAS F16164-0746	pec/merger	0.0272
IRAS F17138-1017	pec/merger	0.0173
IRAS F17207-0014	pec/merger	0.0428
IRAS F18341-5732	SBab	0.0156
IRAS F20551-4250	pec/merger	0.0430
IRAS F23128-5919	pec/merger	0.0446

Table 3.2: The 12 composite galaxies in WiGS (1) - ID of each WiGS galaxy used throughout this thesis (2) - Morphological classification (Rich et al., 2015) (3) - systemic redshift. See individual notes on each galaxy, Appendix B, for more information about the individual systems and previous studies.

Identifier/ID	Morphological Class	z
(1)	(2)	(3)
CALIFA		
IC5376	Sab	0.0168
UGC00036	SA(r)a	0.0210
UGC01057	Sbc	0.0213
NGC0776	SAB(rs)b	0.0164
UGC03253	SB(r)b	0.0138
UGC05359	Sbc	0.0283
NGC4003	SB0	0.0217
NGC4676A	pec/merger	0.0221
NGC4676B	pec/merger	0.0220
NGC5000	SB(rs)bc	0.0187
UGC08267	S	0.0241
IC0944	Sa	0.0234
UGC08778	S	0.0109
NGC5394	pec/merger	0.0115
NGC6032	SB(rs)b	0.0143
UGC10205	Sa	0.0219
NGC7591	SBbc	0.0165
NGC7549	SB(s)cd pec	0.0158

Table 3.3: The 18 composite galaxies in CaLIFA (1) - Name of each galaxy used throughout this chapter (2) - Morphological classification (Sánchez et al., 2012) (3) - systemic redshift. See individual notes on each galaxy in Appendix B for more information about the individual systems and previous studies.

3.3 Derived quantities

3.3.1 Optical data

Values relating to the excitation mechanisms in galaxies are derived from the optical IFS observations. IFS, as has been explored in Chapter 2, can be used to both spatially and spectrally separate different physical processes. In order to determine the excitation mechanisms of the galaxy sample, emission line fluxes and velocity information can be extracted from their spectra through an automated process of emission line fitting.

In Chapter 2 the use of multi-component emission line fitting of galaxy spectra was explored in detail. The emission line fitting of the WiGS galaxies follows a similar process to that described in Chapter 2. The emission lines in each spectrum in each spaxel are simultaneously fit with 1, 2, and 3 Gaussians, representing three different velocity components. The continuum and emission line fitting for the WiGS galaxies was performed by Rich et al. (2015) using the IDL codes `UHSPECFIT` (Zahid et al., 2011) and `MPFIT` (Markwardt, 2009). These are processes that are also used within the emission line fitting process of `LZIFU` (Ho et al., 2016b) described in Chapter 2. The difference in the multi-component decisions to that of Chapter 2 is that the WiGS multiple components were determined by an Astronomer (Rich et al., 2015) and not an Artificial Neural Network (Chapter 2).

The emission lines in the CALIFA galaxies were fit using `LZIFU` (Ho et al., 2016b) with a single Gaussian component. The reason for only fitting a single Gaussian to the CALIFA galaxies is due to the spectral resolution of the observations. Multi-component emission line fitting requires a spectral resolution that can differentiate between different physical processes. The velocity resolution of the R1650 or V1200 grating is $60 - 80\,\mathrm{km/s}$, which is twice the velocity dispersion of a star forming process ($\sim 45\,\mathrm{km/s}$), making it difficult to differentiate between multiple processes.

Seven optical emission line fluxes, velocity dispersions and velocities of each component are extracted from each spaxel of the 30 composite galaxies. The emission line fluxes extracted are [NII]λ6583, [SII]$\lambda\lambda$6716, 6731, Hα, Hβ, [OIII]λ5007, and Hγ (WiGS only). A signal-to-noise cut of 3 is made on the emission line fluxes of each spaxel and/or component from multi-component emission line fitting (hereon after just referred to as components for both CALIFA and WiGS).

Galaxy ID	Observation ID	Date observed	Instrument	PI
IRAS F02072-1025	923	Nov 2000	ACIS	Gary Mamon
IRAS F06076-2139	15052	Dec 2012	ACIS	David Sanders*
IRAS F10038-3338	7807	March 2007	ACIS	David Sanders**
IRAS F10257-4339	3569	May 2003	ACIS	Stephen Murray
IRAS F13373+0105 West	10565	March 2009	ACIS	Douglas Swartz
IRAS F16164-0746	15057	January 2013	ACIS	David Sanders*
IRAS F17138-1017	15063	Aug 2013	ACIS	David Sanders*
IRAS F17207-0014	2035	Oct 2001	ACIS	Tim Heckman
IRAS F20551-4250	2036	Oct 2001	ACIS	Tim Heckman
IRAS F23128-5919	2037	Sep 2001	ACIS	Tim Heckman

Table 3.4: Composite galaxies with archived Chandra X-ray observations. Included are the observation IDs, observation dates, instrument, and the primary investigator (PI) for each observation. * - Observed as a part of C-GOALS (Iwasawa et al., 2011). ** - Observed as a part of Iwasawa et al. (2009)

3.3.2 X-ray data

Ten of the 30 composite galaxies in the sample have been previously studied with the Chandra X-ray Space Observatory and these archived observations have been made available for analysis. Table 3.4 indicates which galaxies have observations, the date observed, type of observation, and the primary investigator (PI) of the observation.

The X-ray observations were processed using the standard reprocessing step, `chandra_repro`, as a part of `CIAOv4.6` (Chandra Interactive Analysis Observation). This step produces an event = 2 image that can be used for the X-ray Hardness Ratio (HR) calculations, Section 3.6. Each observation is split into two separate energy band images: $0.5 - 2$keV and $2 - 8$keV. For each galaxy a region of the observation encompassing the galaxy nucleus was extracted and as well as an annulus outside of the galaxy for background subtraction.

The preprocessing and selections of specific regions result in background corrected photon event counts, or net counts, in each of the two energy bands for the nucleus of each galaxy. These net counts were then used to calculate the Hardness Ratio (HR) of each of the 10 galaxies, Section 3.6, to identify AGN host galaxies.

3.4 Previous studies into the excitation sources of WiGS galaxies

The WiGS sample of composite galaxies are derived from the GOALS survey (Armus et al., 2009), which has been studied in detail for evidence of AGNs and shocks using IR observations (e.g. Inami et al., 2013; Stierwalt et al., 2013, 2014).

Inami et al. (2013) used [NeV] and [NeII], along with the equivalent width of the 6.2 PAH absorption line, to differentiate between galaxies that are dominated by an AGN from those dominated by a starburst. When the equivalent width of the 6.2 PAH is $\leq 0.3\mu$m and the [NeV]/[NeII] ≥ 0.1 the galaxy is AGN dominated. These values have been extracted from Inami et al. (2013) for the WiGS composite galaxies and compared to the results of AGN identifications of this chapter (Sections 3.5 and 3.6).

Another excitation source investigated in Inami et al. (2013), and investigated later in this chapter, are shocks. Strong shocks can be identified using [FeII]/[OIV] versus [OIV]/[NeII] because strong shocks can destroy grains in the ISM (Savage & Sembach, 1996) and release Fe into the gas phase. They can be distinguished from AGNs and starbursts in this manner. However, Inami et al. (2013) found that there was no strong division on this diagnostic in the GOALS sample of U/LIRGs.

The result of the analysis of AGNs described in Inami et al. (2013) on the composite galaxies is discussed in the following sections in comparison to this chapters results.

3.5 Identifying Active Galactic Nuclei (AGN) with optical observations

Previous studies of composite galaxies have included investigations that determine the contribution of AGNs to the nuclear emission line ratios (e.g. Scharwächter et al., 2011; Dopita et al., 2014a; Davies et al., 2014, 2016b). As discussed in Section 3.1, the study of Yuan et al. (2010a) and the composite nature of their galaxies were assumed to arise from the mixture of emission from an AGN and star formation. Other studies, including Panessa et al. (2005), identified that not all their composite galaxies were hosts to AGNs. In the case of merging galaxies, it is expected that at later merging stages the infall of gas

can partially obscure an AGN in the optical thus causing composite emission line ratios due to surrounding star formation. In these cases, composite line ratios may indicate partially obscured AGNs surrounded by circumnuclear star formation.

Studies using IFS observations clearly indicate the power IFS has in differentiating different mechanisms of ionisation within galaxies. Mast et al. (2014) investigated how the increase in spatial resolution of galaxy observations can identify more detailed physical structures in the CALIFA survey. Davies et al. (2016b) showed that IFS can separate AGN from star formation using different spectral components. The spatial and the spectral information of IFS together can disentangle the composition of the 30 composite galaxies in the composite galaxy sample.

3.5.1 Using diagnostic diagrams

The identification of an AGN in this chapter only considers the central 1 kpc of each composite galaxy. As AGNs are only nuclear sources we can use the central regions to diagnose whether AGN emission is contributing to the composite emission. For eight galaxies the 1 kpc apertures are sub-seeing, the central aperture is less than a fibre size and does not contain the entirety of flux that illuminated that fibre. For these galaxies the AGN identification requires further studies to confirm an AGN.

The emission line ratios in the central 1 kpc apertures of each galaxy are calculated and placed on the [NII]/Hα diagnostic diagram and the [SII]/Hα diagnostic diagram. (The [OI]/Hα diagnostic diagram is neither described nor used in this study because the addition of the [OI]/Hα emission line analysis resulted in ratios with significance $< 3\sigma$.) A component is AGN if in both the [NII]/Hα diagnostic diagram and [SII]/Hα diagnostic diagram the components emission line ratios are AGN, or if the component in the [SII]/Hα diagnostic diagram is AGN and composite in the [NII]/Hα diagnostic diagram. This is because the [SII]/Hα emission line ratios are produced in a partially ionised zone at the edge of a nebula and more sensitive to a hard ionising radiation field and thus more sensitive to AGN emission.

Examples of two composite galaxies with AGNs are presented in Figure 3.2, the remainder of the composite galaxies are presented in Appendix B. The two galaxies presented are IC0944 (top row) and IRAS F02072-1025 (bottom row). The first panels are SDSS

r-band and HST images, respectively, of the galaxies in the field-of-view (FoV) of the observations. The second panels show the same FoVs but only spaxels that fall in the central 1 kpc aperture, coloured by whether they are AGN, composite or star-forming in the [NII]/Hα diagnostic diagram. The third and fourth panels show the positions of the emission line ratios of the central 1kpc spaxels on the [NII]/Hα diagnostic diagram and [SII]/Hα diagnostic diagram, respectively. For IRAS F02072-1025 only the results of the second velocity component of the emission line fitting process are shown for space reasons, where the AGN-like emission ratios are identified. The full figure, including all components, is in Appendix B. IC0944 is a CALIFA galaxy with only a single component fit, thus only this component is shown for IC0944.

Eight galaxies are identified as AGN hosts through similar diagnostic diagrams as presented in Figure 3.2. These galaxies are indicated in Figure 3.3 by the medium to dark red points. The figure indicates the fraction of components in the central 1 kpc of each galaxy that are AGN-like. The size of the points indicates the number of components in the central 1 kpc that are used in the calculation of the fraction; not all components have a signal-to-noise ratio > 3. The colour indicates the fraction of components that are AGN-like. The darker the point the more AGN-like the central 1 kpc is when broken down spatially and spectrally indicating possible AGN contributions to these composite galaxies.

Two galaxies are indicated in Figure 3.3, IC0944 and IRAS F17138-1017, by intersecting dashed and dot-dashed lines. IC0944 is an isolated spiral galaxy observed as a part of the CALIFA survey and IRAS F17138-1017 is a late stage merger observed as part of WiGS.

The interest in these two galaxies is because they stand out from the rest of the possible AGN host galaxies. The resulting fraction of AGN components in IC0944 indicates that it is an AGN dominated galaxy. IC0944 has a large number of components with signal-to-noise > 3 in the 1 kpc aperture, but is located in the central part of the composite region. As composite emission line ratios can be caused by the combination of AGN and star forming emission line ratios it is assumed for this chapter that the components that have been cut due to the signal-to-noise ratio were indicative of star formation.

IRAS F17138-1017 is host to an X-ray AGN (see Section 3.6). However, it is seen as star-forming in optical emission and lies close to the dividing curve between star-forming and composite emission line ratios in the 1 kpc aperture. This galaxy may host a possibly

obscured AGN. However, the number of components involved ($\sim$ 13% of all components with emission line fluxes) in the fraction calculation identifying it as having no AGN components in the optical does not mean there is no AGN.

The results of Inami et al. (2013) identified IRAS F17138-1017 as being starburst dominated through an IR study. It is possible that optically composite galaxies could be non-AGN dominated in the IR whilst still being host to an AGN.

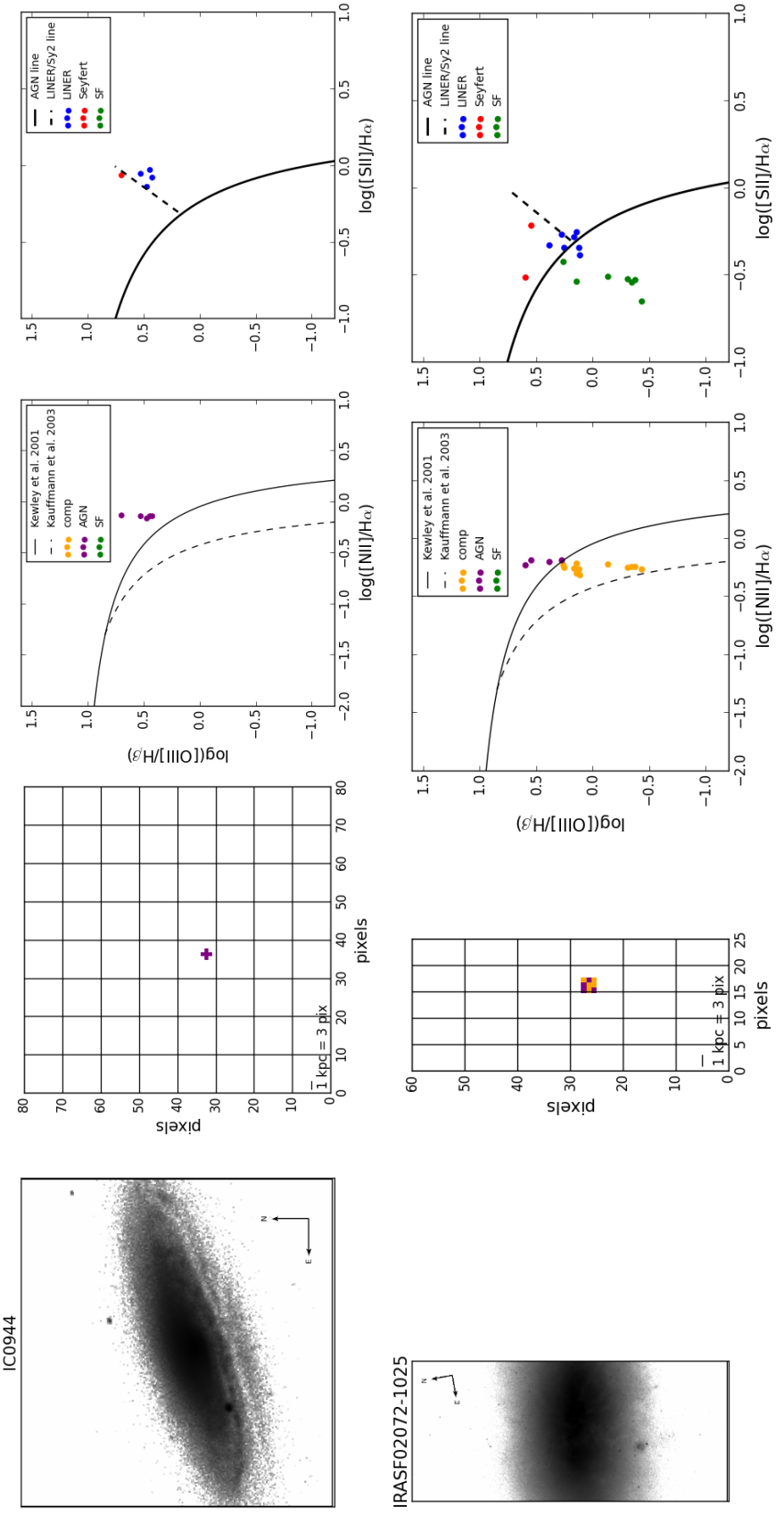

Figure 3.2: Example diagnostic figures for the identification of AGNs in composite galaxies. Top: IC0944, Bottom: IRAS F02072-1025. Left panels are SDSS r-band (top) and HST (bottom) images of each galaxy in the FoV of the observations. Second panels are the same FoV as the first but show the spaxels that fall within the central 1kpc used to diagnose the AGN, colour-coded tby the excitation source. For IRAS F02072-1025 only the map of the second emission line component is presented. The third and last panels are the [NII]/Hα diagnostic diagram and [SII]/Hα diagnostic diagram for each galaxy. The diagnostic diagrams for the remainder of the AGN galaxies are in Appendix B.2.

3.5.2 Identifying AGN type

The difference between a Seyfert 2 (Sy2) AGN galaxy and a LINER galaxy is not inconsequential. Thus, an understanding of the types of AGNs hosted by composite galaxies is important. In Seyfert 2 galaxies, the accretion disk emits strongly in the extreme-UV. A nuclear LINER galaxy, as identified on the [NII]/Hα diagnostic diagram, is usually assumed to be a low luminosity AGN which accretes via advection dominated disk or spherical flows (e.g Kewley et al., 2006). However, this region on the [NII]/Hα diagnostic diagram can also arise from emission from fast shocks (e.g. Allen et al., 2008) or from the photoionisation due to weak post-AGB stars (Binette et al., 1994; Singh et al., 2013; Belfiore et al., 2016).

Using SDSS data, Kewley et al. (2006) demonstrated that L[OIII]/σ^4 can clearly separate Seyferts from LINERs. The ratio L[OIII]/σ^4 can be thought of as a proxy for the Eddington Luminosity ratio because the [OIII]λ5007 luminosity, L[OIII], scales with the bolometric luminosity of an AGN (Heckman et al., 2004) while the stellar velocity dispersion, σ^4, can be used as an estimate of black hole mass (Tremaine et al., 2002).

The central 1 kpc of each AGN galaxy (eight optical and two X-ray AGN galaxies - see Section 3.6) are corrected for reddening using the Balmer Decrement[1] in order to derive the extinction corrected L[OIII]. The Balmer decrement for the WiGS galaxies is calculated from the Hγ/Hβ[2] ratio,while the Hα/Hβ ratio is used for the CALIFA galaxies. The difference in choice of emission lines to calculate the Balmer decrement was to ensure there were no flux calibration errors entered into the emission line flux values, i.e. the emission lines are observed on the same CCD.

The L[OIII]/σ^4 ratios for the central 1 kpc of the ten AGN host galaxies are presented in Figure 3.4 against σ^4. One galaxy, IRAS F16164-0746, is identified as a Sy2 AGN galaxy and IRAS F02072-1025 lies in the cross-over area of Sy2 and LINER galaxies. The

[1]The Balmer decrements are used to calculate the E(B-V) for the ionised gas following the equations in Momcheva et al. (2013, see Appendix therein), and multiplied by 0.44, as prescribed (Calzetti, 1997; Momcheva et al., 2013), to obtain the stellar E(B-V) required for the reddening correction.

[2]The error in the Hγ emission line flux comes from the subtraction of continuum absorption of the Balmer lines. The absorption in Hγ is stronger than Hα in absorption, however the Hγ emission line is almost three times smaller than the Hα emission line, making the Hγ emission line flux more uncertain. The Hγ/Hβ ratio is used despite the addition of this error as the flux calibrations between the red and blue CCDs is not quantified but the Hγ error can be.

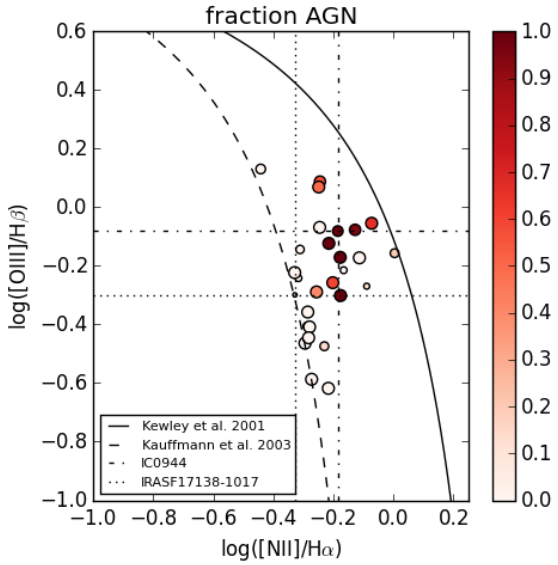

Figure 3.3: The line ratios of the integrated 1kpc of the 30 composite galaxies on the [NII]/Hα diagnostic diagram colour-coded by the spatial (including individual components) fraction of AGN emission within the central 1kpc, determined using the resolved IFU data. Sizes of the data points indicate the number of components used to determine the AGN fraction.

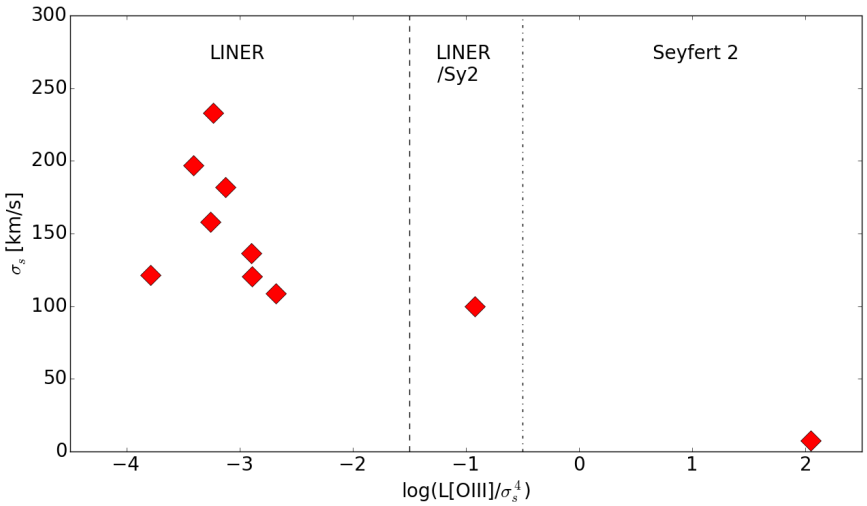

Figure 3.4: Eddington luminosity proxy against the stellar velocity dispersion. One galaxy hosts a Sy2 AGN, one hosts a possible Sy2 AGN and the remaining eight galaxies are LINER.

remaining six optical AGN galaxies have L[OIII]/σ^4 ratios indicative of LINERs. The two X-ray only AGN galaxies (see Section 3.6) are also identified as LINER galaxies from their central 1 kpc L[OIII]/σ^4.

LINER galaxies are not specifically investigated in this chapter and are therefore not separated into possible LLAGN, or postAGB (Belfiore et al., 2016) excitation source galaxies. The study by Singh et al. (2013) investigated LINER galaxies in CALIFA, these are not to be confused with this chapter's composite galaxies. Their galaxies were identified as LINER from 3″, 0.1-0.6 kpc physical size, emission line ratios and thus does not include the galaxies in this study. However, the possibility of the identified LINER composites does need to consider their results as the same may apply here. This is not investigated further, but is left for future work. LLAGN and post-AGB sources are thus grouped together for this study as LINERs.

3.6 Identifying AGN with X-Ray observations

It is not always possible to identify an AGN through optical emission lines. In the case of merging galaxies, gas is funnelled towards the nuclear regions of the galaxies which can cause star formation that obscures the AGN in the observation. When an AGN is obscured by gas, dust, or star formation the resulting emission line ratios in the optical may include the interaction of the AGN in the surrounding gas and dust but not identify the AGN itself. Thus the obscured AGN can still be influencing the composite emission line ratios in the composite galaxies.

It has been known since Pounds (1979) that point-like hard X-ray sources are indicative of AGNs (Pounds, 1979). The highly energetic process of accretion onto a black hole produces high energy photons including X-rays. AGNs are not the only source of X-rays in galaxies but can be distinguished by their physical shape and the hardness or shape of the X-ray spectrum observed.

Often spectral fitting is used to determine the source of X-ray emission, however in some cases the required spectral analysis is not possible. In this study the X-ray emission observed for the 10 composite galaxies with archived Chandra observations is not adequate for detailed spectral fitting. Instead a Hardness Ratio (HR), a measurement of accumulated counts in two or more energy bands, is used to quantify the source of the X-ray

emission.

3.6.1 The X-ray Hardness Ratio

The X-ray Hardness Ratio (HR) is a simple measure to quantify the source of the X-ray emission. The ratio is defined as $HR = (H - S)/(H + S)$, where H is the net counts in the 2-8 keV energy band and S is the net counts in the 0.5-2 keV energy band. This energy band selection follows the study by Iwasawa et al. (2009, 2011) which concentrates on the GOALS sample of galaxies, from which the 10 composite galaxies with archival Chandra observations used here originate.

The HR threshold for an AGN source is dependent on the galaxy types (e.g. U/LIRGs) and redshifts. For moderate redshift galaxies ($z = 1$) a $HR \sim 1.0$ is an indication of an AGN, whereas at high redshifts ($z = 5$) the threshold is lower at $HR \sim -0.5$ (Wang et al., 2004). For the WiGS galaxies we use the threshold defined by Iwasawa et al. (2009) of $HR > -0.3$ to identify possible AGNs.

The HR's for the 10 galaxies in the WiGS sample with X-ray observations are presented in Figure 3.5 and listed in Table 3.5, error bars are determined from the errors in the net counts of each energy band propagated through the HR calculation. The x-axis of Figure 3.5 also indicates the IR luminosity, L_{IR}. The figure indicates that four of the ten galaxies are possible AGN hosts (highlighted red), but there is no correlation with the total IR luminosity of the host galaxy. Three of the X-ray AGN host galaxies were not identified as AGN hosts through the previous optical analysis. The first two of these three galaxies are IRAS F06076-2139 and IRAS F23128-5919 which do not have any emission line components in the 1 kpc aperture after the signal-to-noise cut of 3 in the strong emission lines, and thus there is no optical identification. The remaining galaxy is IRAS F17138-1017 mentioned in the previous section as potentially hosting an obscured AGN or central shocks.

Only one galaxy, IRAS F16164-0746, is confirmed as an AGN host through the X-ray HR, after being identified through its optical emission.

The optical AGN host galaxy IRAS F02072-1025 has a $HR = -0.74 \pm 0.06$. This HR is below the threshold used in this study, and that of Iwasawa et al. (2009, 2011). Although the AGN is not confirmed by the X-ray emission, the optical analysis identified the source

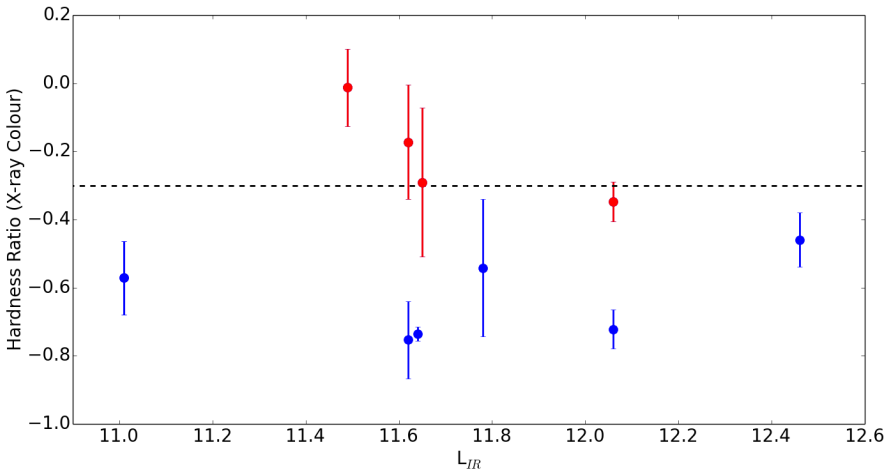

Figure 3.5: The results of the calculation of X-ray hardness ratios for the ten composite galaxies with archival Chandra observations. Four of these galaxies have ratios indicative of an AGN. The X-ray AGNs are highlighted by the red points.

of the emission lines to be a border-line Sy2/LINER type AGN. This galaxy may be an X-ray weak source but still display the broad optical emission lines indicative of an AGN (Wilkes et al., 2002). Further analysis, outside the scope of this chapter, is required to determine if this is the case.

In the study by Inami et al. (2013) all the composite WiGS galaxies are identified as starburst dominated galaxies and not AGN dominated. It is possible that the composite galaxies investigated here, and those in Inami et al. (2013), are 100% starburst galaxies. This is because both studies have used the Kewley et al. (2001b) diagnostic curve as the lower boundary of pure AGN excitation. This diagnostic curve is a maximum starburst line where pure starburst galaxies can lie as starburst emission may have a harder ionising radiation field from Wolf Rayet stars, or a large ISM pressure. Thus the Inami et al. (2013) result is not an indicator that there are not AGNs, just no dominant AGNs.

3.7 Identifying shocks

Shocks are identified in this study by analysis of activity outside of the nuclear region of each galaxy. The assumption here is that within the central 1 kpc the AGN-like emission line ratios on the [NII]/Hα diagnostic diagram are more likely due to an AGN, while the AGN-like (including LINER-like) emission line ratios identified outside of the 1 kpc region

are attributed to shocks.

The ionised gas emission from shocks can appear with that from weak AGN (e.g. Allen et al., 2008) However, when the emission line ratios are used in conjunction with velocity dispersions, it is possible to identify the presence of shocks in the composite galaxies (Monreal-Ibero et al., 2010). An increase in velocity dispersion with the [NII]/Hα and [SII]/Hα emission line ratios is an indication of shocks in a galaxy.

The velocity dispersions themselves can also identify the presence of shocks. Shocked emission line components typically have velocity dispersions between 150-300 km/s (Rich et al., 2015). This is in comparison to regions excited by star formation which typically have narrow peaks (40 km/s) and AGNs that result in broader emission line profiles (300 km/s) (Rich et al., 2015). A velocity dispersion distribution comparison can be used to quickly identify the galaxies that have a peak of velocity dispersions expected of shocked gas.

Shocks identified by the [NII]/Hα diagnostic diagram in a CALIFA galaxy are presented in the top panels of Figure 3.6. The figure shows the results for NGC4676A, one of the two interacting Mice Galaxies. Here the AGN-like emission line ratios are tracing shocks associated with the merger between NGC4676A and NGC4676B (Wild et al., 2014). The presence of shocks can be confirmed by the [SII]/Hα diagnostic diagram right most panel where the AGN-like emission line ratios also trace the shock excited emission line ratios. This identification of AGN-like emission away from the nucleus is performed for each of the 30 composite galaxies.

Using gas velocity dispersions to identify shocks is dependent on the spectral resolution of an observation. The WiGS observations use a spectral grating that results in a velocity resolution of 45 km/s in the red[3]. This means that the resolution is small enough to be used to differentiate between star formation, shocks and AGN components. However, the CALIFA observations use a grating that results in a velocity resolution of 150 km/s in the red. The low resolution of the CALIFA observations mean that the gas velocity dispersions are unable to differentiate different components.

In addition to using the diagnostic diagrams the velocity dispersions are also taken into consideration in identifying shocks for the WiGS composite galaxies. For each WiGS galaxy the distribution of gas velocity dispersions and a comparison to emission line ratios

[3]The velocity dispersions are calculated from the Hα emission line which falls onto the red CCD for both WiGS and CALIFA

of [NII]/Hα and [SII]/Hα are made. An example of using the gas velocity dispersions is presented in the bottom panels of Figure 3.6 for IRAS F16164-0746. The third panel displays the double peaked gas velocity dispersion distribution of this galaxy, which is an indicator of shocks being present. The final panel in the bottom row of Figure 3.6 displays the velocity dispersion against their corresponding emission line ratios for [NII]/Hα and [SII]/Hα. IRAS F16164-0746 has a correlation probability of 0.84 between the emission line ratios and gas velocity dispersion.

The individual shock results for WiGS and CALIFA composites are listed in Tables 3.5 and 3.6, respectively. The diagnostic figures and descriptions of each galaxy are located in Appendix B.

Shocks are identified in 13 of the composite galaxies using either emission line ratios, and/or velocity dispersion distributions.

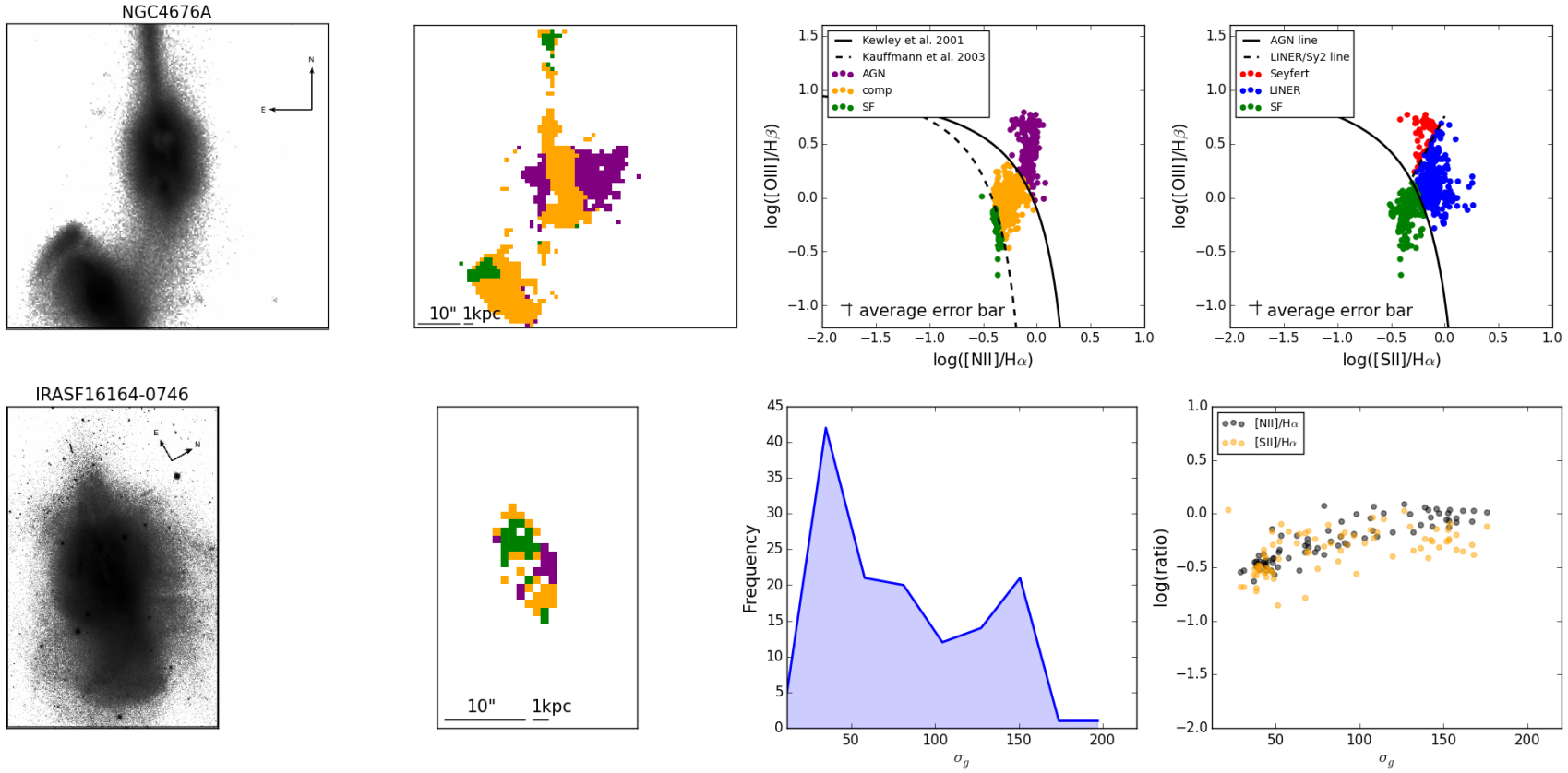

Figure 3.6: Example diagnostic figures for the identification of shocks in composite galaxies. Top: NG4676A, Bottom: IRAS F16164-0746. Left panels are SDSS r-band images of each galaxy with the same FoV as the IFU observations. The second panels show the IFU observations, with the pixels colour-coded to indicate the emission line classification (green=starforming, orange=composite, purple=AGN) as determined by the [NII]/Hα diagnostic diagram. The third and last top panels are the [NII]/Hα diagnostic diagram and [SII]/Hα diagnostic diagram for NGC4676A. The bottom third panel shows the velocity dispersion distribution for IRAS F16164-0746. The bottom last panel compares the velocity dispersion of emission line components to the emission line ratios [NII]/Hα (grey) and [SII]/Hα (orange).The diagnostic diagrams for the remainder of the shock galaxies are in Appendix B.2.

3.8 Identifying star-formation and further composite emission line ratios

The Kewley et al. (2001b) diagnostic curve represents a maximum in possible line ratios achievable through excitation of starbursts. Above this line, the emission line ratios are only achievable through non-stellar excitation (see Kewley et al., 2001b), but below the line it is possible to explain the emission line ratios solely through the harder ionising radiation of a starburst. This means that galaxies in the composite emission line region of the diagnostic diagram could be explained by a starburst.

3.8.1 Using diagnostic diagrams

A component is defined as being star forming if the emission line ratio of that component lies in the star forming region of the [NII]/Hα and [SII]/Hα diagnostic diagrams. However, because the composite region of the [NII]/Hα diagnostic diagram could also be star forming, components in the [NII]/Hα composite region are also considered to be star forming only if the component lies in the star forming region of the [SII]/Hα diagnostic diagram.

Examples of star forming galaxies are presented in Figure 3.7. The top panels are of a CALIFA galaxy (NGC0776) where the emission line ratios are star-forming in both the [NII]/Hα and [SII]/Hα diagnostic diagrams. The bottom panels are of a WiGS galaxy (IRAS F06076-2139) where the star forming components are lying in the composite region of the [NII]/Hα diagnostic diagram. In both cases these galaxies are predominantly star forming with no contribution from an AGN or shocks.

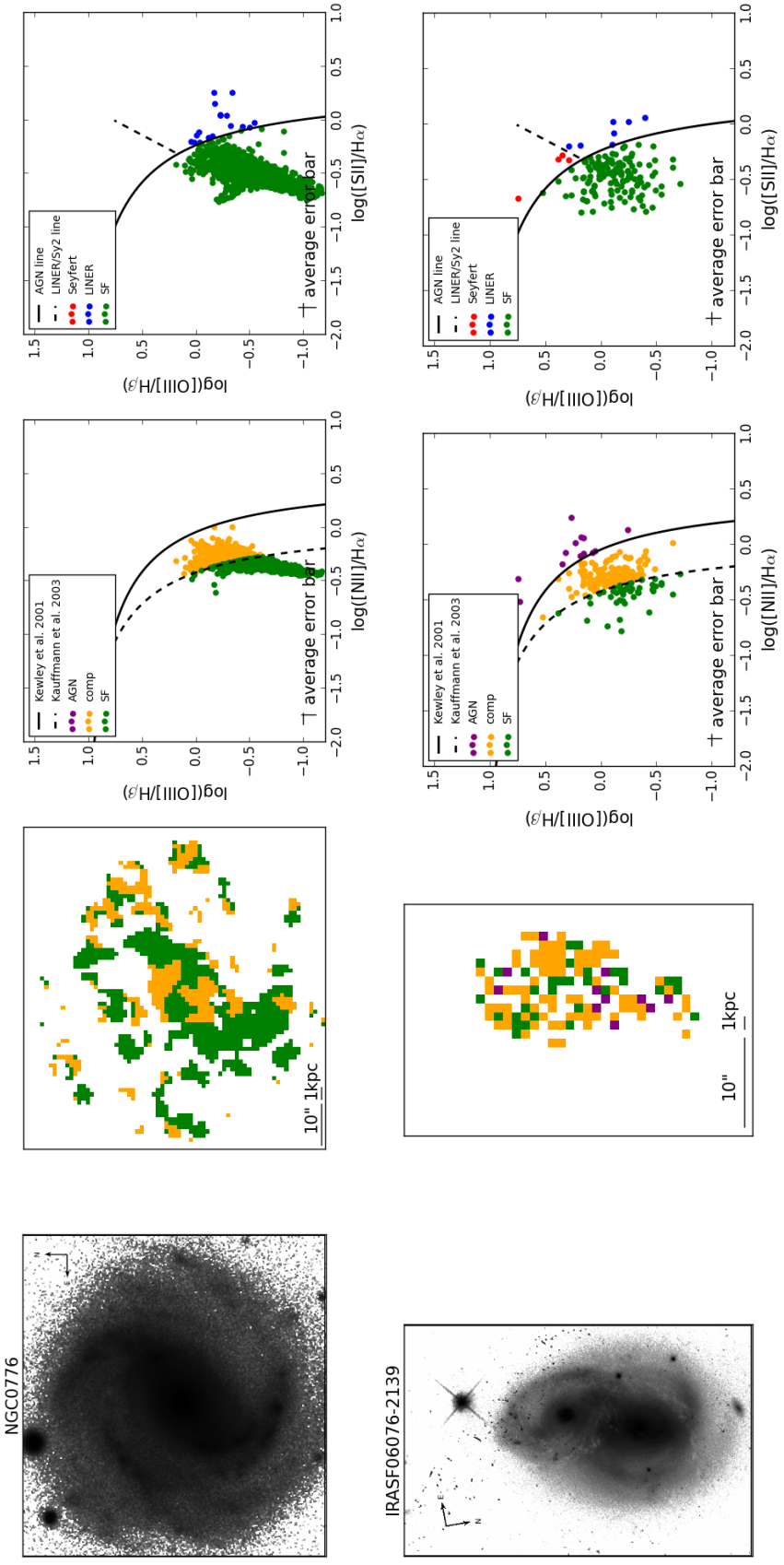

Figure 3.7: Example diagnostic figures for the identification of star formation in composite galaxies. Top: NGC0776, Bottom: IRAS F06076-2139. Left panels are SDSS r-band (top) and HST (bottom) images of each galaxy in the FoV of the observations. Second panels are the same FoV as the first but are colour-coded to the position emission line components are on the [NII]/Hα diagnostic diagram. The third and last panels are the [NII]/Hα diagnostic diagram and [SII]/Hα diagnostic diagram for each galaxy. The diagnostic diagrams for the remainder of the star forming galaxies are in Appendix B.2.

The process of spatial and spectral decomposition of the central 1 kpc still finds components that lie in the composite region of the [NII]/Hα diagnostic diagram. Assumptions are made that the [SII]/Hα diagnostic diagram can be used to determine what process causes these components. However, this is an assumption that may turn out to be unreliable.

This study has already shown, along with other previous studies (e.g. Mast et al., 2014; Davies et al., 2014, 2016b; Rich et al., 2015; Ho et al., 2014), that the spatial and spectral resolution of emission line physics plays a part in the classification of excitation processes. Greater resolution than what is used in this chapter may be able to further dissect the remaining composite emission line ratios observed in the central 1 kpc.

3.9 Discussion of results

Using the information available from IFS, X-ray observations and previous studies the excitation mechanisms of the 30 composite galaxies have been identified as AGN, nuclear star formation, and/or shocks. These results have been tabulated in Tables 3.5 and 3.6, including final classification of the contributing excitation processes, for WiGS and CALIFA respectively.

Galaxy ID		AGN				Shocks		Final classification
(1)	(2)	(3)	(4)	(5)	(6)	(7)	(8)	(9)
WiGS	morphology	log(L[OIII]/σ^4)	Type	HR	[NeV]/[NeII]	Y/N	Correlation Function	all wavelengths
IRAS F02072-1025	spiral	-0.921	LINER/Sy2	-0.739 ± 0.055	0.010	N	$-0.29\,(p \sim 0)$	(LINER/Sy2)/SF
IRAS F06076-2139	merger	-	-	-0.157 ± 0.156	0.060	Y	$0.61\,(p \sim 0)$	AGN^x/shock/SF
IRAS 08355-4944	merger	-	-	-	0.011	N	$0.30\,(p \sim 0)$	SF
IRAS F10038-3338	merger	-	-	-0.556 ± 0.155	0.044	Y	$0.76\,(p \sim 0)$	shock/SF
IRAS F10257-4339	merger	-	-	-0.742 ± 0.016	0.011	Y	$0.61\,(p \sim 0)$	shock/SF
IRAS F13373+0105 West	merger	-	-	-0.771 ± 0.090	0.065	N	$0.24\,(p \sim 0)$	SF
IRAS F16164-0746	merger	2.05	Sy2	-0.154 ± 0.113	0.020	Y	$0.84\,(p \sim 0)$	Sy2/shock/SF
IRAS F17138-1017	merger	-	-	-0.043 ± 0.077	0.011	Y	$0.47\,(p \sim 0)$	AGN^x/shock/SF
IRAS F17207-0014	merger	-	-	-0.454 ± 0.055	0.012	N	$0.23\,(p \sim 0)$	SF
IRAS F18341-5732	bar	-	-	-	0.018	N	$0.53\,(p \sim 0)$	SF
IRAS F20551-4250	merger	-	-	-0.731 ± 0.045	0.083	N	$0.24\,(p \sim 0)$	SF
IRAS F23128-5919	merger	-	-	-0.41 ± 0.04 (south)	0.068	Y	$0.26\,(p \sim 0)$	AGN^x/Shock/SF

Table 3.5: Table of classifications as defined in this chapter for WiGS composites. (1) - Galaxy ID. (2) - galaxy morphology as defined by Rich et al. (2015). (3) - Eddington luminosity in log scale. (4) - resulting AGN type from (3). (5) - X-ray hardness ratio or X-ray colour used to identify if there is a an AGN in archival X-ray observations. (6) - [NeV]/[NeII] (Inami et al., 2013). (7) - Are shocks present? (8) - probability of a correlation between emission line ratios and velocity dispersions. (9) - classification of physical processes based on this study.

3.9.1 AGNs in isolated spiral galaxies

Through the process of merging, galaxies can experience heightened AGN activity as well as circum-nuclear star formation which could consequently lead to an overall composite emission line ratio in the composite region of the [NII]/Hα diagnostic diagram. Galaxies that are not undergoing a merge may also be hosting an AGN with strong nuclear star formation and will appear as a composite galaxy.

The analysis in Section 3.5 & 3.6 identified 13 composite galaxies that are possibly hosts to AGNs. Of the 13 AGN galaxies, one is Sy 2 AGN, one is a borderline Sy2 or LINER, and the remainder are LINER. This study does not differentiate between the possible excitation sources of LINER emission; Low Luminosity AGN, post-AGB stars, or nuclear shocks. In cases where there is nuclear hard X-ray emission (i.e. IRAS F102072-1025) there is a strong likelihood that it is a LLAGN, however for the others we simply classify as LINERs. See the study by Singh et al. (2013) on LINERS and post-AGB stars in CALIFA galaxies.

The 13 AGN-containing composite galaxies have diverse morphologies (as determined through the studies of Rich et al. (2014); Sánchez et al. (2012)). These 13 galaxies include five isolated spiral galaxies, three isolated bar galaxies, and five merging galaxies. The fraction of galaxies hosting an AGN in each morphology group is 83% (spiral), 30% (bar), 36% (merger). The fraction of galaxies in each morphology group with nuclear star formation (SF) and composite emission line ratios (comp) still arising in the 1 kpc aperture despite the spatial and spectral decomposition are 33% (spiral), 90% (bar), 91% (merger) and 83% (spiral), 100% (bar), 73% (merger), SF and composite respectively.

Isolated spiral composite galaxies show the highest percentage of galaxies hosting AGNs and the lowest fraction of galaxies with nuclear star formation. This is directly opposite to isolated bar composite galaxies and merging composite galaxies. However, all three morphology groups present a large ($> 70\%$) fraction of galaxies where the emission line ratios are composite from the [NII]/Hα diagnostic diagram despite spectrally dissecting the 1 kpc nuclear regions.

Galaxy ID		AGN		Shocks	Final classification
(1)	(2)	(3)	(4)	(7)	(11)
CALIFA	morphology	log(L[OIII]/σ^4)	Type	Y/N	all wavelengths
IC5376	bar	-2.90	LINER	N	LINER/SF
UGC00036	spiral	-3.13	LINER	N	LINER/SF
UGC01057	bar	-2.89	LINER	Y	LINER/shock/SF
NGC0776	bar	-	-	N	SF
UGC03253	bar	-	-	N	SF
UGC05359	bar	-3.78	LINER	Y	LINER/shock
NGC4003	bar	-	-	Y	shock/SF
NGC4676A	merger	-	-	Y	shock/SF
NGC4676B	merger	-3.23	LINER	Y	LINER/shock/SF
NGC5000	bar	-	-	Ambiguous	SF
UGC08267	spiral	-2.68	LINER	Ambiguous	LINER/SF
IC0944	spiral	-3.26	LINER	N	LINER/SF
UGC08778	spiral	-2.68	LINER	N	LINER/SF
NGC5394	merger	-	-	Ambiguous	SF
NGC6032	bar	-	-	Y	shock/SF
UGC10205	spiral	-3.41	LINER	Ambiguous	LINER
NGC7591	bar	-	-	N	ambiguous
NGC7549	bar	-	-	Y	shock/SF

Table 3.6: Table of classifications as defined in this chapter for CALIFA composites. (1) - Galaxy ID. (2) - galaxy morphology as defined by Sánchez et al. (2012). (3) - Eddington luminosity in log scale. (4) - resulting AGN type from (3). (7) - Are shocks present? (11) - classification of physical processes based on this study. The column numbers are set to match Table 3.5 of the WiGS composite galaxies.

3.9.2 Shocks in merging and isolated bar galaxies

With only 30% of the merging composite galaxies in this chapter as hosts to AGNs, something else must be causing the nuclear composite emission line ratios to be present in the [NII]/Hα diagnostic diagram. One such possibility is the presence of shocks within a galaxy. Strong shocks can arise in the presence of galactic-scale flows in galaxies, such as found in starburst winds or galactic mergers.

Shocks were identified in 13 of the 30 composite galaxies in Section 3.7. The morphology make-up of these 13 galaxies is; five isolated bar galaxies and eight merging galaxies. None of the isolated spiral galaxies were identified as having shocks.

The morphological comparison of galaxies with shocks is in contrast to the galaxies with AGNs. This result implies that the composite nature of isolated spiral galaxies is more likely to be due to the presence of an AGN, while the composite nature as depicted by the [NII]/Hα diagnostic diagram of isolated bar and merging galaxies is more likely due to shocks. In barred galaxies the shocks are likely to arise due to the build up of gas due to the change in torque at the end of the bar. In merging galaxies the shocks could arise from the large scale gas flows driven by the gravitational torques of the merging process, or from starburst driven winds arising from the merger.

3.9.3 Composites as pre-cursers to Sy2 galaxies?

In Yuan et al. (2010a) the assumption that composite galaxies were a combination of an AGN and star formation led to the interpretation that composite galaxies may be the bridge between star forming galaxies at early merging stages and Sy2 galaxies at the coalesced merger stage in their sample. This study finds that AGN emission is not a significant contributor to the line emission of the composite galaxy sample, and appear to be rarer in systems with disturbed morphologies.

Despite the conclusion of this chapter, the idea that a composite galaxy is a combination of a Sy2 AGN and star forming galaxy is not ruled out. One galaxy, IRAS F02072-1025, is a Sy2 host galaxy, as determined through optical analysis. A comparison of the emission line ratios of the 30 composite galaxies is made to known galaxies hosting a Sy2 AGN and starburst (Davies et al., 2016b).

The panels in Figure 3.8 compare the emission line ratios of each morphological group in the composite sample to the emission line ratios of two Sy2-starburst galaxies from Davies et al. (2016b) on the [NII]/Hα and [SII]/Hα diagnostic diagrams, left and right respectively. The dashed contours in each panel indicate the spread of emission line ratios of the known Sy2-starburst galaxies. The solid contours indicate the spread of emission line ratios from each of the morphological groups (isolated spiral, spiral bar, merging). In both sets of contours, the emission line ratios of every component in each galaxy (signal-to-noise ratio >3) is included.

The results of the comparison in Figure 3.8 are that the 30 composite galaxies in this sample are not like known Sy2-starburst galaxies. This is also seen in Davies et al. (2016b) when determining the different mixing sequences of a larger group of Seyfert and starburst galaxies. However, there are some similarities in the star forming regions of the [NII]/Hα diagnostic diagram and [SII]/Hα diagnostic diagram. None of the solid contours, representing the composite galaxies in this chapter, reach as far into the AGN region of the diagnostic diagrams as the known Sy2-starburst galaxies, indicating that the optical emission in the composite galaxies is not ionised to the same degree by a strong AGN source.

3.9.4 Comparison to previous and future studies of composite galaxies

Composite galaxies are not just AGN and star forming galaxies. This chapter has clearly shown that a composite galaxy may also be a shocked galaxy or a pure star forming galaxy. Therefore the results of previous studies of composite galaxies should be interpreted with caution where they have excluded these other excitation possibilities or assumed all are AGN host galaxies.

The excitation processes of the 30 composite galaxies show the most variation between the three morphological types: merging, isolated bar, and isolated spiral galaxies. The highest fraction of AGN galaxies are in the isolated spiral galaxies, which also had zero shocks contributing to the galaxies' classifications. Yuan et al. (2010a) assumed that all their composite galaxies were AGN and star formation. This assumption led them to calculate an AGN fraction for each of those galaxies.

This chapter shows that the AGN assumption of Yuan et al. (2010a) may have been in-

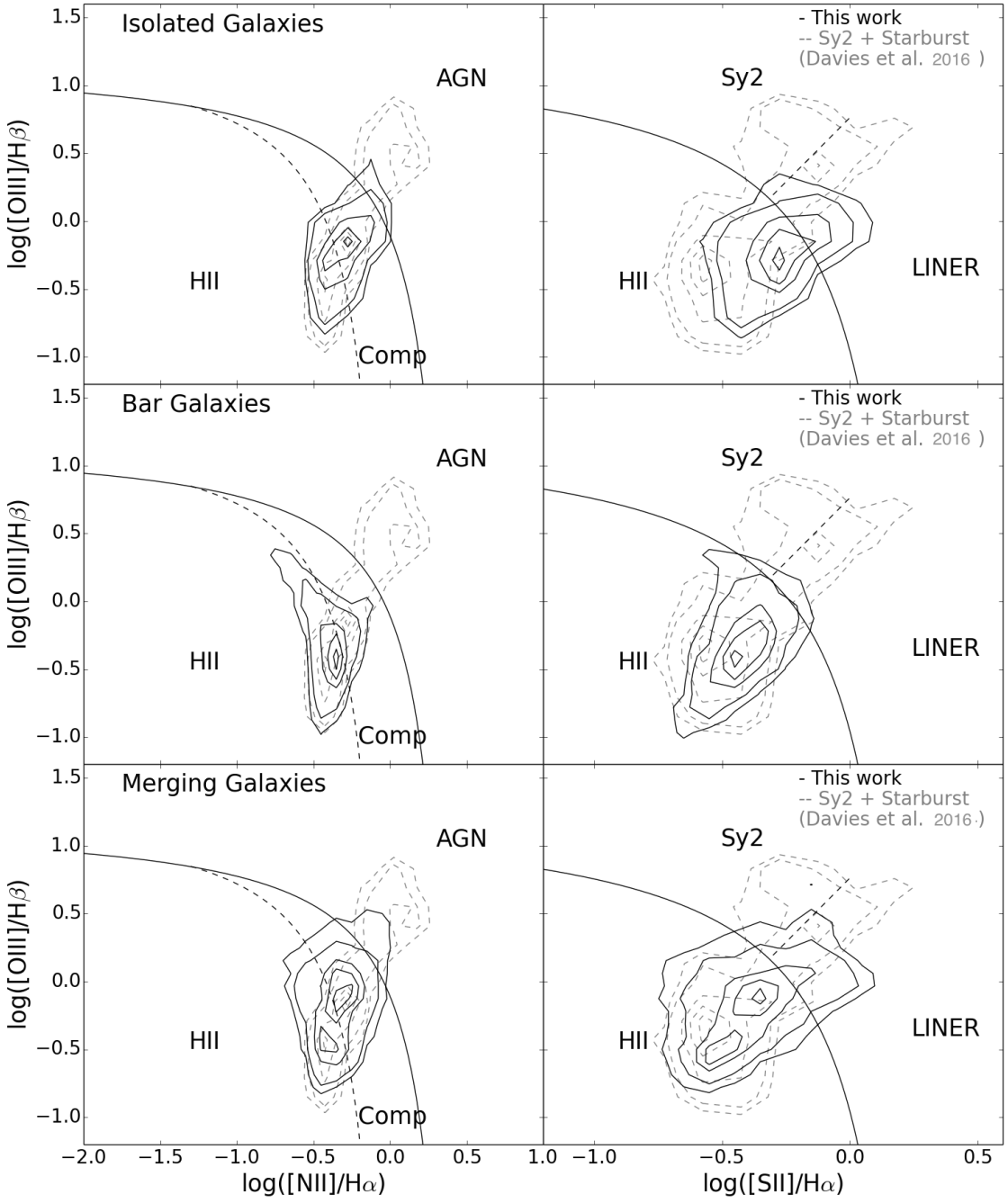

Figure 3.8: Diagnostic diagrams separated by morphology. Top: Isolated galaxies; [NII]/Hα and [SII]/Hα diagnostic diagrams, respectively. Middle: Bar galaxies; [NII]/Hα and [SII]/Hα diagnostic diagrams, respectively. Bottom: Merger galaxies; [NII]/Hα and [SII]/Hα diagnostic diagrams, respectively. Black contours map the density of spaxels in each region of the diagnostic diagrams. Grey dashed contours show the density of spaxels of known Sy2-starburst galaxies from Davies et al. (2016b). The two sets of contours are coincident in the star-forming regions of the diagnostic diagrams but not towards the AGN regions of the [NII]/Hα and [SII]/Hα diagnostic diagrams.

correct, and may have included calculating AGN fractions for galaxies that do not host AGNs. If all of the composite galaxies had been isolated spiral galaxies then this assumption would be appropriate, however their study was of merging galaxies in which this study only found 4/13 merging galaxies host AGNs. The major difference between their study and this one is that this study uses IFS while they used single slit spectra.

This study is not the first to determine that the non-stellar contribution to composite galaxies is not always the strong AGN signature of Seyferts but can also include LINER-like emission. Panessa et al. (2005) and Filho et al. (2004) determined their AGN selected composite galaxies did not host Sy2 type AGNs. Their study used X-ray emission to determine the type of AGNs their galaxies were host to.

While many of the sample of composite galaxies were found to contain nuclear shocks, star-formation or some combination of these plus an AGN, not all of the sample could be clearly identified. The lower spectral resolution of the CALIFA data prevents the clear identification of shocks. In at least one case, NGC7591, the identification remains ambiguous.

This sample only has 30 composite galaxies. To definitively answer the question on what are the drivers of composite emission in different galaxy morphologies, IFS surveys of both higher spectral resolution and larger numbers of galaxies are needed.

The HECTOR galaxy survey (Bryant & Bland-Hawthorn, 2016), will have both the increased spectral resolution and numbers to do such a study. With a spectral resolution of R = 4500 HECTOR will be able to break down the composite emission line ratios as done with the WiGS sample. The final survey size of HECTOR of $\sim 30,000$ galaxies means that on the order of hundreds of composite galaxies will be observed, and be used to constrain the results discussed in this chapter. A statistically significant analysis will go a long way to determining any further similarities or differences between composite galaxies in different environments and morphologies.

3.10 Conclusions

The 30 galaxies in this chapter were identified by the composite emission line ratios of the central 1 kpc of each galaxy. These galaxies are derived from two integral field spectrograph (IFS) surveys: the WiGS (12 galaxies; Rich et al. (2014)) and CALIFA DR1 (18 galaxies;

Sánchez et al. (2012)) samples. The power of IFS observations that cover large parts of a galaxy, and the addition of ancillary data, has been shown here to be a powerful toolkit in determining the excitation mechanisms of the 30 composite galaxies.

The excitation mechanisms within these galaxies that result in nuclear composite emission line ratios have been identified; 13/30 of the composite galaxies were found to host AGNs, 13/30 galaxies were identified to contain shocks, and 10/30 galaxies have neither AGN or shocks identified.

A correlation was found between the exciting nuclear sources in the composite galaxies and the galaxies' morphologies. Five of the six isolated spiral galaxies host AGNs (83%), while only three of the 10 isolated bar galaxies and five of the 13 merging galaxies host AGNs. Shocks are only identified in the isolated bar galaxies and the merging galaxies.

The wealth of information that can be obtained through IFS observations has allowed the dissection and analysis of the physical mechanisms powering these composite galaxies. In the case of the WiGS sample of galaxies, IFS has allowed both the spatial and spectral separation of the multiple physical mechanisms. This spectral separation is invaluable in untangling the composite emission lines ratios observed in galaxies. The CALIFA galaxy sample, although unable to be spectrally dissected, is used in a similar manner to spatially separate the possible multiple causes of composite emission line ratios. IFS observations are key in understanding the physical mechanisms of composite galaxies in a level of detail not possible with single spectrum studies.

This study of the WiGS and CALIFA composite galaxy samples has identified several key properties of composite galaxies;

1. Isolated galaxies are composite through a combination of star formation and AGN emission;

2. Bar and merging galaxies are composite through a combination of star formation and shocked gas emission as well as, in less cases, a combination of star formation and AGN emission;

3. Shocked gas emission is not contributing to the composite emission of the isolated composite galaxies in this chapter.

Overall, this study has affirmed that composite is not a singular definition and identified that the nature of composite classifications change with galaxy morphology. Further

studies with larger sample sizes and greater spectral and spatial resolutions will continue to delve into the nature of composite galaxies and definitively determine the nature of a composite classified galaxy with respect to morphology and environment.

Chapter 4

IRAS F10257-4339; Studying outflows in a merging system with Integral Field Spectroscopy

4.1 Introduction

The wealth of studies on the ongoing physical processes in IRAS F10257-4339 presents a picture of an almost coalesced merger with outflows of ionised and molecular gas from the northern nucleus caused by either a low luminosity AGN or young stellar clusters (Section 4.1.1). The previous studies have used long-slit optical observations to identify the outflows in IRAS F10357-4339. The WiFeS GOALS Survey (Rich et al., 2015) has observed IRAS F10257-4339 using Integral Field Spectroscopy (IFS) across the majority of the merging galaxy system making this an ideal galaxy to test the use of IFS observations in detecting and understanding gas outflows.

In previous chapters of this thesis the utility of using IFS was described. IFS is used in this Chapter to comprehensively understand the spatial impact of the dynamic components in IRAS F10257-4339 in ways not possible with single spectrum analysis. A combination of multicomponent sodium D-line $\lambda\lambda 5890, 5896$ (NaI D) absorption line fits and multi-component emission line fits was utilised to understand the connection between the observed neutral, molecular, and ionised gas physics. This chapter has identified the outflow from the northern nucleus as well as identifying the disk of the southern galaxy

in NaI D.

The previous studies of IRAS F10257-4339 are summarised in Section 4.1.1 and in Section 4.1.2 is a description of the morphology of the merging system. The emission line fitting (Rich et al., 2015) of IRAS F10257-4339 is discussed in Section 4.2.1 and the NaI D absorption line fitting in Section 4.2.2. In Section 4.3 the results of the absorption line fitting are discussed including the calculations of (a) the parameters of the absorption line fits, (b) the line-of-sight hydrogen column densities, and (c) outflow rates of the northern nuclear outflow. The study of IRAS F10257-4339 concludes in Section 4.4 with a description of the physical processes that have been detected through the use of neutral gas studies, along with a comparison to previous studies.

4.1.1 Previous studies

IRAS F10257-4339 is a late-stage merger of two gas-rich galaxies (nuclei separation $\sim 1\,\mathrm{kpc}$) with strong tidal tails (e.g. Lípari et al., 2004; Rich et al., 2011; Bellocchi et al., 2013; Emonts et al., 2014; Sakamoto et al., 2014; Arribas et al., 2014). The southern nucleus is heavily obscured by dust and thus is not visible in the optical (e.g. Boeker et al., 1997; Neff et al., 2003; Sakamoto et al., 2006; Alonso-Herrero et al., 2006; Lira et al., 2008; Díaz-Santos et al., 2008) but could be observed by X-ray, infrared (IR) and radio emission. Previous studies have posited that the northern nucleus is a low luminosity AGN or LINER.

A large number of studies have investigated the possible excitation source of the northern nucleus. Neff et al. (2003) used ratios of radio to X-ray emission to investigate the presence of an AGN. Lehmer et al. (2015) constrained the luminosity of the nuclei to a low luminosity AGN or LINER ($L_{2-10\mathrm{keV}}/L_{\mathrm{Edd}} \leq 10^{-5}$) or a non-AGN process, which is consistent with recent NuSTAR observations that have ruled out a Seyfert AGN (Lehmer et al., 2015). Recent studies do suggest that the X-ray brightness of the nuclei is due to a star-forming nucleus (Alonso-Herrero et al., 2012; Pereira-Santaella et al., 2010; Lira et al., 2008; Alonso-Herrero et al., 2006) which is consistent with Chapter 3 where IRAS F10257-4339 was identified as a composite galaxy dominated by star formation.

IRAS F10257-4339 is one of the nearest extreme starburst galaxies (Lípari et al., 2004). Lípari et al. (2004) used the ESO New Technology Telescope and Hubble Space Telescope

WFPC2 to identify galactic bubbles possibly caused by supernovae. Their study also indicated that the X-ray and radio emission of the northern nucleus could be explained by recent supernovae. The exact nature of the northern nucleus is still undetermined. However, here it is assumed star formation dominates the nucleus as was determined in Chapter 3.

IRAS F10257-4339 is a Luminous Infra-Red Galaxy (LIRG), $\log(L_{IR}/L_{\odot}) = 11.64$, and is host to outflows detected through observations of ionised gas (Lípari et al., 2000), molecular gas (Emonts et al., 2014; Sakamoto et al., 2014), and neutral gas (Heckman et al., 1990, 2000). Luminous Infra-Red Galaxies (LIRGs - $10^{11}L_{\odot} < L_{IR} < 10^{12}L_{\odot}$) are associated with merger activity, which drives intense circum-nuclear star formation, fuelling the Infra-Red (IR) luminosity (Veilleux et al., 1995a; Scoville et al., 2000; Arribas et al., 2004; Alonso-Herrero et al., 2006). The increase in IR luminosity with merger stage is also associated with an increase in galactic wind activity (Rupke et al., 2005b).

4.1.2 IRAS F10257-4339 morphology

The morphology of IRAS F10257-4339 has been constrained by Sakamoto et al. (2014) using CO observations. The northern nucleus is almost face-on, an inclination of 30°, and is surrounded by spiral arms that are highlighted in the HST image of Figure 4.1. Trancho et al. (2007) deduced that the northern nucleus and spiral arms are contained within a gas disk. The southern nucleus is nearly edge-on with an inclination between $70° < i < 85°$. It is clear from previous studies that the southern nucleus is not behind the northern galaxy, but in front of the disk. This does not preclude part of the southern galaxy disk being behind the northern galaxy (Emonts et al., 2014). The inability to observe the southern nucleus is due to the obscuration from its own disk.

Outflows in IRAS F10257-4339 have been identified using a variety of observations. Lípari et al. (2000) identified a nuclear outflow using long-slit observations across the northern nucleus. The observations identified a blue-shifted component of the Hα and [NII] emission lines which they attributed to an outflow. This outflow was detected again by Lípari et al. (2004) both along the northern nucleus and at several hundred parsecs away from the northern nucleus. The same outflow was also detected through the NaI D absorption feature by Heckman et al. (2000) using long-slit observations with the 4m Blanco Telescope. The recent studies by Emonts et al. (2014); Sakamoto et al. (2014) have identified

two molecular outflows using radio observations. One outflow emanates from the northern nucleus towards the observation point, the same outflow identified by Lípari et al. (2004); Heckman et al. (2000). The second outflow emanates from the southern nucleus perpendicular to the line-of-sight.

In Chapter 3 IRAS F10257-4339 was identified as a composite galaxy, consistent with Rich et al. (2011). The study by Rich et al. (2011) on the shocked emission line physics noted considerable NaI D absorption, indicative of an outflow, but did not quantify the absorption feature. Although the outflows in IRAS F10257-4339 have been investigated for NaI D absorption previously (Heckman et al., 2000), they have not been studied using IFS observations. An IFS observation has been used to identify the NaI D features in neutral gas and compare to previous studies of molecular and ionised gas.

4.2 Observation and pre-analysis steps

IRAS F10257-4339 is a merging system from WiGS. As explained in Chapter 3, the WiGS galaxies are a subset of 30 galaxies from the GOALS sample (Great Observatory All-Sky LIRG Survey; Armus et al., 2009), chosen to be observable by the WiFeS (Dopita et al., 2007) instrument on the ANU 2.3m telescope with redshifts $z < 0.05$. This subset of galaxies concentrates on U/LIRGs (Ultra/Luminous Infra-Red Galaxies) at different stages of merging, from isolated galaxies to late stage mergers. Specific wavelength coverage and resolutions for WiGS are presented in Table 3.1, Chapter 3.

The HST (Hubble Space Telescope) image of IRAS F10257-4339 is presented in Figure 4.1 in the F450W and F814W bands. The red box in the top left panel indicates the WiFeS FoV overlaid on the HST image. Note that the HST observation does not fill the entire WiFeS FOV and may cause a truncation to the HST colour calculated in the south-west corner. The bottom left panel of Figure 4.1 is the HST image convolved to the spatial scale of the WiFeS instrument ($1''$/pix). The bottom right panel is the continuum image produced by the WiFeS observation. Note a slight difference in the position of the brightest point between the HST convolved image and the IFS observation. The HST observations do not overlap the wavelength coverage of the WiFeS observation, creating a slight difference in the brightest spaxel between the two bottom panels. The x and y axes of each panel represent the kpcs from the centre of the galaxy, as defined in Rich et al.

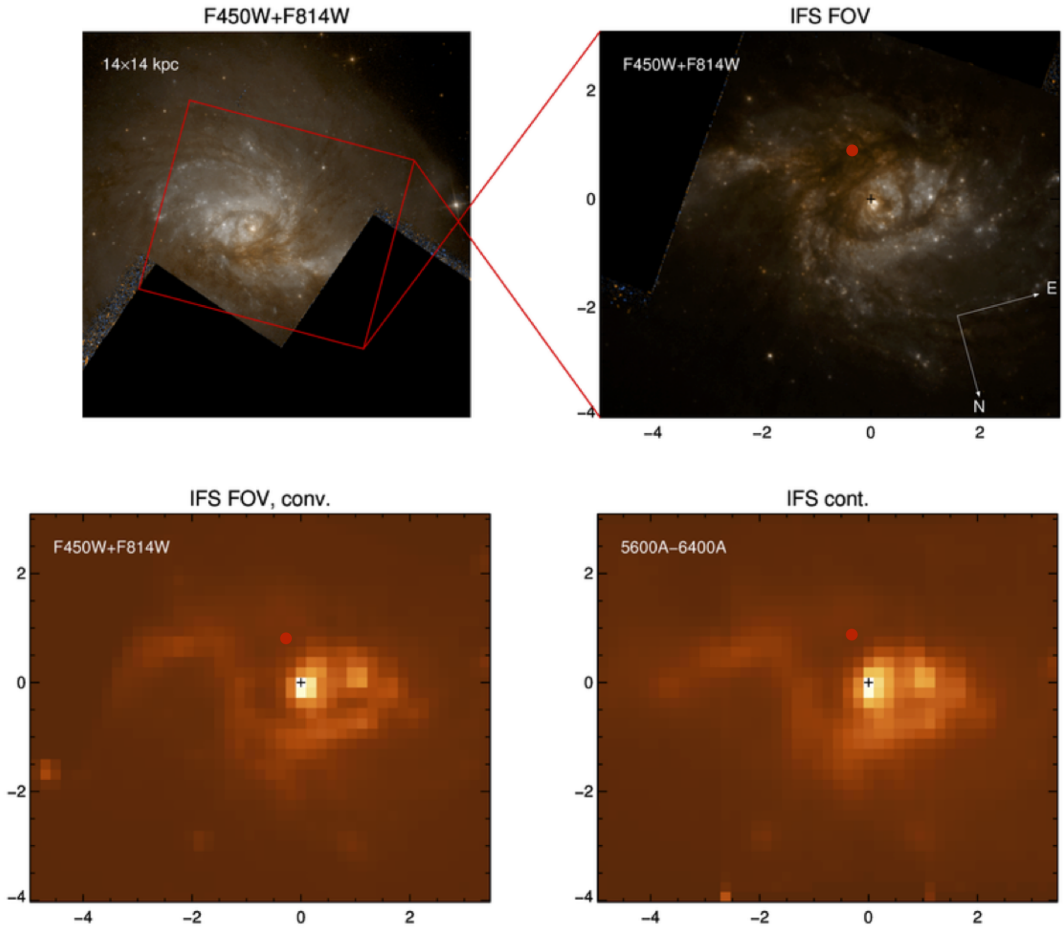

Figure 4.1: HST colour image of IRAS F10257-4339. Top left presents the HST image (F450W+F814W) with the FoV outlined in red. Top right present the FoV of our WiFeS observations. Bottom left is the HST image convolved to the same pixel scale as the WiFeS instrument (1″/pix). Bottom right presents the continuum extracted from the WiFeS datacube itself. The cross represents the position of the northern nucleus identified through the WiFeS continuum image. The red circle is the position of the southern nucleus (Neff et al., 2003).

(2011) for the northern nucleus and identified by the black cross in the bottom panels. The position of the southern nucleus has been highlighted with a red circle.

4.2.1 Emission line fitting

Before IRAS F10257-4339 can be analysed the pre-analysis steps of emission line fitting and absorption line fitting must be completed. The excitation mechanisms of IRAS F10257-4339 were determined in Chapter 3 by analysing the emission line maps defined by the emission line fitting of Rich et al. (2011). The emission line values were extracted using continuum and emission line fitting with `UHSPECFIT` (Zahid et al., 2011) and `MPFIT` (Markwardt, 2009). See Rich et al. (2011, 2015) for a detailed description of the fitting process.

The WiFeS observation of IRAS F10257-4339 has $\sim$ 500 spaxels all fit with stellar continuum models and emission line models of up to three separate Gaussians to describe the multiple physical processes hosted by this galaxy (Rich et al., 2010). The requirement of multiple components implies that IRAS F10257-4339 is a complex galaxy system of ionised gas and may also be a complex system of neutral gas.

4.2.2 Absorption line fitting

For IRAS F10257-4339 this chapter used the same continuum fit as defined by Rich et al. (2011), for consistency between the emission line and absorption line analysis. The absorption line fitting uses the IDL code `ifsfit` (Rupke, 2014). The IDL code and description are located on GitHub at `http://github.com/drupke/ifsfit`. This analysis has only utilised the absorption fitting part of `ifsfit`, using the datacube and continuum fit of IRAS F10257-4339 produced by Rich et al. (2011). `ifsfit` uses the spectra from each individual spaxel, divides through by the continuum fit and scales the resulting spectrum to a continuum level of one. Each spectrum is then fit for the NaI D absorption feature.

The NaID absorption feature is a doublet line, however in this study no distinction has been made between the two as they are blended in wavelength space. Fitting 2-components to the NaI D feature means fitting 2-components to both of the lines in the NaI D absorption feature. In spaxels where the HeIλ5876 line is present, the line is simultaneously fit using a Gaussian of redshift and dispersion derived from the emission line fitting of Hα, in order

to remove any contribution to the NaI D. `ifsfit` calculates the following parameters, along with Monte Carlo errors (Rupke et al., 2005b, section 6.3); Equivalent width W_{eq}, velocity, width of absorption line σ, covering factor C_f, and optical depth τ. Each of these parameters are discussed in detail in Section 4.3.

NaI D absorption can also be present due to the underlying stellar continuum. To ensure the absorption fit by `ifsfit` is not due to stellar contributions the NaI D absorption feature is compared to the MgI b$\lambda\lambda\lambda 5167, 5173, 5185$ absorption feature. The MgIb stellar absorption line is twice the strength of the NaI D stellar absorption (Heckman et al., 2000; Rupke et al., 2005b). No MgIb absorption was detected, which is consistent with previous studies of IRAS F10257-4339. The stellar continuum is dominated by young stars and thus does not have strong absorption in the MgI b and consequently no stellar NaI D contribution. An example of the spectra is presented in Figure 4.2. The top panel is the NaI D fitting, the middle panel indicates the continuum fit in comparison to the data with the NaI D and Helium lines highlighted by the green dashed lines and the bottom panel highlights the MgI b absorption lines. No MgI b absorption is observed in the data that is used to fit the NaI D absorption features and so no stellar component has been included in the analysis.

4.3 Analysis

IRAS F10257-4339 is a complicated system with many studies identifying different processes of ionised and molecular gas. This section expands on how certain parameters, such as W_{eq}, C_f, and τ are calculated in the code `ifsfit` and how they have been used to identify structures in the IFS observation. The previous study of the ionised gas (Chapter 3) is combined with the information about the morphology and the results of this chapter paint a clearer picture of the merging system, IRAS F10257-4339.

4.3.1 Velocities of ionised and neutral gases

The ionised gas velocities have been determined through the fitting of Hα emission lines in each spaxel of the WiFeS observation and are ordered by line width (first = most narrow, etc). The analysis of the emission lines present multiple physical processes through the need for up to three Gaussian profiles to fully describe the emission line features. The

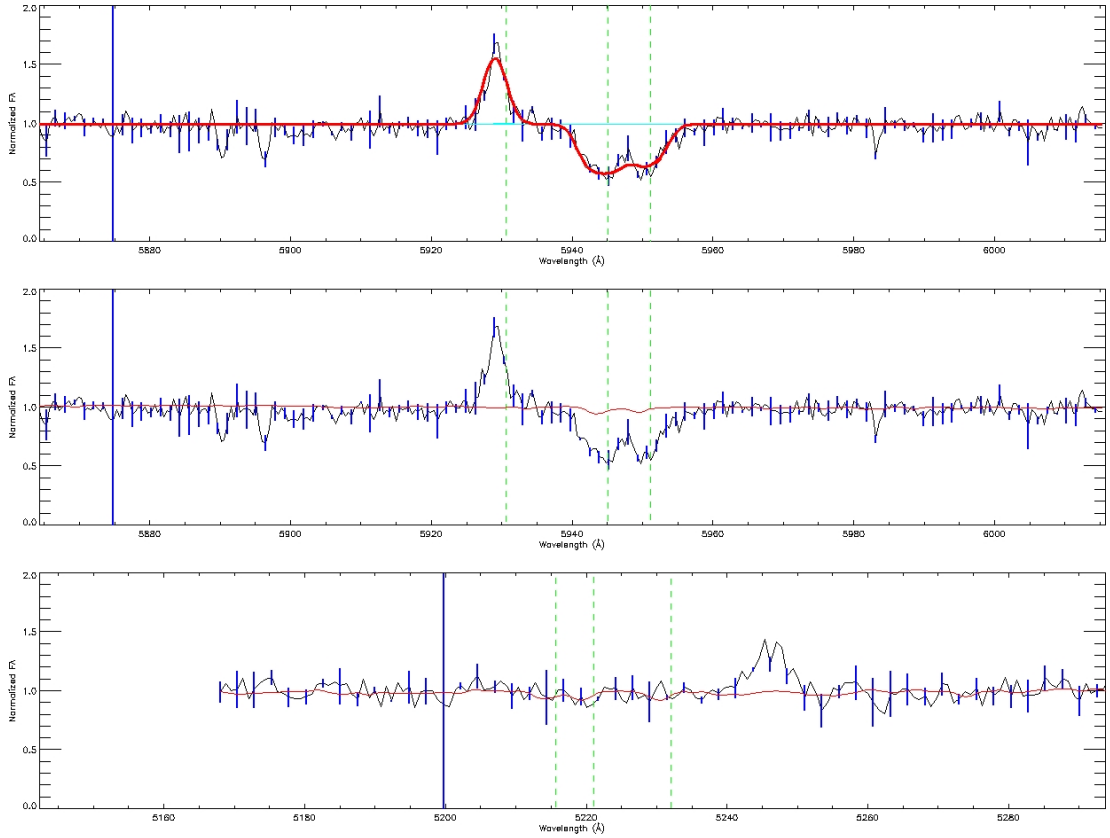

Figure 4.2: Top: example of fitting NaI D absorption feature with `ifsfit`. Middle: data around NaI D feature, the red presents the continuum which has been removed from the data before fitting, green dashed lines indicate the positions of HeI and NaI D. Bottom presents the data around the MgI b absorption feature with the continuum fit presented in red, the green dashed lines indicate the MgI b absorption lines. In all panels the blue represents the error in the flux. Bottom: shows no significant MgI b absorption, thus showing there is negligible NaI D absorption due to underlying stellar continuum.

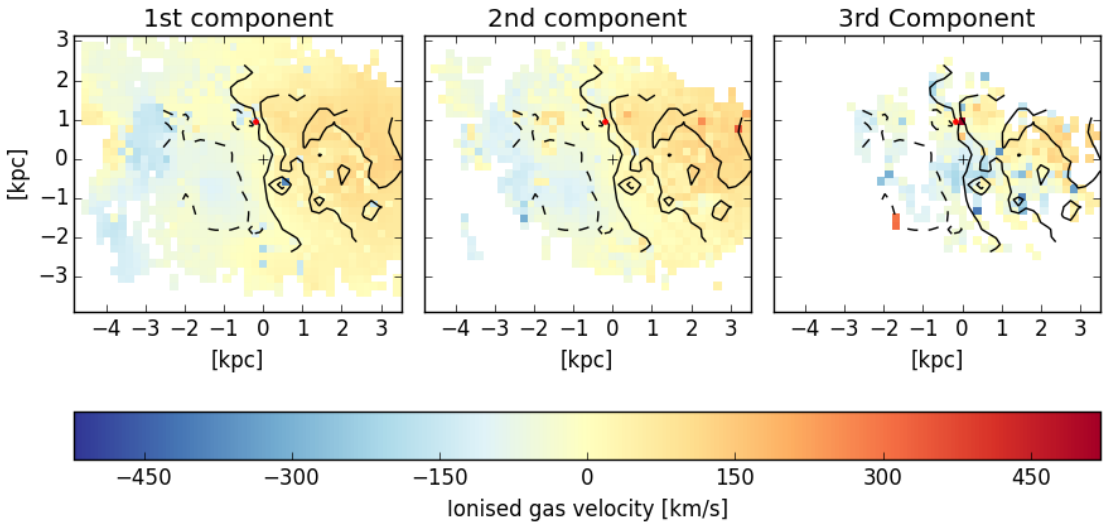

Figure 4.3: The ionised gas velocity maps of IRAS F10257-4339 defined from emission line fitting. There are up to three Gaussian components needed to explain the emission lines observed in this galaxy. The contours represent Gaussian smoothed ionised velocity where dashed contours represent negative velocities and solid contours represent positive velocities (inclusive of zero).

velocity maps of all 3-components are presented in Figure 4.3. The first two components (left and middle panel) show similar velocity structures with a defined rotation structure as is expected of the stellar disk of a galaxy. The rotation curve defined by the first component matches the rotation curve defined by previous studies of IRAS F10257-4339 (e.g. Emonts et al., 2014; Sakamoto et al., 2014; Lípari et al., 2004). The third component (right panel) indicates a different picture, with velocities shifted blue-ward in comparison to the disk gas velocities shown by the first two components. This third component may trace the same ionised outflow detected by Lípari et al. (2004). The contours in all panels of Figure 4.3 are defined by the first component of the velocity (galaxy rotation) with dashed lines indicating negative values of velocity.

The neutral gas velocities have been determined through the fitting of the NaI D absorption line and are ordered by velocity shift (first = smallest shift from systemic). In IRAS F10257-4339 up to two separate components of the NaI D doublet have been allowed, in the same way 3-components were used in the fitting of the emission lines. As described in Section 4.2 the stellar component of the NaI D is not present in the fitting of the doublet and so it is not expected to have the same rotation curve of the ionised gas. The velocity

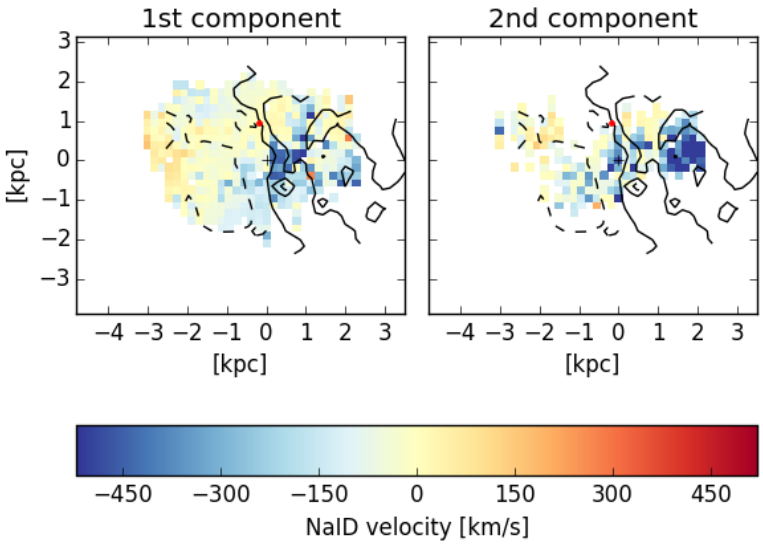

Figure 4.4: The neutral gas velocity maps of IRAS F10257-4339 defined through fitting NaI D absorption features with multiple components. The contours represent Gaussian smoothed ionised velocity where dashed contours represent negative velocities and solid contours represent positive velocities (inclusive of zero).

structure defined by the NaI D fits is presented in Figure 4.4. The velocity scale is the same as used in Figure 4.3 for comparison and the contours are derived from the first ionised velocity component. In the left panel two structures are identified in the velocity map, one mildly shifted both blue and red from systemic towards the southern nucleus and the other heavily blue-shifted towards the northern nucleus.

This picture is quantified in Figure 4.5, which shows that the neutral gas within 1 kpc of the northern nucleus is blue shifted up to -500 km/s, while within 1 kpc of the southern nucleus it is near systemic. Assuming the orientation from Sakamoto et al. (2014), the heavily blue-shifted components could be the outflow along the minor axis of the northern galaxy. The outflow described in Emonts et al. (2014); Sakamoto et al. (2014) from the southern nucleus, however, is red-shifted to the north and blue-shifted to the south in molecular gas. There is no strong evidence for this in our NaI D velocities.

The heavily blue-shifted component is correlated with the third component of the ionised gas velocity. Comparisons of the ionised (y-axis) and neutral (x-axis) velocities are presented in Figure 4.6. The top and middle panels show the limits of the ionised gas between

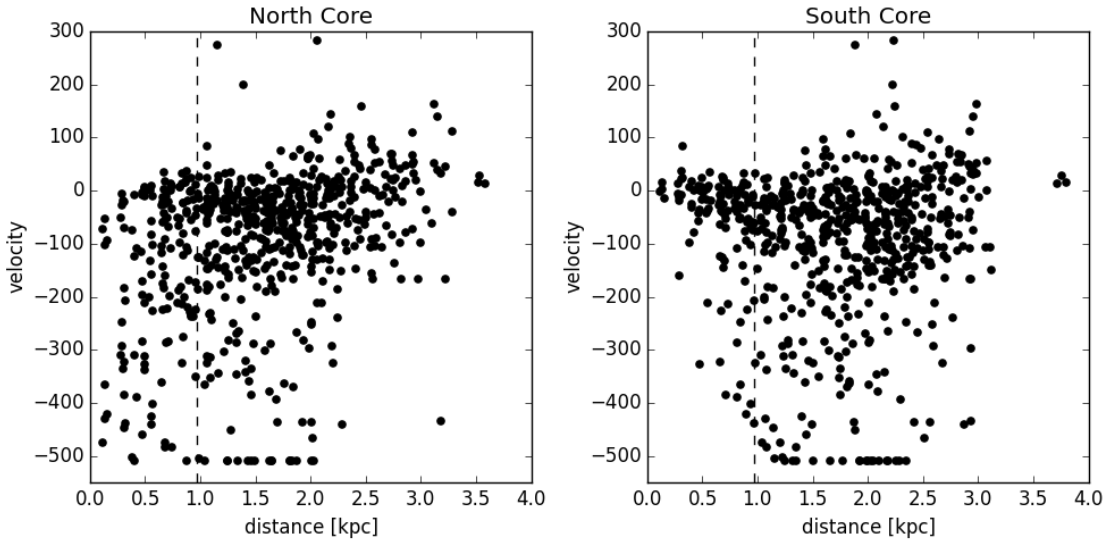

Figure 4.5: The velocity and distances of each spaxels' component from the north (left) and south (right) nuclei of IRAS F10257-4339. The distances are not de-projected. In the left figure we can identify the heavily blue-shifted components which are related to the north core, while the components around systemic velocity are associated with the southern core of this merger. The dashed lines in both panels indicate the distance between the two nuclei.

$\pm$200 km/s as expected from the rotation curve of the galaxy. The neutral gas velocities show groupings shifted slightly from the systemic velocity as has been indicated in the histograms of Figure 4.9. The third component of the ionised velocity has some correlation with the NaI D velocities suggesting the third ionised gas component is also tracing the outflow along the minor axis of IRAS F10257-4339. This is consistent with studies by Lípari et al. (2000, 2004) where they observed the outflow in the ionised gas. However, velocity distributions only tell a part of the story. To determine the physical mechanisms which give rise to the two observed NaI D components this study also investigated the equivalent width of the absorption, W_{eq}, and hydrogen column densities, N(H).

4.3.2 Calculation of equivalent width

The calculation of the equivalent width, W_{eq}, of the absorption lines of NaI D are completed as a part of the absorption fitting code `ifsfit` using the method outlined in Rupke et al. (2005b). The method used in Rupke et al. (2005b) also assumes resolved but blended absorption lines in the doublet, which also applies to our observations, and requires a Gaussian distribution of optical depth in velocity space, τ.

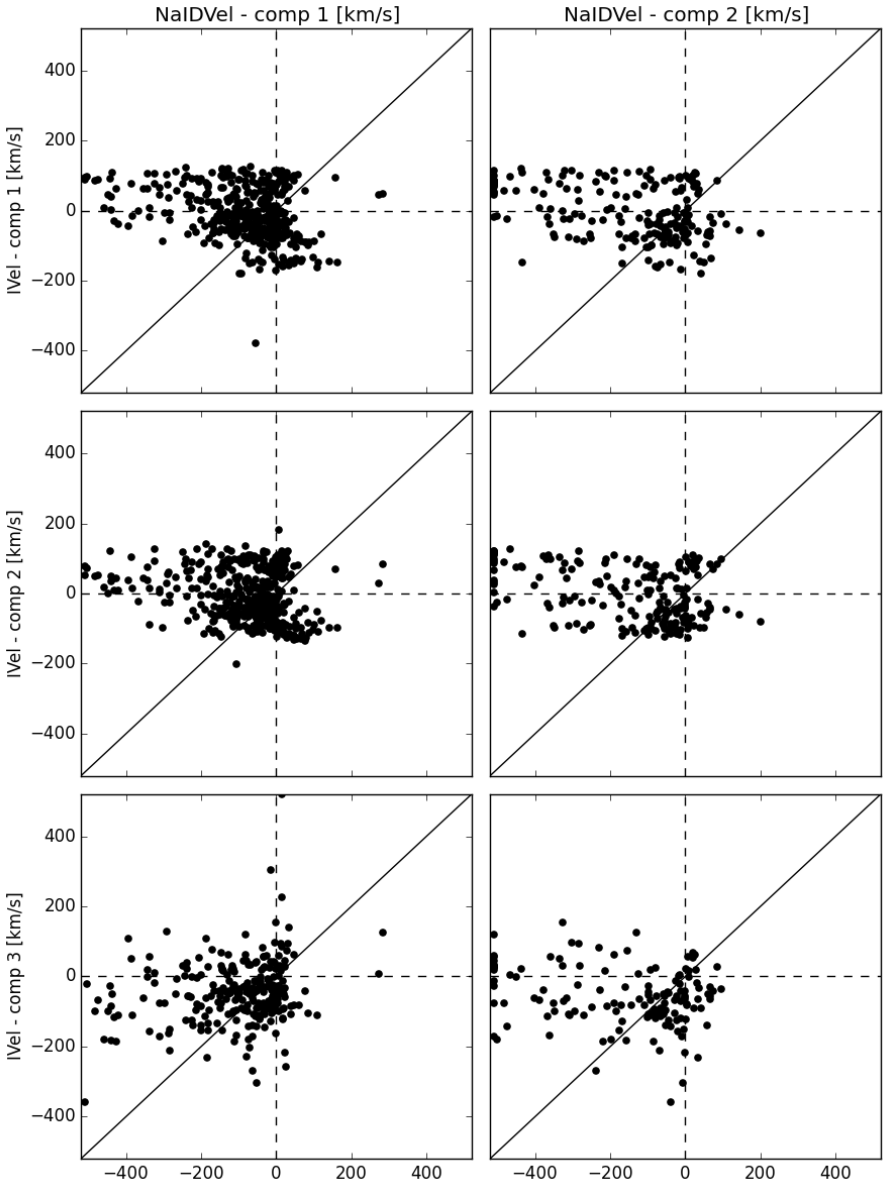

Figure 4.6: The comparison of the ionised (y-axis) and neutral (x-axis) gas velocities as defined through emission line analysis and the fitting of the NaI D absorption lines, respectively. The panels indicate the limits of the ionised gas between ±200 km/s. The neutral gas velocities show groupings shifted slightly from the systemic velocity as has been indicated in the histograms of Figure 4.9. The third component of the ionised velocity has some components that may correlate with the NaI D velocities at -200 km/s, suggesting the third ionised gas component might also trace the outflow along the minor axis of IRAS F10257-4339. However, there are not enough points to say this is definitively the case.

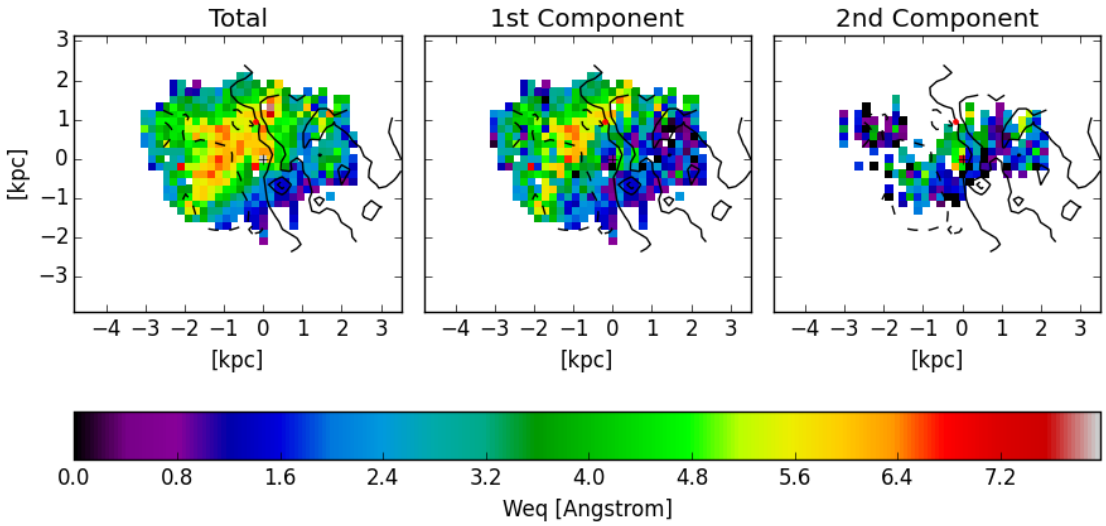

Figure 4.7: Equivalent width, W_{eq}, values from fitting multiple components to NaI D absorption features. Left presents the total W_{eq} calculated at each spaxel, centre presents the W_{eq} of the first component and right presents the W_{eq} of the second component. The contours represent Gaussian smoothed ionised velocity where dashed contours represent negative velocities and solid contours represent positive velocities (inclusive of zero).

Maps of W_{eq} shown in Figure 4.7 were calculated through the `ifsfit` code. This calculation used a signal to noise ratio of 3σ to remove components of low quality. The contours are derived from the first ionised velocity components. The W_{eq} values range from zero to > 7 Å. This figure shows both the first and second components of the NaI D absorption fitting as well as the total W_{eq}.

The highest values are concentrated along the edge-on disk of the southern galaxy, which can be seen in the HST observations, highlighted by the red and yellow spaxels in Figure 4.7. In comparison to the HST image of this galaxy there does not appear to be a direct relation to the morphology of the northern galaxy. However, Sakamoto et al. (2014) identified the possible orientation of the southern galaxy which indicated that the disk of the southern galaxy is perpendicular to the line of the two nuclei. The absorption of NaI D seen in high W_{eq} may be tracing the absorption due to the disk of the southern galaxy.

The lower total W_{eq} is present towards the region of the system where the highly blue-shifted neutral gas velocities are observed. This is indicative of a low column density or the absorption happening away from the thick dusty areas of a galaxy.

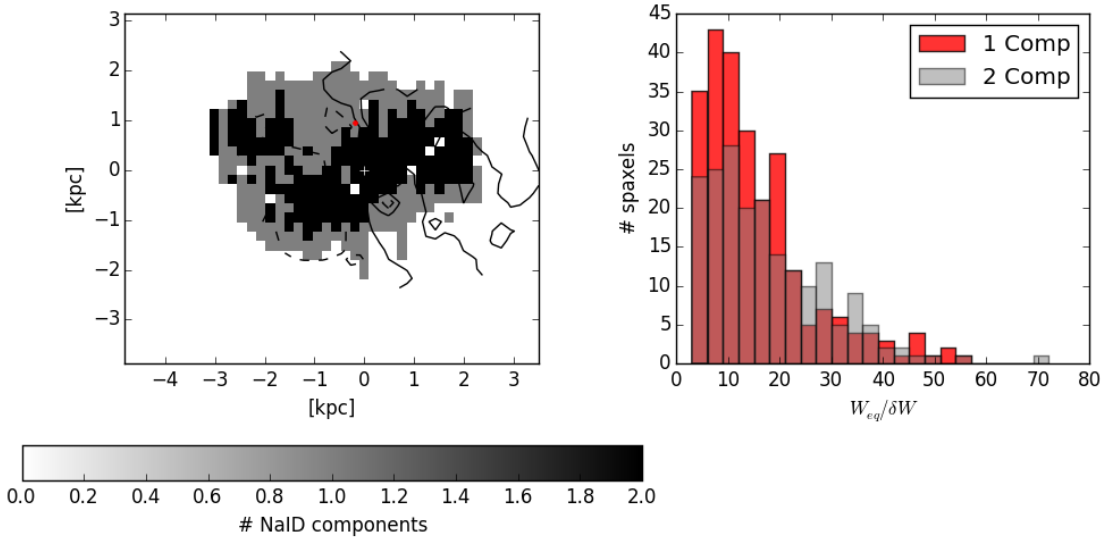

Figure 4.8: Left panel - map of the number of components fit to the NaI D absorption feature in each spaxel. Right panel - the SNR in the total W_{eq} split by the spaxel with 1 (red) and 2 (grey) components.

A map of where the 2-components are in the observations is presented in Figure 4.8 (left panel). In the case of Rupke & Veilleux (2015) the addition of a second component decreased the systemic uncertainty of the W_{eq} values, when compared to dust. However, it was found in this chapter that the addition of a second component neither improved nor worsened the systematic or systemic uncertainty of the W_{eq}. This indicates that the addition of another component is required to describe the absorption feature. For all spaxels a signal-to-noise cut of 3σ was used to remove the most uncertain fits from the analysis.

In order to explicitly show the velocity to W_{eq} structure of IRAS F10257-4339 in the neutral gas, a histogram of the velocities was created (Figure 4.9, left panel) and also a histogram of W_{eq} (right panel). A rudimentary velocity cut-off was defined, using the velocity distribution in Figure 4.5, of -200 km/s to separate the bulk of the NaI D absorption due to the southern galaxy and the outflow from the northern nucleus. This cut-off was applied in Figure 4.9 to identify the W_{eq} associated with the outflow from the northern nucleus. It is apparent from the right panel that the outflows associated W_{eq} does not differ significantly from the rest of the gas in W_{eq} in the remainder of the galaxy. A tail appears in the W_{eq} in the red as the cut-off has not completely excluded all points not associated with outflow or included all points associated with the outflow.

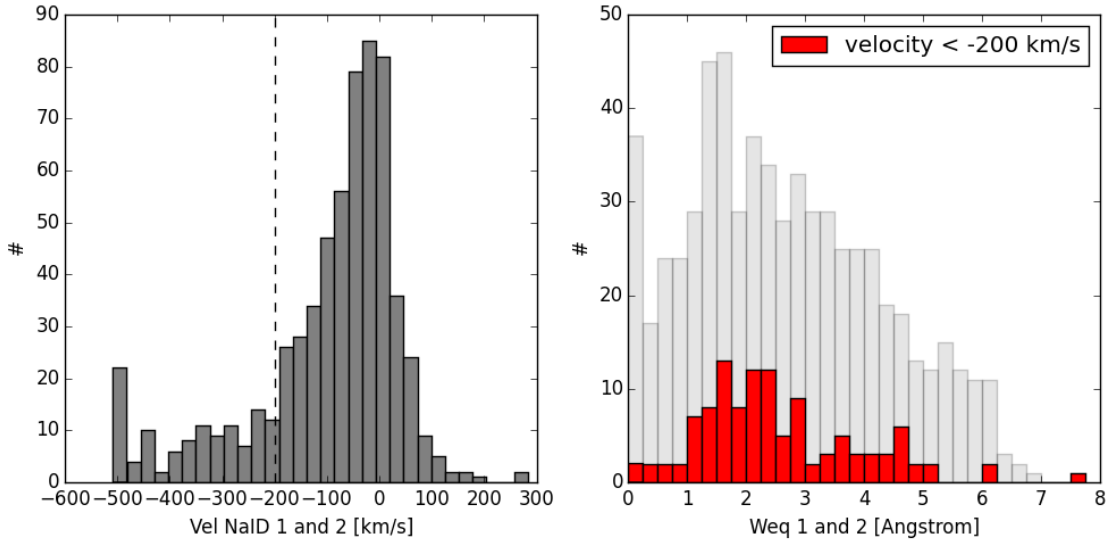

Figure 4.9: Left panel presents a histogram of the NaI D velocities in km/s. The peak of the distribution is around -50 km/s, an off-set from the systemic velocity of the system. The dashed line is the cut-off assumed for where a substantial number of components are due to the outflow along the minor axis of the northern galaxy. Right panel presents the histogram of the W_{eq} for each component. The red histogram shows the W_{eq} for components with velocities below the cut-off for the outflow. The peak of the red histogram shows the smaller W_{eq} as seen in the maps of Figure 4.7.

The study of this galaxy shows two unrelated physical processes occurring; one possibly due to the disk and spiral arms of the southern galaxy and the other due to an outflow along the minor axis of the northern galaxy. In order to confirm the W_{eq} that was observed is due to dust in the southern galaxy (and investigate how W_{eq} correlates across the whole galaxy) it was necessary to compare this to the dust of this galaxy. The dust content of this galaxy was calculated through the HST bands F450W-F814W using archival HST data, and is presented in colour-colour maps in Figure 4.10. The top left panel is the HST image with the WiFeS FoV overlaid in black. Top right panel is the HST image in the WiFeS FoV at the HST resolution (0.05″/pix). Bottom left panel is the colour map adjusted to the resolution of the WiFeS observation (1″/pix). Bottom right panel is the IFS continuum image for comparison of the galaxy structure to the other three panels in Figure 4.10.

Figure 4.11 compares the W_{eq} to the HST colour, or dust attenuation, obtained through the above process of convolving the HST images to our WiFeS spatial resolution. There is a correlation between the colour and total W_{eq} as is often seen in U/LIRGs (Veilleux et al., 1995a; Kim et al., 1998). See also a similar resolved relation (with spatially-resolved observations) in ULIRGs (Rupke & Veilleux, 2013). To understand this correlation physically N(H), hydrogen column density, is needed in order to fully understand the dust observed for IRAS F10257-4339.

4.3.3 Hydrogen column densities

The calculations given in Rupke et al. (2005b) were used to calculate the line-of-sight Hydrogen Column densities. These equations correct for ionisation, depletion and abundance of Na separately, instead of using empirically determined factors as is done in Rupke et al. (2002). Since it is assumed to be a Maxwellian velocity distribution, Equation 4.1 from Spitzer (1978) and subsequently Rupke et al. (2005b) can obtain the line of sight NaI column density from the data.

$$\mathrm{N(NaI)} = \frac{\tau_1 \mathrm{b}}{1.497 \times 10^{-15} \lambda_1 \mathrm{f_1}} [\mathrm{cm}^{-2}] \tag{4.1}$$

The variables, f_1, λ_1 and τ_1 are the oscillator strength, wavelength and central optical depth of the NaI Dλ5896 absorption line. b is the Doppler parameter defined by the width

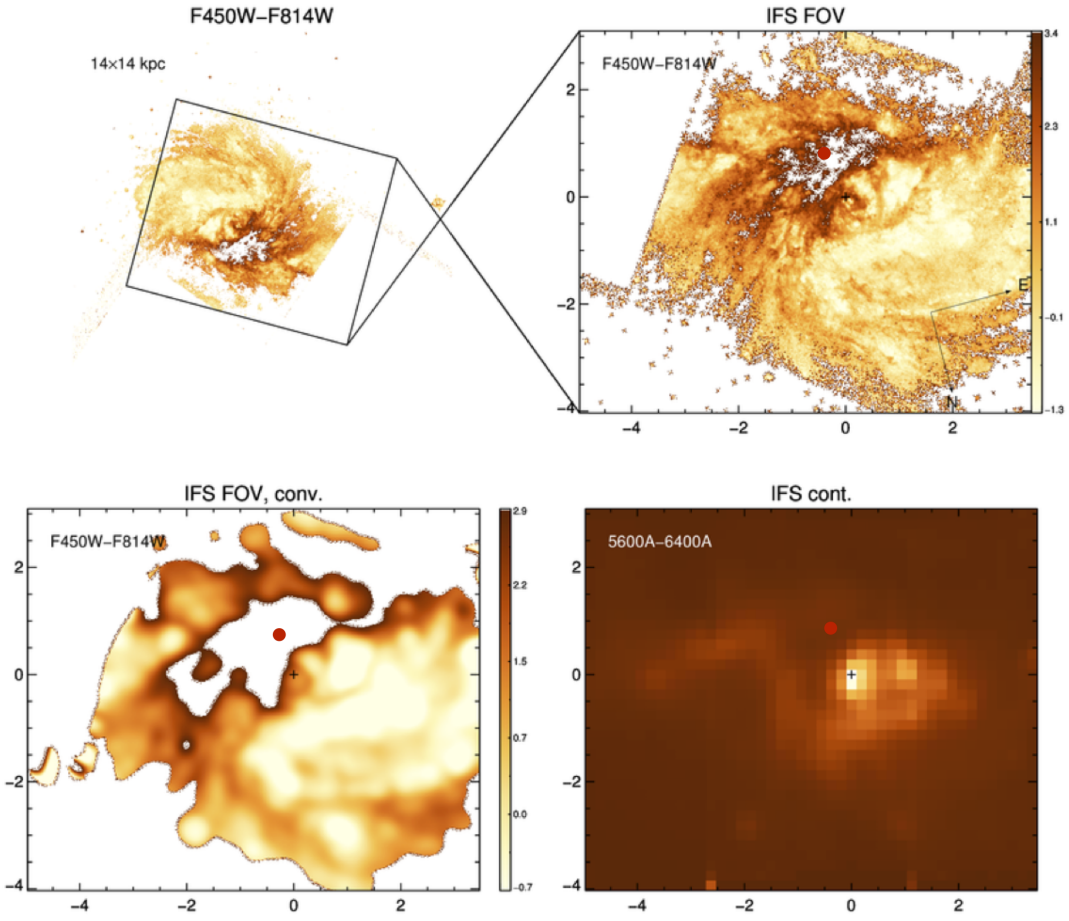

Figure 4.10: HST images used to calculate the dust content in IRAS F10257-4339 through the calculation of F450W-F814W. Top left presents the FoV of the WiFeS instrument overlaid on the HST image and top right presents the cut out of the FoV orientated to the WiFeS observation. Bottom left presents the F450W-F814W image convolved to the same pixel scale as the WiFeS observation. For comparison the IFS continuum image is presented in the bottom right plot.

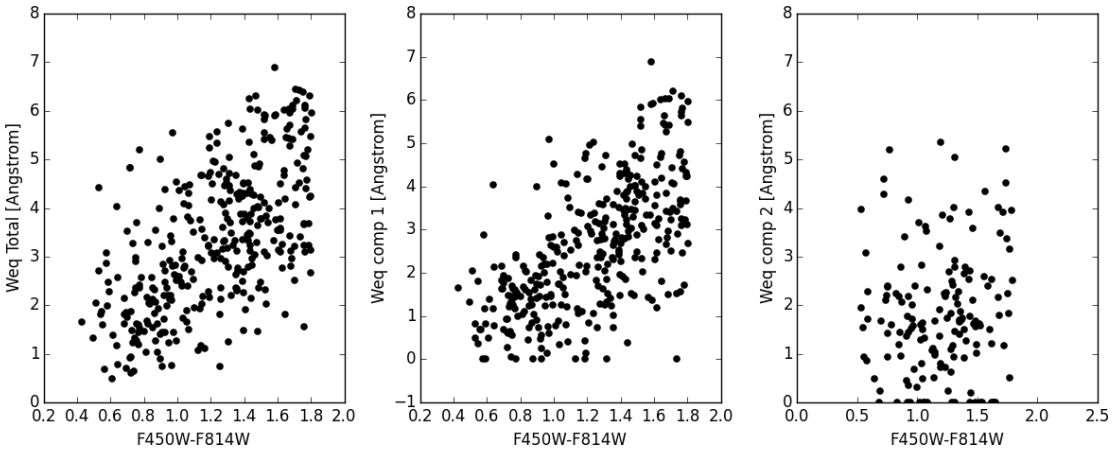

Figure 4.11: The comparison of W_{eq} to F450W-F814W colour. Left is the total W_{eq}, the middle and right are the first and second component W_{eq}, respectively.

of the absorption line in km/s. The values for f_1 and λ_1 are those given in Morton (1991) for NaI Dλ5896, $f_1 = 0.3180$ and $\lambda_1 = 5897.55$Å.

$$N(H) = \frac{N(NaI)}{(1-y)} 10^{-(a+c)} [cm^{-2}] \tag{4.2}$$

Equation 4.2 is then used to calculate the Hydrogen Column densities, taking into account the ionisation, depletion and abundance corrections. a is the abundance of Na in this galaxy, $a = \log[\frac{N(Na)}{N(H)}]_{gal}$. $b = \log[\frac{N(Na)}{N(H)}] - \log[\frac{N(Na)}{N(H)}]_{gal}$ is the depletion of Na atoms onto dust. The observed dust may shield neutral NaI D atoms from being completely ionised. For IRAS F10257-4339 a modest ionisation of N(Na)/N(NaI) = 10 was assumed, which is consistent with a mid range ionisation correction set by the empirical conversions from Na to H as calculated in Stokes (1978) and used in Rupke et al. (2002). This assumption results in $y = 1 - \frac{N(NaI)}{N(Na)} = 0.9$. For IRAS F10257-4339 it is assumed a solar metallicity of $\log[N(Na)/H(H)]_{\odot} = -5.69$ for Na in IRAS F10257-4339 and $c = -0.95$, the canonical Galactic value, for the depletion onto dust (Savage & Sembach, 1996).

The HST colour is representative of the dust attenuation in the galaxy. In the top left panel of Figure 4.12 the computed values of N(H) to F450W-F814W mostly sit along the lines of attenuation (with different R_v) from Calzetti et al. (2000). However, there is a second population of points that follow the curve but lie off it by almost 1 dex. Two types of points are shown in the top left panel to identify the spaxels with 1- and 2-component fits. In the top right panel of Figure 4.12 there are also two populations of points. The

envelope of points comes from the fact that in the optically thin case for $C_f = 1$, N(H) and W_{eq} have a well-defined relationship. For lower C_f, W_{eq} is lower for a given N(H) and a point moves left of the envelope. As the points become more optically thick, N(H) is higher for a given W_{eq} and a point moves up from the envelope.

The bottom panels of Figure 4.12 are the same as the top panels except the points are split by velocity. The velocity cut-off allows the identification of the points that are due to the outflow from the northern nucleus. In both panels there are two groupings of red points with velocities less than -200 km/s. The group in the lower left hand corner of the right panel is associated with the outflow from the northern nucleus. The molecular outflow from the southern nucleus was not identified in this study. However, the NaI D identified towards the southern galaxy is representative of the disk of the galaxy. The high W_{eq}, higher N(H), and the almost Gaussian distribution of velocities about the southern nucleus all point towards this being the case. There is an off-set of the peak of velocities to -50 km/s from the systemic redshift of the system. The redshift is defined from the northern nucleus and Emonts et al. (2014); Sakamoto et al. (2014) both predict that the southern nucleus is in front of the northern face-on disk. This morphology would account for the -50 km/s offset of a disk, another indicator that these spaxels are tracing the almost edge-on southern galaxy disk.

4.3.4 Mass outflow rate of northern outflow

The cause of the outflow from the northern nucleus remains unclear. Chapter 3 looked into the excitation mechanisms of IRAS F10257-4339 and indicated star formation as the central mechanism, which is consistent with previous studies (e.g. Lípari et al., 2004; Alonso-Herrero et al., 2006; Lira et al., 2008; Pereira-Santaella et al., 2010; Alonso-Herrero et al., 2012) that suggest the nucleus is heavily star-forming. The recent study by Sakamoto et al. (2014) indicated that the northern outflow could be easily explained by star formation when they analysed the molecular gas outflow. In this section it is assumed that the northern nucleur outflow is due to star formation and a mass outflow rate was calculated accordingly in order to compare to the lower limit of a mass outflow rate of $dM/dt = 6 M_{\odot} yr^{-1}$ of molecular gas from Sakamoto et al. (2014).

The mass outflow rate, dM/dt, is dependent on the assumptions made of an outflows' morphology and follows the discussion in Rupke et al. (2005c) and Shih & Rupke (2010) on

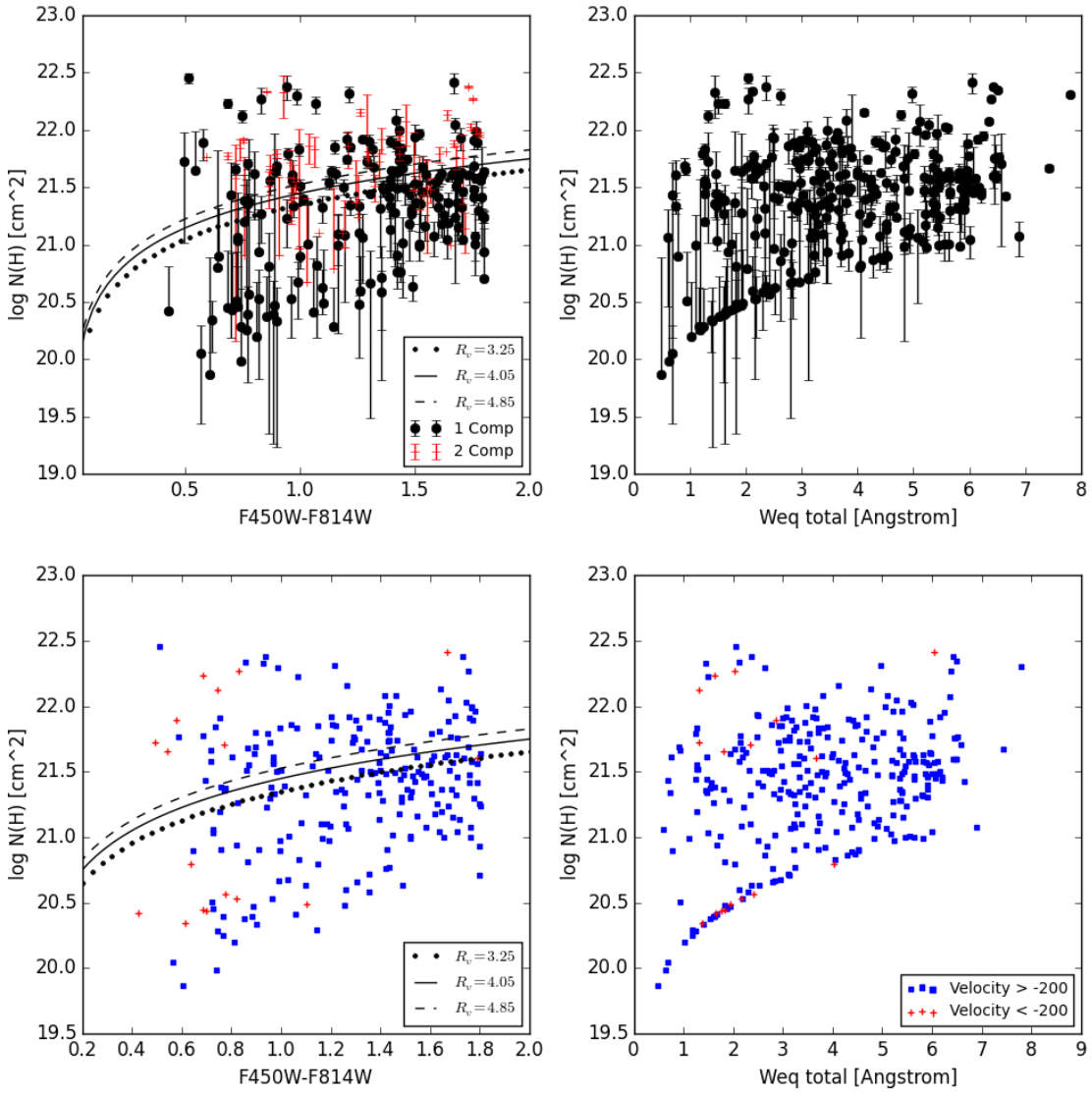

Figure 4.12: Comparisons of Hydrogen column density to HST colour and total W_{eq} of IRAS F10257-4339. Bottom left and right present the same points as the top plots except they have been separated by a velocity of -200 km/s. The velocity separation presents two distributions of points with velocity below -200 km/s. One with low Hydrogen column density and low W_{eq} associated with the outflow.

Outflow
Mass outflow rate: $6.80\,M_{\odot}yr^{-1}$
Momentum outflow rate: $1.52 \times 10^{11}\,erg\,s^{-1}$
Energy outflow rate: 4.76×10^{41} dyne

Table 4.1: Outflow rates calculated for IRAS F10257-4339 using a R = 3 kpc.

possible morphologies of starburst galaxy outflows. This morphology assumes a spherically symmetric outflow based on a thin-shell model. The thin-shell model, of uniform radius (3 kpc) based on the extent of the NaI D observed, is based on previous studies of starburst outflows (Veilleux & Rupke, 2005; Rupke et al., 2005c).

A shell of radius R = 3 kpc is used in Equation 5.1. The velocities are de-projected onto the spherical outflow, v_{dproj}, as is done in Shih & Rupke (2010). The solid angle of the outflow is given by $d\Omega$, μ is the mean molecular weight and m_p is the mass of a proton. The calculation of the mass outflow rates is summed over each component of the outflow and not each spaxel, meaning it has calculated the individual N(H) for each component. The outflow calculation is limited to the regions where there are blue-shifted velocity of -200 km/s or more associated with NaI D absorption.

$$dM/dt = \mu\, m_p\, R \sum N(H)\, v_{dproj}\, sec\_per\_yr * d\Omega\, Cf \tag{4.3}$$

A mass outflow rate of neutral gas of $\sim 6.8\,M_{\odot}yr^{-1}$ is estimated and it is similar to the rate estimated by Sakamoto et al. (2014) for the outflow rate of molecular gas. However, their outflow rate is a lower limit as they did not include velocity components below their detection range of ~ 224 km/s. The star formation rate of the IRAS F10257-4339 is $25\,M_{\odot}yr^{-1}$ (Sakamoto et al., 2014) which indicates that the star formation in and around the northern nucleus could explain the outflow observed in NaI D.

Table 4.1 lists different outflow rates of mass, momentum and energy for the outflow in IRAS F10257-4339. The momentum and energy outflow rates are calculated using similar sums over every component are described in detail in Shih & Rupke (2010).

4.4 Conclusions

The detection of heavily blue-shifted NaI D absorption is an unambiguous identifier of an outflow in a galaxy. The parameters defined by the fitting of the absorption doublet provide information about the physical processes of the neutral gas. This chapter has analysed IRAS F10257-4339 with an IFS observation in both ionised and neutral gas to better understand the outflow detected through previous studies (e.g. Emonts et al., 2014; Sakamoto et al., 2014; Lípari et al., 2000; Heckman et al., 1990, 2000). This analysis has concluded that there are two different processes occurring within IRAS F10257-4339, which are not related, resulting in NaI D absorption;

1. NaI D absorption associated with the outflow from the northern nucleus;
2. NaI D absorption associated with the disk of the southern galaxy disk.

The NaI D absorption, established to be correlated in velocity with the third ionised component of the emission line studies, traces the outflow of gas from the northern nucleus. This supports the blue-shifted emission features seen in long-slit data by Lípari et al. (2000) and the molecular gas studies by Emonts et al. (2014); Sakamoto et al. (2014). The absorption observed shows low $W_{eq} < 3$, lower HST colour and lower N(H) in comparison to the absorption from the second NaI D component. These three indicators present a picture of an un-dusty region with low N(H) due to an outflow of neutral gas along the minor axis. In addition to detecting the outflow in IRAS F10257-4339 it has been possible to spatially resolve the size of the outflow. Assuming the outflow originates from the northern nucleus of the merging pair, the outflow is observed with a R = 3 kpc and a mass flow rate of $6.8\,M_{\odot}yr^{-1}$.

The remainder of the observed NaI D absorption coincides with the disk of the southern galaxy. Dust approximations from HST colour maps and the N(H) in this region of the system indicate a dusty area. The velocities of the NaI D components are peaked at -50 km/s, close to the systemic velocity of the galaxy system indicating that this neutral gas could be associated with the galaxy rotation of a galaxy in front of the northern nucleus for which the redshift is defined. The molecular outflow from the southern nucleus was not detected in neutral gas (Emonts et al., 2014; Sakamoto et al., 2014).

In Chapter 3 it was shown that IRAS F10257-4339 is dominated by star formation in its nucleus (although many studies are still unsure if the northern nucleus is an AGN or star

formation) as well as having on-going star formation and shocks present in the rest of the galaxy. After this study of the neutral gas it can be said that IRAS F10257-4339 is host to an outflow of neutral, molecular, and ionised gas from the northern nucleus. The composite nature of this galaxy is much more complex than originally thought from the ionised gas physics (Chapter 3).

Studies of neutral gas kinematics are a powerful way to understand the physical processes occurring in galaxies. Using IFS allows an understanding of the spatial orientation of components of neutral gas as well as correlating with other studies. IRAS F10257-4339 is one of 24 galaxies in WiGS with detectable NaI D absorption. The use of IFS has allowed a comparison of the ionised and neutral gas processes of this galaxy on a spatial scale. These results have been compared to previous studies of IRAS F10257-4339 and found consistent physical processes. The results of this chapter are expanded in Chapter 5 to include the remaining 23 galaxies in WiGS with detected NaI D absorption in order to study how outflows of neutral gas are related to merging galaxies and their excitation mechanisms.

Chapter 5

Does the frequency of outflows in galaxies increase with merger stage?

5.1 Introduction

The merging of two gas-rich galaxies drives material towards the centres of galaxies, instigating intense circum-nuclear star formation and feeding central black holes. In the later stages of merging, material is ejected out of the galaxies, by these same processes, as outflows. Understanding and tracing outflows as a function of merger stage is key in understanding the order and timescales with which the merger process, inflows, and outflows are occuring.

The high gas densities and subsequent intense circum-nuclear star formation driven by the merger process leads to an increase in the total infrared luminosity, L_{IR}, of a merger system. Galaxies with heightened L_{IR} are known as Luminous InfraRed Galaxies (LIRGs) with $10^{11} < L_{IR}/L_{\odot} < 10^{12}$ and Ultra-Luminous InfraRed Galaxies (ULIRGs) with $L_{IR}/L_{\odot} > 10^{12}$. In the local Universe ULIRGs are mostly late stage mergers of two gas-rich galaxies (Veilleux et al., 2002; Kim et al., 2002; Tacconi et al., 2002; Genzel et al., 2001; Solomon et al., 1997; Sanders et al., 1988). LIRGs, however, are split into two groups; 1) gas-rich galaxies early in their merge moving towards a ULIRG (Ishida, 2004; Arribas et al., 2004), 2) less massive galaxy mergers or isolated galaxies (Ishida, 2004).

Previous works by Rupke et al. (2002) and Martin (2005) used detailed absorption studies to determine that outflows are detected twice as often in ULIRGs than in LIRGs. Based on this, both works argued that outflows are more common in late-stage mergers as compared to galaxies in the earlier stages of merging. Thus there is an expected connection between U/LIRGs, merger stage, and outflows. This chapter explores the increase of outflow frequency with merger stage in the U/LIRG sample of merging galaxies WiGS (Wide Field Spectrograph (WiFeS) Great Observatory All-Sky LIRG Survey (GOALS) sample; Rich et al., 2015) to help understand the importance of outflows along the merger sequence. Also explored is the possible excitation mechanisms of outflows along the merger sequence.

The use of the sodium D (NaI D$\lambda\lambda$5890, 5896) absorption feature is a popular method to detect neutral gas outflows in galaxies (e.g. Heckman et al., 2000; Rupke et al., 2002, 2005b,c; Martin, 2005). NaI D probes the neutral gas of a galaxy due to its low ionisation state of 5.14 keV. A blue-shifted NaI D component is ubiquitous with a galactic wind, or outflow. Outflows can also be detected in emission line features (e.g. Lípari et al., 2004; Ho et al., 2015) and molecular gas studies (e.g. Sakamoto et al., 2014; Emonts et al., 2014).

Integral Field Spectroscopy (IFS) is a powerful tool in studying local galaxies as it is able to both spatially and spectrally map out a galaxy, identifying spatially correlated information and tracing kinematic variations across the FoV (field-of-view). The analysis of the NaI D absorption features and outflow of IRAS F10257-4339 with IFS, Chapter 4, clearly demonstrates the power of using IFS observations for this type of analysis. In this chapter the study of IRAS F10257-4339 is extended to include the remaining 23 galaxies (21 galaxy systems) with observed NaI D absorption in the WiGS sample (Rich et al., 2014) to understand the degree of outflow correlation with merger stage.

In this chapter the mass, energy, and momentum outflow rates for the nine outflow galaxies are calculated for the use of future comparisons. A description of the NaI D subset of WiGS and the relevant data reduction is in Section 5.2. Section 5.3 summarises the results of analysing the nine outflow galaxies. In Section 5.4 the results of the analysis are discussed, leading to Section 6.5 where future studies are outlined that could follow on from these conclusions with a larger, statistically significant sample of merging galaxies hosting outflows.

5.2 Sample and pre-analysis

5.2.1 The sample galaxies

The Wide Field Spectrograph (WiFeS) Great Observatory All-Sky LIRG Survey (GOALS) sample, or WiGS (Rich et al., 2015), is a subset of GOALS (Armus et al., 2009) with $z < 0.05$ and have a northern declination limit of $+15^{\circ}$ in order to be observable with the WiFeS instrument (Dopita et al., 2007) on the ANU 2.3m telescope at Siding Spring Observatory. A detailed description of the observations can be found in Section 2 of Rich et al. (2015). The survey observed 27 galaxy systems, 30 galaxies, with a range of morphologies and L_{IR} consistent with LIRGs and ULIRGs. The ULIRGs are mostly late-stage mergers of gas-rich galaxies, while the LIRGs consist of both ULIRG precursors and less massive mergers or isolated galaxies.

The NaI D subset of WiGS galaxies was determined based on the presence of NaI D absorption that was not associated with any underlying stellar continuum. The non-stellar NaI D absorption arises from both neutral gas within a galaxy, possibly due to tidal interactions, and outflows (Chapter 4). Of the total 30 galaxies, 24 remain in the subset and are listed in Table 5.1 along with L_{IR}, systemic redshift, and merger stage (Section 1.3.1). The subset of NaI D galaxies includes two wide binaries (merger stage a), ten close binaries (merger stage b), nine late-stage mergers (merger stage cde), and four isolated galaxies. Of the 24 galaxies, this chapter identifies only nine galaxies with neutral gas outflows.

5.2.2 Pre-analysis steps

The pre-analysis steps include the data reduction of all 24 galaxy observations. This is the same procedure as explained in Chapter 3 for emission lines (ionised gas) and Chapter 4 for absorption lines (neutral gas). The reduction involved three steps;

1. reduction of each WiGS observation by Rich et al. (2015),
2. resulting continuum and emission line fitting using `UHSPECFIT` (Zahid et al., 2011) and `MPFIT` (Markwardt, 2009) by Rich et al. (2015), and
3. absorption line fitting undertaken using the IDL code `ifsfit` (Rupke, 2014) in the same manner as Chapter 4. Absorption fitting uses the same continuum fit as defined by Rich et al. (2015) and used in the emission line fitting for consistency between

analyses.

The following values were extracted from the WiGS emission and absorption fitting; (1) multi-component emission line maps, (2) ionised gas velocities, (3) ionised gas velocity dispersions, (4) NaI D W_{eq} (equivalent width), (5) C_f (covering fraction), (6) τ (optical depth), (7) neutral gas velocities, and (8) neutral gas velocity dispersions. (4) - (8) are calculated during the absorption line fitting process of `ifsfit`. The fitting of the NaI D absorption feature assumes the NaI D line are blended and that τ is Gaussian in velocity space. See Chapter 4 for more detail.

The N(H) (hydrogen column density) is calculated from HST (Hubble Space Telescope) observations of the subset of the galaxies with HST observations using the equations of Chapter 4 and Rupke et al. (2005b). The calculations assume a modest ionisation of Na/NaI = 10 (Stokes, 1978; Rupke et al., 2002), a solar sodium abundance of $\log(\mathrm{Na/H}) = -5.69$ and the canonical Galactic value of the depletion of Na onto dust of 95% (Savage & Sembach, 1996). See Chapter 4 for a detailed explanation of the equations used.

5.3 Results of individual analysis

Nine of the 24 galaxies in the NaI D sample have distinct blue-shifted NaI D absorption, indicative of an outflow. Two of the 24 galaxies are ambiguous in terms of distinct blue-shifted NaI D absorption but may host possible outflows. These two galaxies require follow-up using higher spatial resolution observations than the WiFeS instrumental resolution of $1''$/pix (Dopita et al., 2007) and are not included in the nine outflow galaxies discussed in the following sections.

The nine galaxies identified with outflows are indicated by an asterisk in Table 5.1. The two ambiguous galaxies are IRAS F16164-0746 and IRAS F16399-0937. The nine outflow galaxies are listed in Table 5.2 along with the physical properties of the galaxies and the outflow rates calculated in this chapter.

The orientations of the outflows that have been identified resemble the outflows of the northern nuclei of IRAS F10257-4339, described in Chapter 4. Outflows along the line-of-sight, or at a small inclination from the line-of-sight are easily identified as the outflow velocities are towards the observer as illustrated in Figure 5.1, a. Outflows perpendicular to the line-of-sight are more difficult to observe as the outflowing gas is moving perpendicular

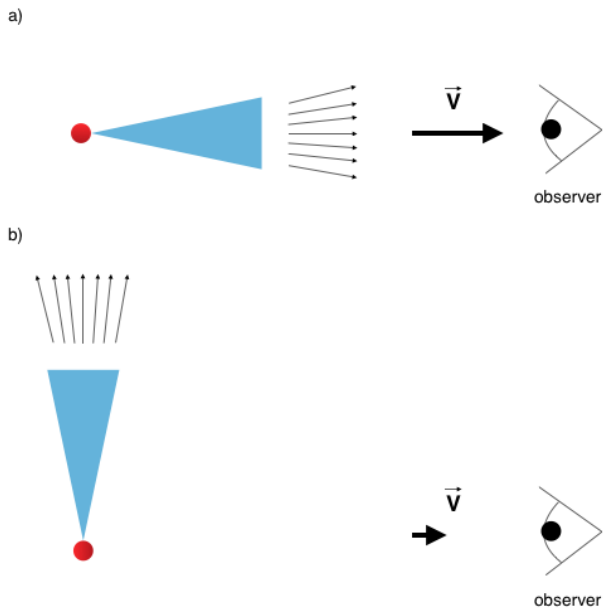

Figure 5.1: Illustration of two outflow possibilities. a) The outflow is in the line-of-sight, resulting in heavily blue-shifted NaI D absorption lines. b) The outflow is perpendicular to the line-of-sight, resulting in a smaller blue-shifted NaI D absorption.

to the motion observed as illustrated in Figure 5.1, b.

5.3.1 Outflow rate calculations

By comparing the outflow rates to the physical process occurring in the galaxies, insight into the outflows' possible launching mechanism can be gained. For example the mass outflow rate can be compared to the SFR (star formation rate) in order to determine if the outflow is stellar driven. In Chapter 4, the SFR of IRAS F10257-4339, $25 M_{\odot} yr^{-1}$, was determined to be sufficient to produce an outflow of $6.8 M_{\odot} yr^{-1}$. For the nine outflow galaxies in this chapter (which includes IRAS F10257-4339) the mass, momentum, and energy outflow rates are calculated.

The outflow rates of mass, momentum, and energy are calculated using the equations of Shih & Rupke (2010) for the nine galaxies. The shell radius, the radius of the outflowing material with the assumption the outflow is spherical (Chapter 4), of each outflow is estimated using the IFS observations and the extent of the NaI D identified for each galaxy. The values of shell radii are listed in Table 5.2. The velocity components of the outflows

are de-projected onto this spherical shell radius, v_{dproj}, for the calculation of outflow rate. The calculation of the mass outflow rate is summed over each component as described in Chapter 4.

Equation 5.1 is used to calculate the mass outflow rate of each neutral gas outflow;

$$dM/dt = \mu\, m_p\, R \sum N(H)\, v_{dproj}\, sec\_per\_yr * d\Omega\, C_f. \tag{5.1}$$

The energy and momentum outflow rates are calculated using similar sums over every neutral gas component, as described in Shih & Rupke (2010) and Chapter 4. The resulting outflow rates of mass, energy and momentum for each of the nine galaxies are tabulated in Table 5.2.

IRAS Identifier	L_{IR}	z	Merger Stage	Nuclear Excitation
(1)	(2)	(3)	(4)	(5)
F01053-1746	11.71	0.0201	b	SF
F06076-2139	11.65	0.0374	b	Unclear
*F10038-3338	11.78	0.0341	cde	SF
*F10257-4339	11.64	0.0094	b	SF
F12043-3140	11.43	0.0232	b	SF
F12592+0436	11.68	0.0375	cde	Sy2
*13120-5453	12.32	0.0308	cde	Sy2
F13373+0105 East	11.62	0.0226	a	SF
F13373+0105 West	11.62	0.0226	a	SF
F15107+0724	11.35	0.0130	iso	SF
F16164-0746	11.62	0.0272	cde	Sy2
F16399-0937	11.63	0.0270	b	LINER
F17138-1017	11.49	0.0173	cde	AGN^x
*F17207-0014	12.46	0.0428	cde	SF
*F17222-5953	11.41	0.0208	iso	SF
F18093-5744 North	11.62	0.0173	b	SF
F18093-5744 South	11.62	0.0165	b	SF
F18293-3413	11.88	0.0182	b	SF
F18341-5732	11.35	0.0156	iso	SF
*F19115-2124	11.93	0.0487	b	SF
*F20551-4250	12.06	0.0430	cde	SF
F21330-3846	11.14	0.0191	b	SF
*F21453-3511	11.42	0.0162	iso	Sy2
*F22467-4906	11.84	0.0430	cde	Unclear

Table 5.1: The subset of 24 U/LIRGs from Rich et al. (2012) with detected NaID absorption (1) - IRAS Identifier (Sanders et al., 2003; Armus et al., 2009), (2) - IR luminosity (Sanders et al., 2003; Armus et al., 2009), (3) systematic redshift (Sanders et al., 2003), (4) - merger stage (Rich et al., 2012), (5) - nuclear optical classification (Rich et al., 2015, Chapter 3); SF - star formation dominated, Sy2 - Seyfert 2 host galaxy, AGN^x- AGN identified through X-ray analysis in Chapter 3, Unclear - galaxies which were not decomposed composites or were not clear in the studies by Rich et al. (2015).

IRAS Identifier	Merger Stage	W_{eq}	log[N(H)]	Radius	Mass outflow rate	Energy outflow rate	Momentum outflow rate
		Å	log[cm^2]	kpc	$M_\odot yr^{-1}$	erg s^{-1}	dyne
(1)	(2)	(3)	(4)	(5)	(6)	(7)	(8)
F10038-3338	cde	1-6	20-22.25	4	10.38	1.23×10^{41}	9.59×10^{10}
F10257-4339	b	0-8	19.5-23	3	8.81	4.03×10^{41}	1.57×10^{11}
13120-5453	cde	3-19	20.5-22.5	4	195.80	2.31×10^{43}	5.39×10^{12}
F17207-0014	cde	2-15	21-23	4	219.35	1.05×10^{43}	4.06×10^{12}
F17222-5953	iso	1-8	20-22.5	3	6.43	5.16×10^{41}	1.32×10^{11}
F19115-2124	b	1-7	20-22.5	6	5.93	1.44×10^{41}	7.21×10^{11}
F20551-4250	cde	0-3.5	19.5-22.5	5	8.92	2.11×10^{41}	1.16×10^{11}
F21453-3511	iso	0-8	20-23	3	6.48	2.49×10^{41}	1.07×10^{11}
F22467-4906	cde	1-10	20.5-22	4	78.17	8.55×10^{42}	2.25×10^{12}

Table 5.2: NaI D fitting results for the seven outflow galaxies. The outflow rates for the two possible outflow galaxies could not be calculated as the outflow parameters could not be constrained. Each galaxy is individually discussed in Appendix C.1. (1) - IRAS Identifier (Sanders et al., 2003; Armus et al., 2009), (2) - merger stage (Rich et al., 2012), (3) - range of W_{eq} (Appendix C.2), (4) - Range of hydrogen column densities N(H) (Appendix C.2), (5) - Radius of outflow in kpc, (6) - Mass outflow rate, (7) - energy outflow rate, (8) - momentum outflow rate.

5.3.2 Bringing together ionised and neutral gas analysis

The combining of ionised and neutral gas analysis of galactic wind galaxies is significant in determining a bigger picture of these galaxy processes (Chapter 4). The ionised gas can inform on the power sources driving galaxies (Chapter 3) which in turn can inform on what may be producing an outflow in this sample of galaxies. By combining the study of ionised gas power sources with the outflow galaxies a possible understanding of the driving mechanism of these outflows can be determined.

The ionised and neutral gas velocities of IRAS13120-5453 are presented in Figure 5.2. This galaxy is a late stage merger in the WiGS sample with an outflow of neutral gas and is dominated by an AGN in all wavelengths (Rich et al., 2015; Iwasawa et al., 2011, 2009; Petric et al., 2011; Pereira-Santaella et al., 2010; Farrah et al., 2007). The ionised gas velocities indicate a rotating disk (Figure 5.2, top panels) and a blue shifted component in the right most panel. The NaI D absorption also identified a blue shifted component, spatially similar to the third ionised gas component (Figure 5.2, bottom right two panels). Figure 5.2 bottom left panel is a HST F814W image of IRAS13120-5453 with the same FoV as the IFS panels. IRAS F13120-5453 is a merging galaxy and thus the outflow caused by the central AGN can be attributed to the merging process. The outflow rates for IRAS13120-5453, using a shell radius of 3 kpc, are listed in Table 5.2.

IRAS F17222-5953 is another isolated galaxy in the WiGS sample. This galaxy appears to host no AGN (Chapter 3), suggesting the outflow must be driven by star-formation. The ionised gas velocity maps (Figure 5.3, top panels) indicate a rotation curve in the first two components and a blue shifted third component. The neutral gas velocities map out a region of blue-shifted outflowing material (Figure 5.3, bottom two right panels). The bottom left panel of Figure 5.3 is an IR image of IRAS F17222-5953 from the SDSS archive with the same FoV as the IFS observations for comparison. The blue-shifted NaI D is positioned in the centre of the IR image, indicating the outflow is from the nucleus of the galaxy.

The two isolated galaxies, IRAS13120-5453 and IRAS F17222-5953, are similar to each other in that the ionised gas velocities hint at a possible outflow that is confirmed through the NaI D absorption line fitting.

Two well studied merging galaxies with neutral gas outflows are IRAS F10257-4339 and

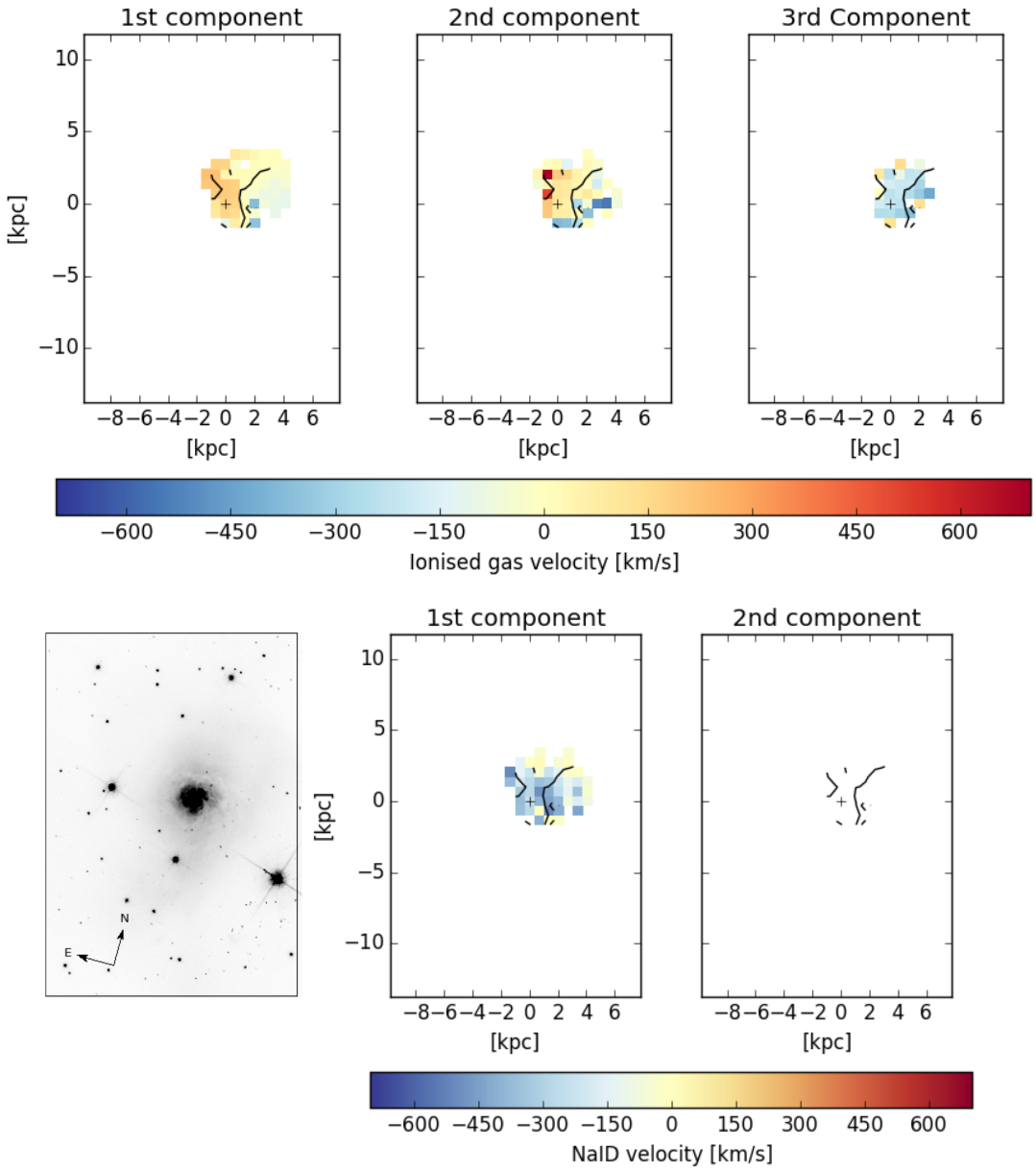

Figure 5.2: IRAS F13120-5453 diagnostic plots. Top panels - The Ionised gas velocity maps of IRAS F13120-5453 defined from emission line fitting are presented in the top panels. There are up to three Gaussian components needed to explain the emission lines observed in this galaxy. Bottom left panel - HST F814W image with the same FoV as the IFS observations for comparison. Bottom right two panels - The neutral gas velocity maps of IRAS F13120-5453 defined through fitting NaI D absorption features with multiple components are presented in the bottom panels. The contours represent Gaussian smoothed ionised velocity where dashed contours represent negative velocities and solid contours represent positive velocities (inclusive of zero). 1pixel = 1″ on sky.

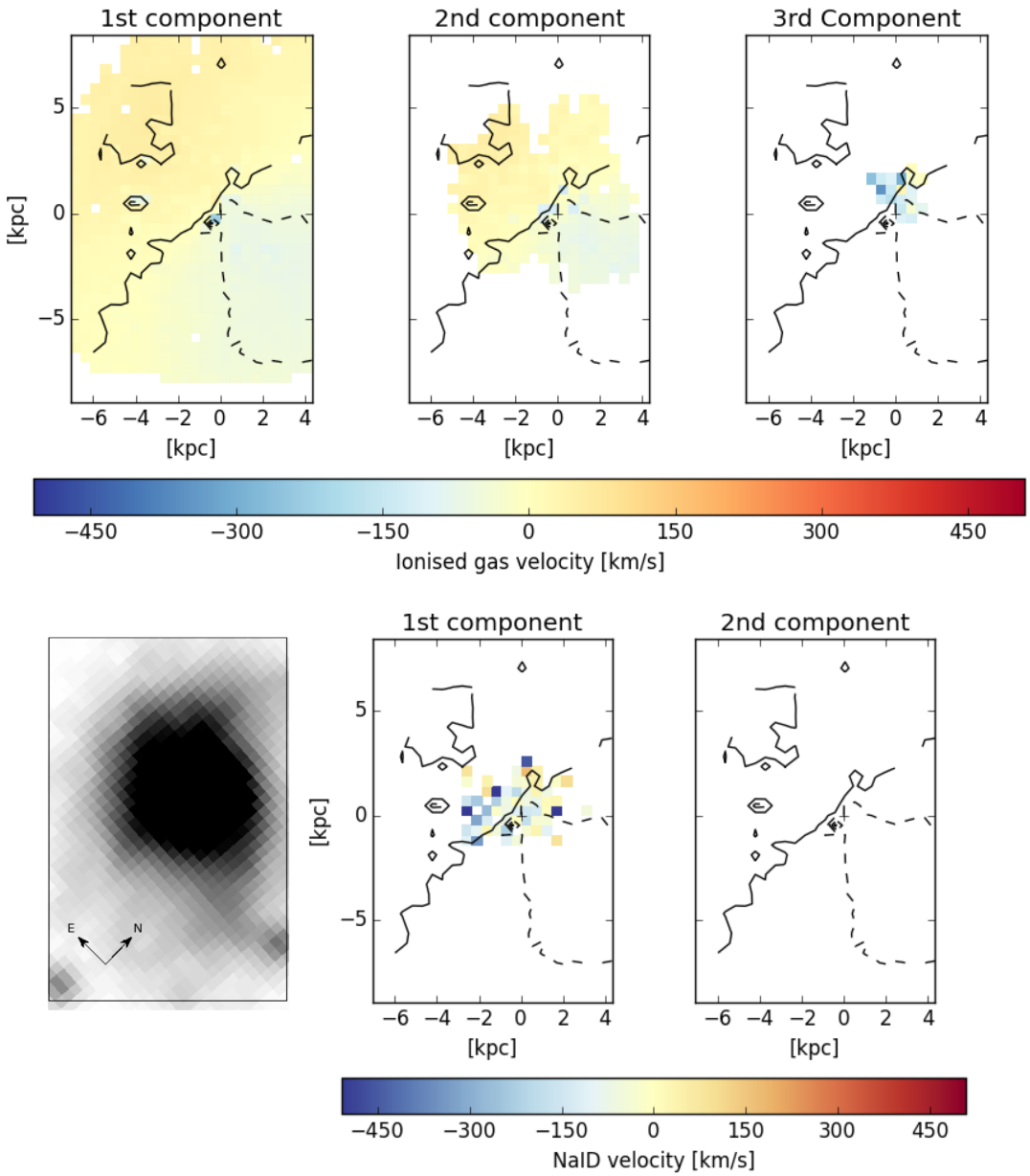

Figure 5.3: IRAS F17222-5953 diagnostic plots. Top panels - The Ionised gas velocity maps of IRAS F17222-5953 defined from emission line fitting are presented in the top panels. There are up to three Gaussian components needed to explain the emission lines observed in this galaxy. Bottom left panel - HST F814W image with the same FoV as the IFS observations for comparison. Bottom panels - The neutral gas velocity maps of IRAS F17222-5953 defined through fitting NaI D absorption features with multiple components are presented in the bottom panels. The contours represent Gaussian smoothed ionised velocity where dashed contours represent negative velocities and solid contours represent positive velocities (inclusive of zero). 1pixel = 1″ on sky.

IRAS F17207-0014. IRAS F10257-4339 (Chapter 4) has an outflow of neutral gas from its northern nucleus. Chapter 4 determined that the neutral gas outflow rate of $6.8\,M_{\odot}\,yr^{-1}$ was consistent with the calculated SFR of $25\,M_{\odot}yr^{-1}$ (Sakamoto et al., 2014).

IRAS F17207-0014 is an optically composite galaxy, like IRAS F10257-4339, but the ionised gas analysis was inconclusive on the central 1 kpc excitation mechanism due to uncertain ($< 3\sigma$) emission line fluxes. However, IRAS F17207-0014 was identified as a star forming galaxy by Rupke et al. (2005b). The outflow rate calculated in this study of $219.35\,M_{\odot}\,yr^{-1}$ is easily produced by the SFR of $306\,M_{\odot}\,yr^{-1}$ (Rupke et al., 2005c). IRAS F17207-0014 is a coalesced merger, the last stage of the merging process.

Not all merging galaxies in the later stages of merging (merger stages cde) can be easily separated into c or d or e merger stages. This leaves some ambiguity on exactly when outflows occur along the merging process. An increased spatial resolution may help separate these laters stages of merging.

The remainder of the nine outflow host galaxies include one other close binary (merger stage b), and four other late stage mergers (merger stage cde) for a total of two isolated galaxies (iso), no wide binaries (a), two close binaries (b), and five late stage mergers (cde).

Each of the 24 galaxies in this study are discussed in detail in Appendix C.1 and the analysis and diagnostic figures for the nine definite outflow galaxies are in Appendix C.2.

5.4 Discussion of results

The preliminary results of this study are presented in Figure 5.4 with the total numbers of galaxies in each merger stage in the left panel. The WiGS sample includes four isolated galaxies, four wide binaries, 13 close binaries, and nine late stage mergers. Of these 30 galaxies, 24 have NaI D detections (green crosses) and only nine of these galaxies have clear signatures of neutral gas outflows (red squares). Also included are the cases of the two ambiguous galaxies (cyan diamonds). The right panel highlights the trends with merger stage of NaI D absorption and outflows. There is a strong increase in the number of outflows with merger stage from wide binaries to late-stage mergers as expected from previous studies of U/LIRGs.

The possible causes of each of these outflows could be attributed to the nuclear excitation source in each galaxy. IRAS F10257-4339 has an outflow due to high levels of star formation in the northern nucleus (Chapter 4). The remainder of outflow galaxies have varying nuclear excitation sources including six star-forming nuclei, three Seyfert AGN host galaxies and one LINER host galaxy. This sample of outflow galaxies is too small to statistically identify if a certain excitation source becomes more important in later merging stages, but it does indicate that there are multiple possibilities for the sources of outflows with merger stage.

The neutral outflow rates for the nine galaxies have been calculated and are presented in Table 5.2. Again, small number statistics do not allow for any extrapolation of how outflows change with merger stages. However, the highest outflow rates, $\sim 100 M_{\odot}\,yr^{-1}$ are attributed to the later merging stages, cde.

The study by Yuan et al. (2010a) analysed ULIRGs and the contributions of the excitation sources with merger stage. In their analysis they determined that a better separation of the late merger stages could identify further trends in their data. A better separation of the late merger stage could uncover trends of outflows in the ULIRG stages of merging for WiGS in frequency and outflow rates. Hopkins et al. (2012) predicted two stages of outflows in the later merger stages; one before coalescence and the other after two gas-rich galaxies have coalesced. The analysis in this study did not separate the late merger stage (cde) due to the ambiguity of the morphologies of our galaxies compared to comparison simulations. At later stages it can be difficult to determine if two galaxies are on their first pass or have been merging for a significantly longer time but are not completely coalesced. A detailed follow-up of the morphologies of the late stage mergers would help to separate them into their different stages in order to untangle the outflows in the late stages of merging.

There are two items of further interest that have been observed in these results. Firstly, the sample of galaxies does not contain any wide binaries with outflows, even though half of the isolated galaxies have outflows. Secondly, all four isolated LIRGs have NaI D absorption, which is not seen in any other merger stage.

There is clearly an indication of a selection bias in WiGS. The sample contains a more complete picture of close binaries than wide binaries. However, these galaxies are selected for their L_{IR} which will be biased towards later stage galaxy mergers. Further investigation

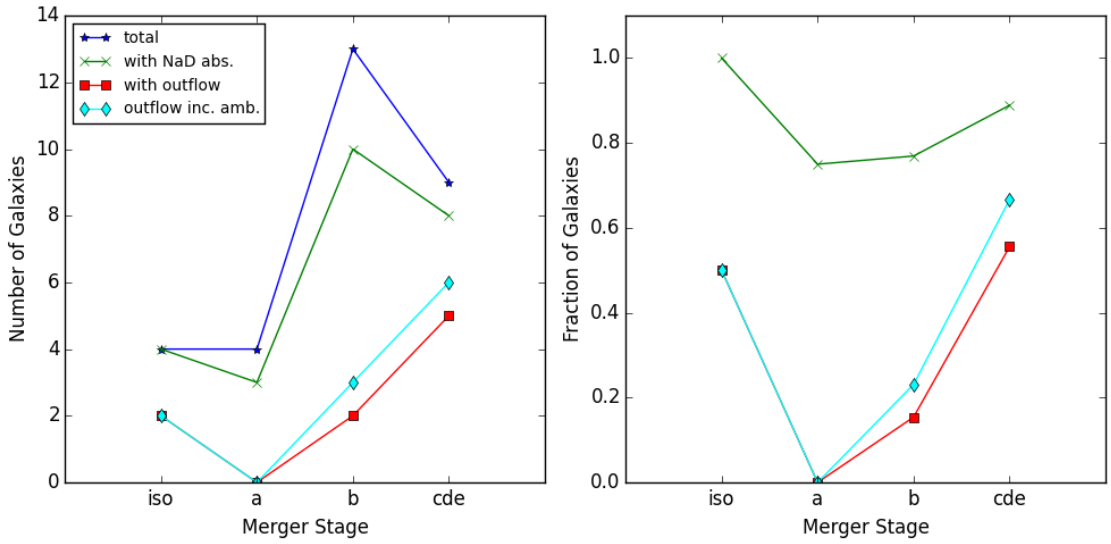

Figure 5.4: Comparison of the number and fraction of galaxies in our sample with NaI D absorption and observed outflows.

is needed in order to define why the four isolated galaxies show NaI D and outflows. A more detailed understanding of the isolated galaxies, which are often used as a control or comparison group of galaxies (Chapter 3), will allow a deeper understanding of differences seen in the merging categories. This will be especially important in comparing to the wide binaries, which are only just starting to interact with one-another.

5.5 Conclusions

The purpose of this study has been to identify if outflows increase in commonness with merger stage. Understanding when neutral gas outflows occur in the evolution of galaxies is key to understanding how and when changes occur during the merging process. The determination of the physical causes of the outflows is also key to understanding the precursor events that happen in order to produce such an event as a neutral gas outflow. Although a small sample, the results of the analysis of the WiGS galaxies have drawn the following conclusions;

1. Outflows of neutral gas are not caused by the same physical mechanisms in every case;

2. Galaxies with neutral gas outflows increase in commonness along the merger se-

quence.

It is proposed that follow-up observations using IFS instruments with higher spatial resolution than $1''$/pix are used to complete the understanding of the outflows in this sample. Instruments such as the Multi Unit Spectroscopic Explorer (MUSE, Bacon et al., 2010) and the IFS methodology TYPHOON (Sturch & Madore, 2012) have similar spectral coverage to the WiFeS instrument, but superior spatial resolution. MUSE has $0.2'' \times 0.2''$ spatial sampling, five times the spatial sampling used in this chapter. TYPHOON uses the 2.5m du Pont telescope at the Las Campanas Observatory in Chile. The spatial resolution of TYPHOON is comparable to WiFeS but is limited by a seeing $< 1''$ giving it a higher spatial resolution when taking into account the average seeing at Siding Spring Observatory of $1''$ to $2.5''$. The advantage of increasing the spatial resolution of the galaxies is to allow a better understanding of the physical characteristics of the outflows, such as size and opening angle for a larger sample of galaxies. Knowing these values for more galaxies will mean further calculations can be performed to determine better mass loss rate of the outflows which in turn can be used to determine if the outflow will cause quenching in the galaxies or if the outflowing material will stay within the system, and in what stages of merging.

The indications of this initial study using WiGS into the numbers of outflows indicate a correlation with merger stage, which is consistent with the picture of LIRGs and ULIRGs (Rupke et al., 2005b). Confirming with higher spatial resolution data, an increased sample size, as well as dissecting the three late stages of merging, will be able to ascertain the physical properties of outflows with merger stage. How material is lost from galaxies in later stages of merging is crucial to understanding how gas-rich galaxies become quiet red elliptical galaxies.

Chapter 6

Summary

This thesis has presented the results of a series of research activities using Integral Field Spectroscopy (IFS) to investigate the physical processes of merging galaxies. The aim has been to increase the knowledge in the field of merging galaxies and better understand the relationship of merger activity and observed spectra. The merging process explored is that when two gas-rich galaxies merge, gas is driven towards the centres of the galaxies creating a fuel reservoir for circum-nuclear star formation or a central AGN. Outflows in later stages are expected to blow out the gas and dust from the centres of merged galaxies to reveal obscured AGNs and deplete the galaxies of fuel. With the depletion of fuel within a galaxy the AGNs become less active and star formation ceases letting the merged galaxy fade to a red elliptical galaxy. This thesis has utilised IFS observations to complete the four steps posed in Chapter 1; 1) Devising a solution to the big data problem of decomposing spectral emission lines into multiple velocity components; 2) Determining the excitation sources of merging galaxies that are neither star formation dominated or AGN dominated, also known as composite galaxies, in order to identify the excitation mechanisms involved in outflows; 3) Identifying the neutral gas outflow in the merging system IRAS F10257-4339, as a test case in identifying outflows in merging systems; 4) Investigating the association of neutral gas outflows with merger stage.

This thesis has identified a number of new facts about the merging galaxies that are important for further research in this field:

1. Composite galaxies are being incorrectly classed as the same type of galaxy when they can range in excitation mechanisms; AGNs (LINERs and Seyfert), shocks, star

formation (Chapter 3),

2. Composite galaxies are not the same between different morphologies (Chapter 3),
3. The outflow from the northern nucleus of IRAS F10257-4339 can be traced in neutral, ionised, and molecular gas, and is easily produced by the the ongoing star formation in this galaxy (Chapter 4),
4. The fraction of galaxies with outflows of neutral gas increases with merger stage (Chapter 5),
5. The excitation mechanisms behind outflows in merging galaxies are not all the same (Chapter 5).

As well as answering the four steps in Chapter 1 this thesis has also covered the implementation of an Artificial Neural Network in determining the number of Gaussian components that best model the emission line spectra. `LZComp` (Hampton et al., 2017) has provided an important capability to deal with large numbers of galaxies and the vast amount of spatial data created using IFS.

The following subsections summarise the research undertaken for this thesis. Recommendations for further work, expanding the analysis with new sets of observations that are now becoming available, are described in Section 6.5.

6.1 Using Artificial Neural Networks in multi-component emission line fitting

The latest IFS galaxy surveys are observing hundreds to thousands of galaxies with spatially resolved spectra. These surveys include SAMI (Sydney-AAO Multi-object Integral field spectrograph, Croom et al., 2012), S7 (Siding Spring Southern Seyfert Spectroscopic Snapshot Survey, Dopita et al., 2014a), CALIFA (Calar Alto Legacy Integral Field Area, Sánchez et al., 2012), and MaNGA (Mapping Nearby Galaxies at Apache Point Observatory, Bundy et al., 2015). Each of these surveys are providing a wealth of information capable of exploring galaxy evolution as a function of morphology, environment, and spectral type. However, such a wealth of data also requires a more automated reduction and analysis process to be analysed.

`LZIFU` (Ho et al., 2016a) has automated the fitting process of emission lines in IFS datacubes. It is capable of fitting up to 3-components to an emission line, describing different physical ongoing processes in each spaxel. What `LZIFU` is unable to do is determine the number of components that are best for each spaxel.

Early on, different avenues of making the decisions were explored. It was determined that making the choices on the number of Gaussians through F-tests did not return the results that were expected in comparison to astronomers looking at the fits. Using astronomers was deemed far too time consuming given each spaxel of the IFS datacube in the thousands of galaxies in the surveys needed to be classified, which could easily scale to years for the target surveys.

An Artificial Neural Network (ANN), however, was determined to be capable of matching a group of astronomers in decision making. `LZComp` (Lay-Ze-Components) is an ANN written in the programming language `Octave` based on matrix multiplication. `LZComp` can quickly and reliably identify the best number of components for a given spaxel based on the input it receives from the fitting process of `LZIFU`.

The results of Chapter 2 clearly indicate that astronomers disagree with each other when deciding on the best set of fits for an emission spectrum. However, using the astronomers results creates a benchmark for `LZComp` to meet. The recall and precision, the measures of accuracy, for `LZComp` in both the SAMI and S7 galaxy surveys are within these tolerances calculated from the Astronomers.

As a final demonstration of `LZComp's` capabilities, the resulting component maps of the S7 galaxy NGC5782 were explored. In this active galaxy the spatial coherence of the star formation dominated disk, an AGN affected ionisation cone, and a 3rd high ionisation component tracing the edges of the ionisation cone, are clearly identified by the components selected by `LZComp`.

6.2 The complex nature of composite merging galaxies

The physical conditions of ionised gas can be determined through the use of emission line ratios and diagnostic diagrams (Baldwin et al., 1981; Osterbrock & De Robertis, 1985; Veilleux & Osterbrock, 1987). One of the major uses of the diagnostic curves (Kewley et al., 2001b; Kauffmann et al., 2003) is to distinguish possible excitation sources of the

emission-line gas in galaxies of star formation, AGN, and shocks. The excitation of some galaxies is not clear; these are known as composite galaxies.

Chapter 3 defines a sample of composite classified galaxies through the emission line ratios of their central 1 kpcs. This sample of 30 galaxies includes 12 galaxies from WiGS (Rich et al., 2015) and 18 galaxies from CALIFA (Sánchez et al., 2012) of a variety of morphologies, including merging galaxies. Using the spectral and spatial resolution of the IFS data and complimentary X-ray observations the study determined that the composite nature of these galaxies is driven by a mixture of star formation, AGN emission, and shocks. There are similarities between the excitation sources of merging galaxies and isolated bar galaxies (shocks), while isolated spiral galaxies have the greatest fraction of AGN host galaxies of the three morphology groups.

The previous study by Yuan et al. (2010a) supposed that composite galaxies were precursors to late stage merged Seyfert 2 galaxies. The comparison of the composite sample components emission line ratios to those of known Seyfert 2 and star forming galaxies clearly indicated that this is not the case.

6.3 Tracing outflows with NaI D in IRAS F10257-4339

IRAS F10257-4339 is a complex system of two merging gas-rich galaxies with known outflows of molecular (Emonts et al., 2014; Sakamoto et al., 2014) and ionised gas (Lípari et al., 2000, 2004). Previous studies of IRAS F10257-4339s northern nucleus have been unable to definitively determine if the excitation source is an AGN or strong nuclear star formation. The analysis conducted in Chapter 3 determined the nucleus to be star-forming consistent with the majority of studies. The outflow from the northern nucleus was identified in Chapter 4 in neutral gas using multi-component NaI D absorption fitting with a mass outflow rate of $\sim 6.8\,M_{\odot}yr^{-1}$. This outflow rate is sustainable by the SFR ($25\,M_{\odot}yr^{-1}$) of the northern galaxy.

The disk of the southern galaxy was also identified by the neutral gas using the NaI D absorption and through comparisons to the morphology of the merging system put forward by Emonts et al. (2014); Sakamoto et al. (2014).

The study of IRAS F10257-4339 ascertained that the combination of emission line studies and absorption line studies are complimentary in the understanding of a galaxy with an

outflow.

6.4 The increase of outflows with merger stage

Models of gas-rich galaxy mergers predict that outflows play an important part in their evolution. In particular outflows are predicted to be most common in the later stages of merging due to supernovae and AGN accretion blowing out gas from the nuclear regions. This in turn creates a deficit in the fuel reservoir for further star formation and AGN accretion. The importance of outflows in galaxy evolution is clear in simulations, but is it as clear in observations?

Chapter 5 expanded on the study of outflows in IRAS F10257-4339 by adding another 23 galaxies to study outflows with merger stage. Nine of the 24 galaxies with NaI D absorption features have neutral gas outflows. A comparison of the fraction of galaxies with outflows to the 30 galaxies in WiGS as a function of merger stage was conducted and discovered that outflows do increase with merger stage for WiGS. The later merger stages (c, d, and e) are all combined into a single grouping of late stage mergers. Analysis of these three last stages of merging separately will help to understand if these outflows are due to the driving of gas towards the nuclei or if they are associated with the subsequent stage of massive star formation predicted in the simulations of Hopkins et al. (2012).

6.5 Future directions

This thesis has clearly demonstrated what a powerful tool IFS is in understanding the excitation and kinematics of gas in galaxies, merging galaxies in particular. IFS studies and surveys of galaxies are still in their early stages. However, there is a need to develop the tools to analyse such data now (Chapter 2). The possibility to distinguish outflows from regular gas motions and trace the extent of these outflows across multiple phases (Chapters 4 & 5) will significantly improve the understanding of how galaxies evolve. With large surveys like SAMI (Croom et al., 2012), MaNGA (Bundy et al., 2015), CALIFA (Sánchez et al., 2012), and S7 (Dopita et al., 2014a) there is a wealth of galaxies which could be utilised to further the understanding of gas motions across all galaxies, not just mergers.

This thesis has clearly demonstrated the complex natures of the excitation sources at the

centres of merging galaxies and the increase in the numbers of galaxies hosting outflows at later merging stages. Yet these findings are limited by the low numbers of the samples. This suggests two ways forward to definitively answer the questions of the excitation of composite sources and outflows in galaxies:

- The SAMI Galaxy Survey (Croom et al., 2012) now has over 1,000 galaxies all fit with multi-component emission lines from `LZIFU` (Ho et al., 2016b) and `LZComp` (Hampton et al., 2017). This will enable a statistical analysis of hundreds of composite galaxies to identify any similarities between composite galaxies with similar excitation mechanisms that was not evident in the sample of 30. The SAMI Galaxy Survey contains galaxies across the merging sequence, and is not specific to U/LIRGs. These points will allow the comparison of merging U/LIRGs to non U/LIRGs both isolated and merging to obtain a broader picture of what a composite galaxy is.
- In all the studies in this thesis the three last stages of merging have been placed in the same group of late stage mergers. The study of neutral gas outflows indicates that these last three stages contain the most galaxies with outflows but where in the last stages are they most important to the galaxies evolution is still unknown. A thorough study of the WiGS galaxies in the late stages to isolate the three smaller groups will enable the identification of how outflows increase or decrease before galaxies become red elliptical galaxies.

The recommended further research requires a new set of observations. For the first, a larger sample size is required which is available from the SAMI Galaxy Survey. New instruments are coming online including HECTOR (Bryant & Bland-Hawthorn, 2016), the next evolution of SAMI with higher spatial and spectral resolutions, which could also be utilised for this study. The second will require new and deeper observations of each of our NaI D galaxies to identify more about the individual outflows. The coverage required can be obtained using MUSE (Bacon et al., 2010) or TYPHOON (Sturch & Madore, 2012). This will also require a study of theoretical models and comparisons to identify the exact stage of the merger that each of the late merger stage galaxies have arrived at.

Appendix A

A simplified introduction to how an Artificial Neural Network works

An Artificial Neural Network (ANN) is a computer system comprised of nodes, or units, that perform calculations with a pre-determined equation. These nodes sit in layers that have different jobs depending on where they sit in the ANN design. Figure A.1 presents a simplified example of an ANN to classify something as a cat or not a cat based on observable properties such as the number of legs and size.

Each node in the input layer, represented as x_j in Figure A.1, is a parameter value making up a feature vector that, in this case, describes the number of legs and size of the things we want to classify as a cat or not a cat. The feature vector values are propagated through to the first hidden layer where a sigmoid function is used to calculate the values for the second hidden layer. When at the output layer a final set of sigmoid functions are calculated and the node with the highest c_i value is the result.

In the case of this cat example, in Figure A.1, only two parameters were chosen but these are not enough to adequately classify something as a cat or not. For example, a baby wombat would be classified as a cat using this ANN. For this reason it is necessary to give an ANN enough information to adequately describe the classifications required.

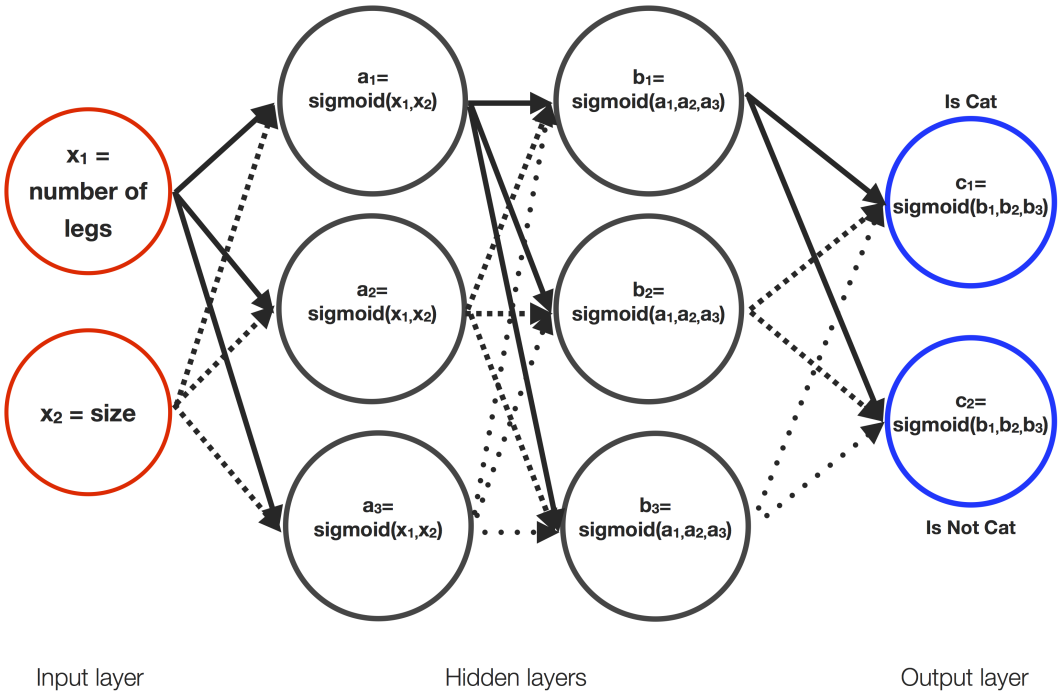

Figure A.1: A simple Artificial Neural Network design. The circles indicate the nodes and are grouped into the 3 layer types: Input, hidden and output. This ANN is used to decide if something with the input parameters of size and number of legs is a cat or not a cat. At each layer calculations are done with the values of the previous layer. The final classification is then decided based on which node in the output layer has the largest value.

Appendix B

Notes and diagnostic plots for individual composite galaxies

B.1 Notes on individual composite galaxies

This section describes each galaxy in the composite galaxy sample of Chapter 3. It includes information from previous studies and the individual results of the research for this thesis.

IRAS F02072-1025

IRAS F02072-1025 is a nearly edge on late stage merger from the WiGS survey. It is studied thoroughly in Rich et al. (2010) and Howell et al. (2010). Their studies found shocks associated with a starburst driven outflow. Chapter 3 has confirmed the presence of shocks using diagnostic diagrams and also identified a possible Sy2 AGN/ LINER at its core. However, the X-ray analysis did not confirm the AGN at the core of this galaxy. Diagnostic plots are presented in Figure B.1.

IRAS F06076-2139

IRAS F06076-2139 is an interacting pair of galaxies studied in detail in Arribas et al. (2008) and their study of ULIRGs. Hα maps show the pair are interacting (Elmegreen & Elmegreen, 2006; Arribas et al., 2008). This galaxy has been studied in detail in Rich et al. (2014) where they found that the northern galaxy is dominated by star formation and the

southern galaxy dominated by composite ratios. Chapter 3 has determined the presence of an AGN, using archival Chandra data, in the southern composite core. The optical emission line ratios of the core of this galaxy did not reveal an optical AGN. Diagnostic plots are presented in Figure B.2.

IRAS 08355-4944

IRAS 08355-4994 is a late stage merger with remnant tidal tails seen in the HST I-band image (Rich et al., 2014). Rich et al. (2014) found this galaxy to be dominated by star formation and shocks associated with a galactic wind (Monreal-Ibero et al., 2010). Chapter 3 also finds evidence of shocks, through the [SII]/Hα diagnostic diagram and velocity dispersions. Diagnostic plots are presented in Figure B.3.

IRAS F10038-3338

IRAS F10038-3338 is a post merger galaxy with a significant remnant tidal arm towards the south west. There is evidence for off-nuclear shock induced emission consistent with Rich et al. (2014); Monreal-Ibero et al. (2010). X-ray emission shows no evidence for an AGN. Rich et al. (2014) found the optical emission points towards an actively star-forming core. Diagnostic plots are presented in Figure B.4.

IRAS F10257-4339

IRAS F10257-4339 is a late stage merger with a heavily extinguished second nuclei (Alonso-Herrero et al., 2002; Rothberg & Fischer, 2010). Rich et al. (2014) determined that the central 6kpc is where most of the ongoing star formation is occurring and found evidence for widespread shocks (Rich et al., 2011). This is consistent with Chapter 3. There is a correlation between the [NII]/Hα and associated velocity dispersions which is consistent with the analysis of the [NII]/Hα and [SII]/Hα diagnostic diagrams for the presence of shocks in the outer regions of this system. There is no evidence for an AGN using archival Chandra data. Diagnostic plots are presented in Figure B.5.

IRAS F13373+0105 West

IRAS F13373+0105 West is a distant merger which was found to be predominately star-forming and has a composite core. This is consistent with Rich et al. (2014). There is no

evidence of shocked emission. AGN emission was not confirmed by the archival Chandra data. Diagnostic plots are presented in Figure B.6.

IRAS F16164-0746

IRAS F16164-0746 is a coalesced merger showing evidence of an AGN and an ionisation cone. There is a strong correlation between the [NII]/Hα and associated velocity dispersions. Archival Chandra data confirms the presence of an AGN in this coalesced galaxy as well as previous X-ray and IR studies of this galaxy (Iwasawa et al., 2009; Petric et al., 2011). Rich et al. (2014) discuss this galaxy as being composite, starburst and Seyfert-like in the nucleus, consistent with Chapter 3. Diagnostic plots are presented in Figure B.7.

IRAS F17138-1017

IRAS F17138-1017 is a coalesced merger. The Chapter 3 results are consistent with Rich et al. (2014); Monreal-Ibero et al. (2010). The galaxy is mostly star-forming, however the [NII]/Hα diagnostic diagram is ambiguous. There is evidence of shocks in the outer regions of the galaxy from the [SII]/Hα diagnostic diagram and the strong bimodal distribution in σ_g. It was determined that this galaxy is host to an AGN from archival Chandra data. Diagnostic plots are presented in Figure B.8.

IRAS F17207-0014

IRAS F17207-0014 is a well studied late stage merger (Franceschini et al., 2003; Arribas & Colina, 2003; Rupke et al., 2005b,c; Iwasawa et al., 2011; Petric et al., 2011; Stierwalt et al., 2012; Medling et al., 2015). Rupke et al. (2005b,c) found evidence for a galactic wind in this galaxy using NaI D absorption. The optical analysis is inconclusive as the S/N cut of 3 has resulted in only a few (8) spaxels for analysis. The X-ray data does not indicate an AGN. Diagnostic plots are presented in Figure B.9.

IRAS F18341-5732

IRAS F18341-5732 is an isolated galaxy not seen to be undergoing any interactions with other galaxies. There is evidence of star formation. There is no archived Chandra data for this galaxy. Rich et al. (2014) determined that the highest points of star formation were occurring at the ends of the central bar of this galaxy and the nucleus is dominated by an

ageing population. Dopita et al. (2002) determined the presence of knots of star formation along the spiral arms using Hα imaging. Diagnostic plots are presented in Figure B.10.

IRAS F20551-4250

IRAS F20551-4250 is a late stage merger. Chapter 3 consistent with previous studies (Veilleux et al., 1995a; Kewley et al., 2001a) as being dominated by star formation towards its centre with shock excitation towards the outer parts of this galaxy. The Chandra analysis did not find evidence for an AGN which is consistent with Ptak et al. (2003); Grimes et al. (2005); Iwasawa et al. (2009, 2011) but not with an XMM study by Franceschini et al. (2003). There is evidence in the IR for a heavily obscured AGN (Imanishi et al., 2010; Sani et al., 2008; Nardini et al., 2008) and mid-IR (Petric et al., 2011; Stierwalt et al., 2012). However, Inami et al. (2013) did not find this galaxy to be AGN dominated which is more consistent with Chapter 3's analysis where these galaxies are not dominated by AGNs or starformation. Diagnostic plots are presented in Figure B.11.

IRAS F23128-5919

IRAS F23128-5919 is a closely interacting pair. There is evidence for non nuclear shocks in the [NII]/Hα diagnostic diagram. An X-ray AGN is associated with the Southern galaxy (Franceschini et al., 2003; Petric et al., 2011; Iwasawa et al., 2011). Chapter 3 indicates that the northern nucleus is predominately star-forming, consistent with Rich et al. (2014). Diagnostic plots are presented in Figure B.12.

IC5376

IC5376 is an edge on barred spiral galaxy. Chapter 3 finds substantial star formation in the outer areas of the galaxy and a LINER at its core. Diagnostic plots are presented in Figure B.13.

UGC00036

UGC00036 is an isolated spiral galaxy with strong evidence for shocks. Diagnostic plots are presented in Figure B.14.

UGC01057

UGC01057 is a barred spiral galaxy. The core of this galaxy sits squarely in the composite region but is predominately star-forming with a possible LINER. Diagnostic plots are presented in Figure B.15.

NGC0776

NGC0776 is a face on barred spiral galaxy. This galaxy is predominately star-forming with the majority of star formation seen in the spiral arms of the galaxy. It appears that there are slightly elevated emission line ratios towards where the spiral arms meet the central part of the galaxy. Diagnostic plots are presented in Figure B.16.

UGC03253

UGC03253 is a barred spiral galaxy. There is evidence of shocks but this galaxy is predominantly star-forming. Diagnostic plots are presented in Figure B.17.

UGC05359

UGC05359 is an edge on barred spiral galaxy. The optical emission line maps show a gap of emission line ratio information across the centre of this galaxy. Diagnostic plots are presented in Figure B.18.

NGC4003

NGC4003 is an edge on barred spiral galaxy showing clear signs of off nuclear shocks. The shocks look to be circum-nuclear and caused by the central bar of this galaxy. Diagnostic plots are presented in Figure B.19.

NGC4676A & NGC4676B

NGC4676A and NGC4676B are most commonly known as the Mice Galaxies. This system of merging galaxies are well studied. NGC4676B has an X-ray classified AGN and a possible outflow (Wild et al., 2014, and references therein). The analysis of the CALIFA data has concluded that there is a possible optical AGN, shocks, and star formation powering NGC4676B. The shocks can be attributed to the merging process but may also

be explained by the possible outflow (Wild et al., 2014). NGC4676A has no known AGN. The shocked gas seen in NGC4676A is most likely due to the merging process and ram pressure stripping on the right side. The results are consistent with the Wild et al. (2014) study of these galaxies also using the CALIFA data. Diagnostic plots are presented in Figures B.20 and B.21.

NGC5000

NGC5000 is a face on barred spiral galaxy. It is heavily star-forming with a composite core that may host circum-nuclear shocks due to its bar. However the S/N outwards from the core tracing the extent of the bar stops us from analysing this area of the galaxy. The large gap in emission line ratio information leads to an ambiguous classification of the central 1kpc. Diagnostic plots are presented in Figure B.22.

UGC08267

UGC08267 is an edge on spiral galaxy which is predominantly star-forming. Diagnostic plots are presented in Figure B.23.

IC0944

IC0944 is an almost edge on spiral galaxy. There is evidence of an AGN and star formation from diagnostic diagrams. The AGN type is LINER. Diagnostic plots are presented in Figure B.24.

UGC08778

UGC08778 is an almost edge-on isolated spiral galaxy showing signs of a LINER AGN and star formation. Diagnostic plots are presented in Figure B.25.

NGC5394

NGC5394 is a barred spiral undergoing a merger. The core of this galaxy sits well in the composite region. There is evidence for off nuclear star formation and star formation occurring in one of the spiral arms. Unfortunately, it was not possible to analyse the 2nd spiral arm which is interacting with the merging pair due to the S/N cut on the emission

lines at the position of the second spiral arm. Diagnostic plots are presented in Figure B.26.

NGC6032

NGC6032 is a barred spiral galaxy. There is a circum-nuclear ring of heightened emission line ratios which may be produced by a strong outflow from the centre or bar shocks. Diagnostic plots are presented in Figure B.27.

UGC10205

UGC10205 is an isolated (6 Mpc) spiral galaxy. This galaxy has a strong dust lane running across its centre in observations. There is evidence of shocks from diagnostic diagrams. Diagnostic plots are presented in Figure B.28.

NGC7549

NGC7549 is a face on barred spiral galaxy. There is strong evidence for shocks in this galaxy. The shocks are prominent on either side of one of this galaxy's spiral arms. There are knots or clumps of heavier star formation along each spiral arm, traced by the emission line ratios. There is no evidence of an AGN. Diagnostic plots are presented in Figure B.29.

NGC7591

NGC7591 is a face on barred spiral galaxy. This galaxy has been classed as ambiguous due to the S/N cut of 3σ where the central 1 kpc could not be determined. Diagnostic plots are presented in Figure B.30.

B.2 Diagnostic plots for individual composite galaxies

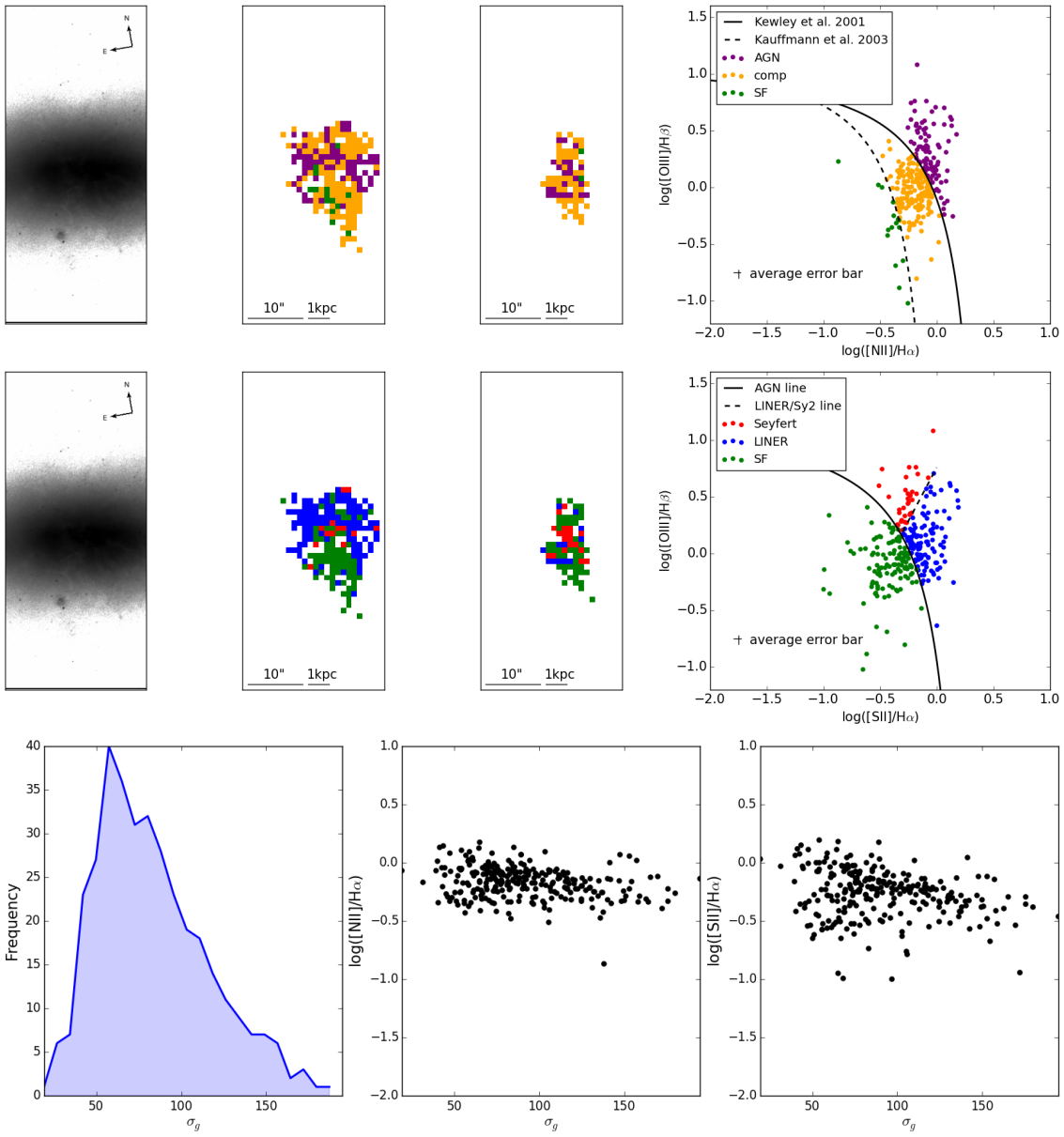

Figure B.1: IRAS F02072-1025: Top: WFPC2 F814W image (left), Galaxy map with colours corresponding to the regions of the [NII]/Hα diagnostic diagram the emission lines lie in (middle), [NII] diagnostic diagram for (right). Green indicates star-forming and yellow indicates composite. Middle: WFPC2 F814W image (left), galaxy map with colours corresponding to the regions of the [SII] diagnostic diagram the emission lines lie in (middle), [SII]/Hα diagnostic diagram for (right). Green indicates star-forming, red indicates Seyfert like, and blue indicates LINER like emission. Bottom: left presents the velocity dispersion distribution, middle presents the [NII]/Hα versus gas velocity dispersions, right presents the [SII]/Hα versus gas velocity dispersions.

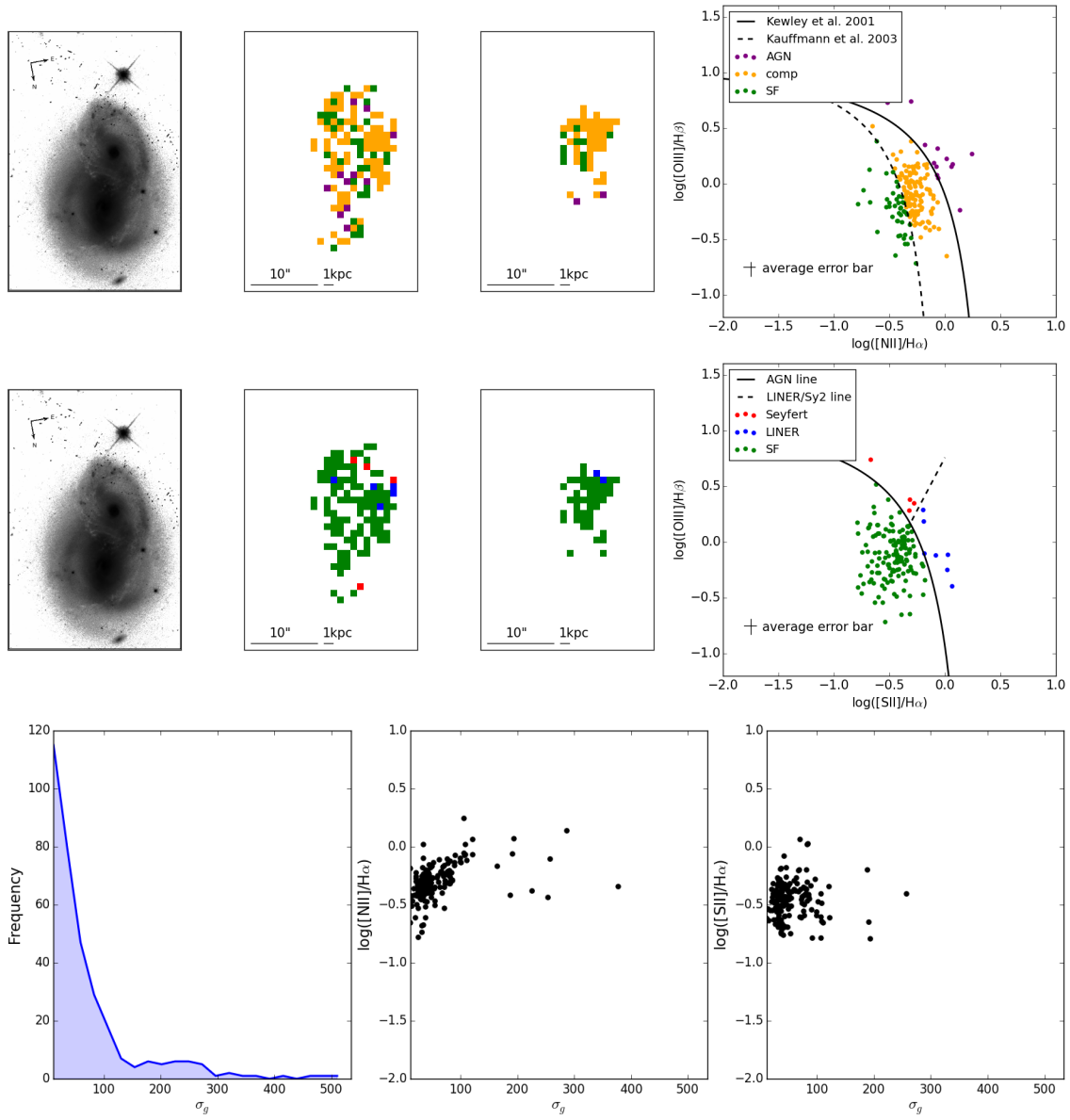

Figure B.2: IRAS F06076-2139: Top: ACS WFC F814W image (left), Galaxy map with colours corresponding to the regions of the [NII]/Hα diagnostic diagram the emission lines lie in (middle), [NII] diagnostic diagram for (right). Green indicates star-forming and yellow indicates composite. Middle: ACS WFC F814W image (left), galaxy map with colours corresponding to the regions of the [SII] diagnostic diagram the emission lines lie in (middle), [SII]/Hα diagnostic diagram for (right). Green indicates star-forming, red indicates Seyfert like, and blue indicates LINER like emission. Bottom: left presents the velocity dispersion distribution, middle presents the [NII]/Hα versus gas velocity dispersions, right presents the [SII]/Hα versus gas velocity dispersions.

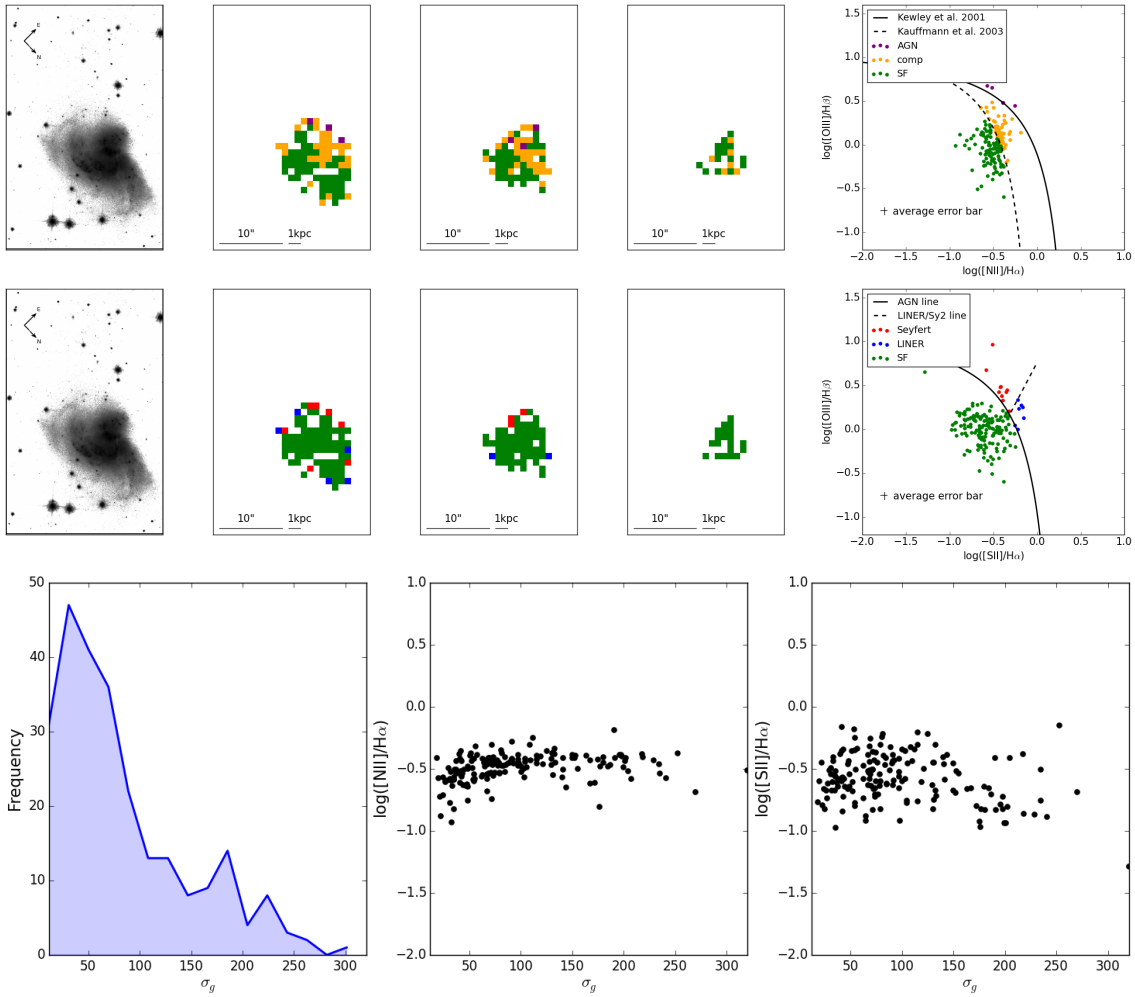

Figure B.3: IRAS08355-4944: Top: ACS WFC F814W image (left), Galaxy map with colours corresponding to the regions of the [NII]/Hα diagnostic diagram the emission lines lie in (middle), [NII] diagnostic diagram for (right). Green indicates star-forming and yellow indicates composite. Middle: ACS WFC F814W image (left), galaxy map with colours corresponding to the regions of the [SII] diagnostic diagram the emission lines lie in (middle), [SII]/Hα diagnostic diagram for (right). Green indicates star-forming, red indicates Seyfert like, and blue indicates LINER like emission. Bottom: left presents the velocity dispersion distribution, middle presents the [NII]/Hα versus gas velocity dispersions, right presents the [SII]/Hα versus gas velocity dispersions.

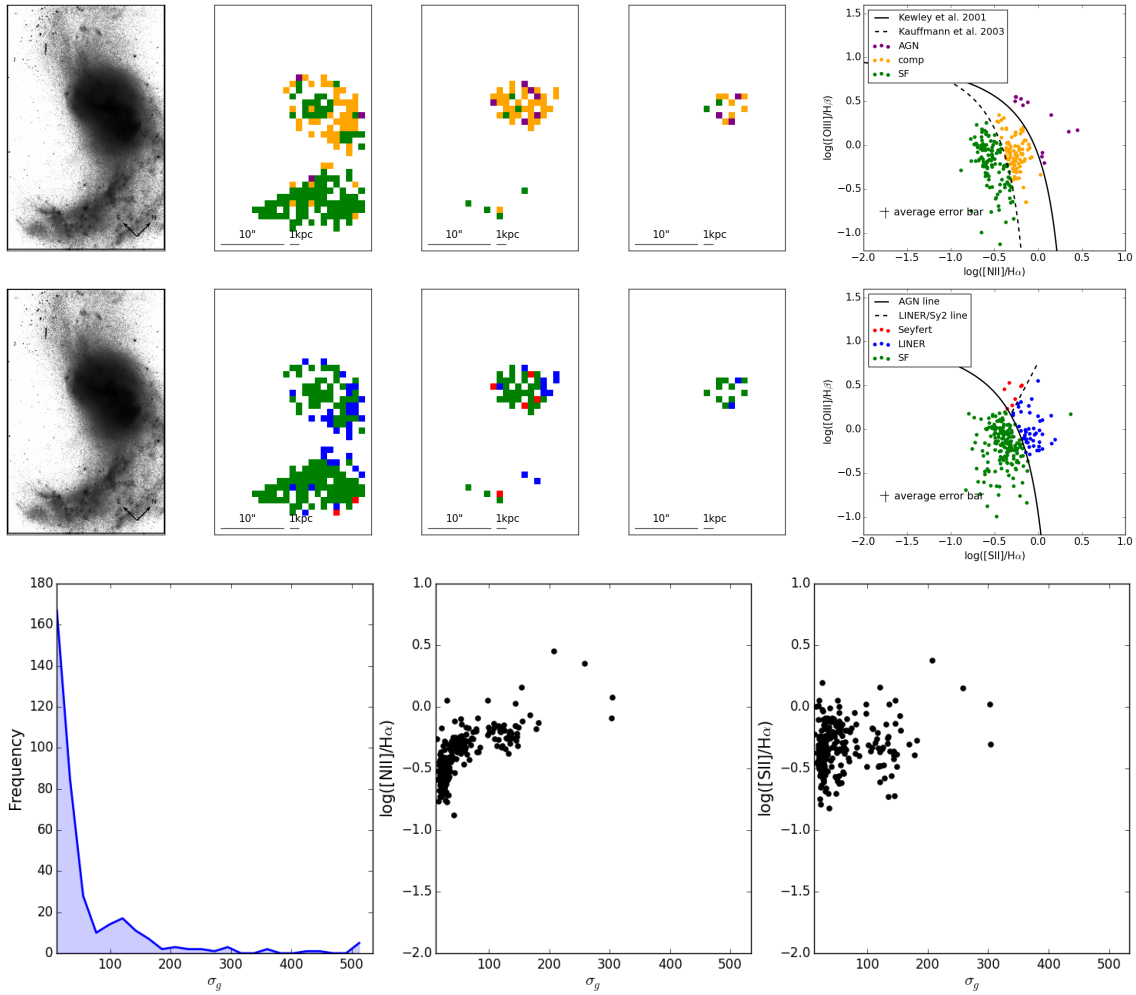

Figure B.4: IRAS F10038-3338: Top: ACS WFC F814W image (left), Galaxy map with colours corresponding to the regions of the [NII]/Hα diagnostic diagram the emission lines lie in (middle), [NII] diagnostic diagram for (right). Green indicates star-forming and yellow indicates composite. Middle: ACS WFC F814W image (left), galaxy map with colours corresponding to the regions of the [SII] diagnostic diagram the emission lines lie in (middle), [SII]/Hα diagnostic diagram for (right). Green indicates star-forming, red indicates Seyfert like, and blue indicates LINER like emission. Bottom: left presents the velocity dispersion distribution, middle presents the [NII]/Hα versus gas velocity dispersions, right presents the [SII]/Hα versus gas velocity dispersions.

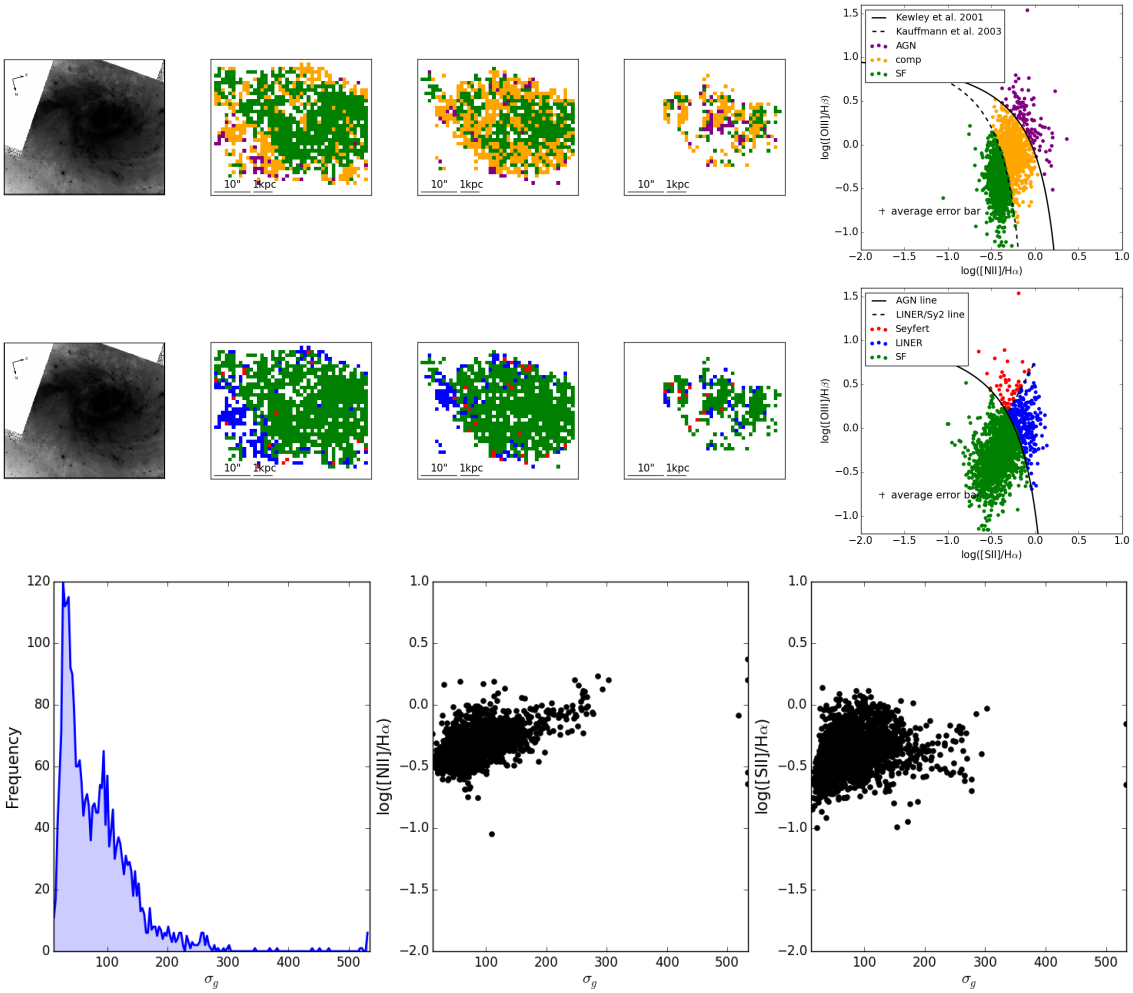

Figure B.5: IRAS F10257-4339: Top: WFPC2 F814W image (left), Galaxy map with colours corresponding to the regions of the [NII]/Hα diagnostic diagram the emission lines lie in (middle), [NII] diagnostic diagram for (right). Green indicates star-forming and yellow indicates composite. Middle: WFPC2 F814W image (left), galaxy map with colours corresponding to the regions of the [SII] diagnostic diagram the emission lines lie in (middle), [SII]/Hα diagnostic diagram for (right). Green indicates star-forming, red indicates Seyfert like, and blue indicates LINER like emission. Bottom: left presents the velocity dispersion distribution, middle presents the [NII]/Hα versus gas velocity dispersions, right presents the [SII]/Hα versus gas velocity dispersions.

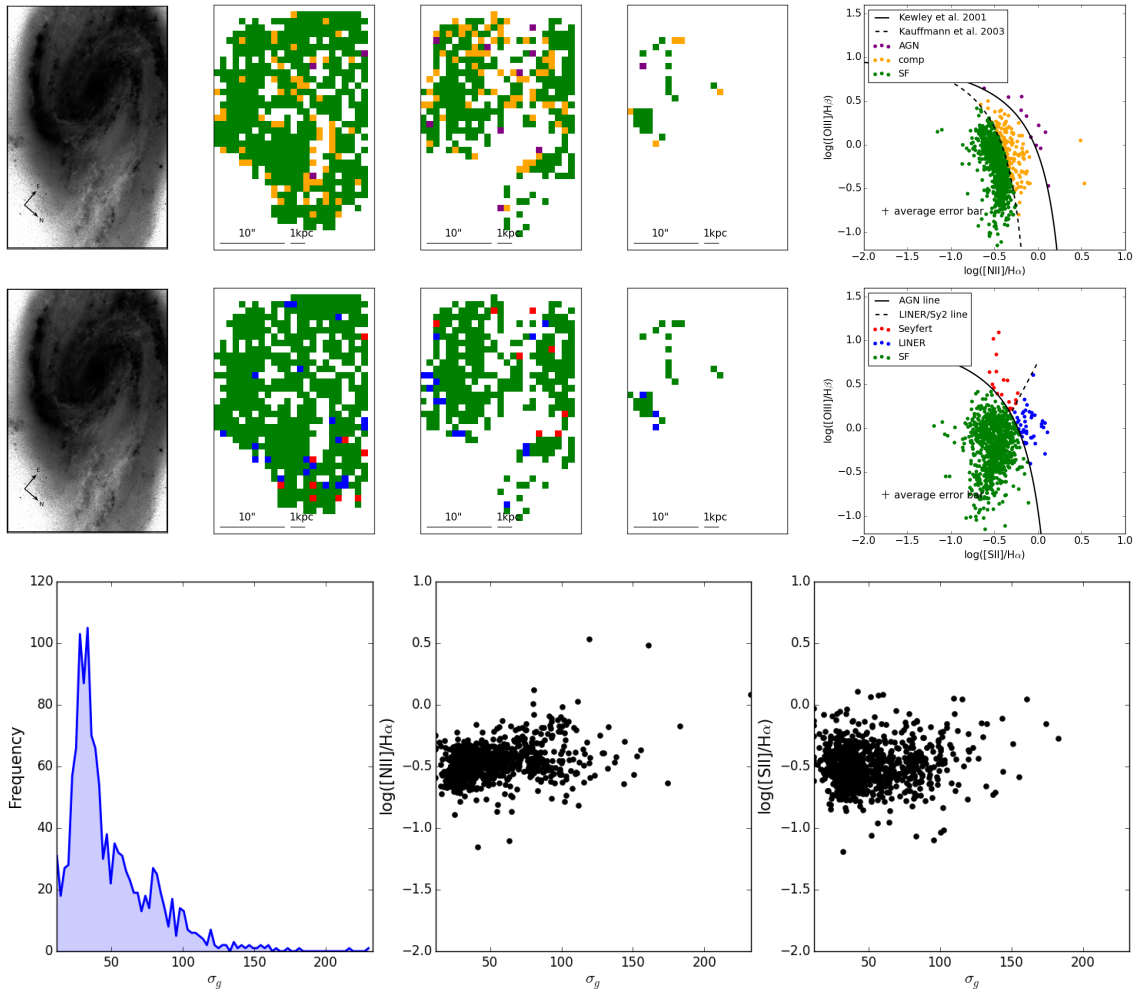

Figure B.6: IRAS F13373+0105 West: Top: ACS WFC F814W image (left), Galaxy map with colours corresponding to the regions of the [NII]/Hα diagnostic diagram the emission lines lie in (middle), [NII] diagnostic diagram for (right). Green indicates star-forming and yellow indicates composite. Middle: ACS WFC F814W image (left), galaxy map with colours corresponding to the regions of the [SII] diagnostic diagram the emission lines lie in (middle), [SII]/Hα diagnostic diagram for (right). Green indicates star-forming, red indicates Seyfert like, and blue indicates LINER like emission. Bottom: left presents the velocity dispersion distribution, middle presents the [NII]/Hα versus gas velocity dispersions, right presents the [SII]/Hα versus gas velocity dispersions.

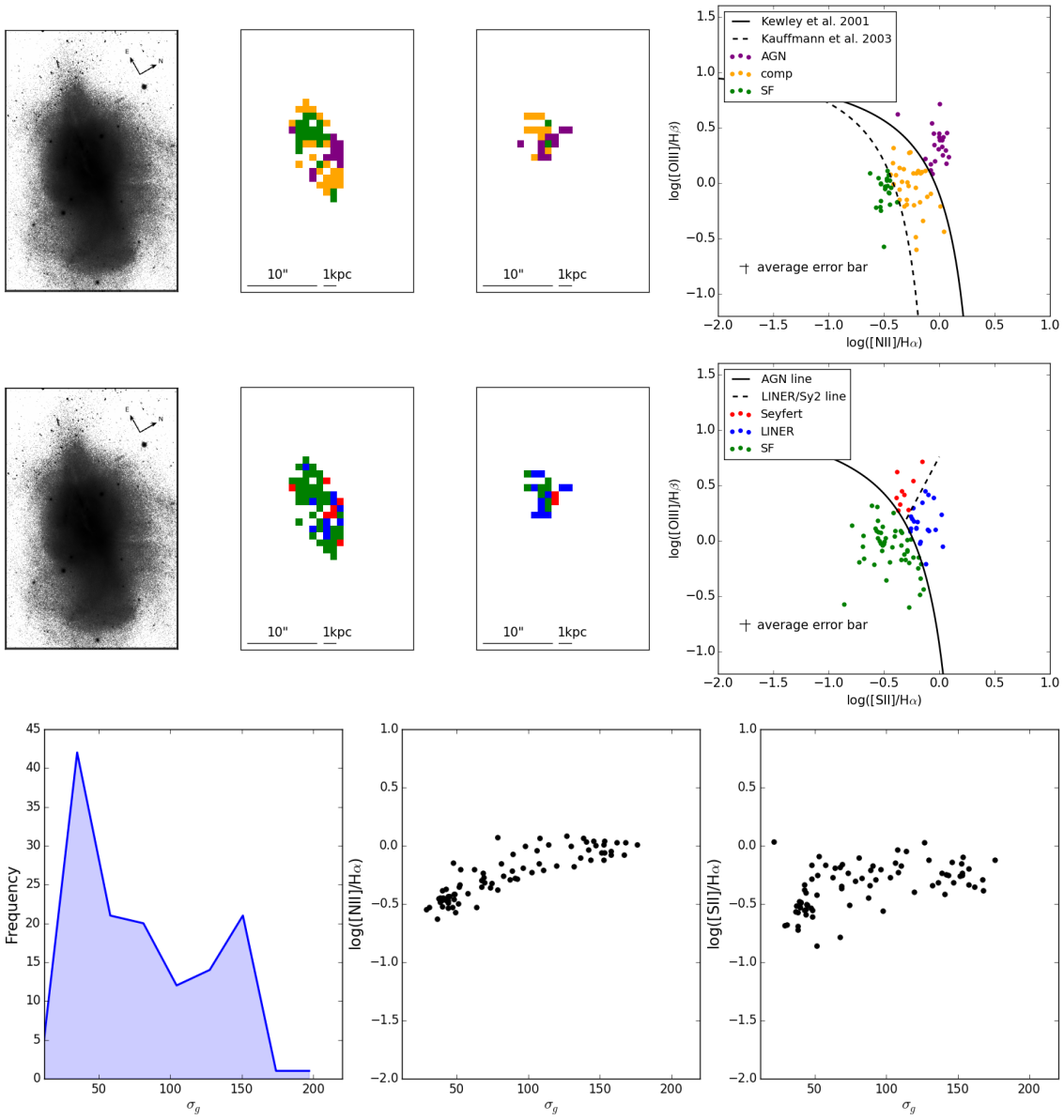

Figure B.7: IRAS F16164-0746: Top: SDSS r-band image (left), galaxy map with colours corresponding to the regions of the [NII]/Hα diagnostic diagram the emission lines lie in (middle), [NII] diagnostic diagram for (right). Green indicates star-forming and yellow indicates composite. Middle: SDSS r-band image (left), galaxy map with colours corresponding to the regions of the [SII] diagnostic diagram the emission lines lie in (middle), [SII]/Hα diagnostic diagram for (right). Green indicates star-forming, red indicates Seyfert like, and blue indicates LINER like emission. Bottom: left presents the velocity dispersion distribution, middle presents the [NII]/Hα versus gas velocity dispersions, right presents the [SII]/Hα versus gas velocity dispersions.

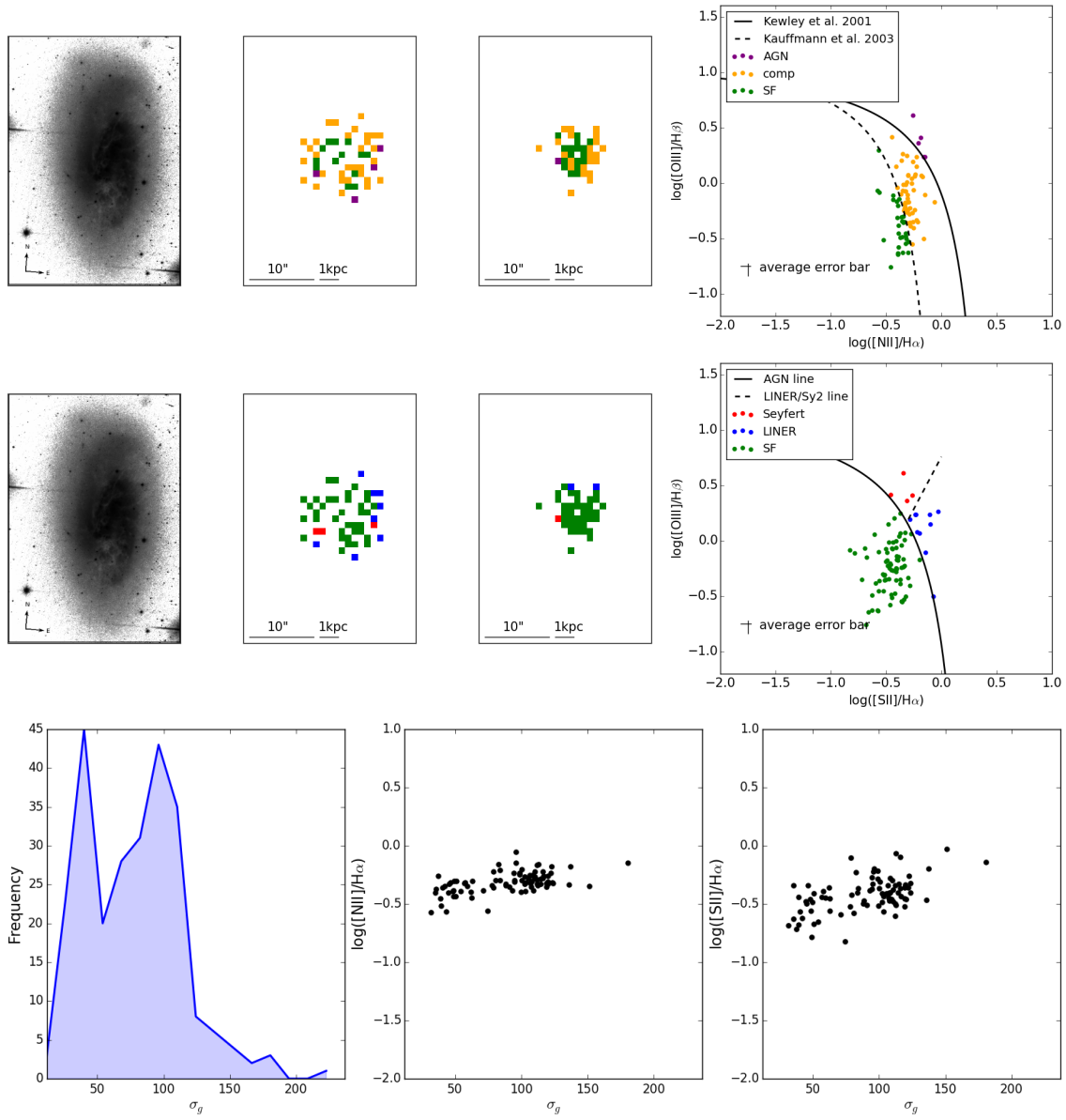

Figure B.8: IRAS F17138-1017: Top: ACS WFC F814W image (left), galaxy map with colours corresponding to the regions of the [NII]/Hα diagnostic diagram the emission lines lie in (middle), [NII] diagnostic diagram for (right). Green indicates star-forming and yellow indicates composite. Middle: ACS WFC F814W image (left), galaxy map with colours corresponding to the regions of the [SII] diagnostic diagram the emission lines lie in (middle), [SII]/Hα diagnostic diagram for (right). Green indicates star-forming, red indicates Seyfert like, and blue indicates LINER like emission. Bottom: left presents the velocity dispersion distribution, middle presents the [NII]/Hα versus gas velocity dispersions, right presents the [SII]/Hα versus gas velocity dispersions.

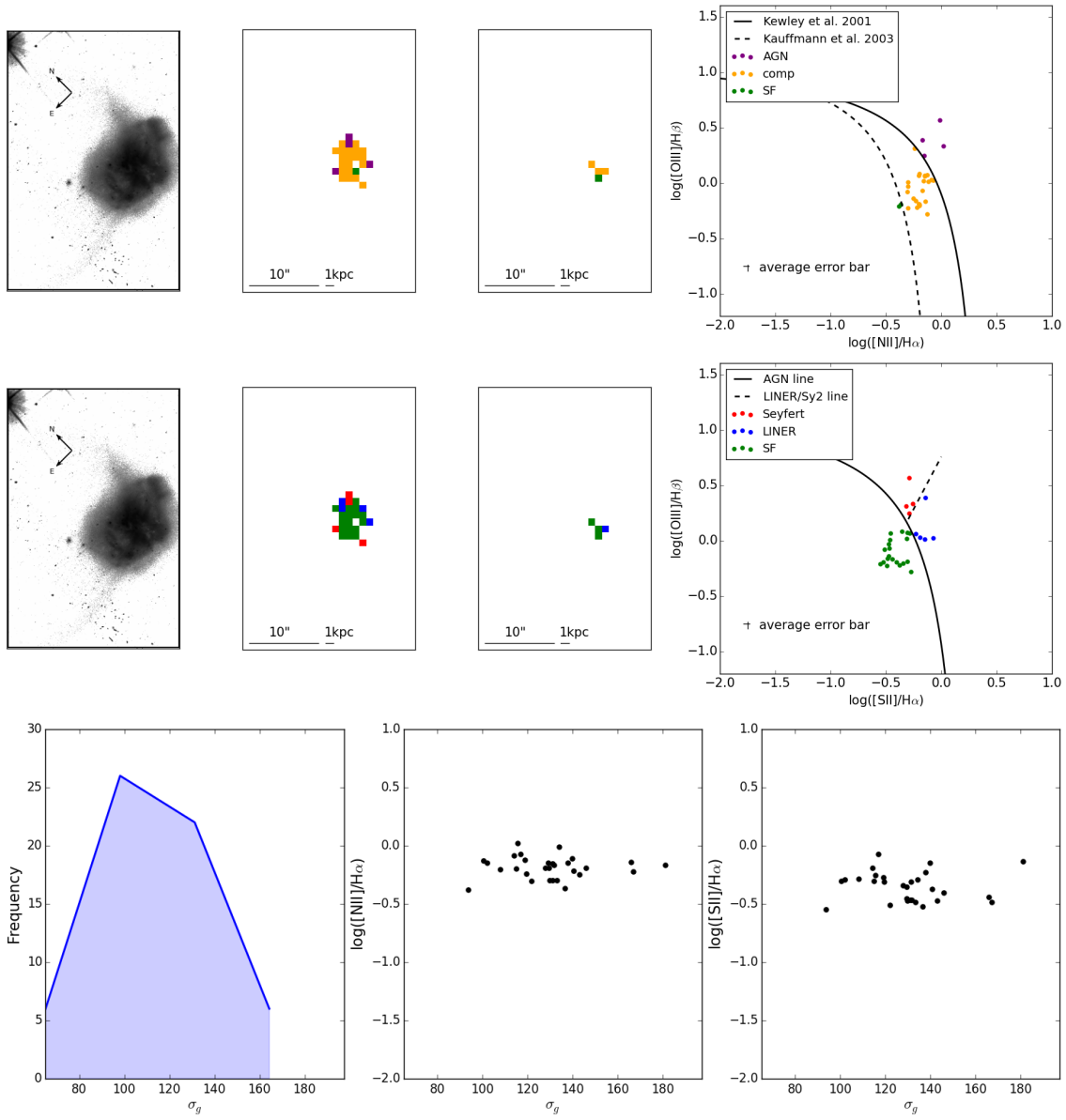

Figure B.9: IRAS F17207-0014: Top: ACS WFC F814W image (left), galaxy map with colours corresponding to the regions of the [NII]/Hα diagnostic diagram the emission lines lie in (middle), [NII] diagnostic diagram for (right). Green indicates star-forming and yellow indicates composite. Middle: ACS WFC F814W image (left), galaxy map with colours corresponding to the regions of the [SII] diagnostic diagram the emission lines lie in (middle), [SII]/Hα diagnostic diagram for (right). Green indicates star-forming, red indicates Seyfert like, and blue indicates LINER like emission. Bottom: left presents the velocity dispersion distribution, middle presents the [NII]/Hα versus gas velocity dispersions, right presents the [SII]/Hα versus gas velocity dispersions.

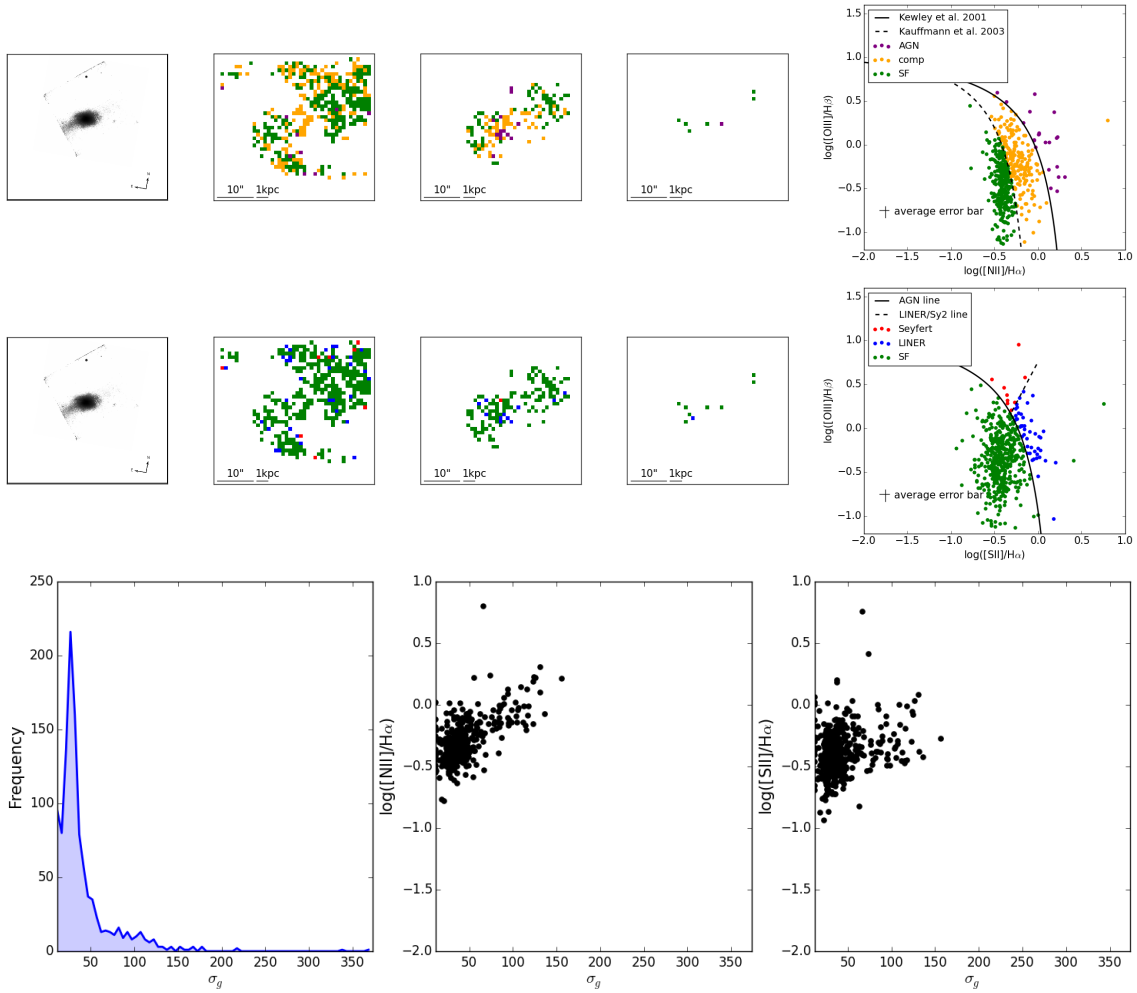

Figure B.10: IRAS F18341-5732: Top: NIC NIC2 F187N image (left), galaxy map with colours corresponding to the regions of the [NII]/Hα diagnostic diagram the emission lines lie in (middle), [NII] diagnostic diagram for (right). Green indicates star-forming and yellow indicates composite. Middle: NIC NIC2 F187N image (left), galaxy map with colours corresponding to the regions of the [SII] diagnostic diagram the emission lines lie in (middle), [SII]/Hα diagnostic diagram for (right). Green indicates star-forming, red indicates Seyfert like, and blue indicates LINER like emission. Bottom: left presents the velocity dispersion distribution, middle presents the [NII]/Hα versus gas velocity dispersions, right presents the [SII]/Hα versus gas velocity dispersions.

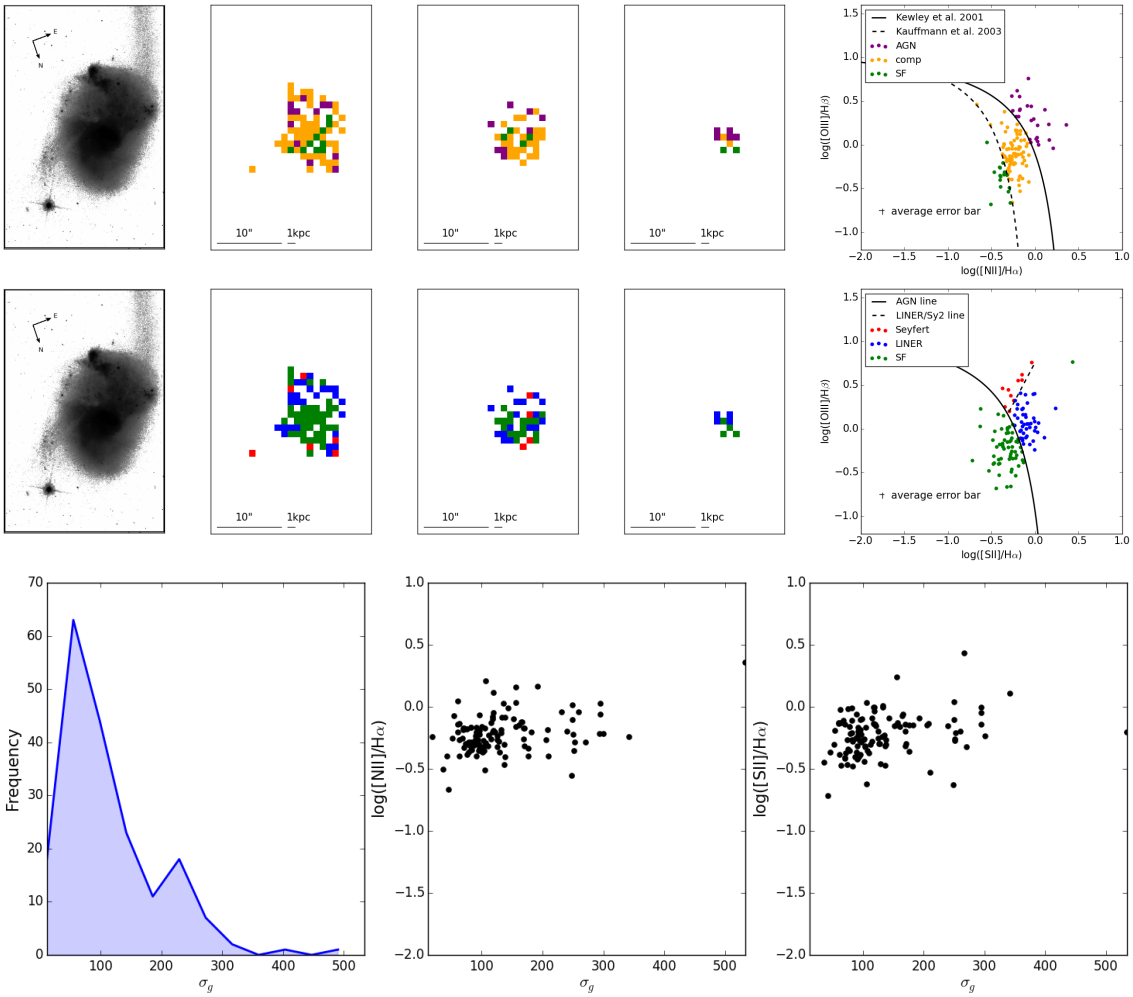

Figure B.11: IRAS F20551-4250: Top: ACS WFC F814W image (left), galaxy map with colours corresponding to the regions of the [NII]/Hα diagnostic diagram the emission lines lie in (middle), [NII] diagnostic diagram for (right). Green indicates star-forming and yellow indicates composite. Middle: ACS WFC F814W image (left), galaxy map with colours corresponding to the regions of the [SII] diagnostic diagram the emission lines lie in (middle), [SII]/Hα diagnostic diagram for (right). Green indicates star-forming, red indicates Seyfert like, and blue indicates LINER like emission. Bottom: left presents the velocity dispersion distribution, middle presents the [NII]/Hα versus gas velocity dispersions, right presents the [SII]/Hα versus gas velocity dispersions.

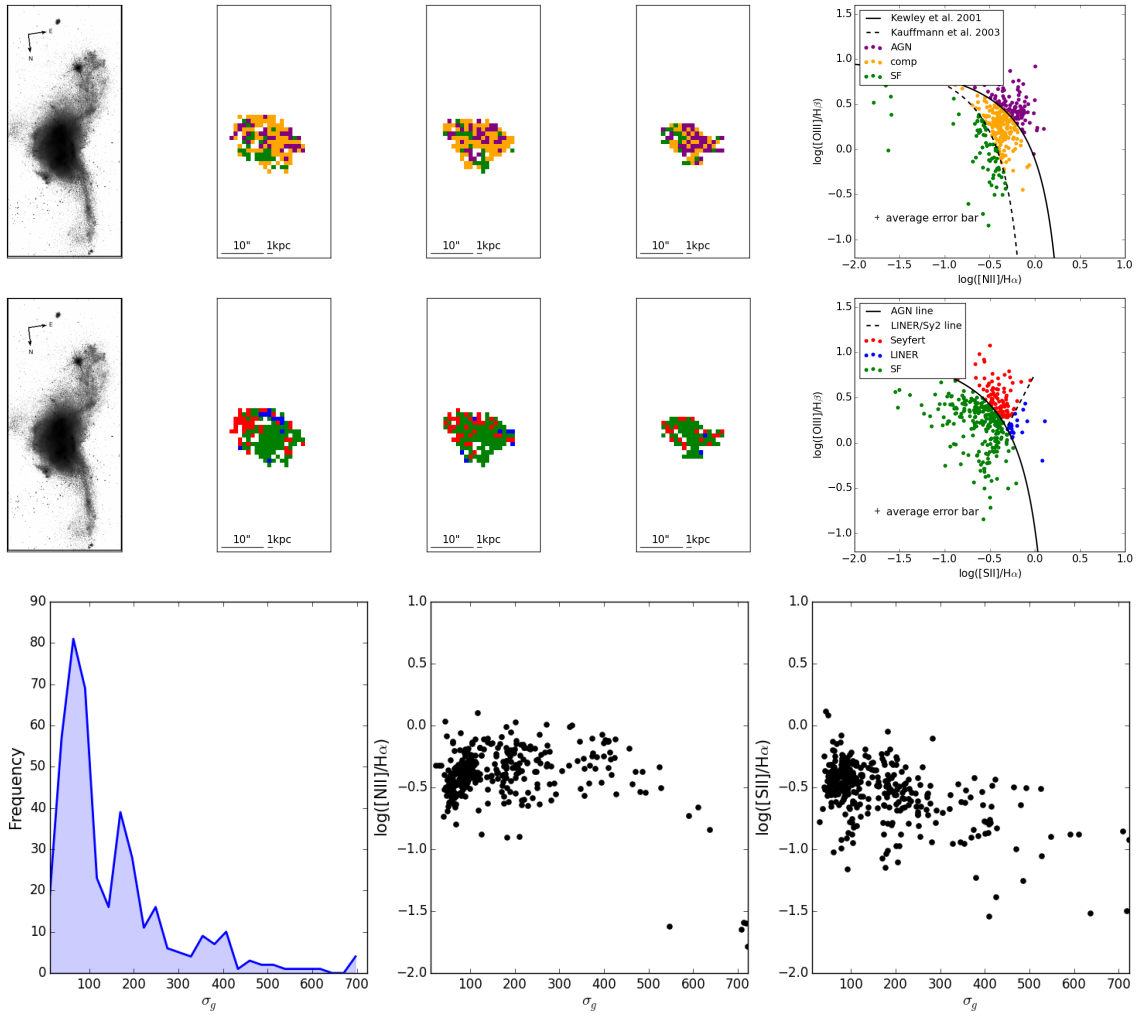

Figure B.12: IRAS F23128-5915: Top: ACS WFC F814W image (left), galaxy map with colours corresponding to the regions of the [NII]/Hα diagnostic diagram the emission lines lie in (middle), [NII] diagnostic diagram for (right). Green indicates star-forming and yellow indicates composite. Middle: ACS WFC F814W image (left), galaxy map with colours corresponding to the regions of the [SII] diagnostic diagram the emission lines lie in (middle), [SII]/Hα diagnostic diagram for (right). Green indicates star-forming, red indicates Seyfert like, and blue indicates LINER like emission. Bottom: left presents the velocity dispersion distribution, middle presents the [NII]/Hα versus gas velocity dispersions, right presents the [SII]/Hα versus gas velocity dispersions.

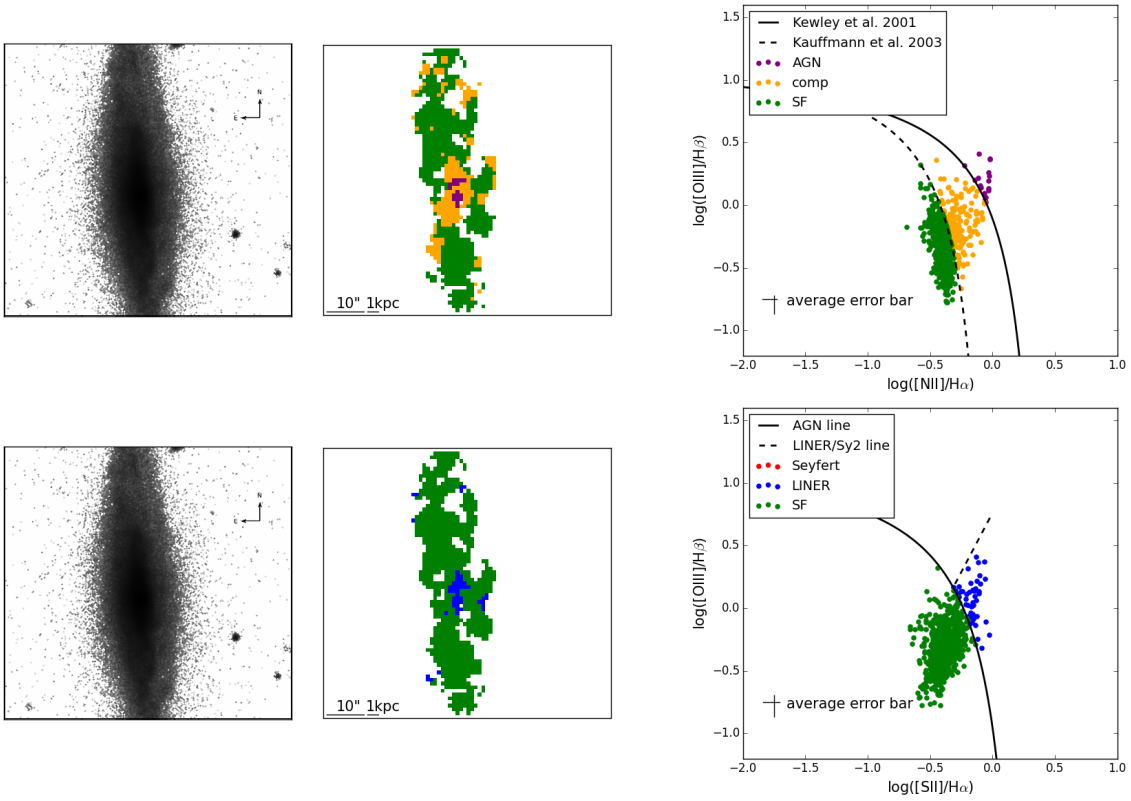

Figure B.13: IC5376: Top: SDSS III DR12 r-band image (left), galaxy map with colours corresponding to the regions of the [NII]/Hα diagnostic diagram the emission lines lie in (middle), [NII]/Hα diagnostic diagram for (right). Green indicates star-forming and yellow indicates composite. Bottom: SDSS III DR12 r-band image (left), galaxy map with colours corresponding to the regions of the [SII]/Hα diagnostic diagram the emission lines lie in (middle), [SII]/Hα diagnostic diagram (right). Green indicates star-forming, red indicates Seyfert like, and blue indicates LINER like emission.

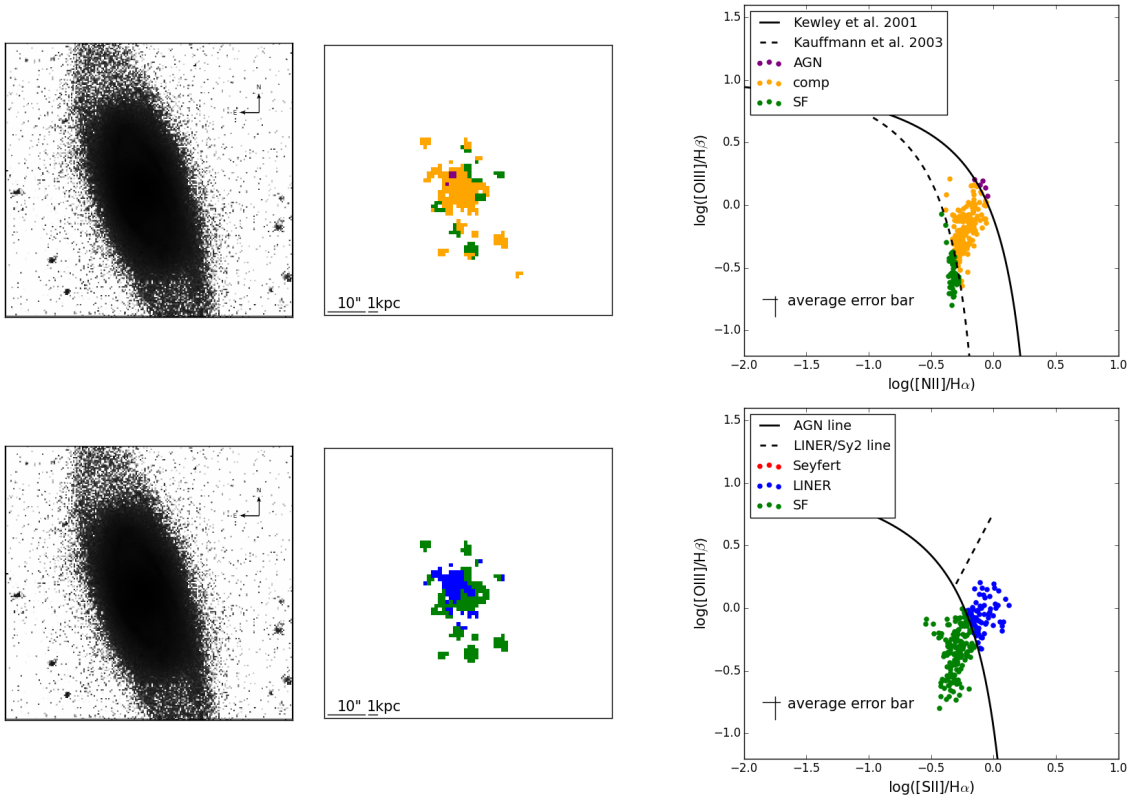

Figure B.14: UGC00036: Top: SDSS III DR12 r-band image (left), Galaxy map with colours corresponding to the regions of the [NII]/Hα diagnostic diagram the emission lines lie in (middle), [NII]/Hα diagnostic diagram for (right). Green indicates star-forming and yellow indicates composite. Bottom: SDSS III DR12 r-band image (left), Galaxy map with colours corresponding to the regions of the [SII]/Hα diagnostic diagram the emission lines lie in (middle), [SII]/Hα diagnostic diagram (right). Green indicates star-forming, red indicates Seyfert like, and blue indicates LINER like emission.

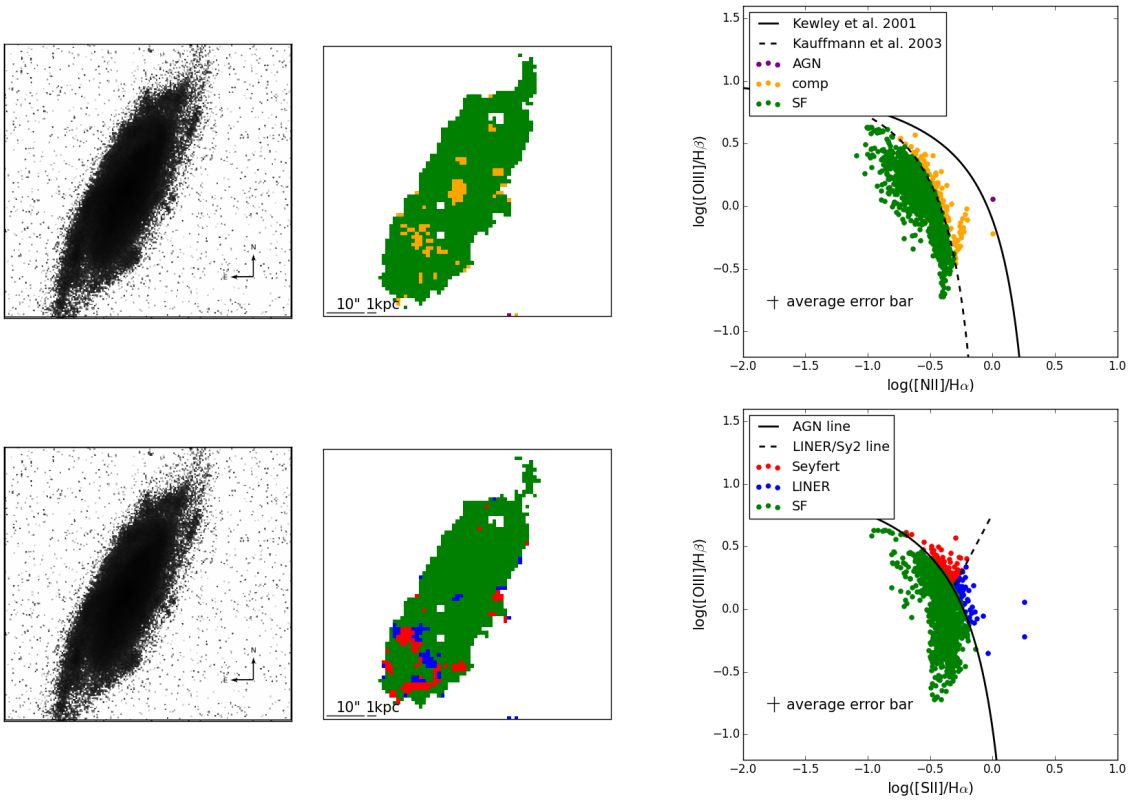

Figure B.15: UGC01057: Top: SDSS r-band image (left), galaxy map with colours corresponding to the regions of the [NII]/Hα diagnostic diagram the emission lines lie in (middle), [NII]/Hα diagnostic diagram for (right). Green indicates star-forming and yellow indicates composite. Bottom: SDSS r-band image (left), galaxy map with colours corresponding to the regions of the [SII]/Hα diagnostic diagram the emission lines lie in (middle), [SII]/Hα diagnostic diagram for (right). Green indicates star-forming, red indicates Seyfert like, and blue indicates LINER like emission.

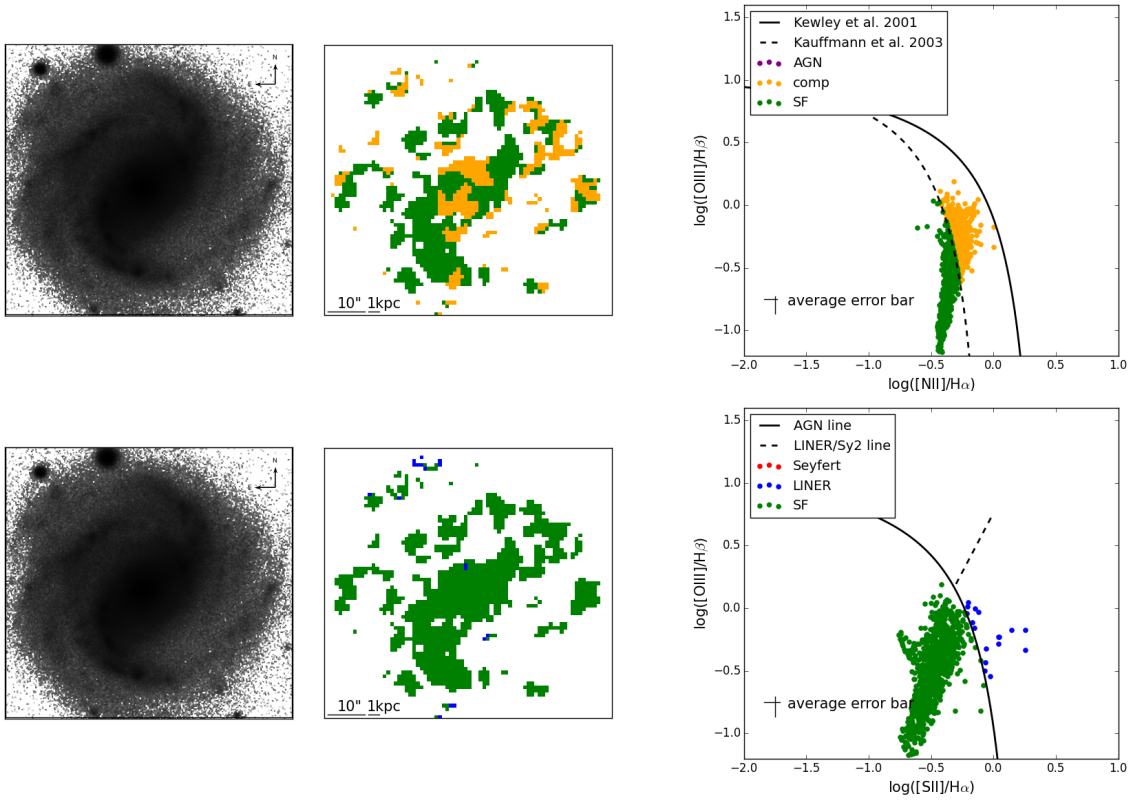

Figure B.16: NGC0776: Top: SDSS III DR12 r-band image (left), galaxy map with colours corresponding to the regions of the [NII]/Hα diagnostic diagram the emission lines lie in (middle), [NII]/Hα diagnostic diagram for (right). Green indicates star-forming and yellow indicates composite. Bottom: SDSS III DR12 r-band image (left), galaxy map with colours corresponding to the regions of the [SII]/Hαdiagnostic diagram the emission lines lie in (middle), [SII]/Hα diagnostic diagram for (right). Green indicates star-forming, red indicates Seyfert like, and blue indicates LINER like emission.

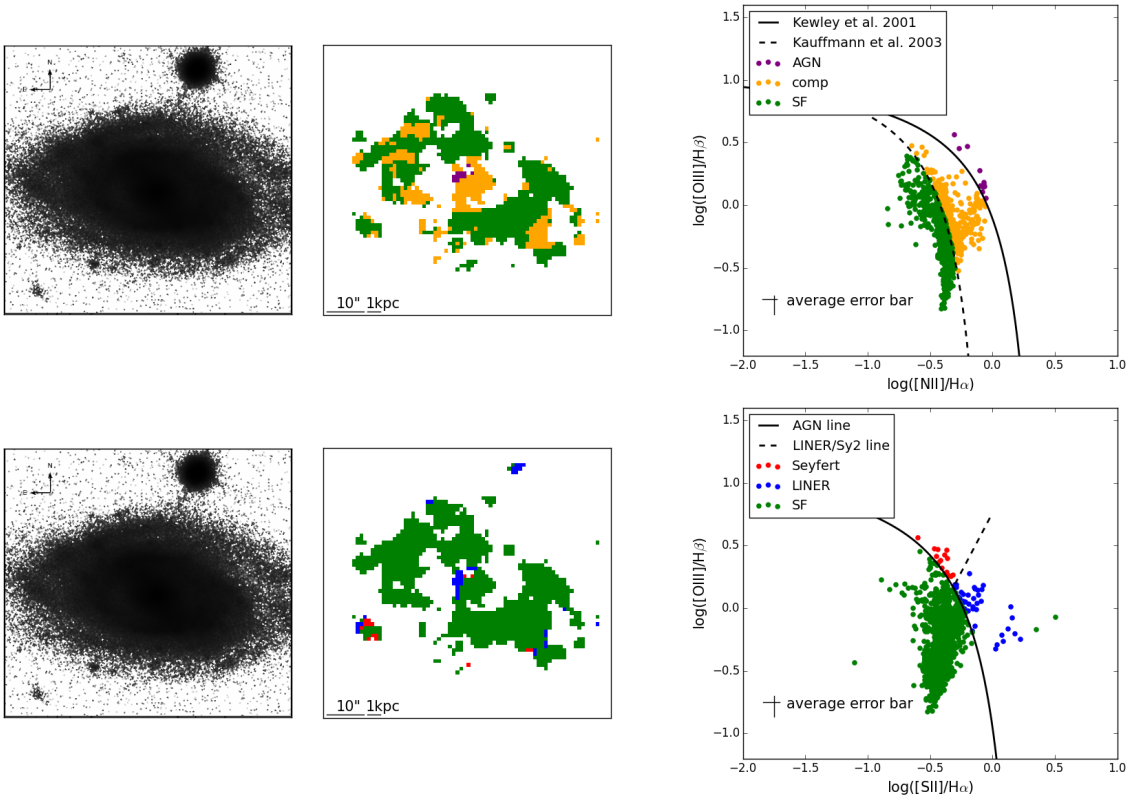

Figure B.17: UGC03253: Top: SDSS III DR12 r-band image (left), galaxy map with colours corresponding to the regions of the [NII]/Hα diagnostic diagram the emission lines lie in (middle), [NII]/Hα diagnostic diagram for (right). Green indicates star-forming and yellow indicates composite. Bottom: SDSS III DR12 r-band image (left), galaxy map with colours corresponding to the regions of the [SII]/Hα diagnostic diagram the emission lines lie in (middle), [SII]/Hα diagnostic diagram for (right). Green indicates star-forming, red indicates Seyfert like, and blue indicates LINER like emission.

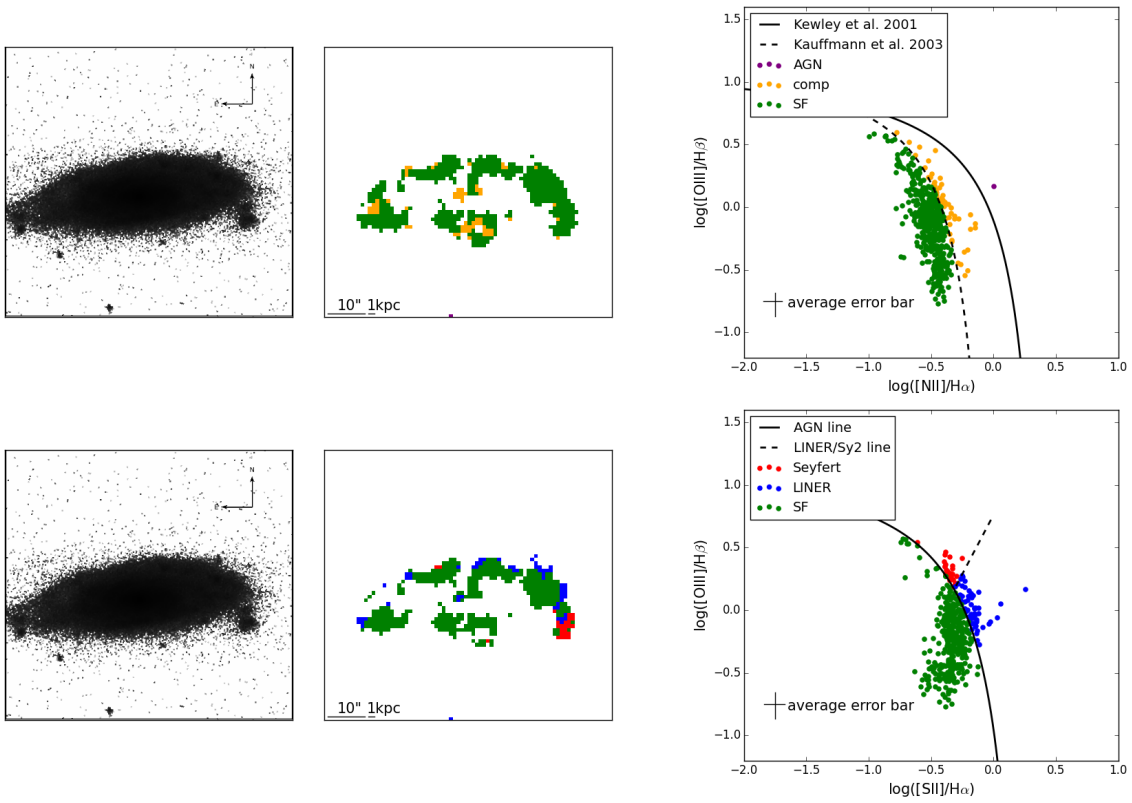

Figure B.18: UGC05359: Top: SDSS III DR12 r-band image (left), galaxy map with colours corresponding to the regions of the [NII]/Hα diagnostic diagram the emission lines lie in (middle), [NII]/Hαdiagnostic diagram for (right). Green indicates star-forming and yellow indicates composite. Bottom: SDSS III DR12 r-band image (left), galaxy map with colours corresponding to the regions of the [SII]/Hα diagnostic diagram the emission lines lie in (middle), [SII]/Hα diagnostic diagram for (right). Green indicates star-forming, red indicates Seyfert like, and blue indicates LINER like emission.

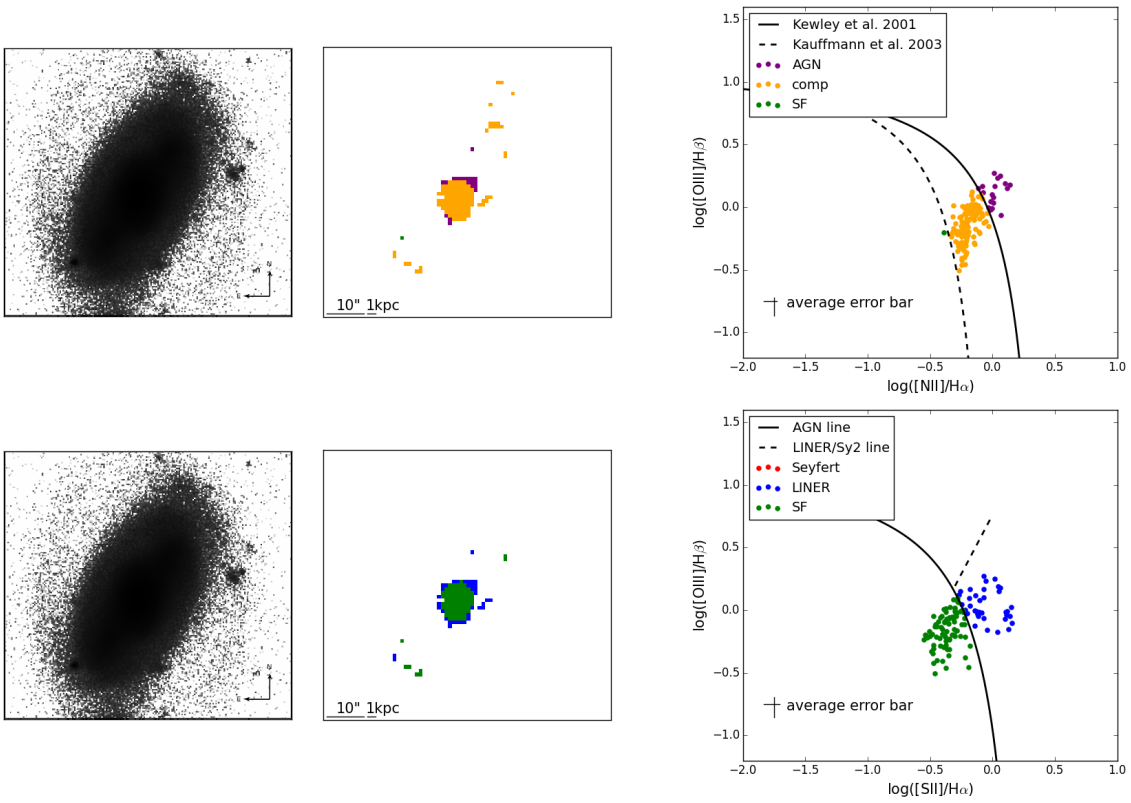

Figure B.19: NGC4003: Top: SDSS III DR12 r-band image (left), galaxy map with colours corresponding to the regions of the [NII]/Hα diagnostic diagram the emission lines lie in (middle), [NII]/Hα diagnostic diagram for (right). Green indicates star-forming and yellow indicates composite. Bottom: SDSS III DR12 r-band image (left), galaxy map with colours corresponding to the regions of the [SII]/Hαdiagnostic diagram the emission lines lie in (middle), [SII]/Hα diagnostic diagram for (right). Green indicates star-forming, red indicates Seyfert like, and blue indicates LINER like emission.

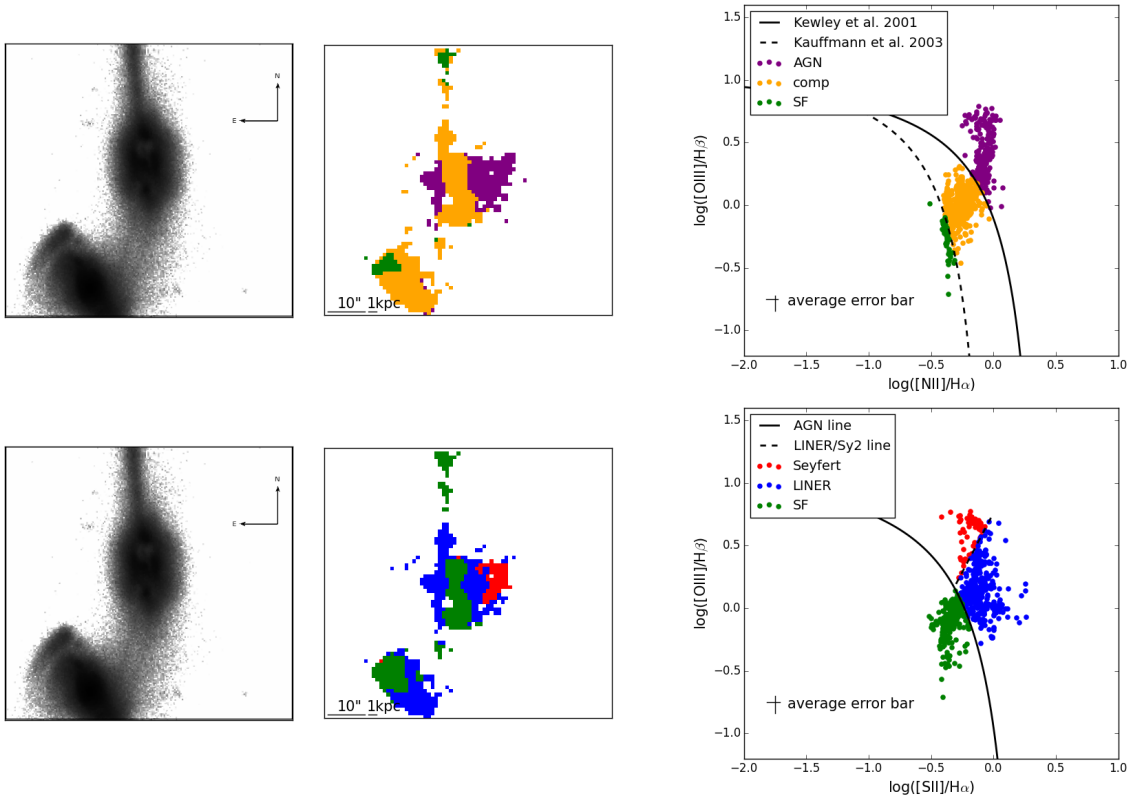

Figure B.20: NGC4676A: Top: SDSS III DR12 r-band image (left), galaxy map with colours corresponding to the regions of the [NII]/Hα diagnostic diagram the emission lines lie in (middle), [NII]/Hα diagnostic diagram for (right). Green indicates star-forming and yellow indicates composite. Bottom: SDSS III DR12 r-band image (left), galaxy map with colours corresponding to the regions of the [SII]/Hα diagnostic diagram the emission lines lie in (middle), [SII]/Hα diagnostic diagram for (right). Green indicates star-forming, red indicates Seyfert like, and blue indicates LINER like emission.

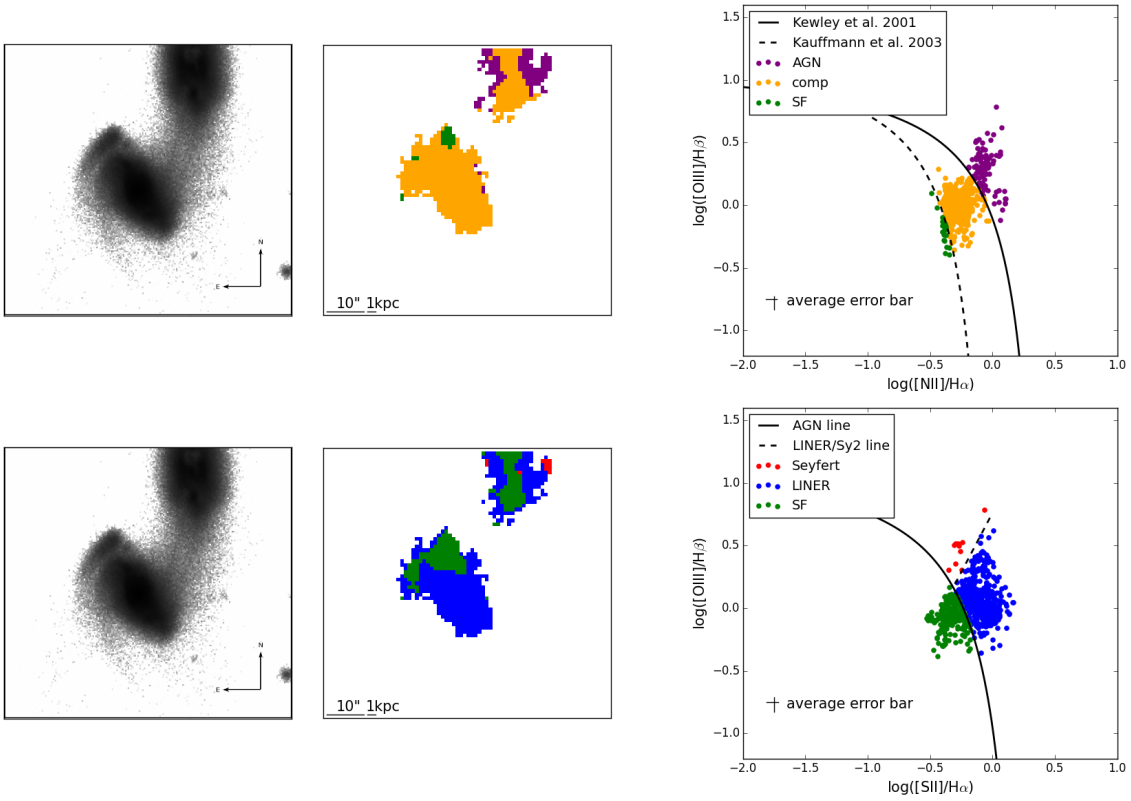

Figure B.21: NGC4676B: Top: SDSS III DR12 r-band image (left), galaxy map with colours corresponding to the regions of the [NII]/Hα diagnostic diagram the emission lines lie in (middle), [NII]/Hα diagnostic diagram for (right). Green indicates star-forming and yellow indicates composite. Bottom: SDSS III DR12 r-band image (left), galaxy map with colours corresponding to the regions of the [SII]/Hα diagnostic diagram the emission lines lie in (middle), [SII]/Hα diagnostic diagram for (right). Green indicates star-forming, red indicates Seyfert like, and blue indicates LINER like emission.

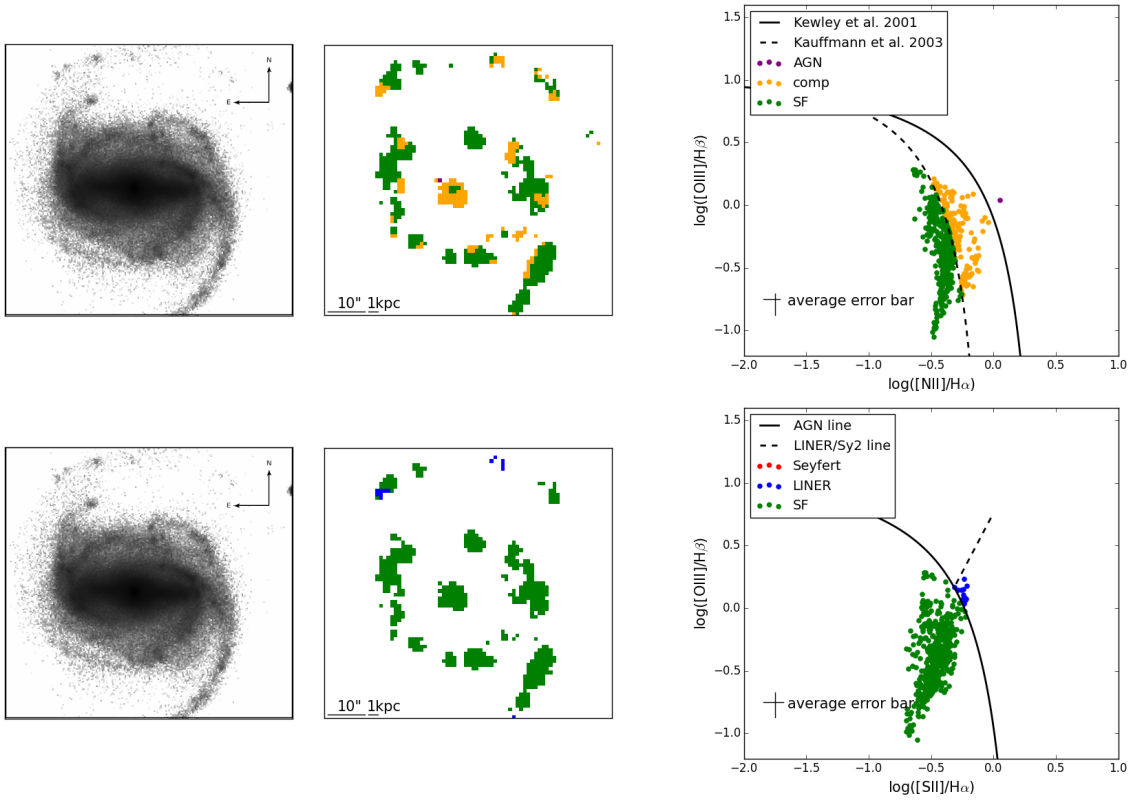

Figure B.22: NGC5000: Top: SDSS III DR12 r-band image (left), galaxy map with colours corresponding to the regions of the [NII]/Hα diagnostic diagram the emission lines lie in (middle), [NII]/Hα diagnostic diagram for (right). Green indicates star-forming and yellow indicates composite. Bottom: SDSS III DR12 r-band image (left), galaxy map with colours corresponding to the regions of the [SII]/Hα diagnostic diagram the emission lines lie in (middle), [SII]/Hα diagnostic diagram for (right). Green indicates star-forming, red indicates Seyfert like, and blue indicates LINER like emission.

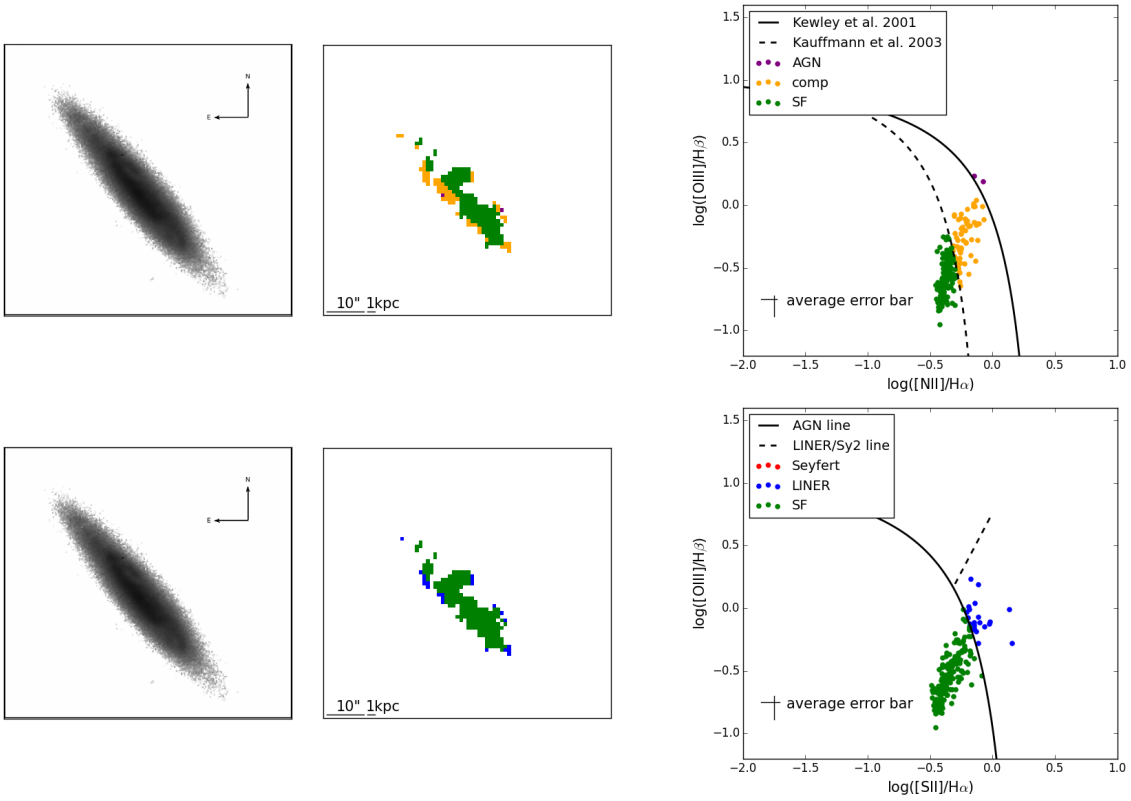

Figure B.23: UGC08267: Top: SDSS III DR12 r-band image (left), galaxy map with colours corresponding to the regions of the [NII]/Hα diagnostic diagram the emission lines lie in (middle), [NII]/Hα diagnostic diagram for (right). Green indicates star-forming and yellow indicates composite. Bottom: SDSS III DR12 r-band image (left), galaxy map with colours corresponding to the regions of the [SII]/Hα diagnostic diagram the emission lines lie in (middle), [SII]/Hα diagnostic diagram for (right). Green indicates star-forming, red indicates Seyfert like, and blue indicates LINER like emission.

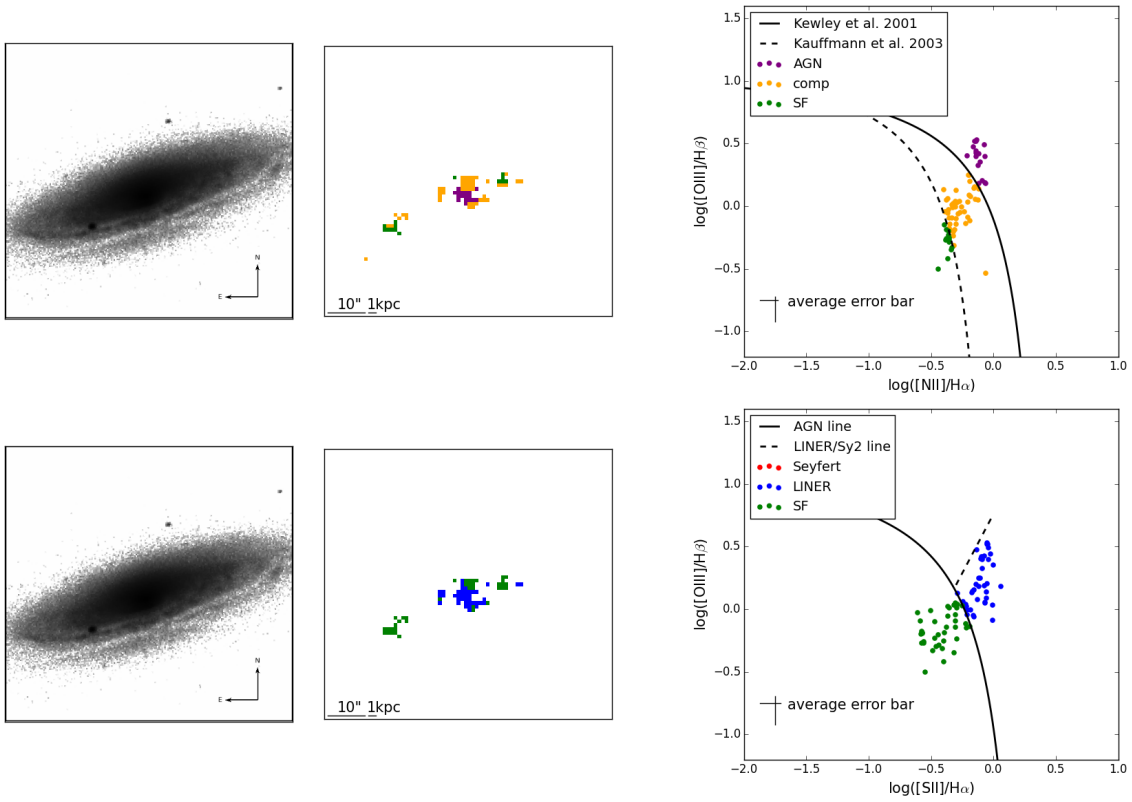

Figure B.24: IC0944: Top: SDSS r-band image (left), galaxy map with colours corresponding to the regions of the [NII]/Hα diagnostic diagram the emission lines lie in (middle), [NII]/Hα diagnostic diagram for (right). Green indicates star-forming and yellow indicates composite. Bottom: SDSS r-band image (left), galaxy map with colours corresponding to the regions of the [SII]/Hα diagnostic diagram the emission lines lie in (middle), [SII]/Hα diagnostic diagram for (right). Green indicates star-forming, red indicates Seyfert like, and blue indicates LINER like emission.

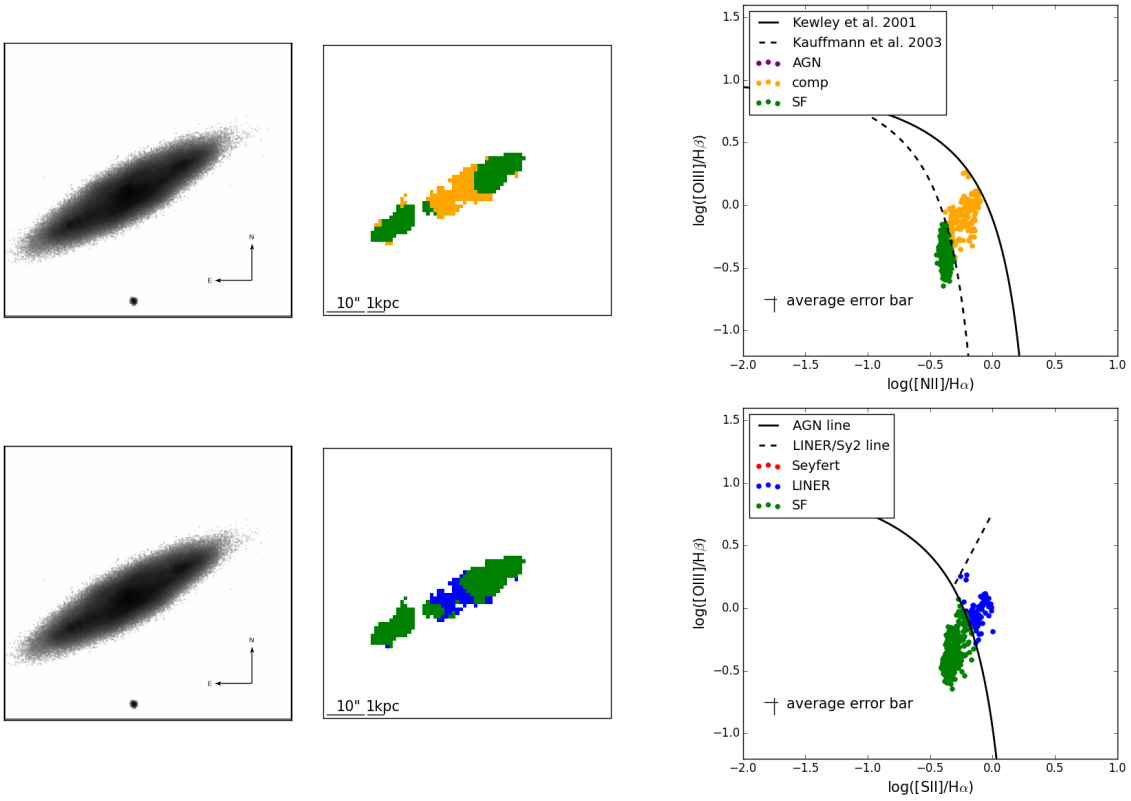

Figure B.25: UGC08778: Top: SDSS III DR12 r-band image (left), galaxy map with colours corresponding to the regions of the [NII]/Hα diagnostic diagram the emission lines lie in (middle), [NII]/Hα diagnostic diagram for (right). Green indicates star-forming and yellow indicates composite. Bottom: SDSS III DR12 r-band image (left), galaxy map with colours corresponding to the regions of the [SII]/Hα diagnostic diagram the emission lines lie in (middle), [SII]/Hα diagnostic diagram for (right). Green indicates star-forming, red indicates Seyfert like, and blue indicates LINER like emission.

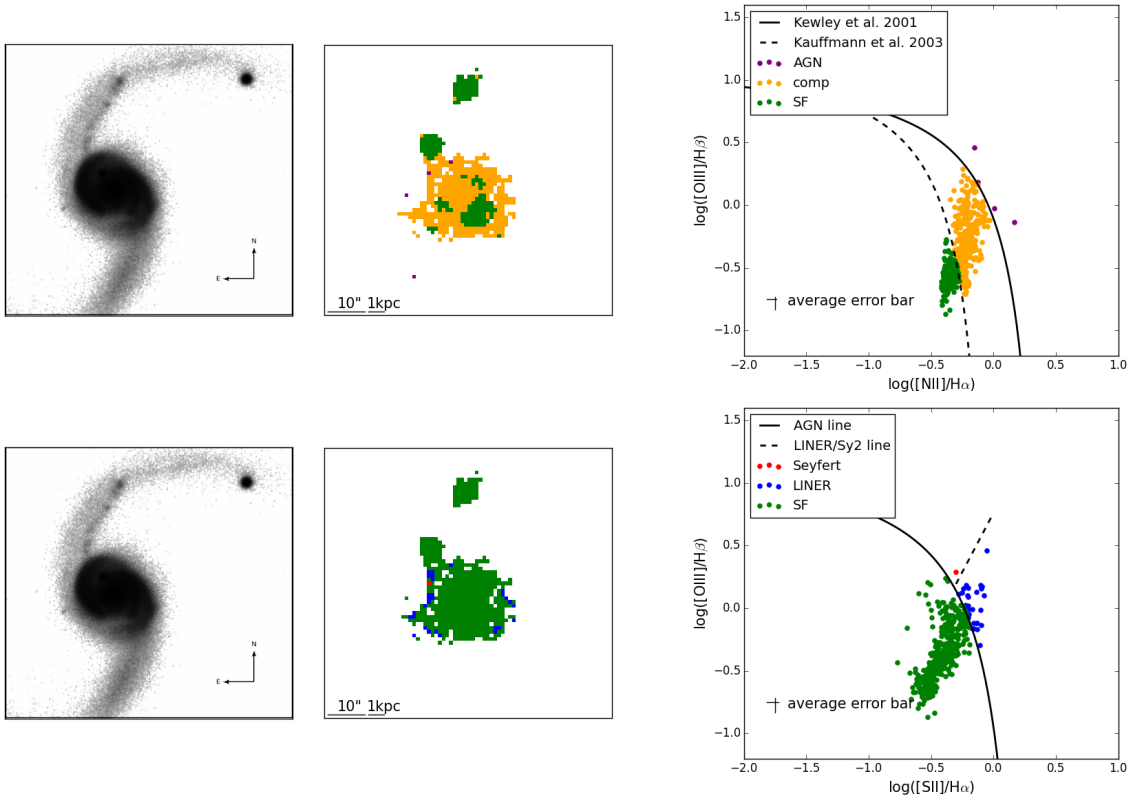

Figure B.26: NGC5394: Top: SDSS III DR12 r-band image (left), galaxy map with colours corresponding to the regions of the [NII]/Hα diagnostic diagram the emission lines lie in (middle), [NII]/Hα diagnostic diagram for (right). Green indicates star-forming and yellow indicates composite. Bottom: SDSS III DR12 r-band image (left), galaxy map with colours corresponding to the regions of the [SII]/Hα diagnostic diagram the emission lines lie in (middle), [SII]/Hα diagnostic diagram for (right). Green indicates star-forming, red indicates Seyfert like, and blue indicates LINER like emission.

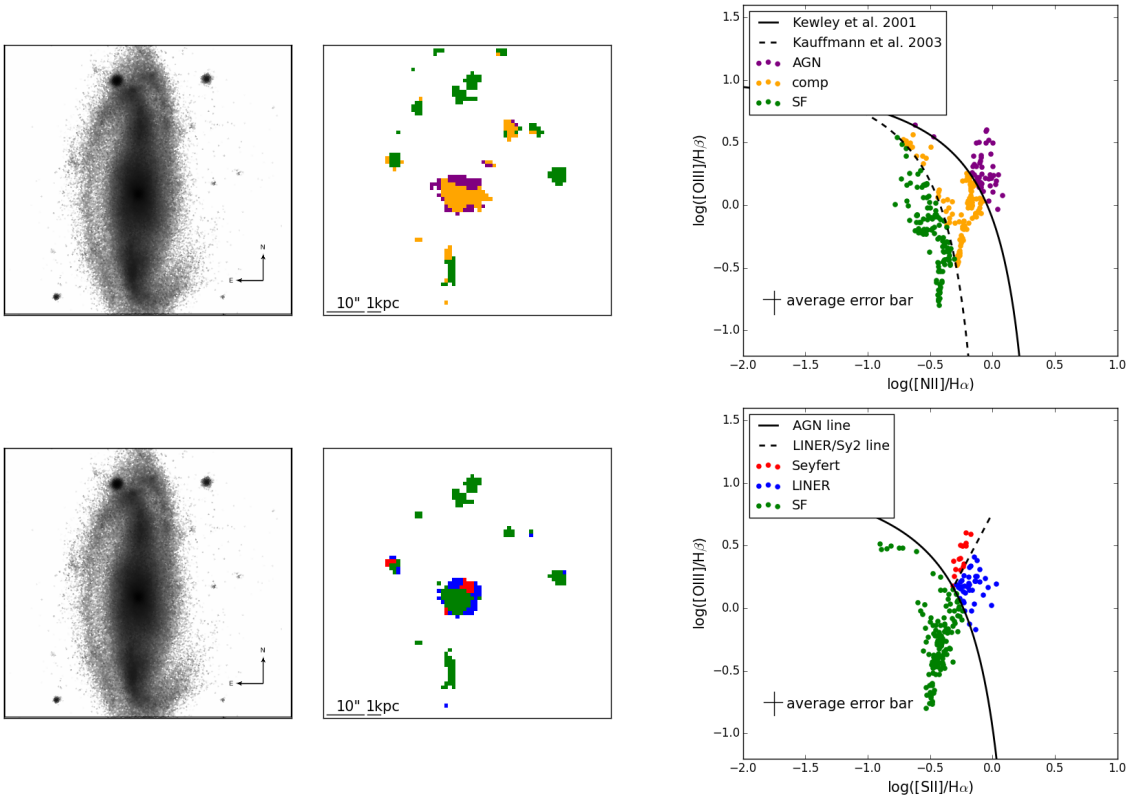

Figure B.27: NGC6032: Top: SDSS III DR12 r-band image (left), galaxy map with colours corresponding to the regions of the [NII]/Hα diagnostic diagram the emission lines lie in (middle), [NII]/Hα diagnostic diagram for (right). Green indicates star-forming and yellow indicates composite. Bottom: SDSS III DR12 r-band image (left), galaxy map with colours corresponding to the regions of the [SII]/Hα diagnostic diagram the emission lines lie in (middle), [SII]/Hα diagnostic diagram for (right). Green indicates star-forming, red indicates Seyfert like, and blue indicates LINER like emission.

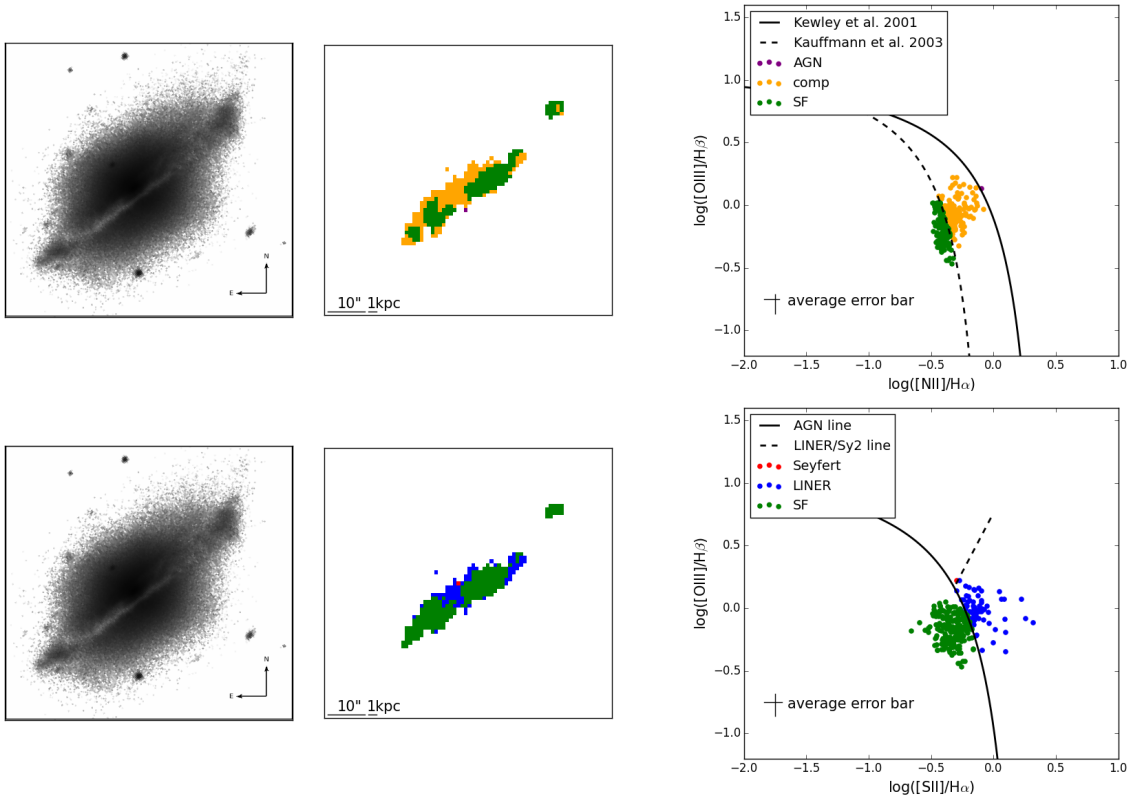

Figure B.28: UGC10205: Top: SDSS III DR12 r-band image (left), galaxy map with colours corresponding to the regions of the [NII]/Hα diagnostic diagram the emission lines lie in (middle), [NII]/Hα diagnostic diagram for (right). Green indicates star-forming and yellow indicates composite. Bottom: SDSS III DR12 r-band image (left), galaxy map with colours corresponding to the regions of the [SII]/Hα diagnostic diagram the emission lines lie in (middle), [SII]/Hα diagnostic diagram for (right). Green indicates star-forming, red indicates Seyfert like, and blue indicates LINER like emission.

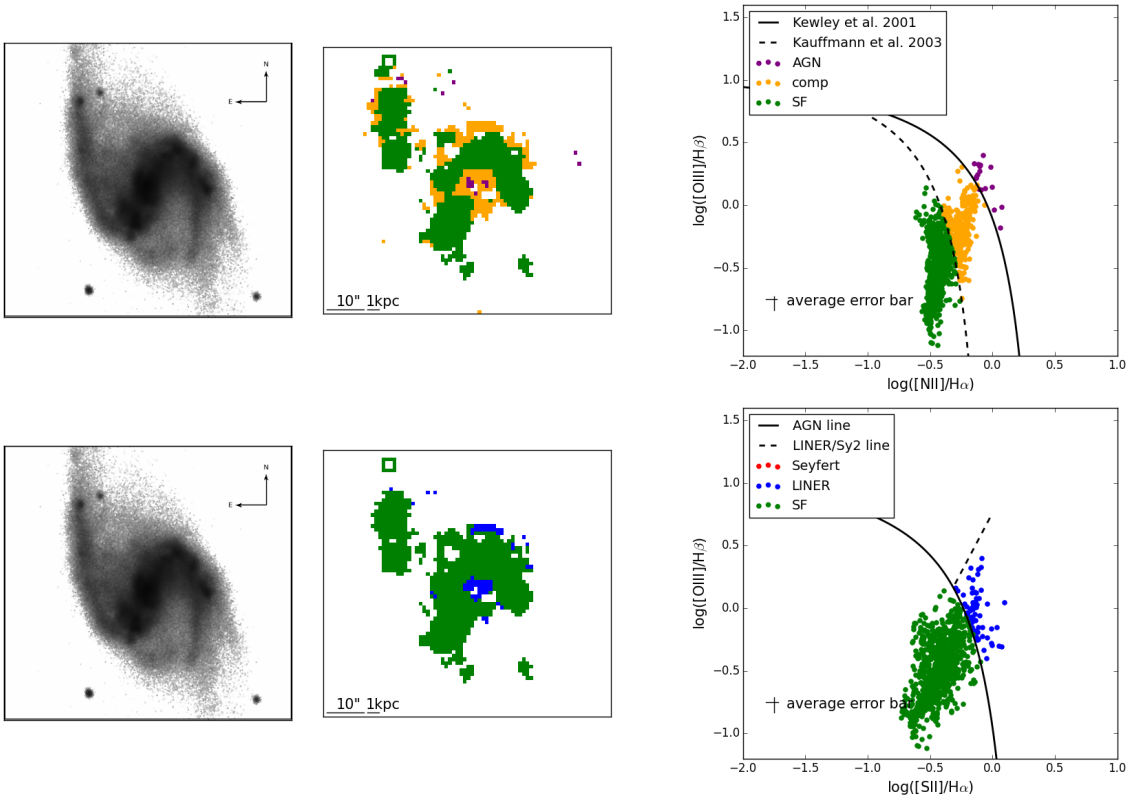

Figure B.29: NGC7549: Top: SDSS III DR12 r-band image (left), galaxy map with colours corresponding to the regions of the [NII]/Hα diagnostic diagram the emission lines lie in (middle), [NII]/Hα diagnostic diagram for (right). Green indicates star-forming and yellow indicates composite. Bottom: SDSS III DR12 r-band image (left), galaxy map with colours corresponding to the regions of the [SII]/Hα diagnostic diagram the emission lines lie in (middle), [SII]/Hα diagnostic diagram for (right). Green indicates star-forming, red indicates Seyfert like, and blue indicates LINER like emission.

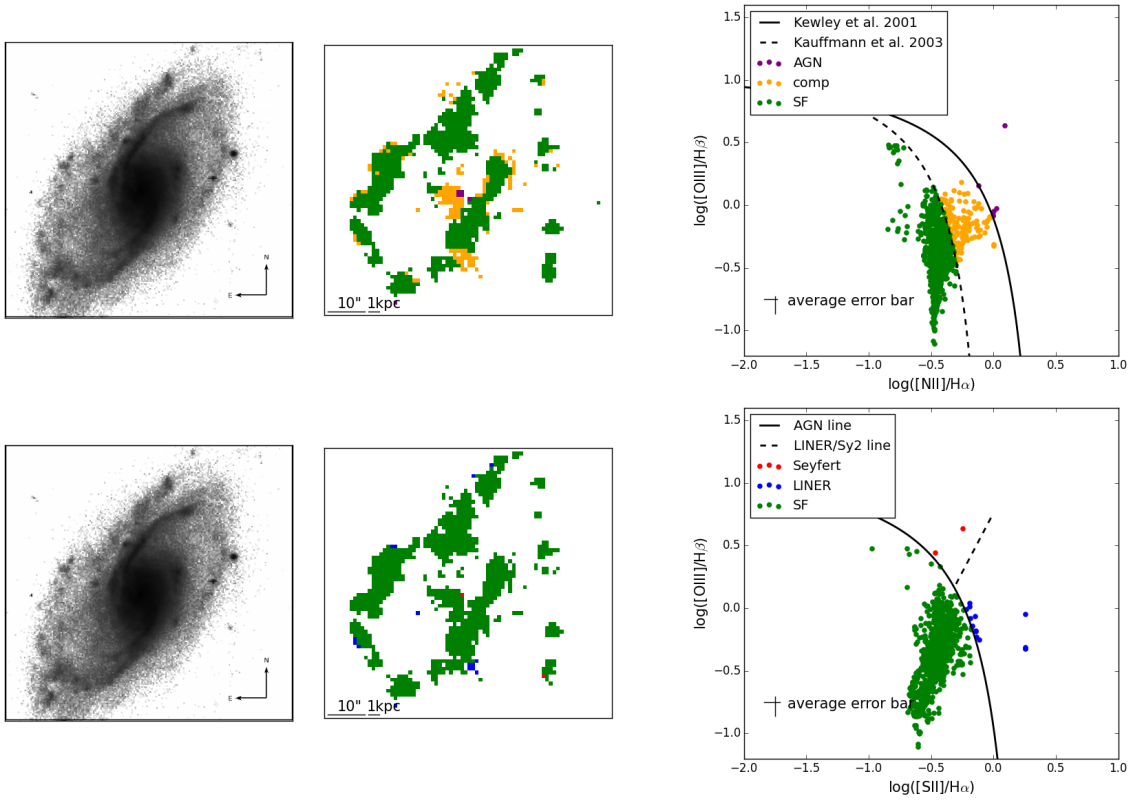

Figure B.30: NGC7591: Top: SDSS III DR12 r-band image (left), galaxy map with colours corresponding to the regions of the [NII]/Hα diagnostic diagram the emission lines lie in (middle), [NII]/Hα diagnostic diagram for (right). Green indicates star-forming and yellow indicates composite. Bottom: SDSS III DR12 r-band image (left), galaxy map with colours corresponding to the regions of the [SII]/Hα diagnostic diagram the emission lines lie in (middle), [SII]/Hα diagnostic diagram for (right). Green indicates star-forming, red indicates Seyfert like, and blue indicates LINER like emission.

Appendix C

Notes and diagnostic plots for individual NaI D galaxies

C.1 Notes on individual NaI D galaxies

Chapter 5 discusses the results of fitting NaI D absorption features to 24 galaxies in the survey WiGS (Rich et al., 2015). This section details the results of the fitting for each individual galaxy. The figures related to the nine galaxies with an outflow are presented in Appendix C.2. Figures related to the remaining galaxies have been excluded due to space constraints.

IRAS F01053-1746

IRAS F01053-1746 is a closely interacting pair of spiral galaxies. Rich et al. (2011) studied this galaxy in detail for evidence of shock excited gas. The two nuclei, east and west, are visible in the HST observations. The east nuclei is enshrouded in dust, stopping our WiFeS observations from detecting the underlying star formation. However the star-forming core has been observed in the IR (e.g. Howell et al., 2010).

The rotation curve of this galaxy is evident in the first ionised gas velocities along the north south direction. A comparison of the ionised gas velocities to the neutral gas velocities shows that there is a correlation between the two gases' velocities. The neutral gas velocity peaks at -150 km/s and has W_{eq} between $0 - 8$ Å . Analysis of the N(H) obtained values of $19 - 23$ dex with some correlation to W_{eq}. There is a trend with N(H) to higher dust attenuation values.

IRAS F01053-1746 is a dusty system with shock induced ionised gas resulting from the merger (Rich et al., 2011). The blue-shifted neutral gas observed is consistent with the velocity of the ionised gas in the same region of the galaxy and thus suggests the NaI D absorption is tracing the ionised gas.

IRAS F06076-2139

IRAS F06076-2139 is a close pair of interacting galaxies (Arribas et al., 2008; Elmegreen & Elmegreen, 2006). The northern galaxy of this pair is dominated by star formation (Rich et al., 2014) while the southern core hosts a possible AGN, identified through X-ray hardness ratios in Chapter 3.

The NaI D absorption feature is concentrated towards the northern core and between the north and south cores. The ionised gas velocities present an interesting picture of systemic velocities towards the northern core, while the velocities of the ionised gas towards the southern core are highly redshifted, indicating the two cores may be separated along the line of sight. There was an observation of a trail of red-shifted ionised gas north of the northern core. The velocities of the neutral gas are both blue and red-shifted around the systemic velocity of the galaxy system. The NaI D traces the space between the two cores indicating there may be tidal interactions between the two galaxies, but not an outflow.

A calculation of the N(H) of IRAS F06076-2139 indicates a $\log[\mathrm{N(H)}] = 20.75 - 22.5$ dex for the spaxels where there is significant ($> 3\sigma$) $\mathrm{W_{eq}}$. A comparison of dust and N(H), indicates a possible trend but the scatter is large and there are few (16) spaxels with both dust and N(H) values.

IRAS F10038-3338

IRAS F10038-3338 is a post merger galaxy with a significant remnant tidal arm towards the south west (Figure C.1). An off-nuclear shock was observed, consistent with Rich et al. (2014); Monreal-Ibero et al. (2010), in Chapter 3. Rich et al. (2014) found the optical emission points towards an actively star-forming core.

The ionised gas velocities in the first and second components (Figure C.2, top panels left and middle) are consistent with a galaxy rotation around the systemic velocity. The third ionised component, presented in the right panel, is both heavily blue and red shifted around the core of this galaxy. The NaI D absorption is towards the core of the galaxy and is blue-shifted (Figure C.2, bottom panels). The only correlation between the ionised

gas and neutral gas is between the third ionised component and the neutral component (Figure C.3). In this case only half of the neutral gas is correlated with the ionised gas, where the ionised gas is blue shifted to twice that of the neutral gas. It is unlikely in this case that it is the same physical process behind the ionised gas and neutral gas.

The W_{eq} of IRAS F10038-3338 ranges from $1.2 - 5.4$ Å (Figure C.4) with the highest values towards the core of the galaxy. W_{eq} correlates partially with N(H) (Figure C.5), but there was not see a trend of W_{eq} with the calculated HST colour. The position of the NaI D absorption is consistent with the off-nuclear shock determined in Chapter 3. It is concluded that the neutral gas being traced by the NaI D absorption is due to the gas settling around the core of the galaxy in its late stage of merging.

IRAS F10257-4339

The NaI D absorption observed in IRAS F10257-4339 is detailed in Chapter 4. This chapter determined that the galaxy hosted an outflow, consistent with previous studies using long-slit observations (Armus et al., 1989; Heckman et al., 1990, 2000; Lípari et al., 2000). The first component of the NaI D absorption is possibly associated with the second galaxy in the merge or it is a tidal feature. The second component of the NaI D absorption is related to the third ionised component of the emission lines, supporting the blue-shifted emission observed by Lípari et al. (2000). The figures for IRAS F10257-4339 are located in Chapter 4.

IRAS F12043-3140

IRAS F12043-3140 is a closely interacting pair of galaxies. There are currently no HST observations available to identify its morphology. However, Rich et al. (2015) used DSS imaging to identify tidal features due to the ongoing merge. Monreal-Ibero et al. (2010); Rich et al. (2015) discovered a cone extending from the north and south of the southern galaxy. NaI D absorption was used to determine if this cone is related to an outflow.

The ionised gas velocities identify one galaxy on the left and another on the right. It was observed that most of the NaI D is along the left (or southern) galaxy. The neutral gas velocities towards the southern galaxy not correlated with the ionised gas velocities and peak at 0 km/s. The W_{eq} ranges from $0 - 7$ Å and shows a correlation with N(H). The velocities are consistent with tidal interactions between the two galaxies.

IRAS F12592+0436

IRAS F12592+0436 is a late-stage merger. The HST observations highlight the dusty merger with a tidal tail towards the east edge of our observation. The dust is concentrated towards the core of the galaxy as indicated by the HST observation. The emission line studies by Rich et al. (2014) were unable to determine the physical processes behind the ionised gas due to S/N cuts on the emission line fits. However, studies by (Poggianti & Wu, 2000; Petric et al., 2011; Stierwalt et al., 2012) determined the nucleus to be star-forming with no indication of an AGN.

The ionised gas velocities indicate a rotation curve in the south-east to north-west direction. The neutral gas velocities are mostly blue shifted but the majority are below -100 km/s and do not correlate with the ionised gas velocities. The W_{eq} ranges from $1 - 10$ Å and correlates with N(H). The N(H) for IRAS F12592+0436 ranges between $20.5 - 23$ dex. The HST colour indicates that the spaxels with NaI D absorption with larger dust fractions are related to the high N(H).

IRAS F12592+0436 is a dusty merger with NaI D absorption off nucleus. The absorption may be due to the merge, however the velocities observed do not indicate a fast moving outflow from the galaxy.

IRAS F13120-5453

IRAS F13120-5453 is an isolated ULIRG dominated by an AGN in all wavelengths (Rich et al., 2015; Iwasawa et al., 2011, 2009; Petric et al., 2011; Pereira-Santaella et al., 2010; Farrah et al., 2007). The ionised gas velocities indicate a rotating disk (Figure C.6, top panels) and a blue shifted component in the right most panel. The NaI D absorption also identifies a blue shifted component (bottom panels), spatially similar to the third ionised gas component (Figure C.7. The blue shifted NaI D is indicative of an outflow from the centre of this AGN dominated galaxy.

The W_{eq} peaks at the centre of the galaxy (Figure C.8), where the AGN is. There is a correlation of W_{eq} with N(H) between $21 - 22.5$ dex (Figure C.9). There are presently no HST observations of this galaxy in the bands B or I, therefore cannot compare the results to dust attenuation. Future follow-up of this galaxy with HST F814W and F435W is recommended.

IRAS F13373+0105 East

IRAS F13373+0105 East is the distant merger to IRAS F13373+0105 West. The two galaxies are similar in mass and luminosity. Rich et al. (2014) found the east galaxy to be dominated by older stars and very little line-emission. The HST observations show a dusty spiral galaxy, with spiral arms going past the FoV of the WiFeS observation. The dustiest parts of the spiral are traced by the HST colour image.

The ionised gas velocities show a clear galaxy rotation north-east to south-west in both the first and second ionised components. The neutral gas velocities do not follow the galaxy rotation outlined by the ionised gas. Both neutral and ionised gas velocities are between $\pm 200\,\mathrm{km/s}$. The neutral gas velocities peak at systemic velocity with a small tail to more blue-shifted values of -400 km/s. The number of spaxels in this tail is only 5, thus it can not be conclusively determined that it is an outflow.

The calculation of the N(H) for this galaxy defines two populations of spaxels, one with $\log[\mathrm{N(H)}] \sim 18.5$ and the other with $\log[\mathrm{N(H)}] \sim 20$. These two populations do not correlate with $\mathrm{W_{eq}}$ or with HST colour. However, N(H) does look to trace the spiral arms of IRAS F13373+0105 East. There is no strong indication of an outflow in this merging galaxy.

IRAS F13373+0105 West

IRAS F13373+0105 West is a distant merger. This galaxy was found to be predominately star-forming in Chapter 3, consistent with Rich et al. (2014). There was no evidence of shocked emission or AGN emission. IRAS F13373+0105 West is of similar mass and luminosity to its east counterpart and is also a spiral galaxy showing star-forming lanes and dust throughout.

The ionised velocity structure of IRAS F13373+0105 West is consistent with a galaxy rotation curve. The major axis of the galaxy is along the east-west direction. The neutral gas velocities are consistent with the galaxies' rotation curve. A comparison of the gas velocities finds a strong correlation between the neutral and ionised gases, indicating these are from the same physical process.

The $\mathrm{W_{eq}}$ values are between $0.5 - 5\,\mathrm{Å}$, peaking at $\sim 2\,\mathrm{Å}$. The velocities of the neutral gas peak around the systemic velocity. The calculated N(H) was between $20 - 22.5\,\mathrm{dex}$. The NaI D absorption in this galaxy is consistent with the neutral gas of a rotating disk.

IRAS F15107+0724

IRAS F15107+0724 is an undisturbed isolated spiral galaxy (Haan et al., 2011; Yuan et al., 2010a). Rich et al. (2015) determined the emission line spectrum is dominated by star formation with some contribution from shocks, consistent with previous studies (Kim et al., 1995; Veilleux et al., 1995a). The ionised gas velocities are indicative of a rotating disk. The neutral gas velocities show a tight collection of velocities, between $\pm 100\,\mathrm{km/s}$.

The W_{eq} values are spread between $1 - 6\,\text{Å}$ and show a correlation with N(H). There was no evidence of an outflow in this galaxy.

IRAS F16164-0746

IRAS F16164-0746 is a coalesced merger hosting an AGN (Iwasawa et al., 2009, 2011; Petric et al., 2011) (Figure C.10). Rich et al. (2014) studied the emission line ratios of this galaxy and determined they were consistent with star formation and shocks. This is consistent with the results in Chapter 3.

The ionised gas velocities presented in Figure C.11 (top panels) indicate the galaxy rotation and a heavily blue-shifted component. The rotation of the galaxy is identified by the almost systemic velocities of the first component and the 2nd component. In the case of this galaxy the rotation component has been identified as components in the west and east of the galaxy. The values of neutral gas velocity are only towards the heavily blue-shifted ionised gas component (Figure C.11, bottom panels). A comparison of the gas velocities shows that there is no correlation (Figure C.12. This indicates the heavily blue-shifted ionised gas is not necessarily associated with the blue-shifted NaI D absorption.

The W_{eq} values range from $1 - 4.5\,\mathring{A}$ (Figure C.13). The W_{eq} is not correlated with N(H), nor is N(H) correlated with HST colour (Figure C.14). It is possible the neutral gas is associated with the shocks indicated in the emission line ratios and with the blue-shifted ionised gas. However, our IFS observation does not map out the entire galaxy. The blue-shifted ionised gas is associated with star-forming emission line ratios which may indicate there is an outflow due to star formation in this galaxy. A follow up observation using a higher spatial resolution, and longer exposure is suggested to separate out this complex set of physical processes.

IRAS F16399-0937

IRAS F16399-0746 is a close merger pair. Rich et al. (2014) found this galaxy system to

be star formation dominated with some indication of shock-like emission line ratios due to a possible outflow. However, no fit to the NaI D absorption was conducted in their study. The two nuclei of this system are easily identified in the HST image presented in Figure C.15 (top panels). The HST colour images (bottom panels) highlight the dust north of the northern nuclei and the tidal arm around the two nuclei in the west. The HST colour image is unable to provide much information when convolved to the WiFeS spatial resolution. A higher spatial resolution IFS observation would allow a better comparison to the HST colour.

The ionised gas velocities presented in Figure C.16 (top panels) indicate a galaxy rotation in the north-east to south-west direction. The neutral gas velocities follow a similar rotation curve (bottom panels). The NaI D absorption is concentrated on the southern nuclei and up to the northern nuclei. The neutral gas velocities do not correlate with any of the ionised components (Figure C.17). The W_{eq} ranges from $2 - 12$ Å (Figure C.18) and has little correlation with N(H) (Figure C.19). However, the smaller W_{eq} does have lower N(H). It was not possible to definitively determine whether this galaxy is host to an outflow or if we are tracing the neutral gas between the two nuclei; further follow-up is recomended.

IRAS F17138-1017

IRAS F17138-1017 is a coalesced merger. The study of the emission line physics of this galaxy in Chapter 3 is consistent with Rich et al. (2014); Monreal-Ibero et al. (2010). The galaxy is predominantly star-forming. There is evidence of shocks in the outer regions of the galaxy from the [SII]/Hα diagnostic diagram and the strong bimodal distribution in velocity dispersion. IRAS F17138-0746 is host to a possible LINER/Sy2 AGN.

The ionised gas velocities show the strong rotation curve of the galaxy in the first ionised component. The neutral gas velocities present a similar rotation of the neutral gas. A comparison of the velocities between the ionised and neutral gas velocities shows some correlation between the second ionised component and the neutral gas.

There is a correlation between the total W_{eq} and N(H) and there is another component that is not correlated. The colour calculated through the HST images is zero for much of the galaxy. This indicates that the emission in the F814W and F435W bands is comparable. There is no evidence of an outflow.

IRAS F17207-0014

IRAS F17207-0014 is a well studied late stage merger (Franceschini et al., 2003; Arribas & Colina, 2003; Rupke et al., 2005b,c; Iwasawa et al., 2011; Petric et al., 2011; Stierwalt et al., 2012; Medling et al., 2015), Figure C.20. Rupke et al. (2005b,c) found evidence for a galactic wind in this galaxy using NaI D absorption. The emission line analysis in Chapter 3 was inconclusive on the physical processes related to ionised gas studies. However, it has been possible to detect NaI D absorption, consistent with previous studies.

The ionised gas velocities presented in Figure C.21 (top panels) shows a rotation curve about the centre of the galaxy indicating the major axis to be along the north-south direction. The outflow, seen in previous studies, is evident through the heavily blue-shifted NaI D absorption velocities (Figure C.21, bottom panels). The blue-shifted neutral gas we have detected is $\sim 5 \times 5$ kpc in size. A comparison to the ionised gas velocities shows no correlation, indicating the ionised gas does not trace the same physical processes in this galaxy (Figure C.22). The neutral gas velocities span -100 to -500 km/s.

The W_{eq} calculated for IRAS F17207-0014 ranges from $4 - 14$ Å (Figure C.23). This is correlated with the N(H) calculated (Figure C.24 right panel) between $21 - 23$ dex. There is a single point of HST colour for this galaxy, as can be seen in Figure C.24 (left panel). Although the HST colour is present in the FoV of the WiFeS observation at the resolution of the HST image, the convolution to the WiFeS spatial scale leaves very few values to work with. A suggestion to minimise this would be to compare the HST colour with a spatially comparable IFS observation.

IRAS F17222-5953

IRAS F17222-5953 is an isolated galaxy with strong star formation. Rich et al. (2015) found the emission line ratios of this galaxy to match the shape of the SDSS sequence of local star-forming galaxies on the [NII]/Hα vs [OIII]/Hβ diagnostic diagram (Kewley et al., 2006).

The ionised gas velocity maps (Figure C.25, top panels) indicate a rotation curve in the first two components and a blue shifted third component. The neutral gas velocities also map out a similar region with blue-shifted material (bottom panels). The W_{eq} ranges from $0 - 6.4$ Å with the majority of components below 4 Å (Figure C.27). A calculation of N(H) provides two groupings of points, one correlated with W_{eq} and the other not (Figure C.28). The N(H) ranges from $20 - 22.5$ dex. The blue-shifted neutral material is

consistent with an outflow in this galaxy with velocities between $100 - 500\,\mathrm{km/s}$.

IRAS F18093-5744 North

IRAS F18093-5744 North is the northern galaxy in a triplet merger. The closest galaxy in the merger is IRAS F18093-5744 C, for which we found no NaI D absorption. The most distant galaxy in the merger is IRAS F18093-5744 South. IRAS F18093-5744 North is classified as a Wolf-Rayet galaxy (Kovo & Contini, 1999; Fernandes et al., 2004). Rich et al. (2014) determined through their emission line study that the WiFeS observation encompasses both the north and C galaxies in this merger.

The ionised gas velocities identify the galaxy rotation in the north-east to south-west direction in both the first and second ionised gas components. The third ionised gas component is at generally larger velocities. The neutral gas velocities do not correlate with the ionised gas velocities. However, the velocities span a similar velocity-space with the neutral gas velocities centred on -50 km/s. The W_{eq} calculated from this galaxy span $1 - 8.5\,\text{Å}$ with a concentration of the higher W_{eq} towards the core of the galaxy.

The NaI D absorption identified is consistent with the galaxy's rotational velocities and possibly due to the tidal interaction with IRAS F18093-5744 C.

IRAS F18093-5744 South

IRAS F18093-5744 South is the southern galaxy of the above mentioned triplet galaxy merger. The south galaxy is in a wide merger, showing less morphological disruptions that the north and C galaxies. The galaxy is star-forming (Howell et al., 2010) and Rich et al. (2014) have assumed it to be a part of the merging system despite the large separation.

The ionised gas velocities indicate a rotation curve south-east to north-west. The neutral gas velocities are red-shifted, indicating the listed redshift for this galaxy is not quite adequate. A comparison of the two gases' velocities shows some correlation between the second and third ionised gas velocities, but it is evident that it is all red-shifted. The W_{eq} values range from $1 - 5\,\text{Å}$. The values calculated for N(H) show an almost anti-correlation with HST colour, while having a correlation with W_{eq}.

The analysis of the NaI D absorption does not show evidence of an outflow associated with IRAS F18093-5744 South. The analysis does suggest a newer calculation of the redshift is required.

IRAS F18293-3413

IRAS F18293-3413 is a close merger system. Rich et al. (2014) determined the northern nuclei to be dominated by star formation with some contribution from shock excitation. A study of the X-ray emission concluded that there is no indication of an AGN but there is an indication of a possible outflow (Iwasawa et al., 2009, 2011). The HST images indicate a dusty galaxy with spiral features, consistent with in-depth studies of the morphology of this galaxy (Väisänen et al., 2008; Haan et al., 2011). The study by Rich et al. (2014) indicates this galaxy has no emission spectra and is made up of an old stellar population.

The ionised gas velocities cover both the northern nuclei and most of the less bright southern nuclei. The rotation curve is along the same axis as the two nuclei. The NaI D absorption is detected for a considerable amount of the galaxy, almost the same area containing ionised gas velocities. The neutral gas velocity is concentrated around the systemic velocity of the galaxy with peaks at $\pm 50\,\mathrm{km/s}$. The ionised and neutral gas velocities are not spatially correlated.

The W_{eq} values range from $2 - 18\,\text{Å}$ with the largest values along the axis of rotation between the two galaxies. The W_{eq} values are correlated with the calculated values of N(H), but show two distinct groupings at a higher N(H) and lower N(H) value than the first population. This results may be indicating that there are two different sources of NaI D absorption. The comparison to HST colour is inconclusive as there appears to be no correlation. The study of IRAS F18293-3413 south suggests a possible outflow along with a large NaI D component due to tidal interactions.

IRAS F18341-5732

IRAS F18341-5732 is an isolated galaxy not undergoing any interactions. Rich et al. (2015) identified large clumps of star formation at the ends of the bar of the galaxy. Dopita et al. (2002) identified knots of further star formation along the spiral arms. The ionised gas velocity maps highlight the undisturbed ionised gas rotation of the galaxy. The neutral gas shows a similar rotation about the centre of the galaxy.

The W_{eq} values range from $0 - 8\,\text{Å}$ and are concentrated along the bar of the galaxy. The N(H) does correlate with W_{eq} but also shows a scatter of $\sim 3\,\mathrm{dex}$. There is no evidence of an outflow in this galaxy.

IRAS F19115-2124

IRAS F19115-2124 is a close merger with a very complex morphological structure (Väisänen et al., 2008) as is evident in Figure C.29. The ionised gas velocities show an interesting pattern of gas (Figure C.30, top panels). The north-south galaxy is highlighted by a rotation curve in the north-south direction. The second galaxy in the merger is highlighted by blue-shifted velocities in the west. The NaI D absorption is observed in only a fraction of the total galaxy system and is concentrated towards the core of the north-south galaxy.

The ionised gas velocities span a large range but they do not correlate with the neutral gas velocities which are predominately blue-shifted (Figure C.31). The blue-shifted neutral gas could be an indication of an outflow, however the S/N cut has removed many spaxels from the analysis of the total W_{eq} (Figure C.32), comparisons with HST colour and N(H) (Figure C.33).

IRAS F20551-4250

IRAS F20551-4250 is a late stage merger. The HST image is presented in Figure C.34, top panels. IRAS F20551-4250 is dominated by star formation towards the core with shock excitation towards the outer parts, consistent with previous studies (Veilleux et al., 1995a; Kewley et al., 2001a). Previous studies into a possible AGN are inconclusive as Ptak et al. (2003); Grimes et al. (2005); Iwasawa et al. (2009, 2011) did not find evidence of an AGN but an XMM study by Franceschini et al. (2003) did. There is also evidence in the IR for a heavily obscured AGN (Imanishi et al., 2010; Sani et al., 2008; Nardini et al., 2008) and mid-IR (Petric et al., 2011; Stierwalt et al., 2012). There was no evidence for an AGN (Chapter 3) in either X-ray or the optical.

The ionised gas velocity structure (Figure C.35 top panels) indicates an interesting structure of systemic velocities and a third ionised component heavily blue shifted and there is a similarly blue-shifted component in the neutral gas velocities (Figure C.35 bottom panels). There is some correlation between the components in the ionised and neutral gases (Figure C.36) but it is not a strong correlation.

The W_{eq} ranges from $0.4 - 3$ Å (Figure C.37) with no strong correlation to N(H) (Figure C.38).This galaxy contains shocks, however, due to the uncertainty in the core of this galaxy it has not been possible to identify the cause of the shocks. As a late stage merger it is expected that there are shocks due to the merge itself. Understanding the origin of the shocks in the ionised gas and the NaI D absorption requires a determination of whether

this galaxy does host an AGN or is a star-forming core.

IRAS F21330-3846

IRAS F21330-3846 is a close interacting pair. Rich et al. (2015) found tidal tails in the DSS image and line ratios consistent with shocks outside the nucleus. The ionised gas velocity structure displays a complicated arrangement of the interacting pair of galaxies. The neutral gas velocities are mostly correlated with the ionised gas velocities indicating they may be tracing the same physical process of tidal interactions.

The W_{eq} spans a range of $1 - 4$ Å, concentrating on both nuclei. The N(H) ranges from $20 - 22$ dex and does not show a strong correlation with W_{eq}. There is no evidence of an outflow in this isolated galaxy.

IRAS F21453-3511

IRAS F21353-3511 is an isolated spiral galaxy host to a Seyfert 2 AGN (Rich et al., 2015; Iwasawa et al., 2011; Petric et al., 2011). The outskirts of the galaxy are star-forming (Rich et al., 2015; Monreal-Ibero et al., 2010). The ionised gas velocities presented in Figure C.39 (top panels) highlight the face-on nature of this galaxy. The third ionised component is heavily blue-shifted and forms a ring about the Sy2 nucleus.

The neutral gas velocities also highlight blue-shifted material in the galaxy, not completely concentrated around the nucleus. A comparison of the two gas states velocities indicates no correlation between the two (Figure C.40). The W_{eq} values range from $0 - 8$ Å and follows the spiral arms of the galaxy (Figure C.41). There is a strong correlation of W_{eq} with N(H) for a part of the galaxy and much scatter at higher values of N(H) (Figure C.42). There is no evidence of an outflow in this galaxy ranging in velocity from $200 - 500$ km/s.

IRAS F22467-4960

IRAS F22467-4960 is a compact late stage merger with possible shocked emission (Rich et al., 2014) shown in Figure C.43. Although Rich et al. (2014) determined high emission line ratios consistent with a LINER, the X-ray study by Iwasawa et al. (2011) determined the X-ray emission is not consistent with an AGN. Rich et al. (2014) suspect shock-induced star formation as the overall power source of the emission line spectrum.

The study detected heavily blue-shifted NaI D absorption in IRAS F22467-4960. However, the spatial information obtained for this galaxy does not give a clear understanding of the impact of the blue-shifted emission. The ionised gas velocity components indicate a

small galaxy (with the spatial resolution avaliable) that has a rotation curve east-west (Figure C.44, top panels). The neutral gas velocities in the same region are rotating in the opposite direction to the ionised gas, with the heavily blue-shifted absorption as a second component of the fit (Figure C.44, bottom panels). A direct comparison of the two gas velocities are shown in Figure C.45.

The W_{eq} values range from $1 - 6$ Å and are highest towards the positions of the blue-shifted NaI D (Figure C.46). The two components of the absorption fitting are presented in velocity space in Figure C.46 (bottom left panel) as the components around -100 km/s and the components at -500 km/s. The highest W_{eq} values are associated with larger N(H) $20.4 - 21.8$ dex and there may be a trend with HST colour. Although there is a possible outflow in this galaxy the impact or cause is not determined from the spatial information. This requires a higher spatial resolution IFS observation to determine the physical processes causing the NaI D absorption that has been detected.

C.2 Diagnostic plots for individual NaI D galaxies

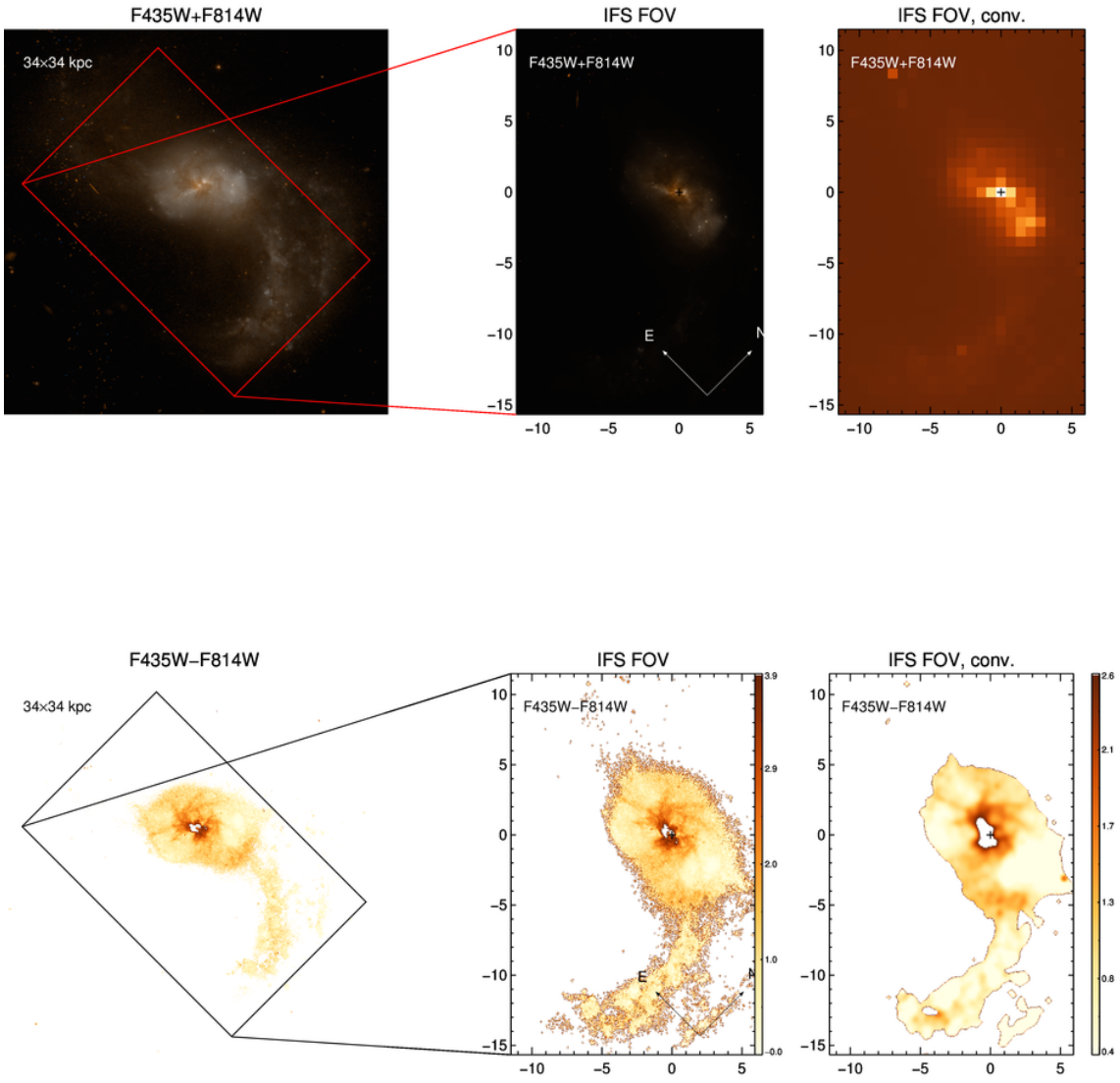

Figure C.1: IRAS F10038-3338 diagnostic plots. HST colour image of IRAS F10038-3338. Top right presents the HST image (F435W+F814W) with the FoV outlined in red. Top middle present the FoV of our WiFeS observations. Top right is the HST image convolved to the same pixel scale as the WiFeS instrument (1″/pix). Presented here are the HST images used to calculate the dust content in IRAS F10038-3338 through the calculation of F435W-F814W in the bottom panels. Bottom left presents the FoV of the WiFeS instrument overlaid on the HST image and bottom middle presents the cut out of the FoV orientated to the WiFeS observation. Bottom right presents the F435W-F814W image convolved to the same spatial scale as the WiFeS observation.

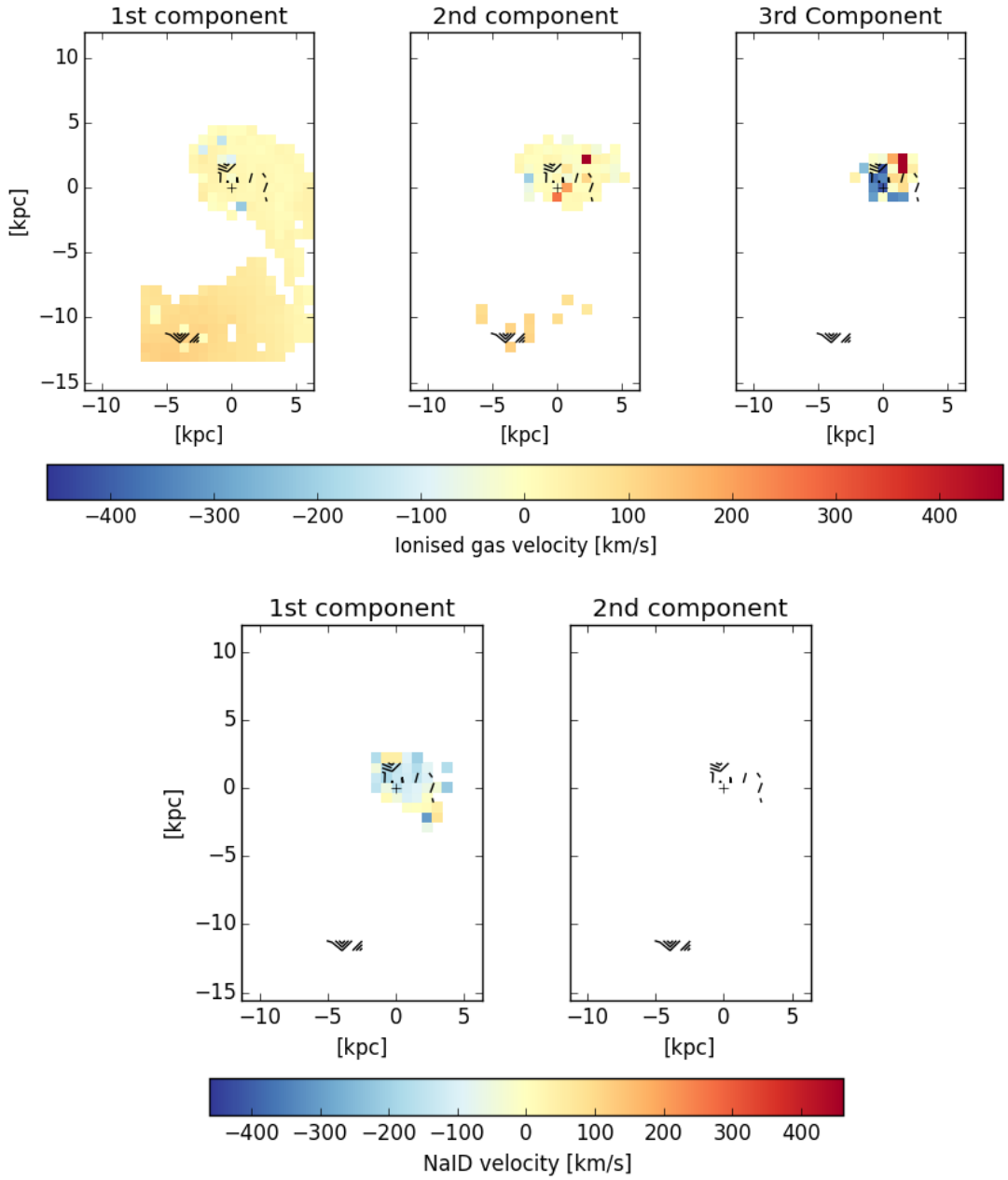

Figure C.2: IIRAS F10038-3338 diagnostic plots continued. Top panels - The ionised gas velocity maps of IRAS F10038-3338 defined from emission line fitting are presented in the top panels. There are up to three Gaussian components needed to explain the emission lines observed in this galaxy. Bottom panels - The neutral gas velocity maps of IRAS F10038-3338 defined through fitting NaI D absorption features with multiple components are presented in the bottom panels. The contours represent Gaussian smoothed ionised velocity where dashed contours represent negative velocities and solid contours represent positive velocities (inclusive of zero).

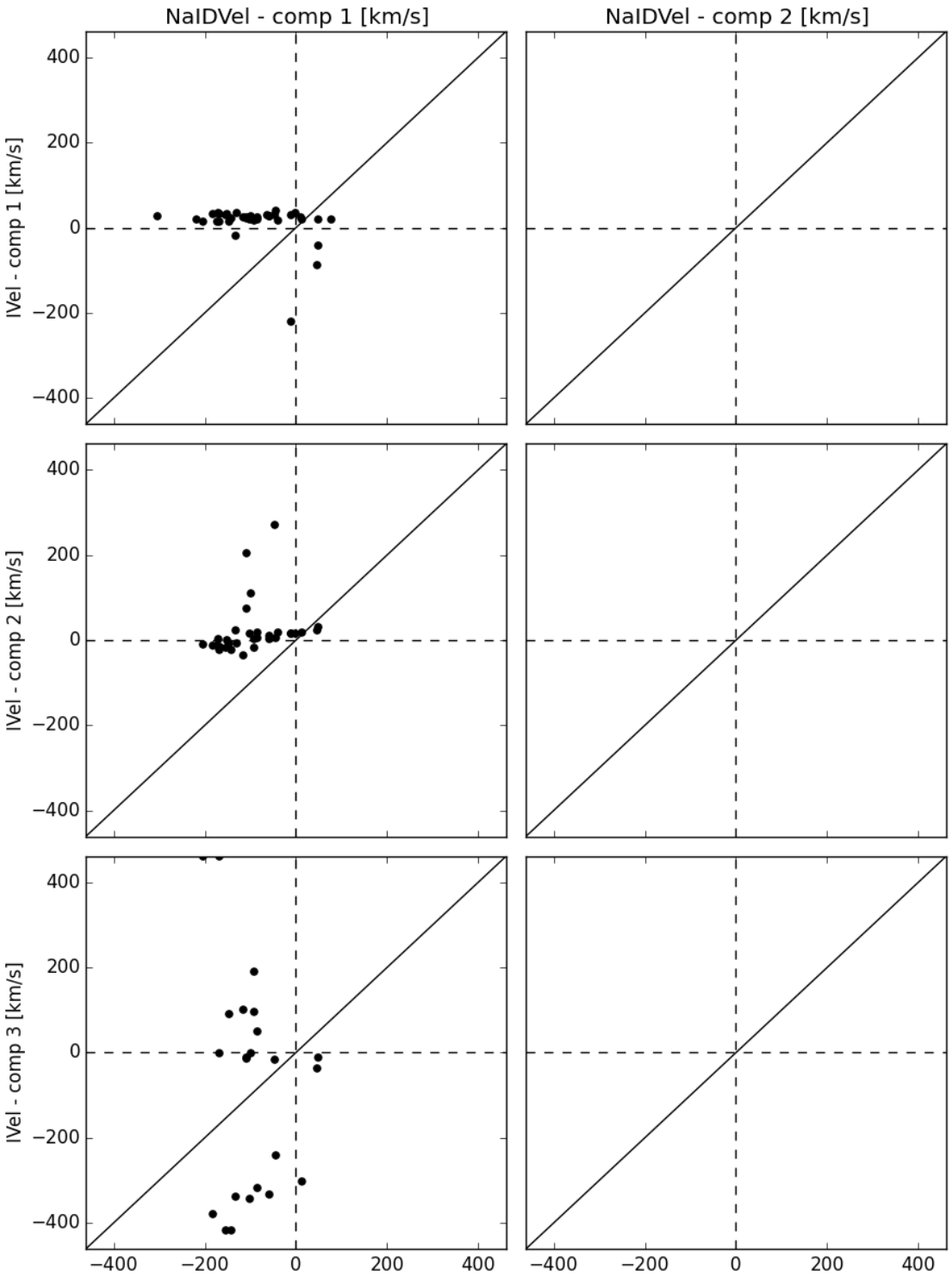

Figure C.3: IRAS F10038-3338 diagnostic plots continued. These panels show the comparison of the ionised (y-axis) and neutral (x-axis) gas velocities as defined through emission line analysis and the fitting of the NaI D absorption lines, respectively.

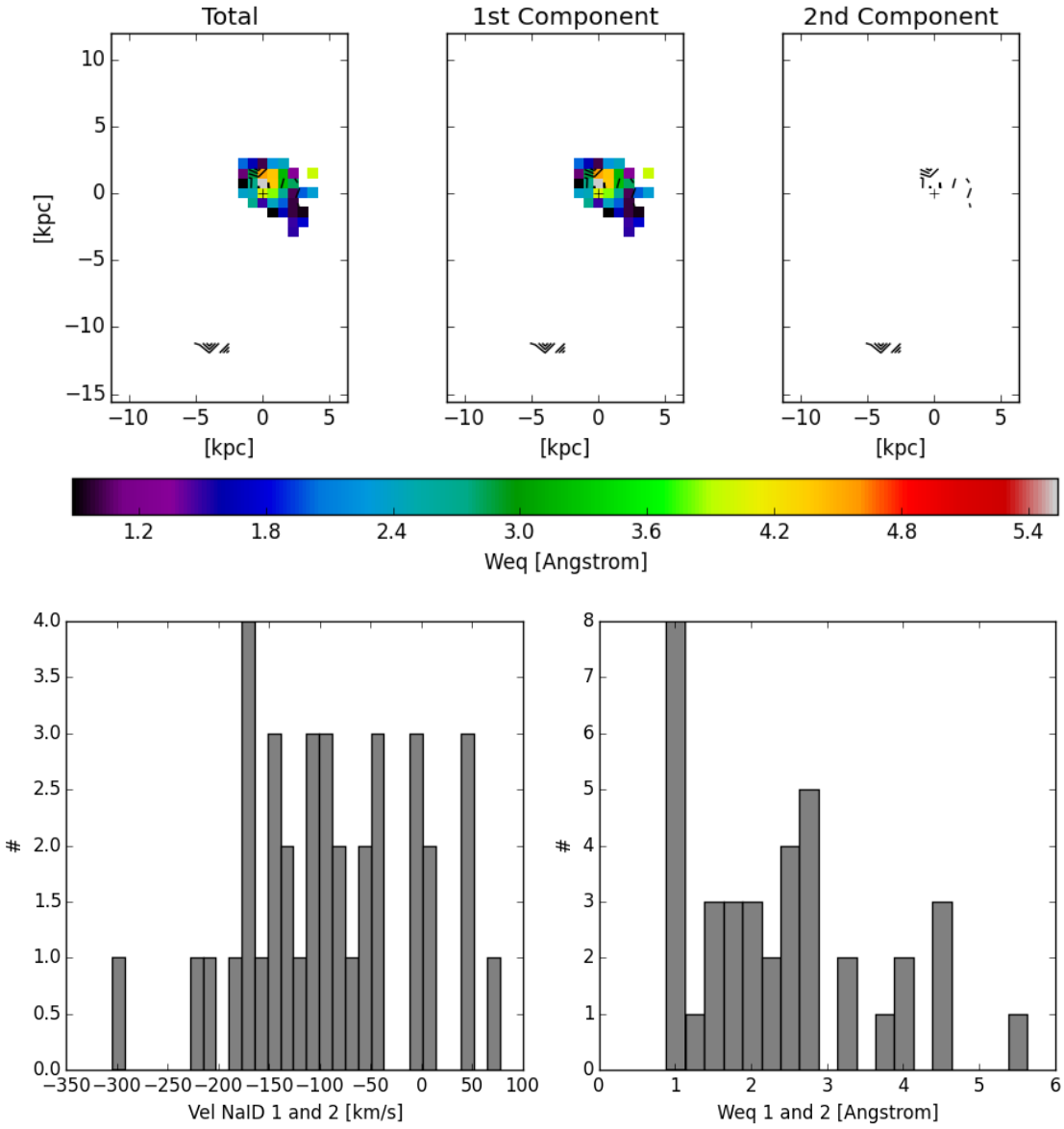

Figure C.4: IRAS F10038-3338 diagnostic plots continued. Top panels - Equivalent width, W_{eq}, values from fitting multiple components to NaI D absorption features. Left presents the total W_{eq} calculated at each spaxel, centre presents the W_{eq} of the first component and right presents the W_{eq} of the second component. The contours represent Gaussian smoothed ionised velocity where dashed contours represent negative velocities and solid contours represent positive velocities (inclusive of zero). Bottom panels - Left presents a histogram of the NaI D velocities in km/s. Right panels presents the histogram of the W_{eq} for each component.

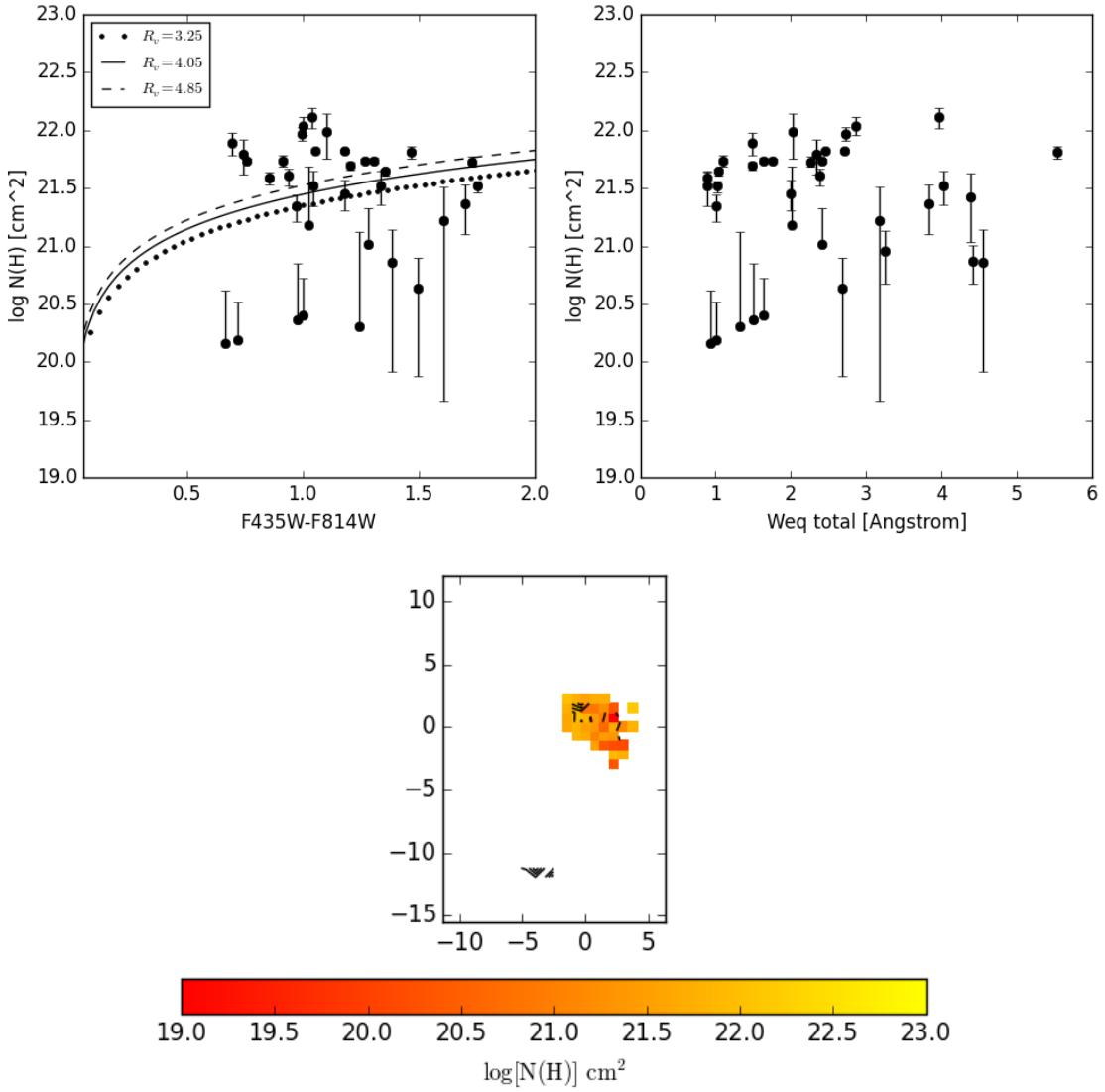

Figure C.5: IRAS F10038-3338 diagnostic plots continued. Top panels - Comparisons of Hydrogen column density to HST colour (left) and total W_{eq} of IRAS F10038-3338 (right). Bottom panel - map of the calculated N(H).

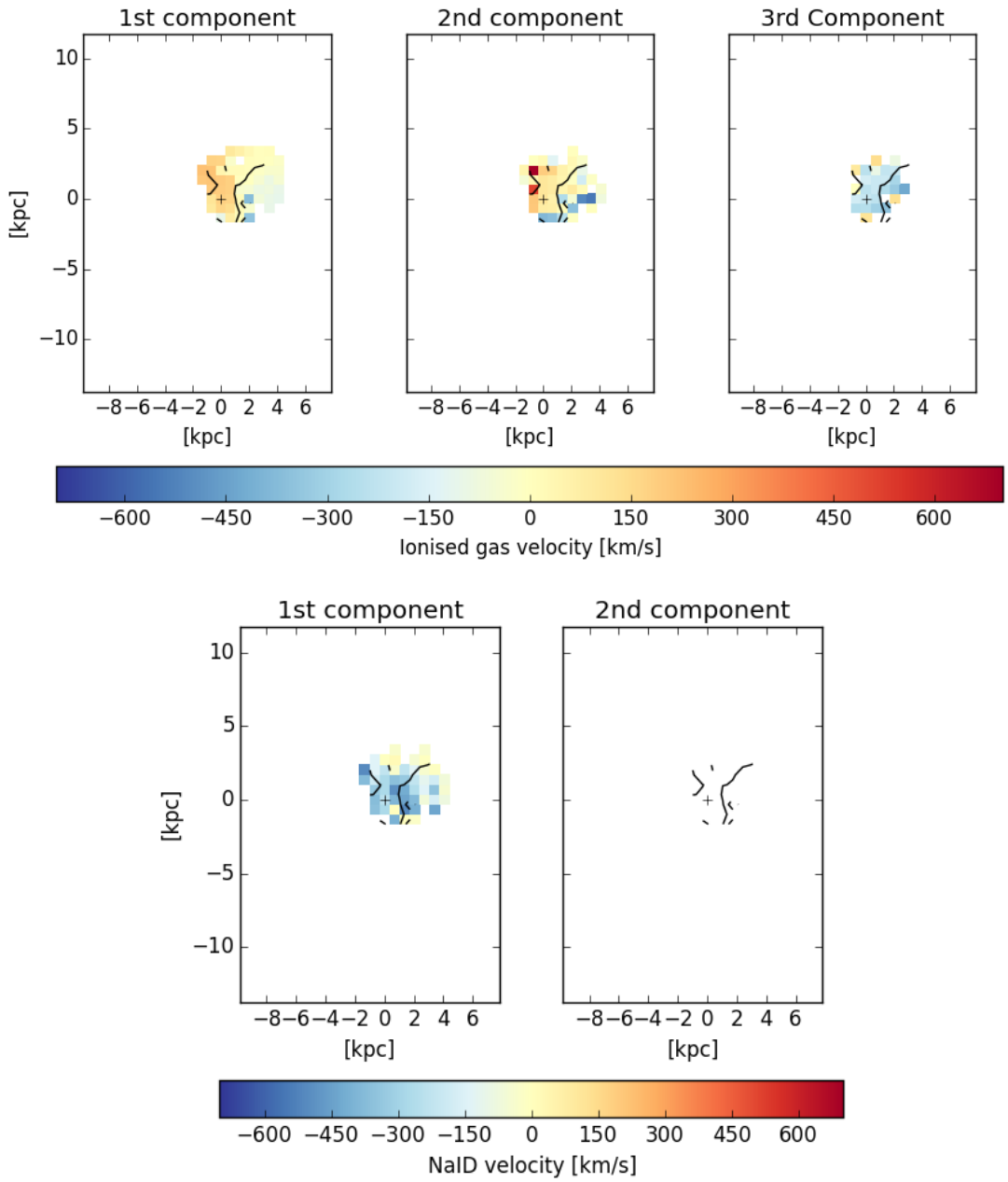

Figure C.6: IRAS F13120-5453 diagnostic plots. Top panels - The ionised gas velocity maps of IRAS F13120-5453 defined from emission line fitting are presented in the top panels. There are up to three Gaussian components needed to explain the emission lines observed in this galaxy. Bottom panels - The neutral gas velocity maps of IRAS F13120-5453 defined through fitting NaI D absorption features with multiple components are presented in the bottom panels. The contours represent Gaussian smoothed ionised velocity where dashed contours represent negative velocities and solid contours represent positive velocities (inclusive of zero).

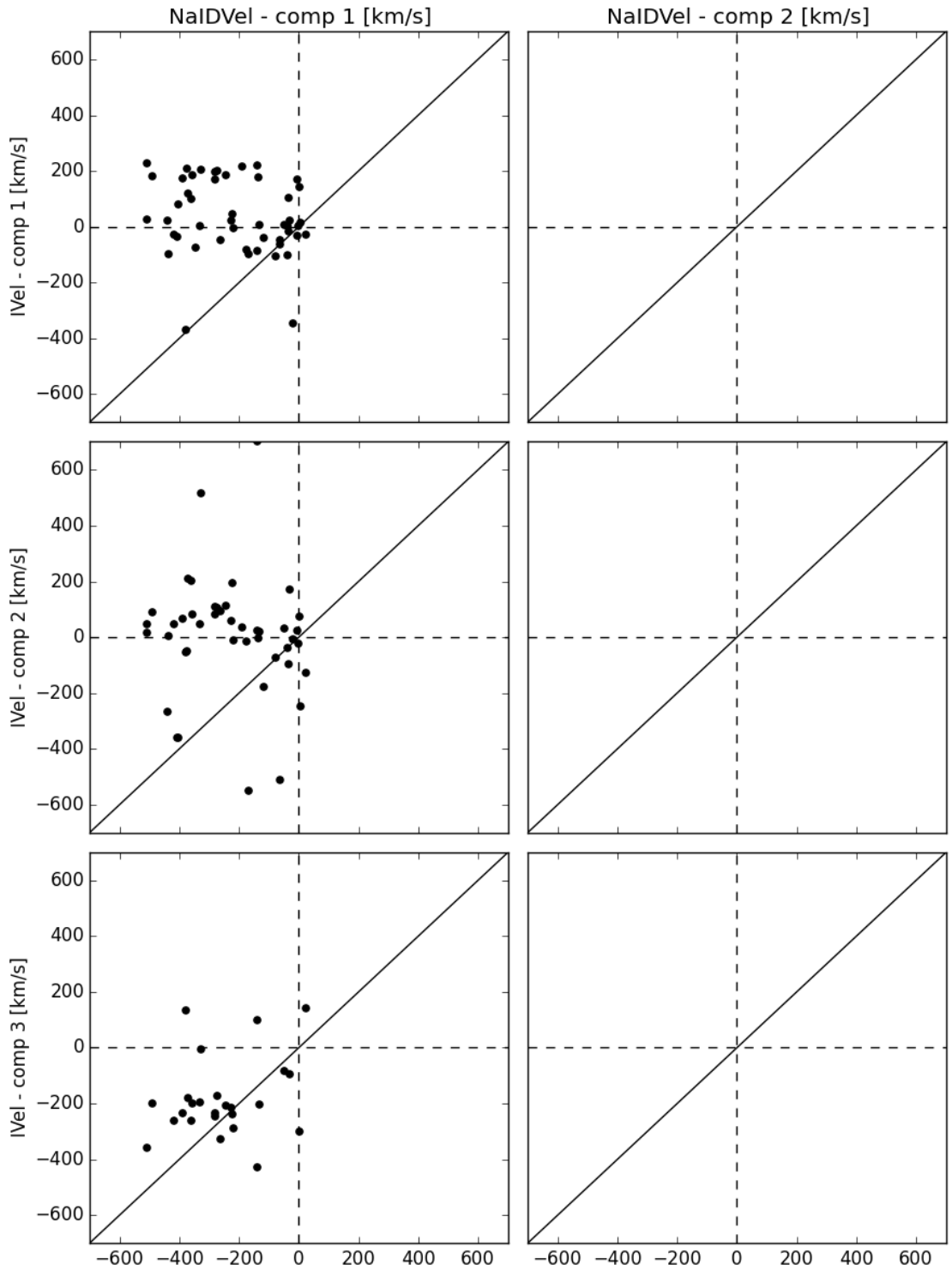

Figure C.7: IRAS F13120-5453 diagnostic plots continued. These panels show the comparison of the ionised (y-axis) and neutral (x-axis) gas velocities as defined through emission line analysis and the fitting of the NaI D absorption lines, respectively.

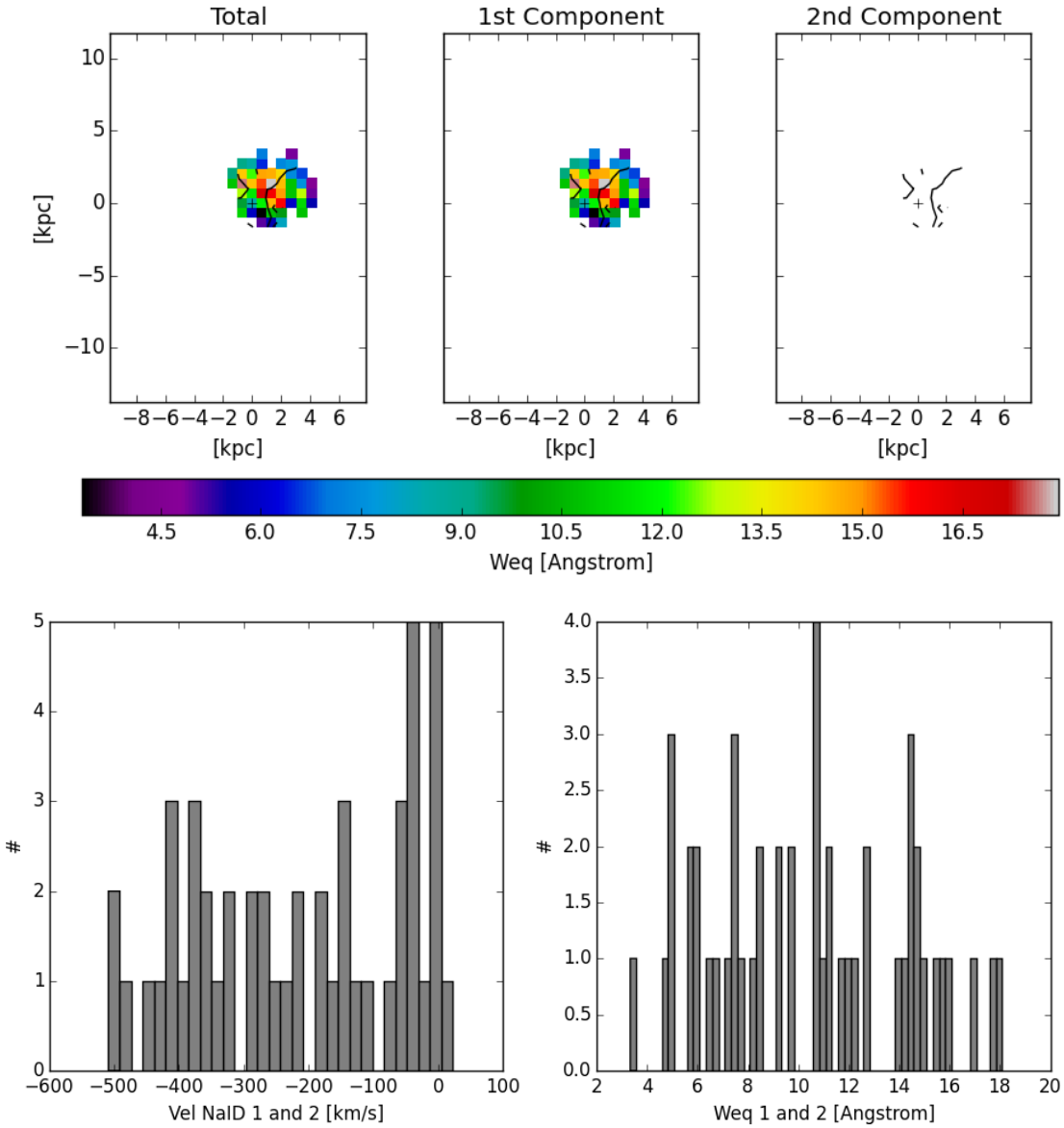

Figure C.8: IRAS F13120-5453 diagnostic plots continued. Top panels - Equivalent width, W_{eq}, values from fitting multiple components to NaI D absorption features. Left presents the total W_{eq} calculated at each spaxel, centre presents the W_{eq} of the first component and right presents the W_{eq} of the second component. The contours represent Gaussian smoothed ionised velocity where dashed contours represent negative velocities and solid contours represent positive velocities (inclusive of zero). Bottom panels - Left presents a histogram of the NaI D velocities in km/s. Right panels presents the histogram of the W_{eq} for each component.

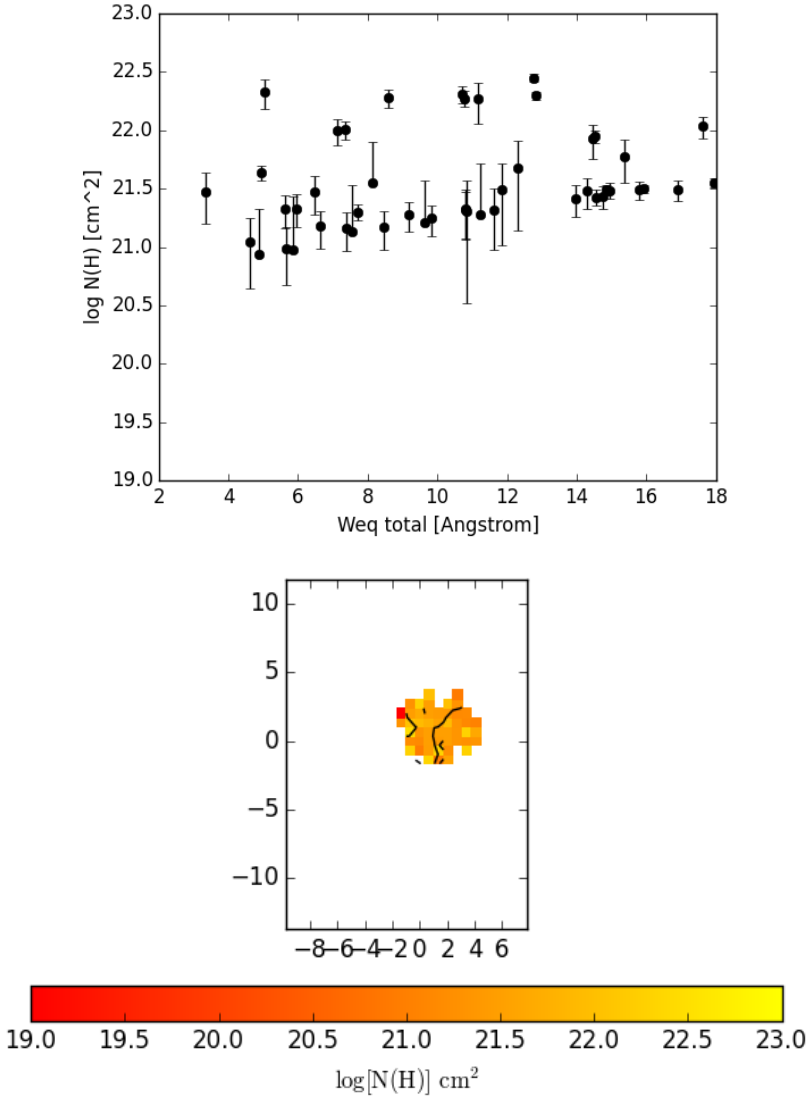

Figure C.9: IRAS F13120-5453 diagnostic plots continued. Top panel - Comparisons of Hydrogen column density to total W_{eq} of IRAS F13120-5453. Bottom panel - map of the calculated N(H).

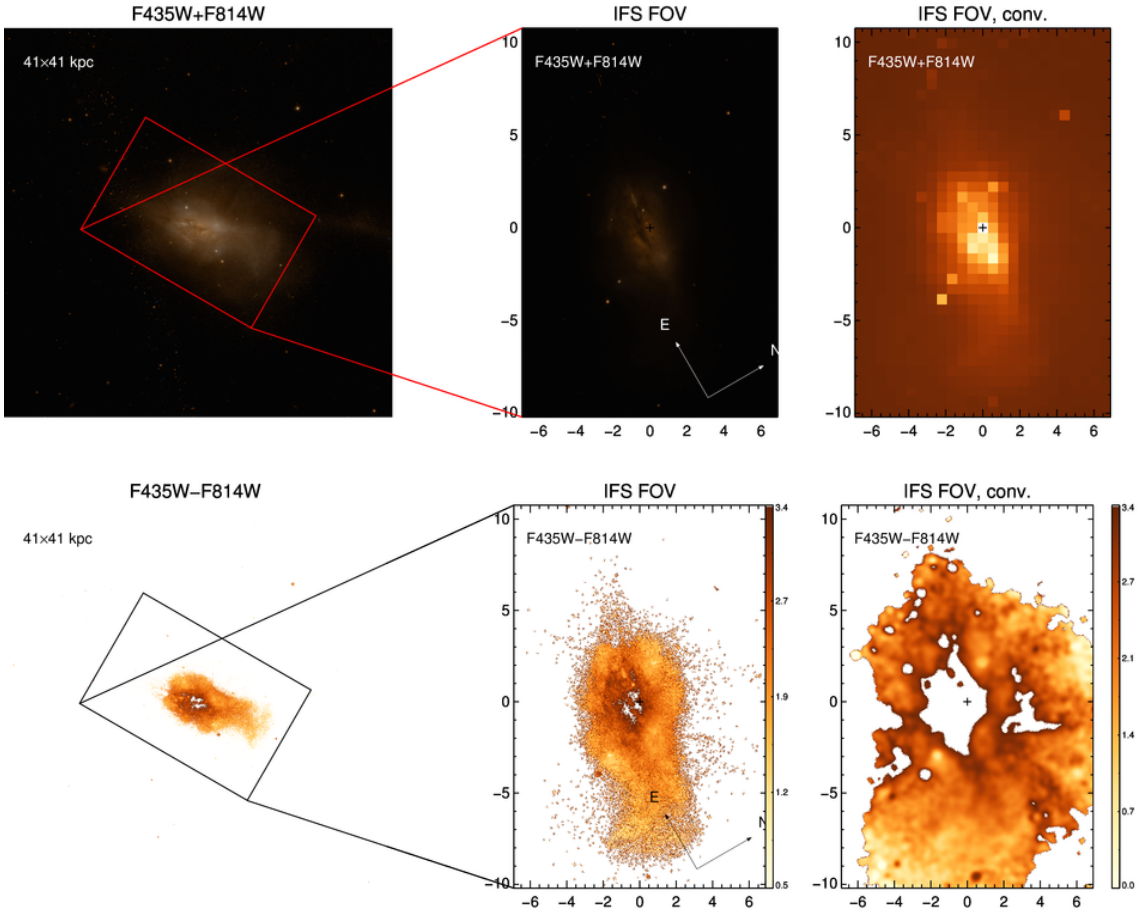

Figure C.10: IRAS F16164-0746 diagnostic plots. HST colour image of IRAS F16164-0746. Top right presents the HST image (F435W+F814W) with the FoV outlined in red. Top middle present the FoV of our WiFeS observations. Top right is the HST image convolved to the same pixel scale as the WiFeS instrument (1″/pix). Presented here are the HST images used to calculate the dust content in IRAS F16164-0746 through the calculation of F435W-F814W in the bottom panels. Bottom left presents the FoV of the WiFeS instrument overlaid on the HST image and bottom middle presents the cut out of the FoV orientated to the WiFeS observation. Bottom right presents the F435W-F814W image convolved to the same spatial scale as the WiFeS observation.

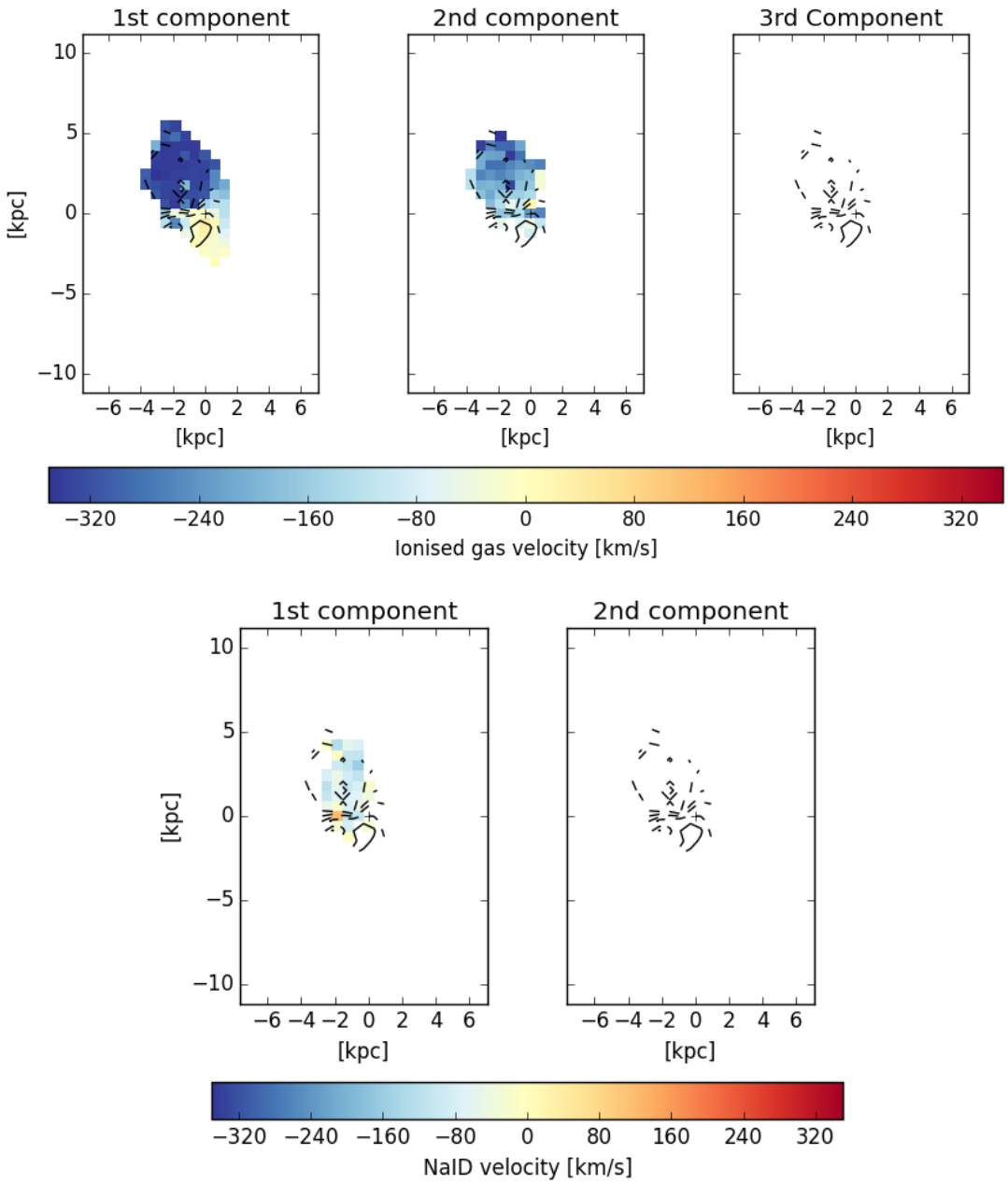

Figure C.11: IRAS F16164-0746 diagnostic plots continued. Top panels - The ionised gas velocity maps of IRAS F16164-0746 defined from emission line fitting are presented in the top panels. There are up to three Gaussian components needed to explain the emission lines observed in this galaxy. Bottom panels - The neutral gas velocity maps of IRAS F01053-1746 defined through fitting NaI D absorption features with multiple components are presented in the bottom panels. The contours represent Gaussian smoothed ionised velocity where dashed contours represent negative velocities and solid contours represent positive velocities (inclusive of zero).

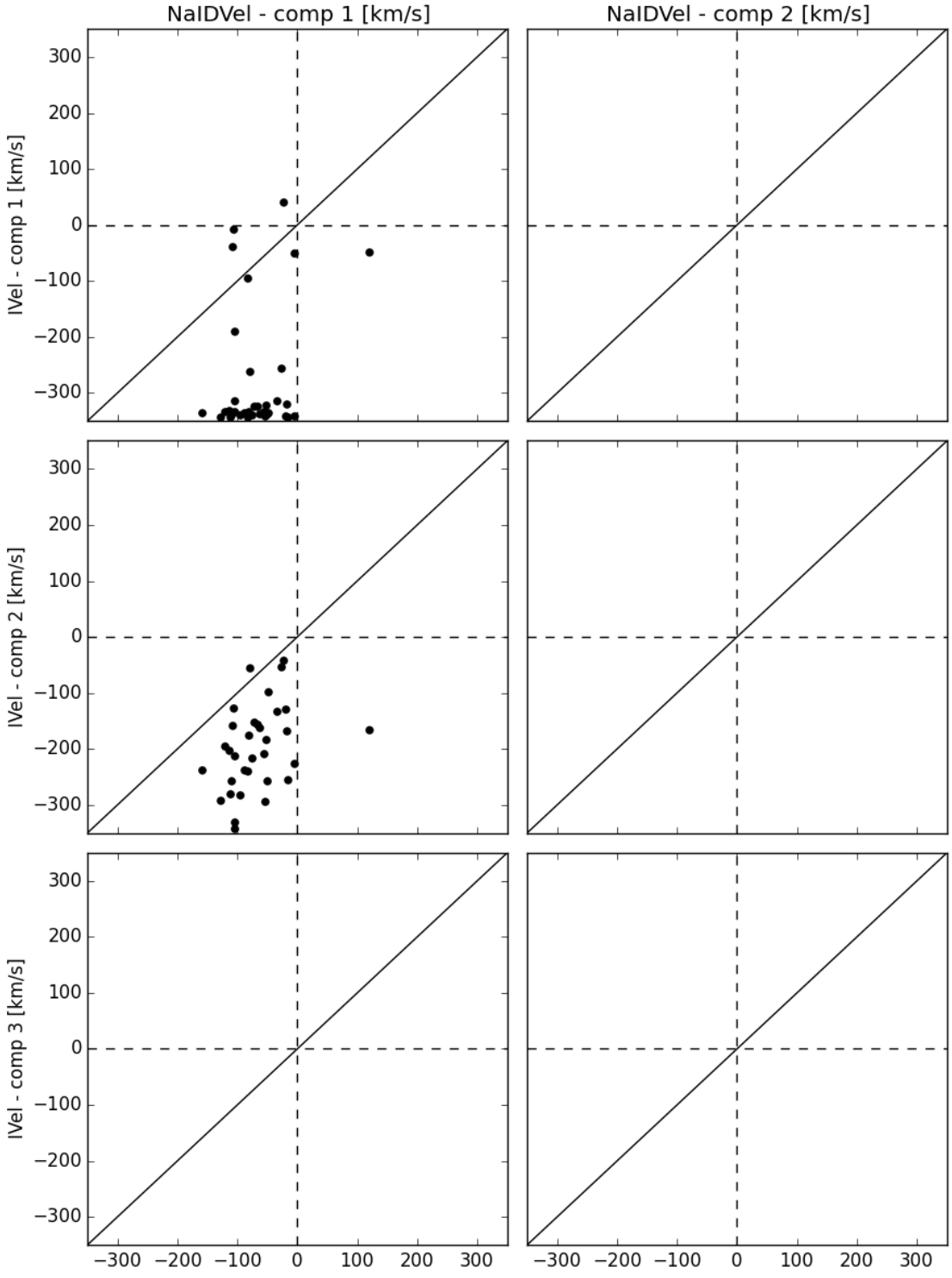

Figure C.12: IRAS F16164-0746 diagnostic plots continued. These panels show the comparison of the ionised (y-axis) and neutral (x-axis) gas velocities as defined through emission line analysis and the fitting of the NaI D absorption lines, respectively.

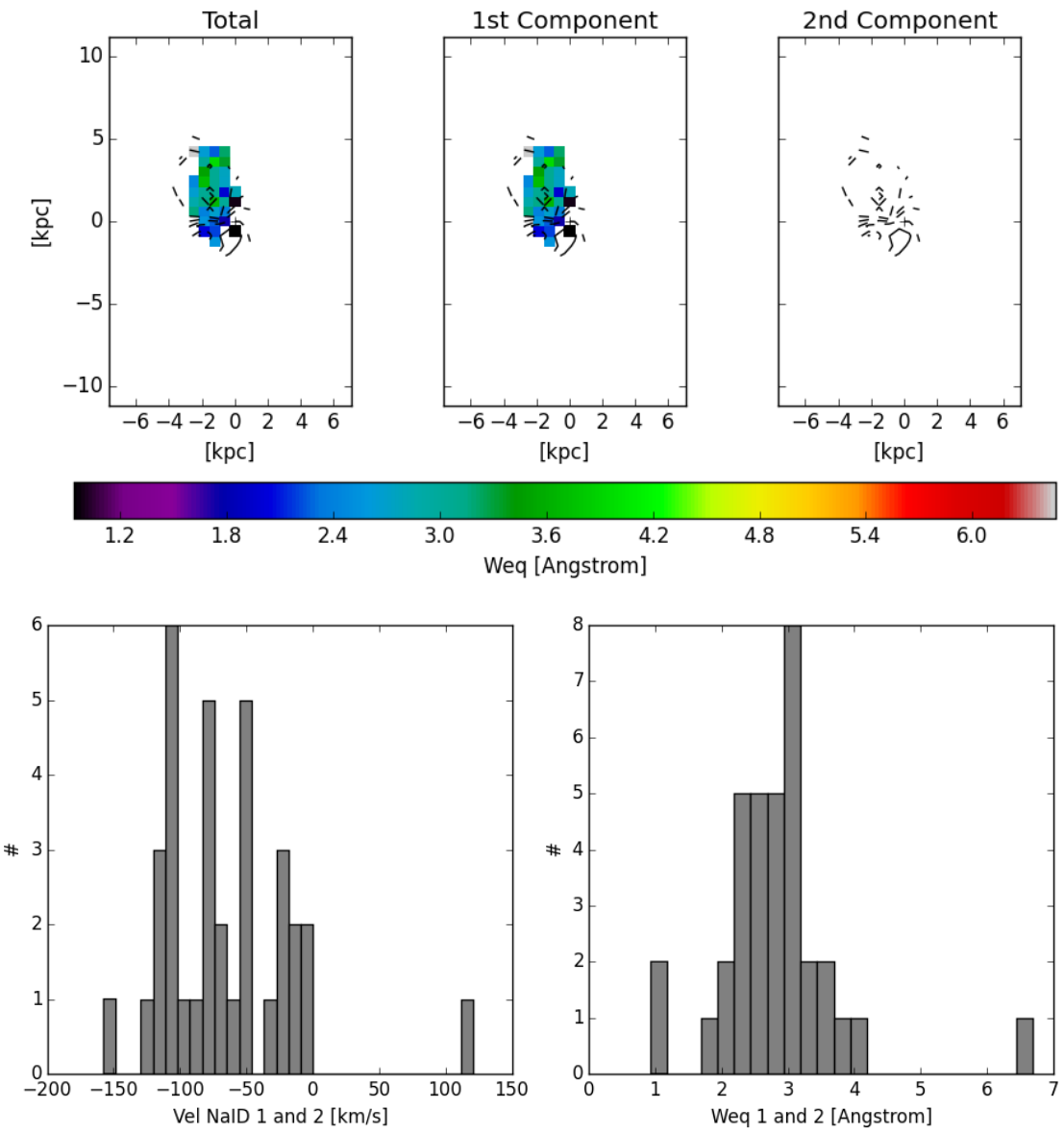

Figure C.13: IRAS F16164-0746 diagnostic plots continued. Top panels - Equivalent width, W_{eq}, values from fitting multiple components to NaI D absorption features. Left presents the total W_{eq} calculated at each spaxel, centre presents the W_{eq} of the first component and right presents the W_{eq} of the second component. The contours represent Gaussian smoothed ionised velocity where dashed contours represent negative velocities and solid contours represent positive velocities (inclusive of zero). Bottom panels - Left presents a histogram of the NaI D velocities in km/s. Right panels presents the histogram of the W_{eq} for each component.

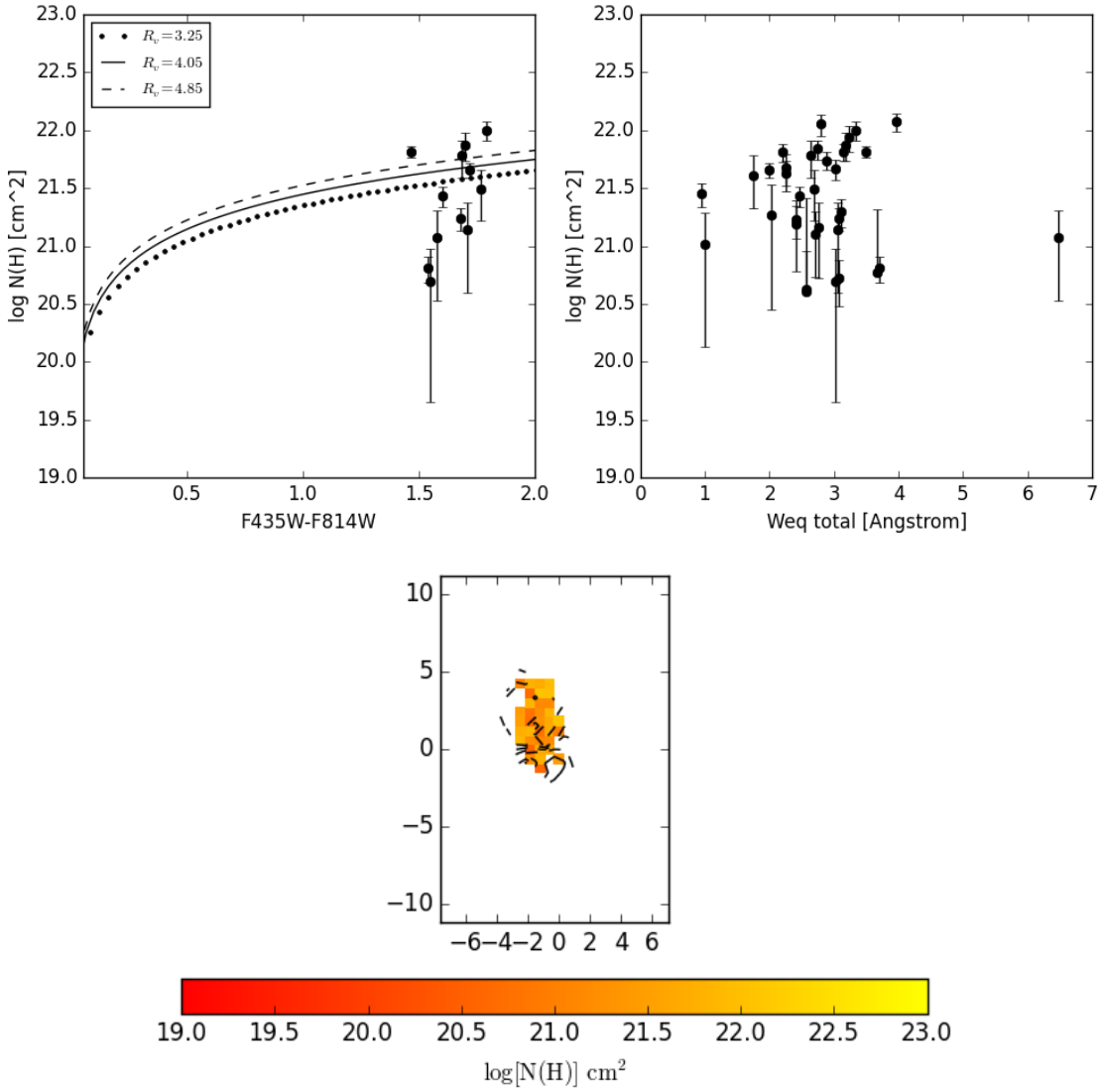

Figure C.14: IRAS F16164-0746 diagnostic plots continued. Top panels - Comparisons of Hydrogen column density to HST colour (left) and total W_{eq} of IRAS F16164-0746 (right). Bottom panel - map of the calculated N(H).

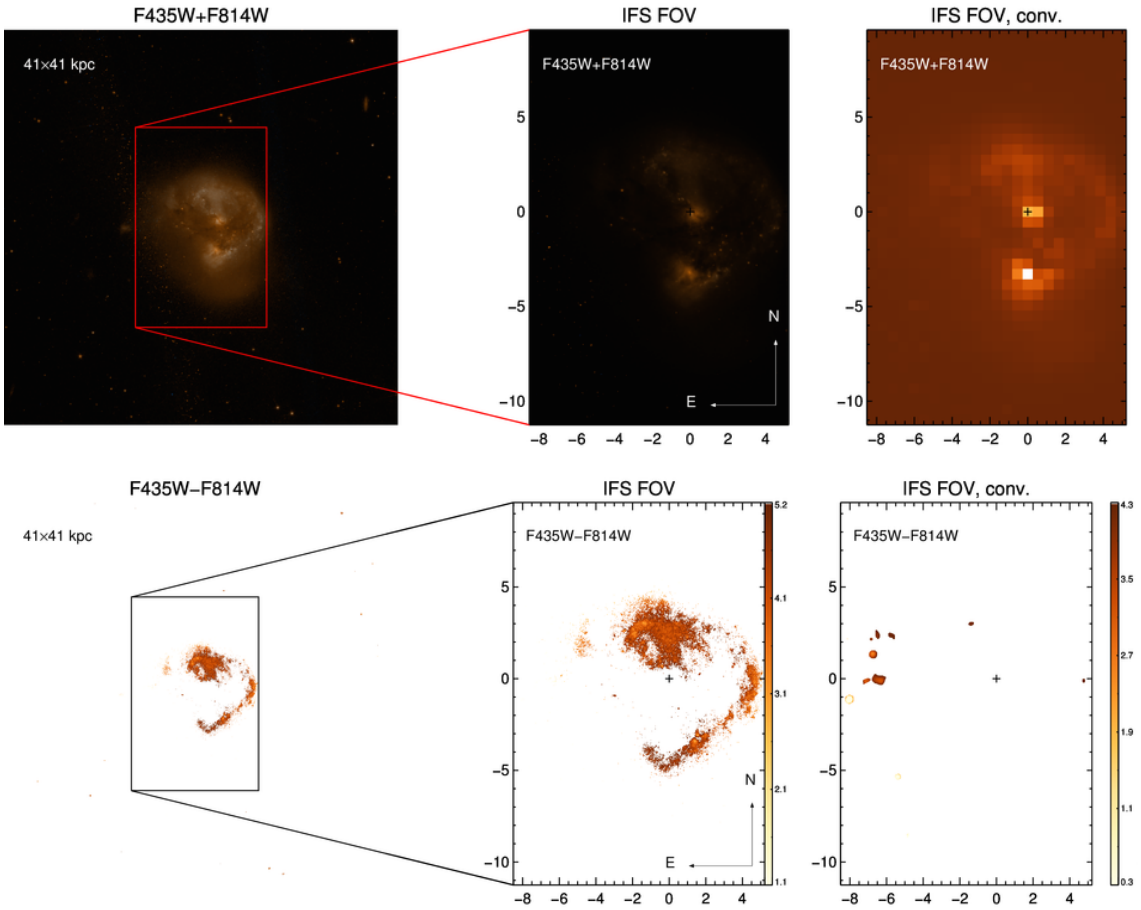

Figure C.15: IRAS F16399-0937 diagnostic plots. HST colour image of IRAS F16399-0937. Top right presents the HST image (F435W+F814W) with the FoV outlined in red. Top middle present the FoV of our WiFeS observations. Top right is the HST image convolved to the same pixel scale as the WiFeS instrument (1″/pix). Presented here are the HST images used to calculate the dust content in IRAS F16399-0937 through the calculation of F435W-F814W in the bottom panels. Bottom left presents the FoV of the WiFeS instrument overlaid on the HST image and bottom middle presents the cut out of the FoV orientated to the WiFeS observation. Bottom right presents the F435W-F814W image convolved to the same spatial scale as the WiFeS observation.

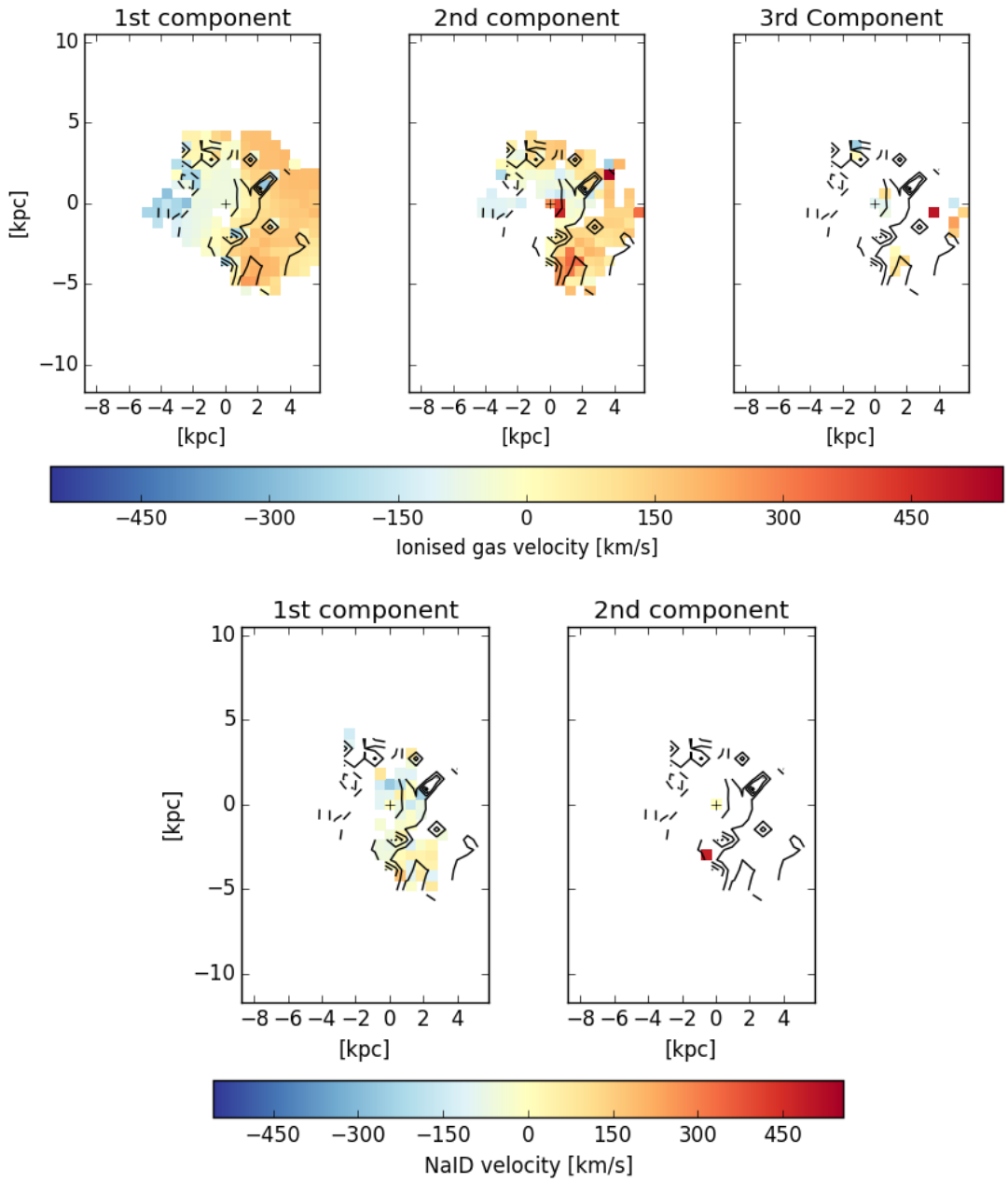

Figure C.16: IRAS F16399-0937 diagnostic plots continued. Top panels - The ionised gas velocity maps of IRAS F16399-0937 defined from emission line fitting are presented in the top panels. There are up to three Gaussian components needed to explain the emission lines observed in this galaxy. Bottom panels - The neutral gas velocity maps of IRAS F16399-0937defined through fitting NaI D absorption features with multiple components are presented in the bottom panels. The contours represent Gaussian smoothed ionised velocity where dashed contours represent negative velocities and solid contours represent positive velocities (inclusive of zero).

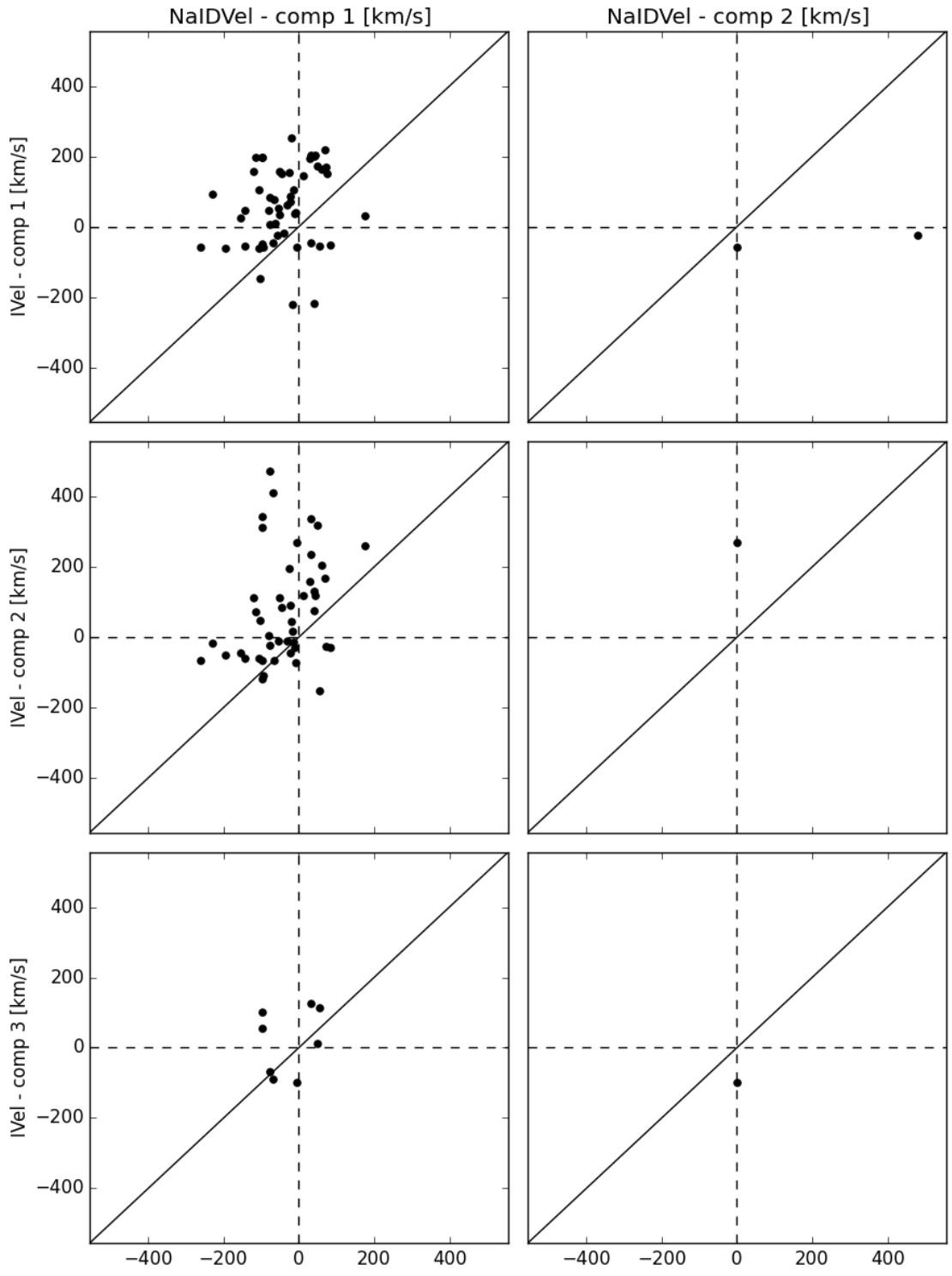

Figure C.17: IRAS F16399-0937 diagnostic plots continued. These panels show the comparison of the ionised (y-axis) and neutral (x-axis) gas velocities as defined through emission line analysis and the fitting of the NaI D absorption lines, respectively.

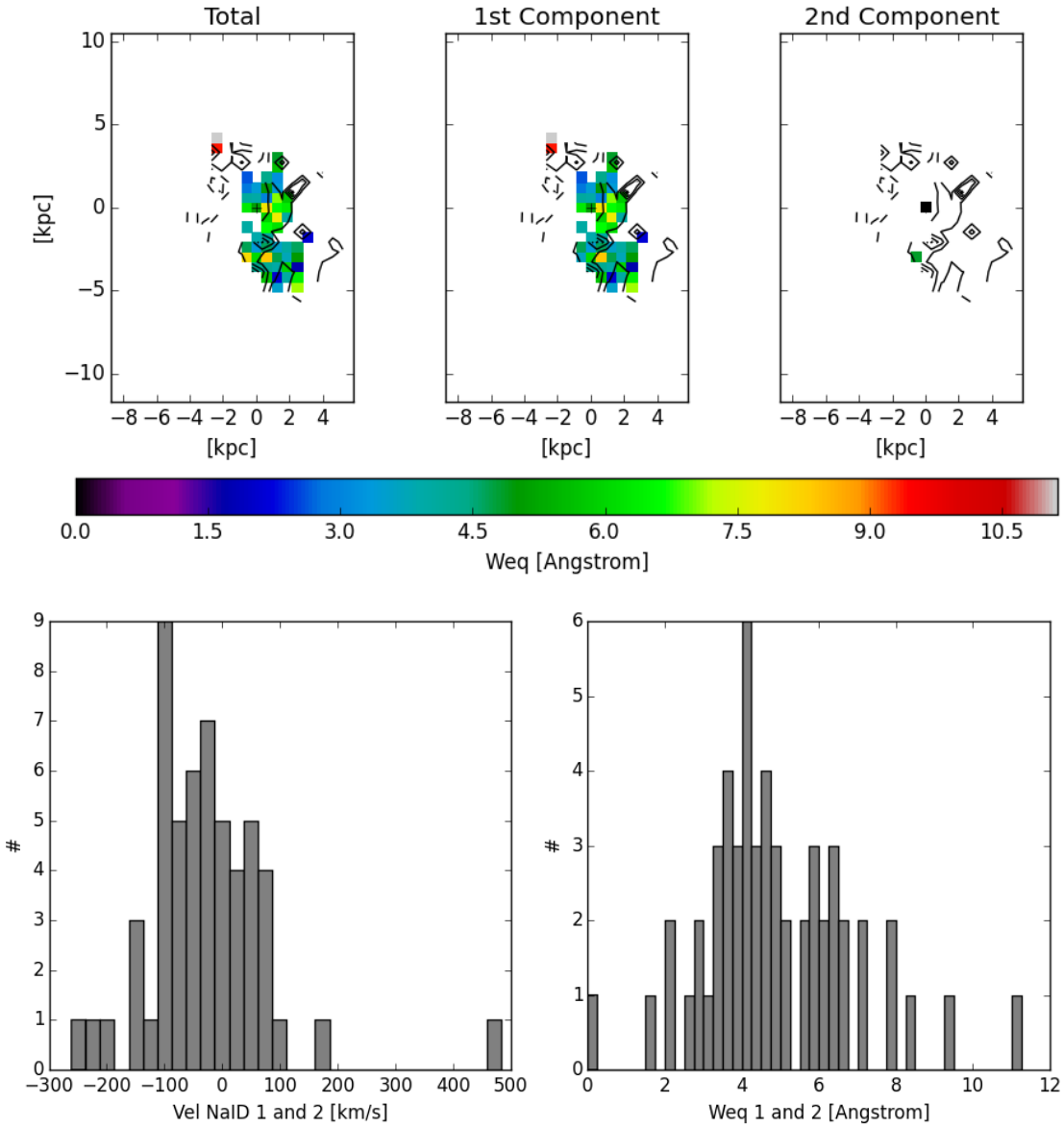

Figure C.18: IRAS F16399-0937 diagnostic plots continued. Top panels - Equivalent width, W_{eq}, values from fitting multiple components to NaI D absorption features. Left presents the total W_{eq} calculated at each spaxel, centre presents the W_{eq} of the first component and right presents the W_{eq} of the second component. The contours represent Gaussian smoothed ionised velocity where dashed contours represent negative velocities and solid contours represent positive velocities (inclusive of zero). Bottom panels - Left presents a histogram of the NaI D velocities in km/s. Right panels presents the histogram of the W_{eq} for each component.

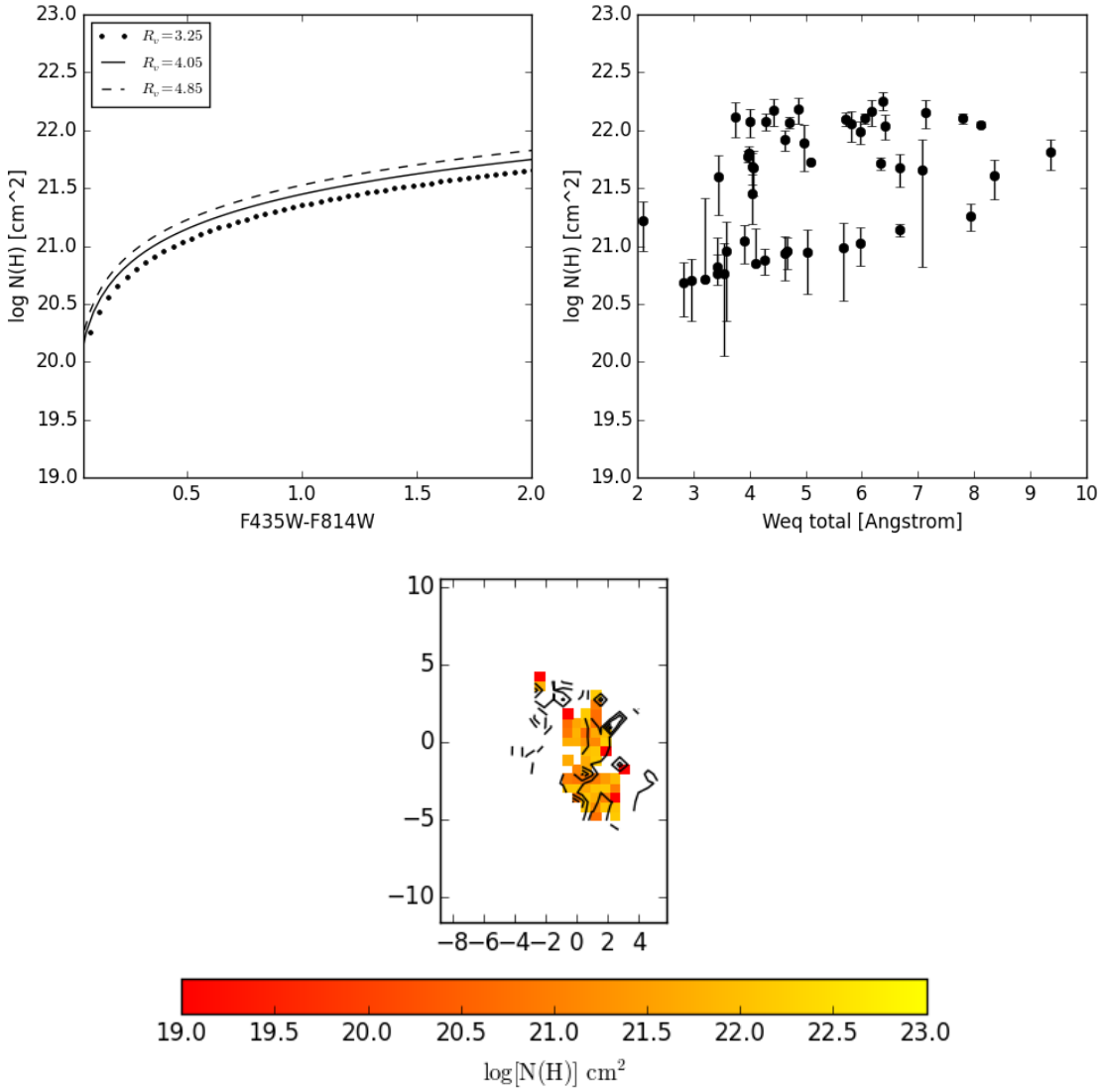

Figure C.19: IRAS F16399-0937 diagnostic plots continued. Top panels - Comparisons of Hydrogen column density to HST colour (left) and total W_{eq} of IRAS F16399-0937 (right). Bottom panel - map of the calculated N(H).

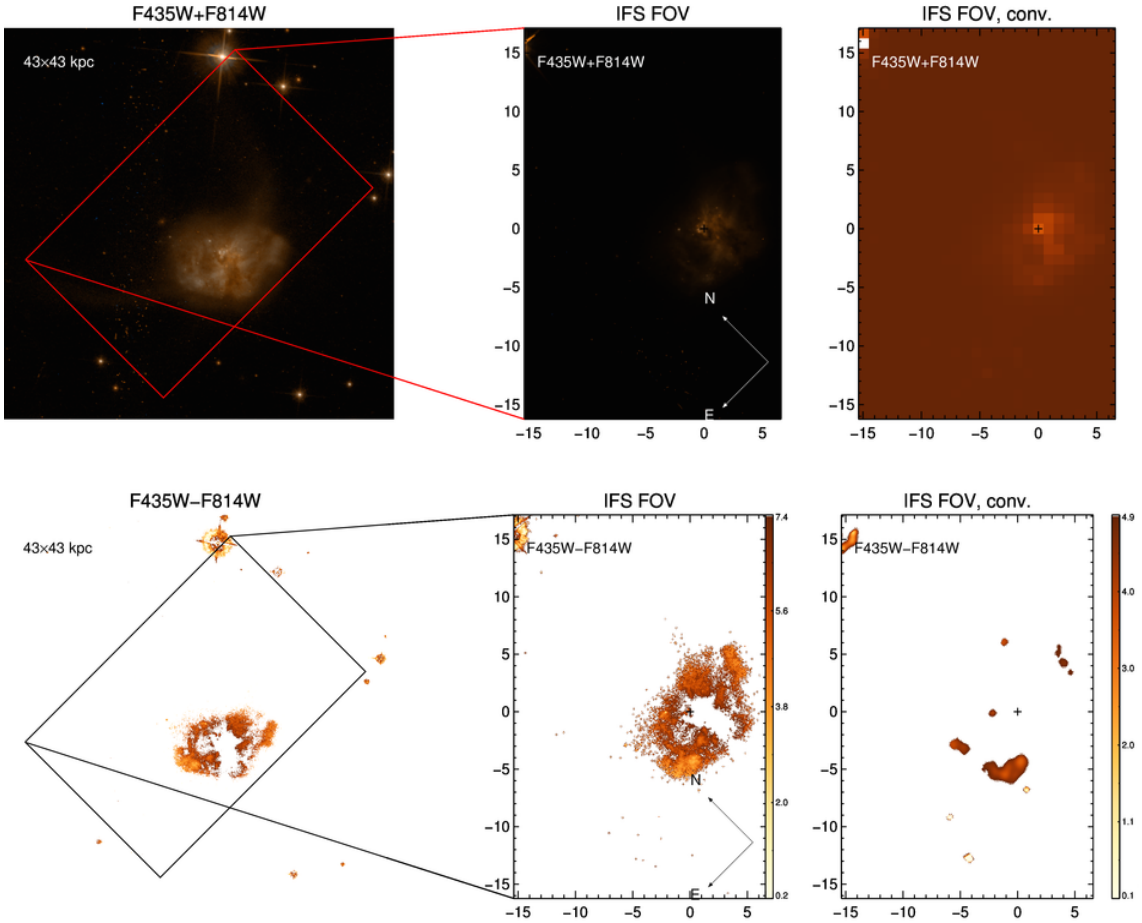

Figure C.20: IRAS F17207-0014 diagnostic plots. HST colour image of IRAS F17207-0014. Top right presents the HST image (F435W+F814W) with the FoV outlined in red. Top middle present the FoV of our WiFeS observations. Top right is the HST image convolved to the same pixel scale as the WiFeS instrument (1″/pix). Presented here are the HST images used to calculate the dust content in IRAS F17207-0014 through the calculation of F435W-F814W in the bottom panels. Bottom left presents the FoV of the WiFeS instrument overlaid on the HST image and bottom middle presents the cut out of the FoV orientated to the WiFeS observation. Bottom right presents the F435W-F814W image convolved to the same spatial scale as the WiFeS observation.

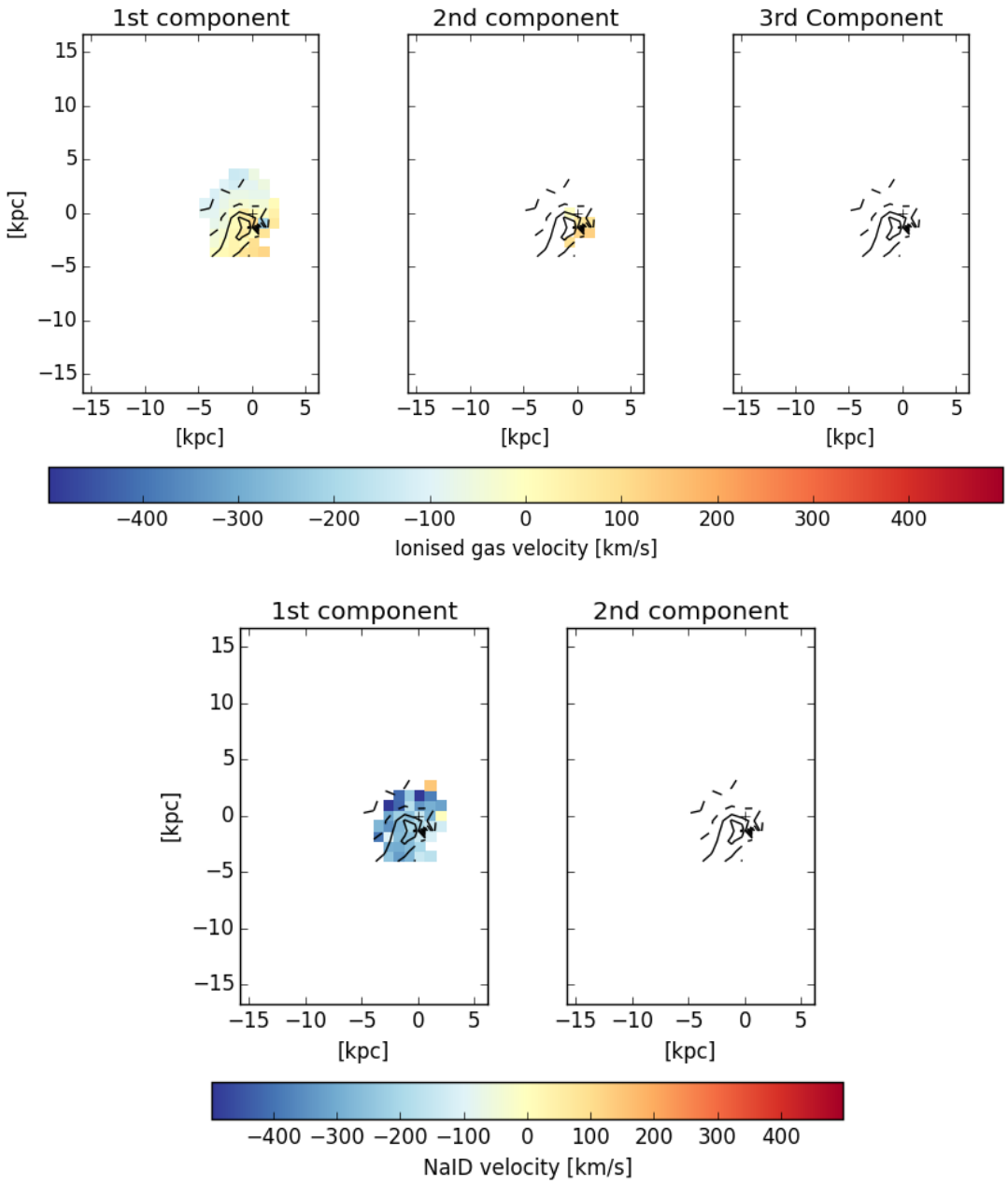

Figure C.21: IRAS F17207-0014 diagnostic plots continued. Top panels - The ionised gas velocity maps of IRAS F17207-0014 defined from emission line fitting are presented in the top panels. There are up to three Gaussian components needed to explain the emission lines observed in this galaxy. Bottom panels - The neutral gas velocity maps of IRAS F01053-1746 defined through fitting NaI D absorption features with multiple components are presented in the bottom panels. The contours represent Gaussian smoothed ionised velocity where dashed contours represent negative velocities and solid contours represent positive velocities (inclusive of zero).

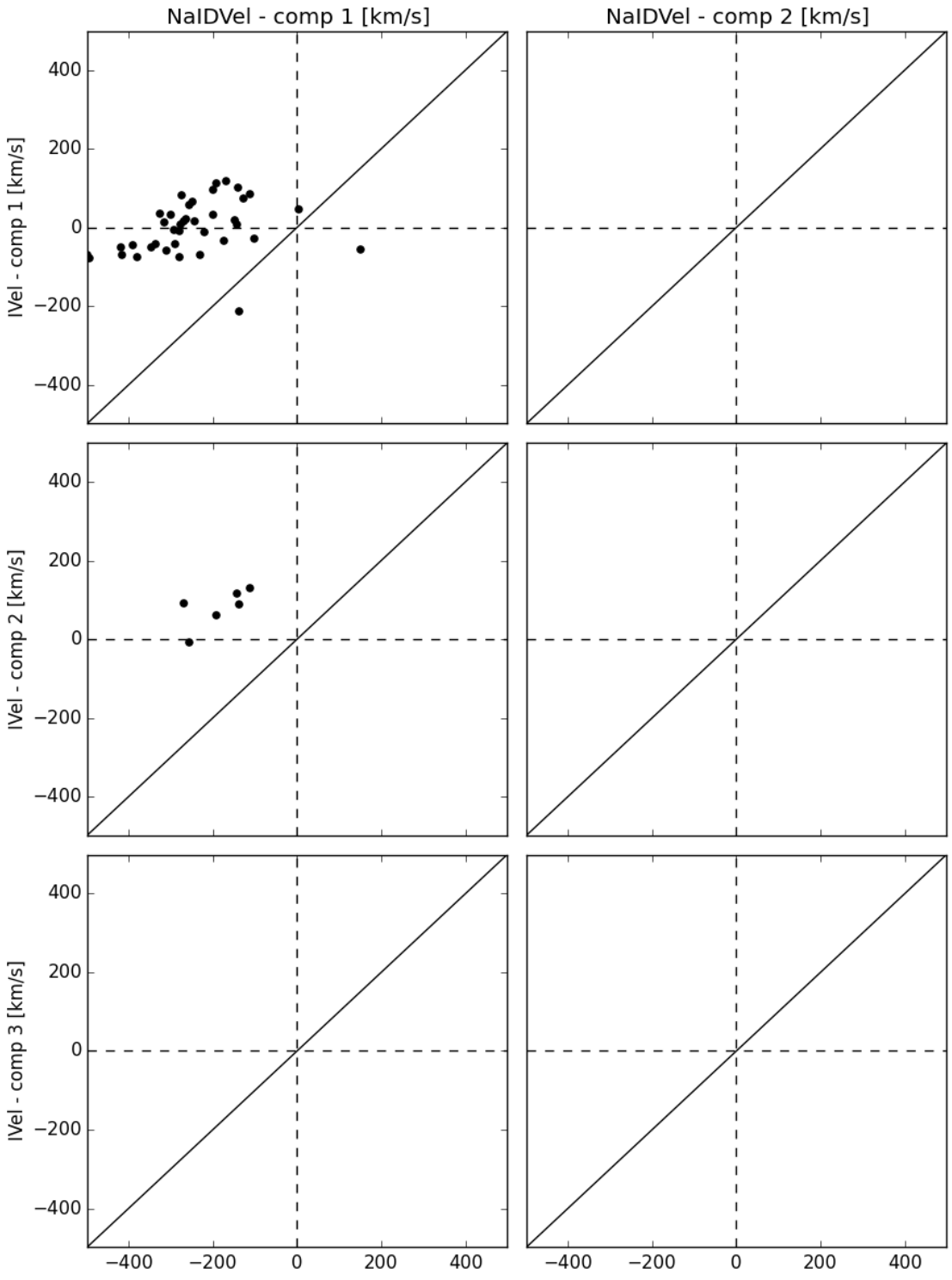

Figure C.22: IRAS F17207-0014 diagnostic plots continued. These panels show the comparison of the ionised (y-axis) and neutral (x-axis) gas velocities as defined through emission line analysis and the fitting of the NaI D absorption lines, respectively.

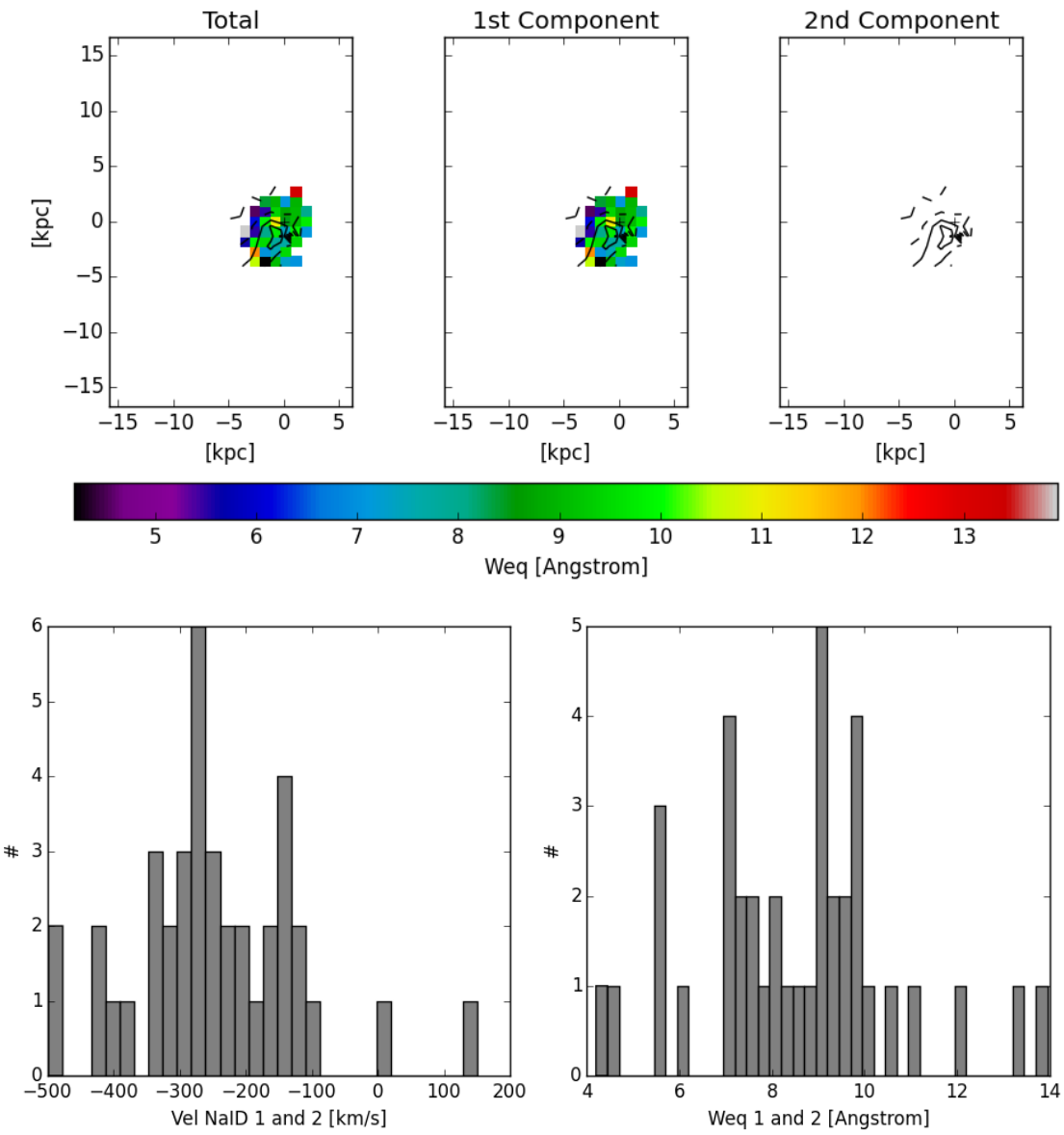

Figure C.23: IRAS F17207-0014 diagnostic plots continued. Top panels - Equivalent width, W_{eq}, values from fitting multiple components to NaI D absorption features. Left presents the total W_{eq} calculated at each spaxel, centre presents the W_{eq} of the first component and right presents the W_{eq} of the second component. The contours represent Gaussian smoothed ionised velocity where dashed contours represent negative velocities and solid contours represent positive velocities (inclusive of zero). Bottom panels - Left presents a histogram of the NaI D velocities in km/s. Right panels presents the histogram of the W_{eq} for each component.

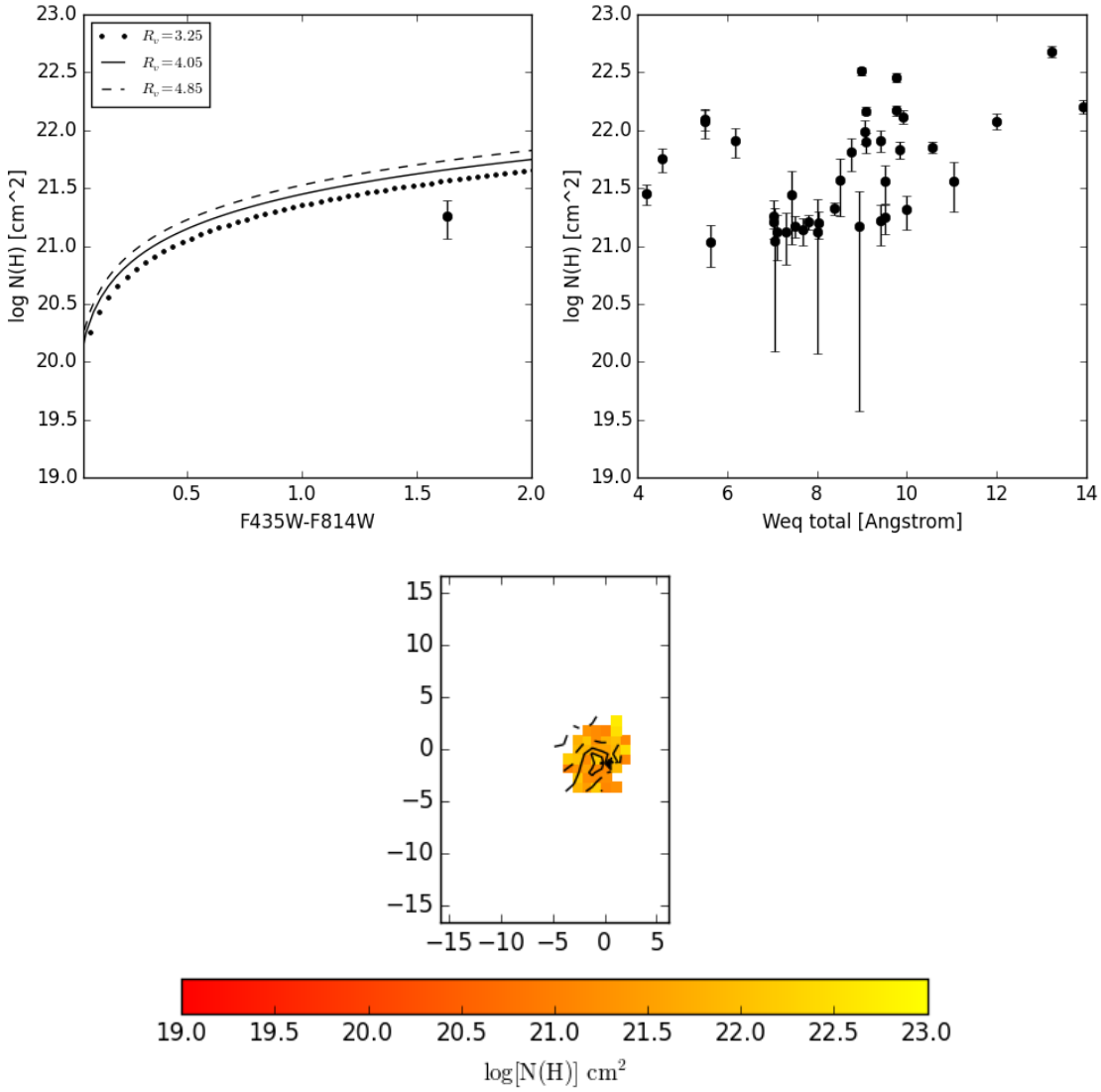

Figure C.24: IRAS F17207-0014 diagnostic plots continued. Top panels - Comparisons of Hydrogen column density to HST colour (left) and total W_{eq} of IRAS F17207-0014 (right). Bottom panel - map of the calculated N(H).

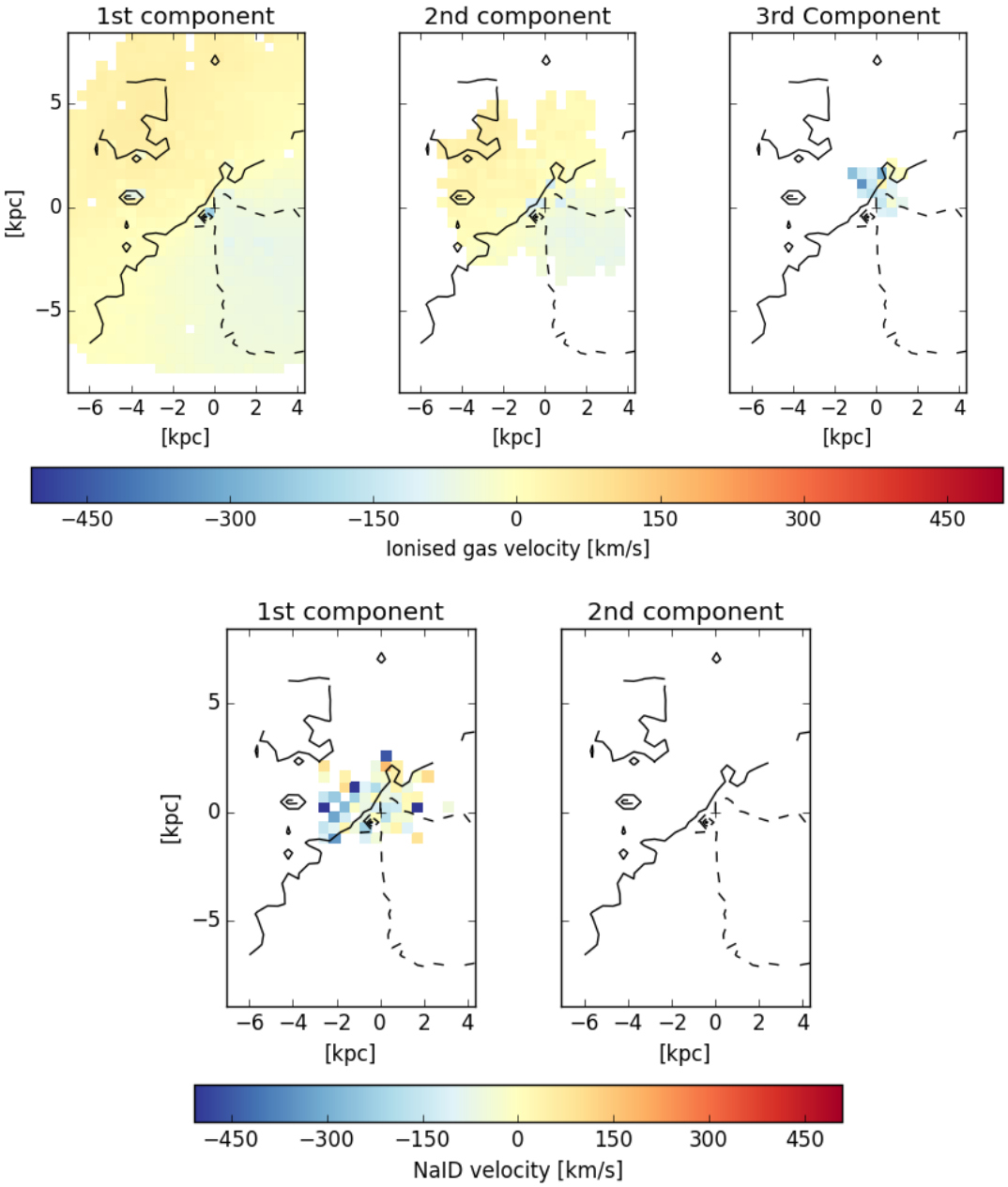

Figure C.25: IRAS F17222-5953 diagnostic plots. Top panels - The ionised gas velocity maps of IRAS F17222-5953 defined from emission line fitting are presented in the top panels. There are up to three Gaussian components needed to explain the emission lines observed in this galaxy. Bottom panels - The neutral gas velocity maps of IRAS F17222-5953 defined through fitting NaI D absorption features with multiple components are presented in the bottom panels. The contours represent Gaussian smoothed ionised velocity where dashed contours represent negative velocities and solid contours represent positive velocities (inclusive of zero).

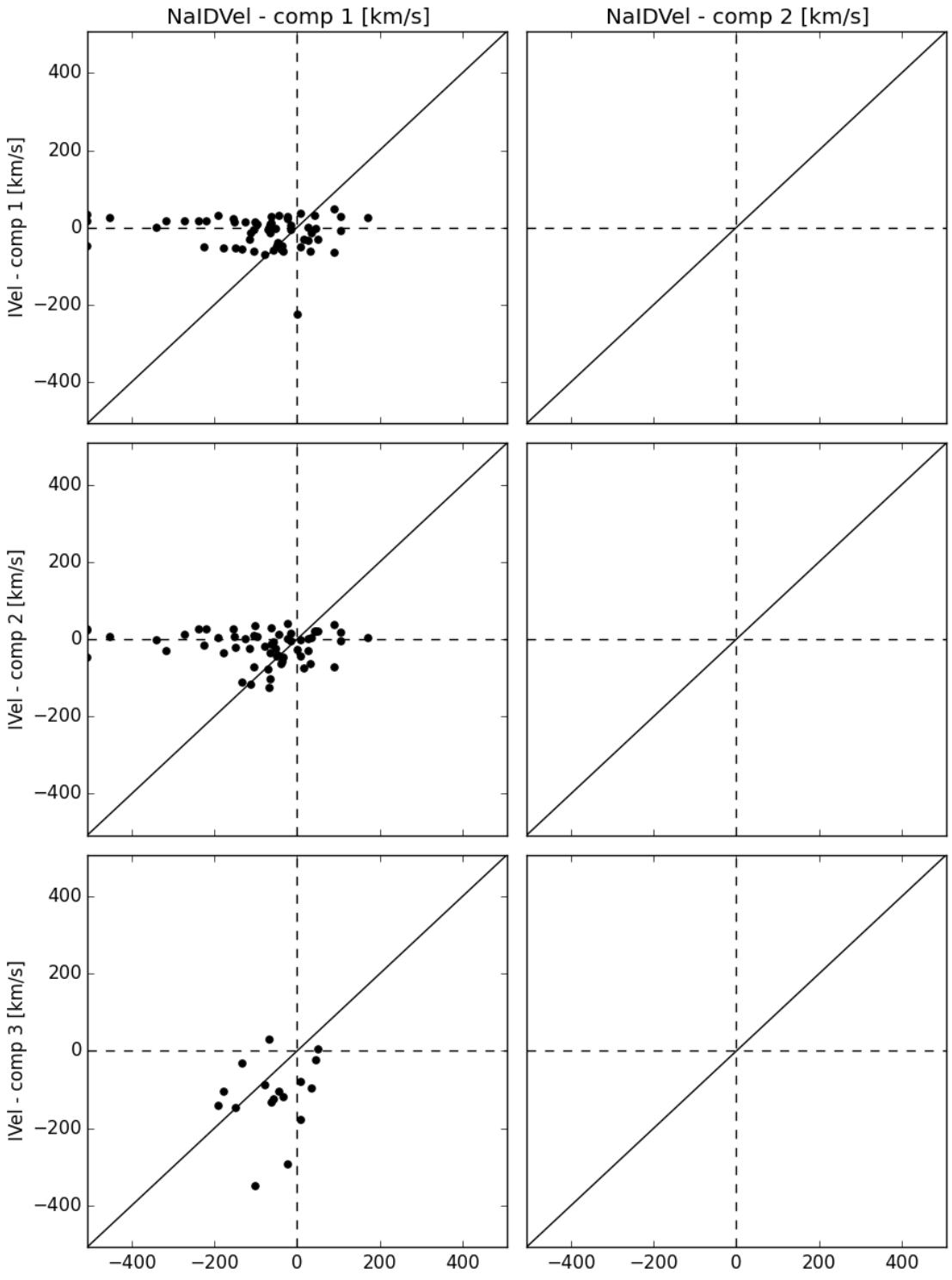

Figure C.26: IRAS F17222-5953 diagnostic plots continued. These panels show the comparison of the ionised (y-axis) and neutral (x-axis) gas velocities as defined through emission line analysis and the fitting of the NaI D absorption lines, respectively.

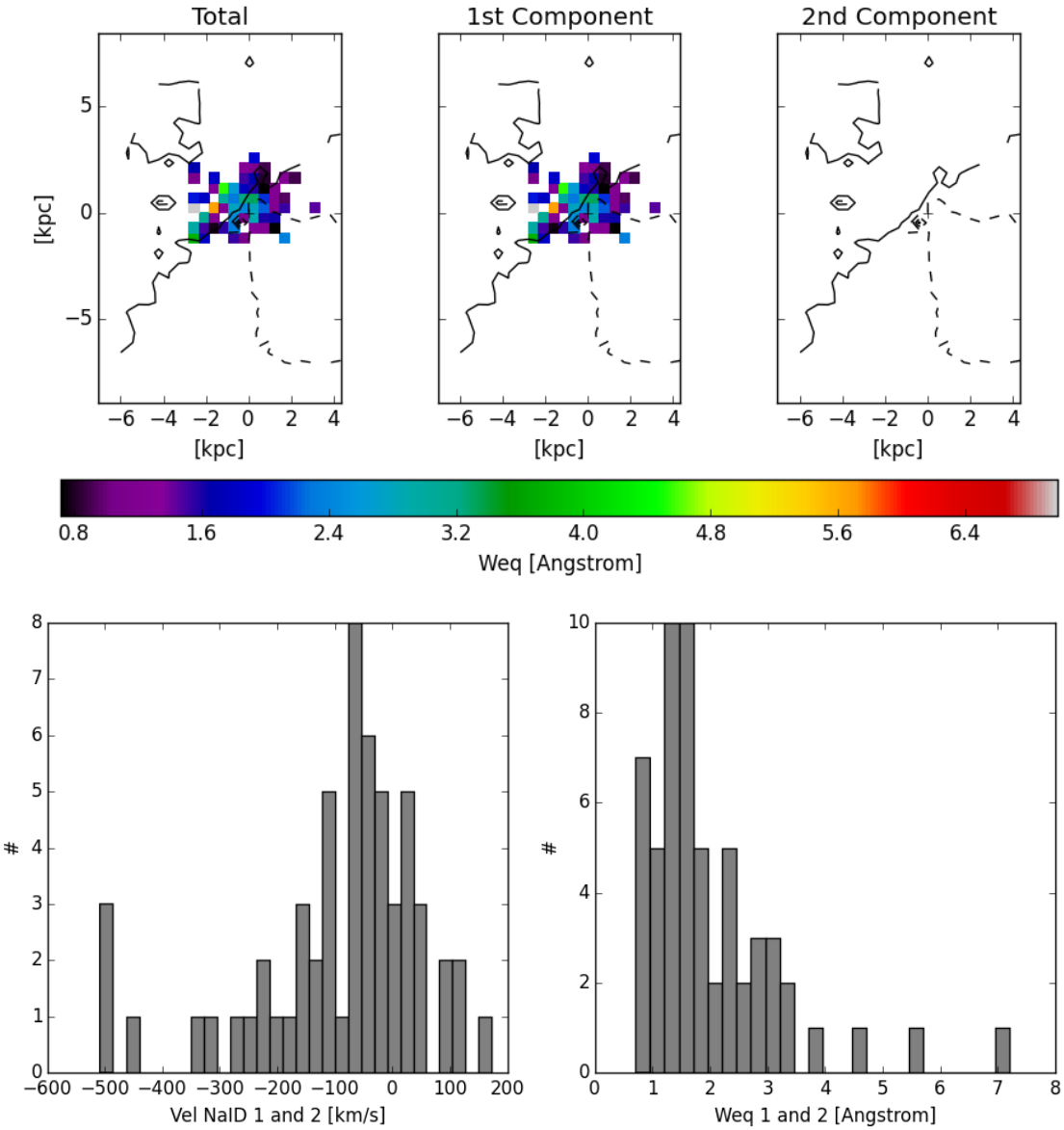

Figure C.27: IRAS F17222-5953 diagnostic plots continued. Top panels - Equivalent width, W_{eq}, values from fitting multiple components to NaI D absorption features. Left presents the total W_{eq} calculated at each spaxel, centre presents the W_{eq} of the first component and right presents the W_{eq} of the second component. The contours represent Gaussian smoothed ionised velocity where dashed contours represent negative velocities and solid contours represent positive velocities (inclusive of zero). Bottom panels - Left presents a histogram of the NaI D velocities in km/s. Right panels presents the histogram of the W_{eq} for each component.

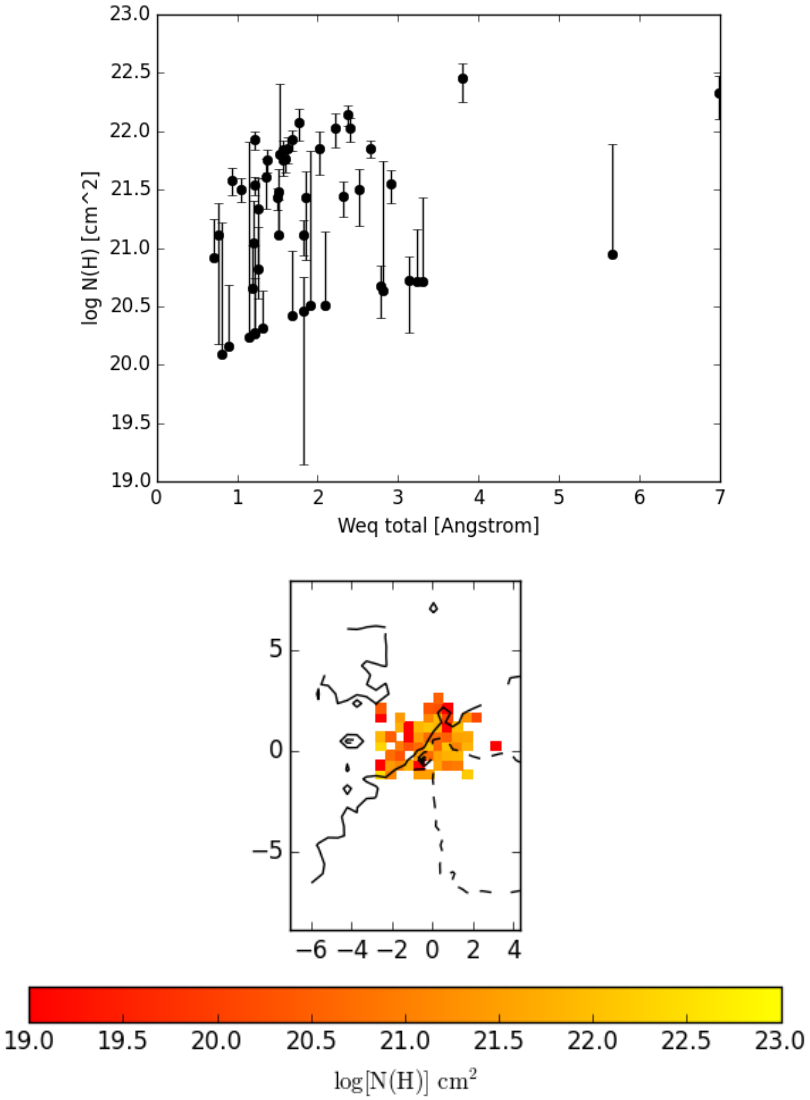

Figure C.28: IRAS F17222-5953 diagnostic plots continued. Top panel - Comparisons of Hydrogen column density to total W_{eq} of IRAS F17222-5953. Bottom panel - map of the calculated N(H).

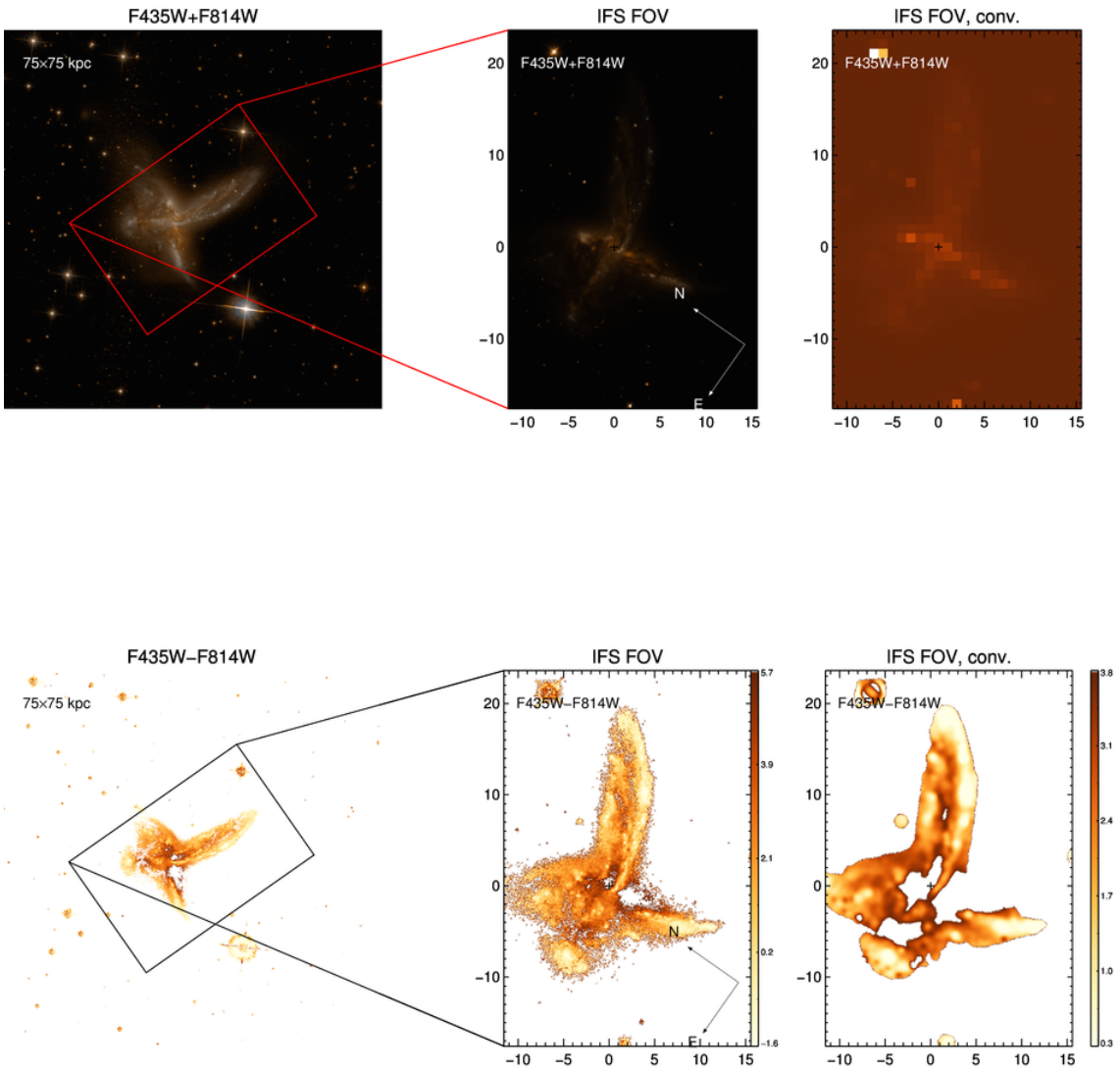

Figure C.29: IRAS F19115-2124 diagnostic plots. HST colour image of IRAS F19115-2124. Top right presents the HST image (F435W+F814W) with the FoV outlined in red. Top middle present the FoV of our WiFeS observations. Top right is the HST image convolved to the same pixel scale as the WiFeS instrument (1″/pix). Presented here are the HST images used to calculate the dust content in IRAS F19115-2124 through the calculation of F435W-F814W in the bottom panels. Bottom left presents the FoV of the WiFeS instrument overlaid on the HST image and bottom middle presents the cut out of the FoV orientated to the WiFeS observation. Bottom right presents the F435W-F814W image convolved to the same spatial scale as the WiFeS observation.

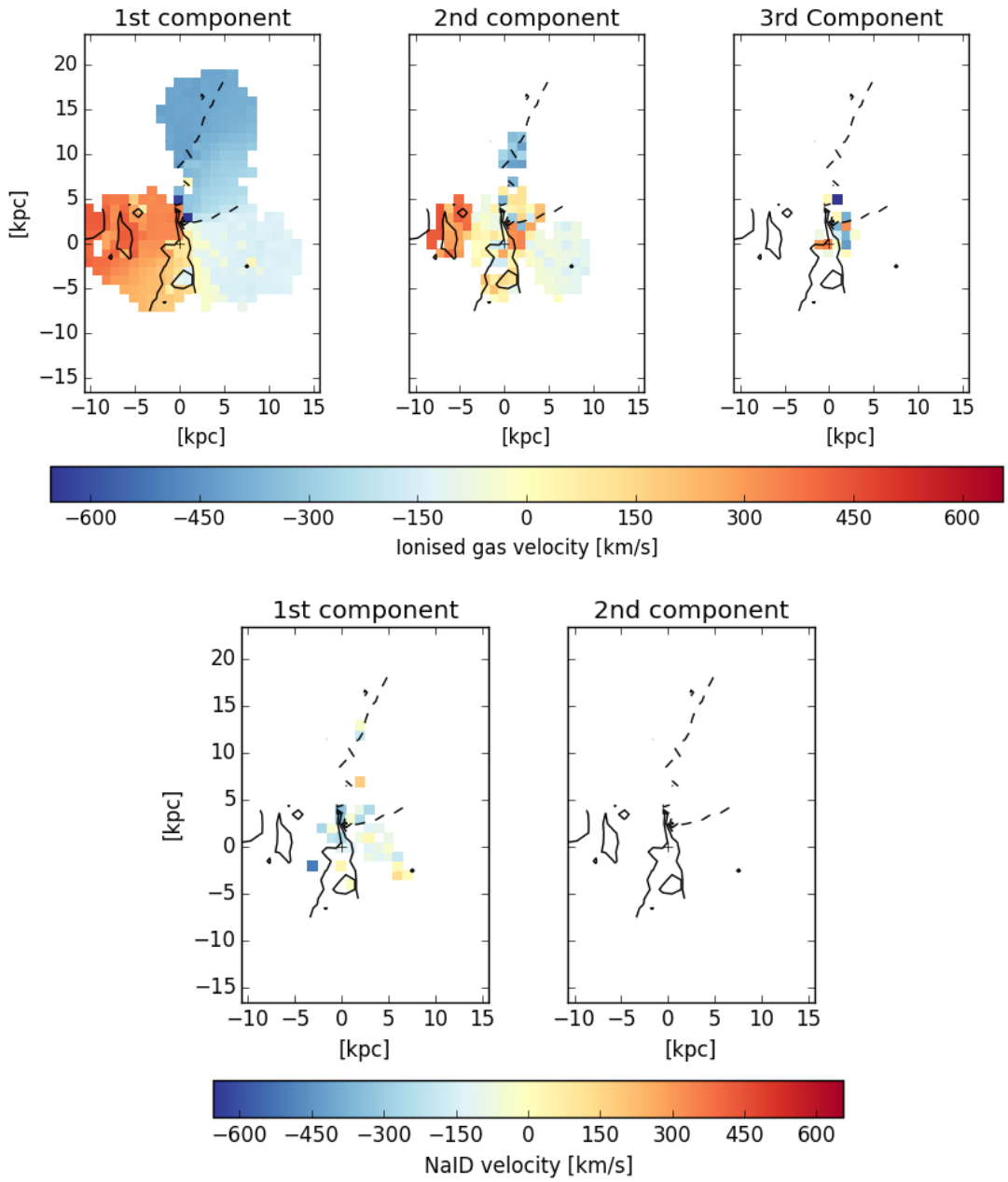

Figure C.30: IRAS F19115-2124 diagnostic plots continued. Top panels - The ionised gas velocity maps of IRAS F19115-2124 defined from emission line fitting are presented in the top panels. There are up to three Gaussian components needed to explain the emission lines observed in this galaxy. Bottom panels - The neutral gas velocity maps of IRAS F19115-2124 defined through fitting NaI D absorption features with multiple components are presented in the bottom panels. The contours represent Gaussian smoothed ionised velocity where dashed contours represent negative velocities and solid contours represent positive velocities (inclusive of zero).

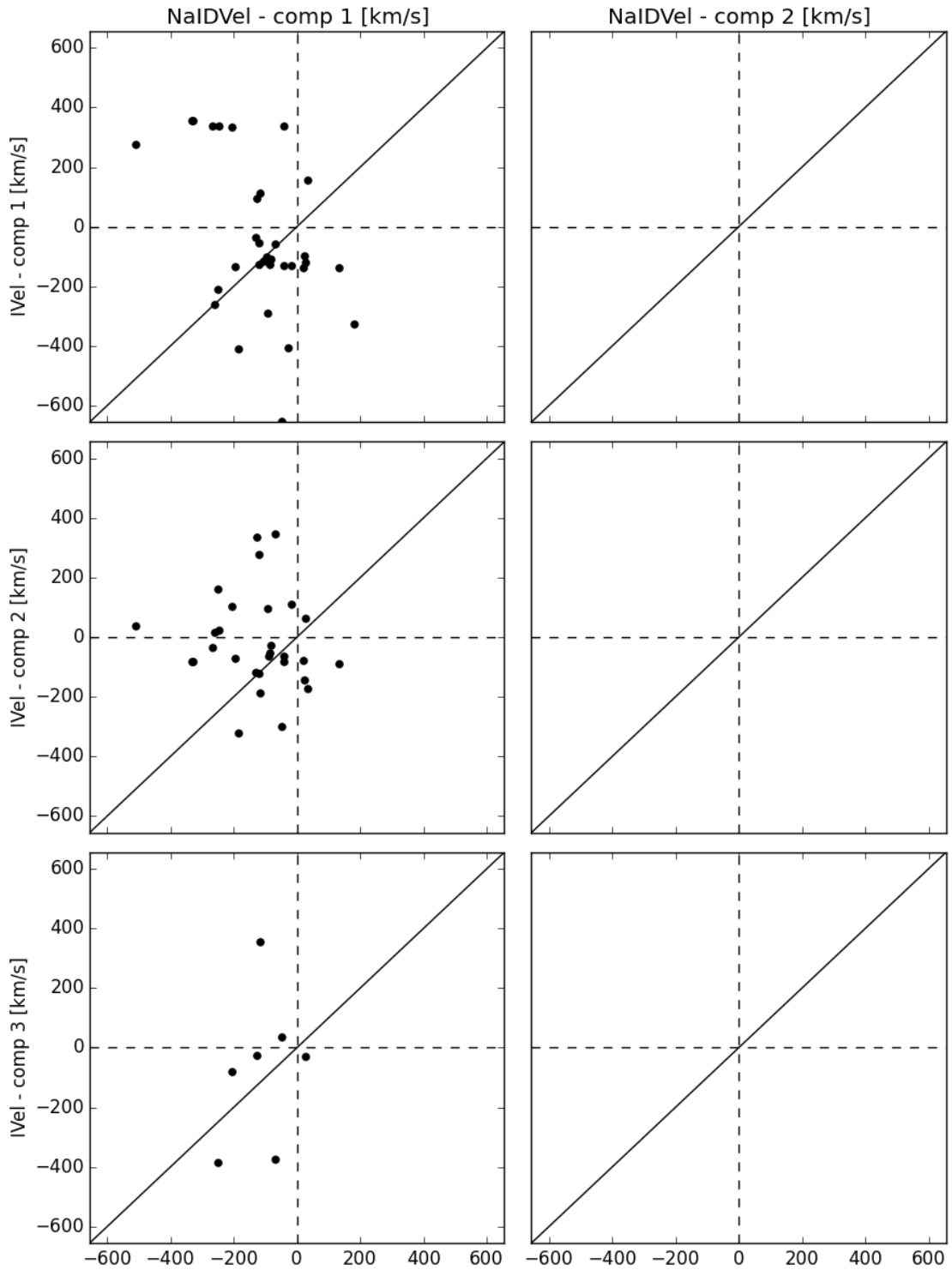

Figure C.31: IRAS F19115-2124 diagnostic plots continued. These panels show the comparison of the ionised (y-axis) and neutral (x-axis) gas velocities as defined through emission line analysis and the fitting of the NaI D absorption lines, respectively.

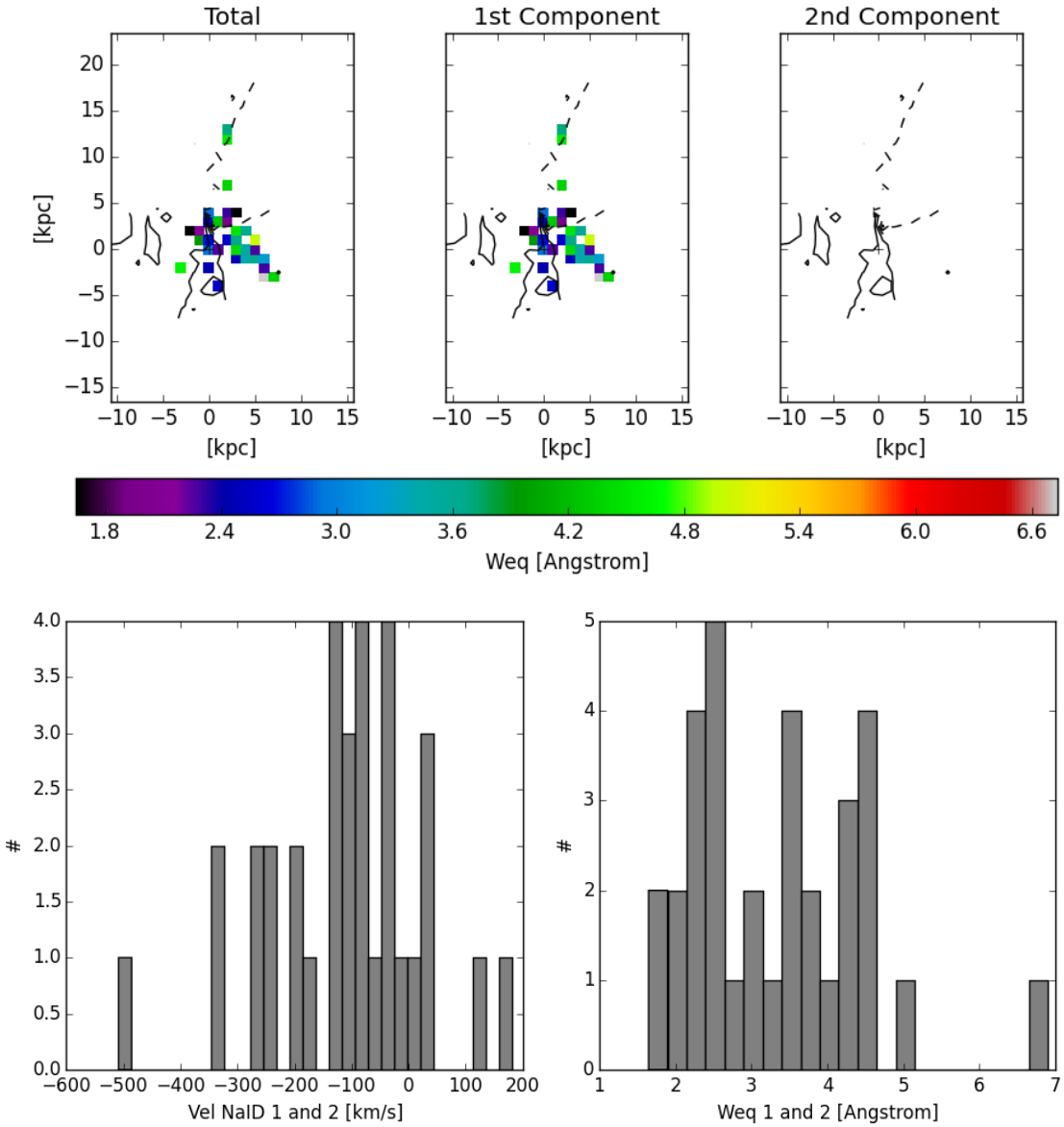

Figure C.32: IRAS F19115-2124 diagnostic plots continued. Top panels - Equivalent width, W_{eq}, values from fitting multiple components to NaI D absorption features. Left presents the total W_{eq} calculated at each spaxel, centre presents the W_{eq} of the first component and right presents the W_{eq} of the second component. The contours represent Gaussian smoothed ionised velocity where dashed contours represent negative velocities and solid contours represent positive velocities (inclusive of zero). Bottom panels - Left presents a histogram of the NaI D velocities in km/s. Right panels presents the histogram of the W_{eq} for each component.

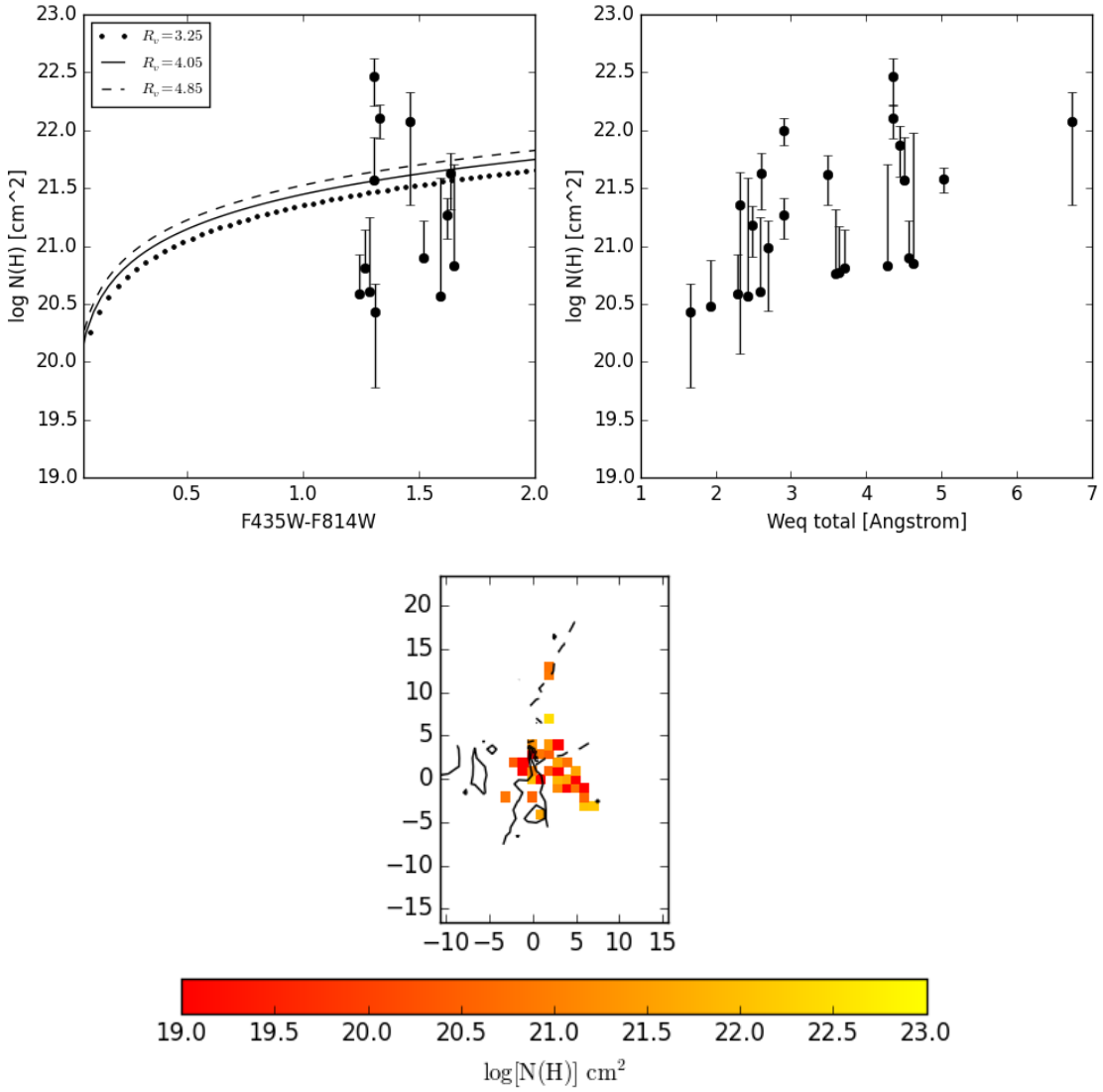

Figure C.33: IRAS F19115-2124 diagnostic plots continued. Top panels - Comparisons of Hydrogen column density to HST colour (left) and total W_{eq} of IRAS F19115-2124 (right). Bottom panel - map of the calculated N(H).

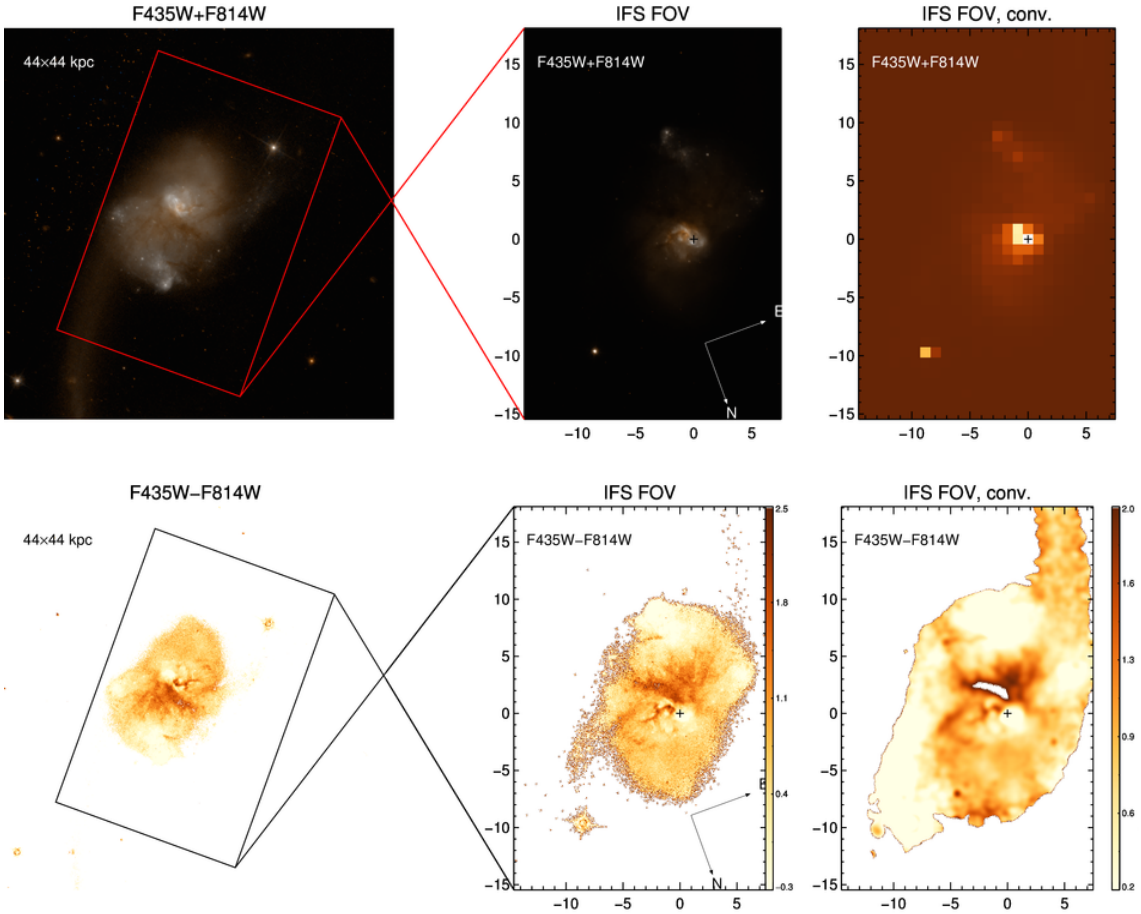

Figure C.34: IRAS F20551-4250 diagnostic plots. HST colour image of IRAS F20551-4250. Top right presents the HST image (F435W+F814W) with the FoV outlined in red. Top middle present the FoV of our WiFeS observations. Top right is the HST image convolved to the same pixel scale as the WiFeS instrument (1″/pix). Presented here are the HST images used to calculate the dust content in IRAS F20551-4250 through the calculation of F435W-F814W in the bottom panels. Bottom left presents the FoV of the WiFeS instrument overlaid on the HST image and bottom middle presents the cut out of the FoV orientated to the WiFeS observation. Bottom right presents the F435W-F814W image convolved to the same spatial scale as the WiFeS observation.

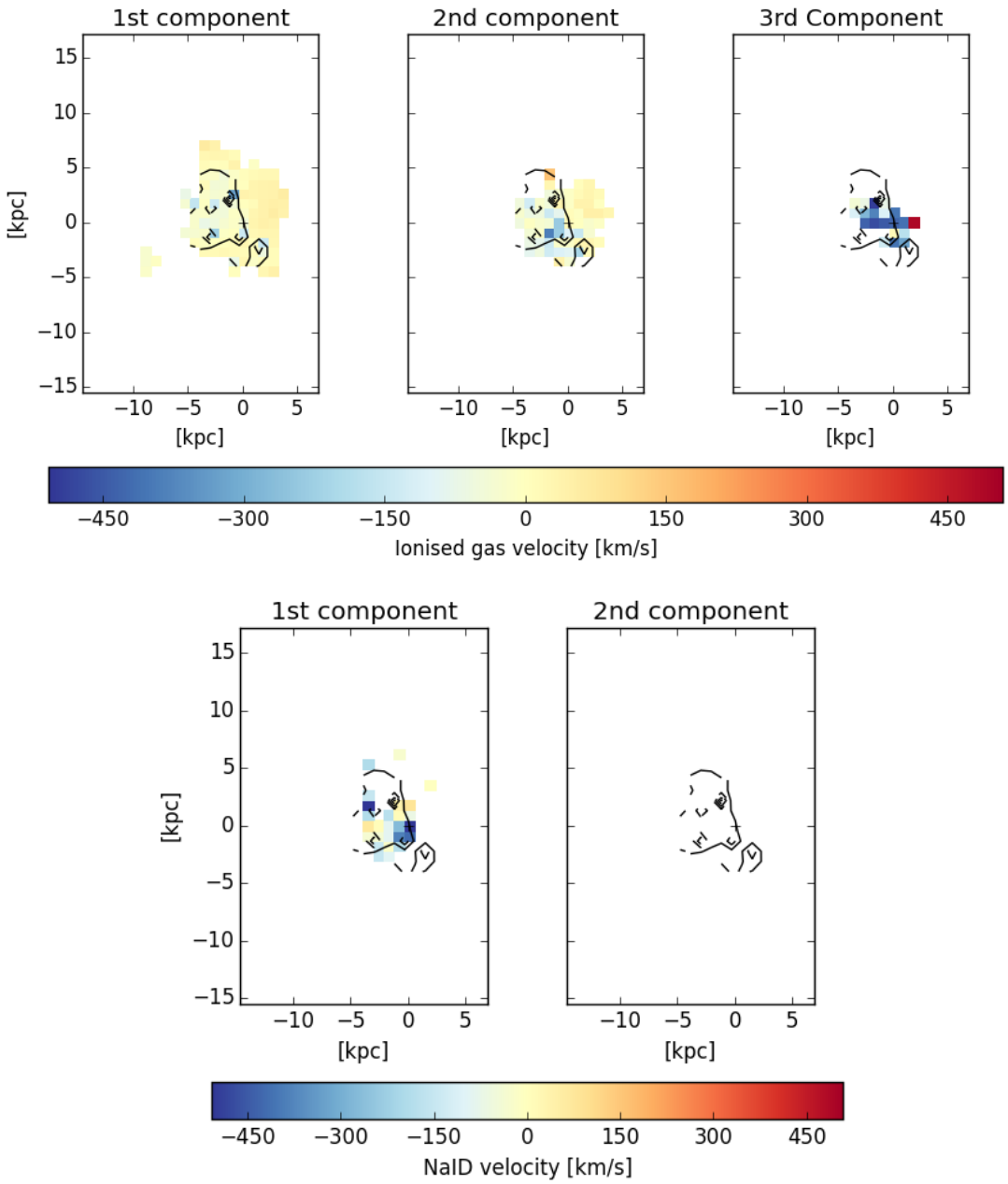

Figure C.35: IRAS F20551-4250 diagnostic plots continued. Top panels - The ionised gas velocity maps of IRAS F20551-4250 defined from emission line fitting are presented in the top panels. There are up to three Gaussian components needed to explain the emission lines observed in this galaxy. Bottom panels - The neutral gas velocity maps of IRAS F20551-4250 defined through fitting NaI D absorption features with multiple components are presented in the bottom panels. The contours represent Gaussian smoothed ionised velocity where dashed contours represent negative velocities and solid contours represent positive velocities (inclusive of zero).

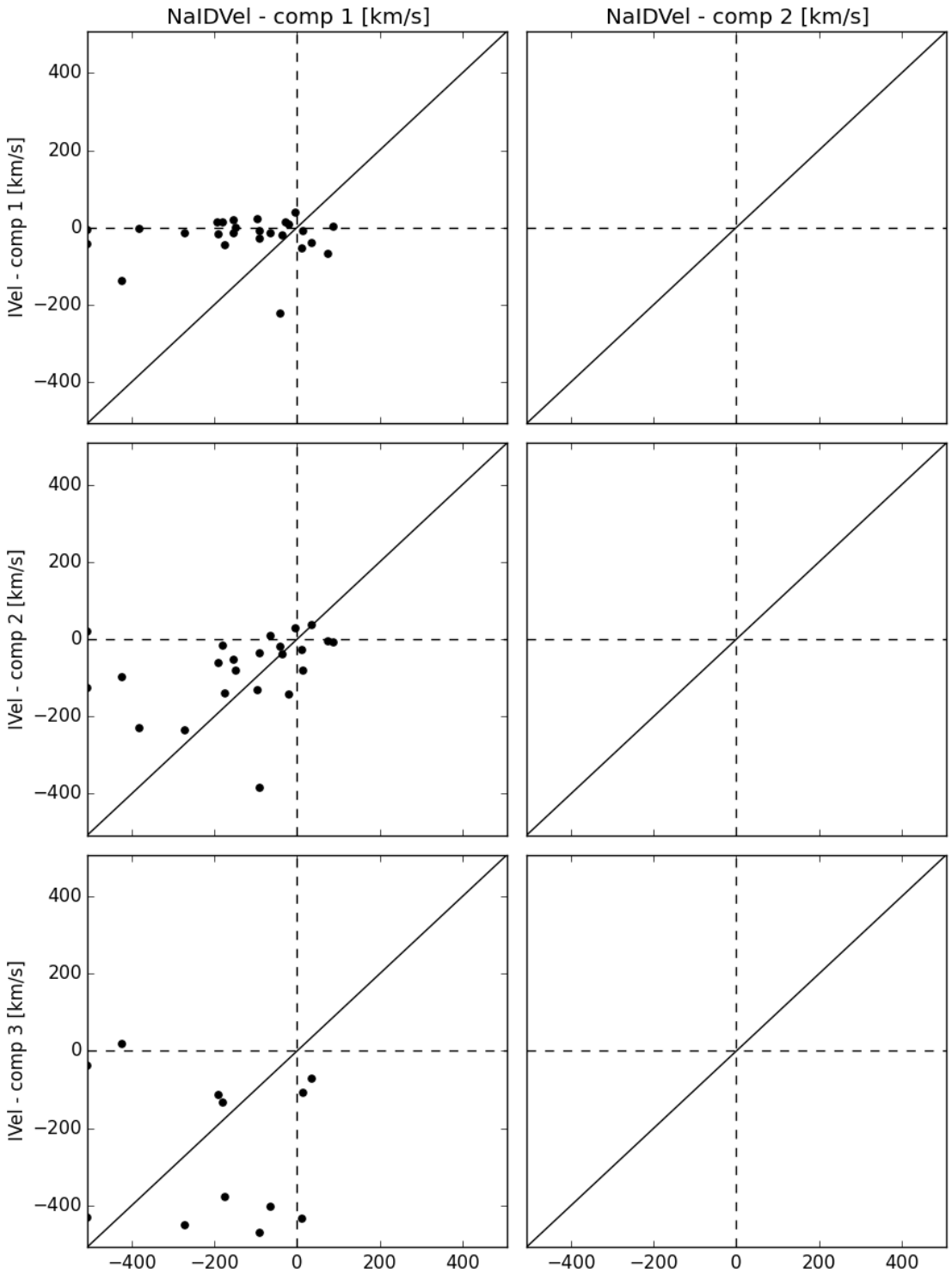

Figure C.36: IRAS F20551-4250 diagnostic plots continued. These panels show the comparison of the ionised (y-axis) and neutral (x-axis) gas velocities as defined through emission line analysis and the fitting of the NaI D absorption lines, respectively.

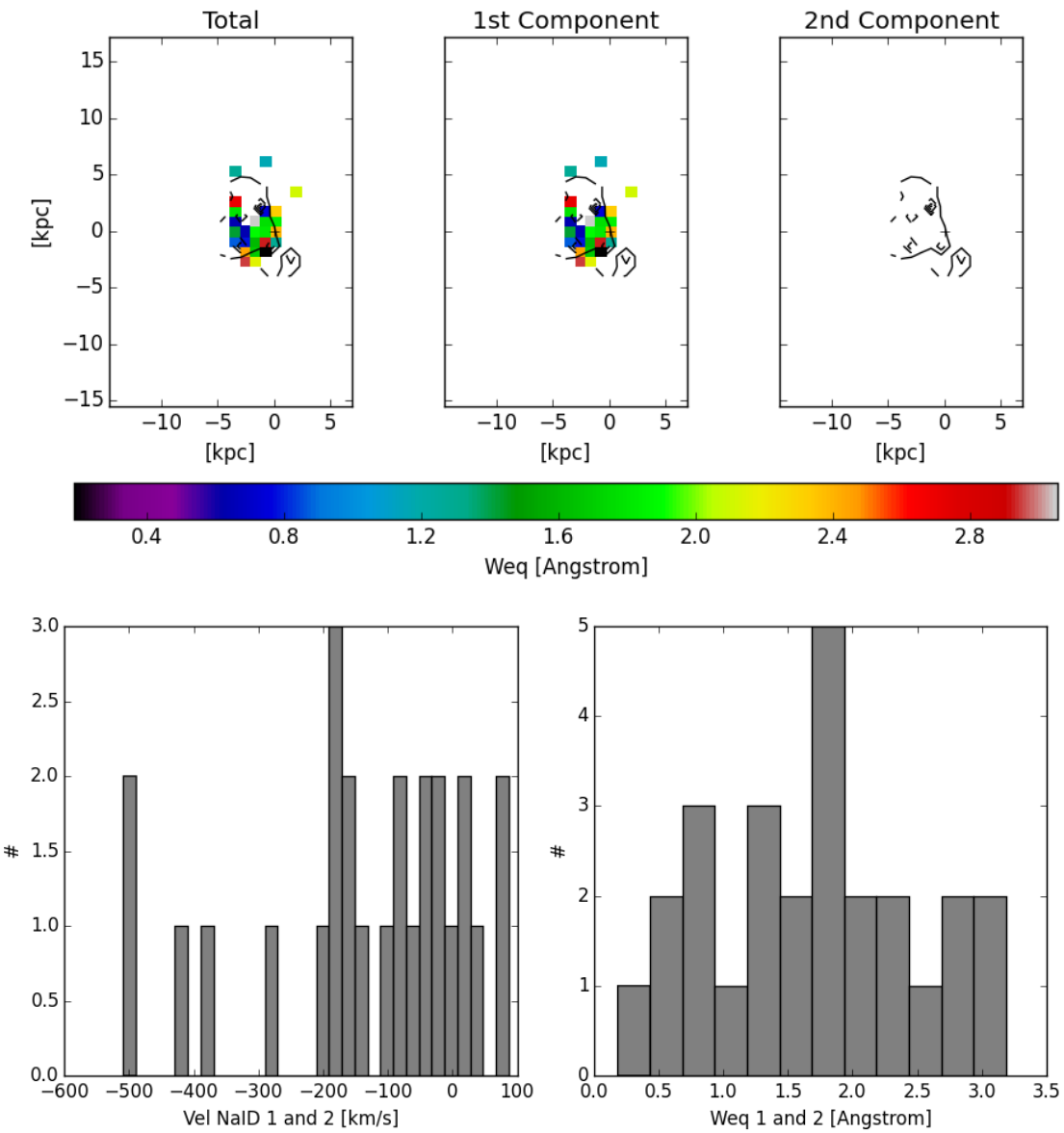

Figure C.37: IRAS F20551-4250 diagnostic plots continued. Top panels - Equivalent width, W_{eq}, values from fitting multiple components to NaI D absorption features. Left presents the total W_{eq} calculated at each spaxel, centre presents the W_{eq} of the first component and right presents the W_{eq} of the second component. The contours represent Gaussian smoothed ionised velocity where dashed contours represent negative velocities and solid contours represent positive velocities (inclusive of zero). Bottom panels - Left presents a histogram of the NaI D velocities in km/s. Right panels presents the histogram of the W_{eq} for each component.

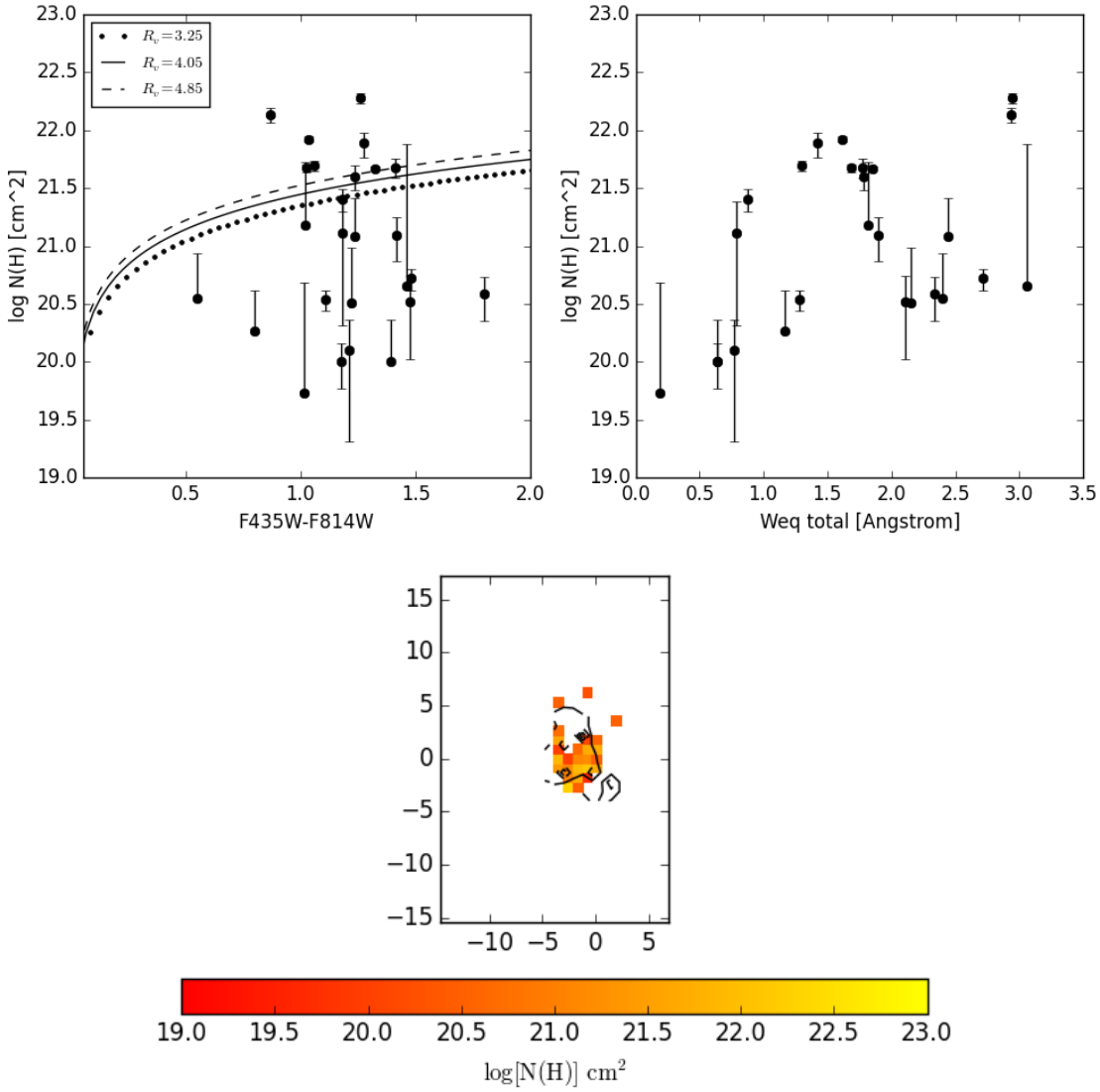

Figure C.38: IRAS F20551-4250 diagnostic plots continued. Top panels - Comparisons of Hydrogen column density to HST colour (left) and total W_{eq} of IRAS F20551-4250 (right). Bottom panel - map of the calculated N(H).

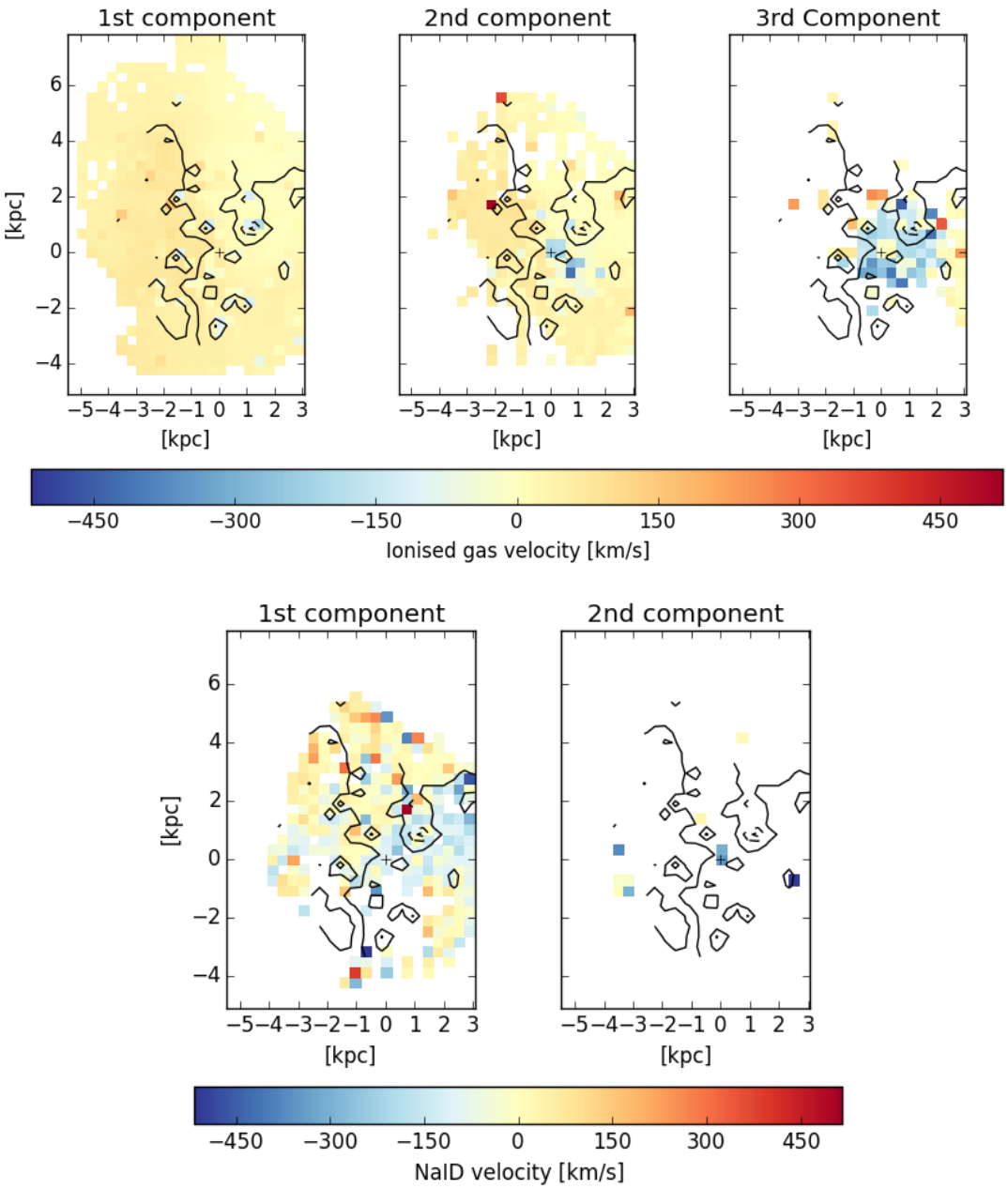

Figure C.39: IRAS F21453-3511 diagnostic plots. Top panels - The ionised gas velocity maps of IRAS F21453-3511 defined from emission line fitting are presented in the top panels. There are up to three Gaussian components needed to explain the emission lines observed in this galaxy. Bottom panels - The neutral gas velocity maps of IRAS F21453-3511 defined through fitting NaI D absorption features with multiple components are presented in the bottom panels. The contours represent Gaussian smoothed ionised velocity where dashed contours represent negative velocities and solid contours represent positive velocities (inclusive of zero).

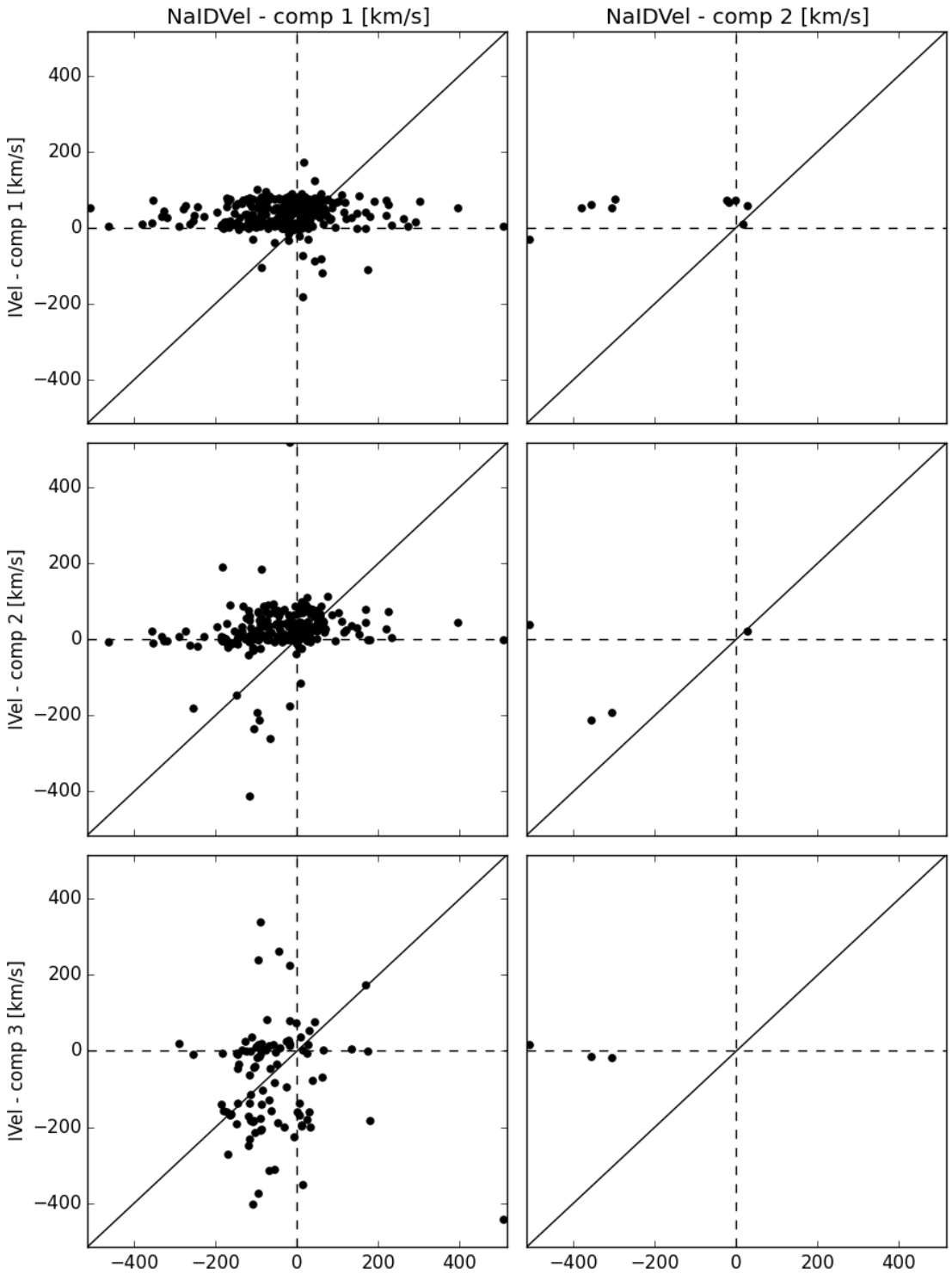

Figure C.40: IRAS F21453-3511 diagnostic plots continued. These panels show the comparison of the ionised (y-axis) and neutral (x-axis) gas velocities as defined through emission line analysis and the fitting of the NaI D absorption lines, respectively.

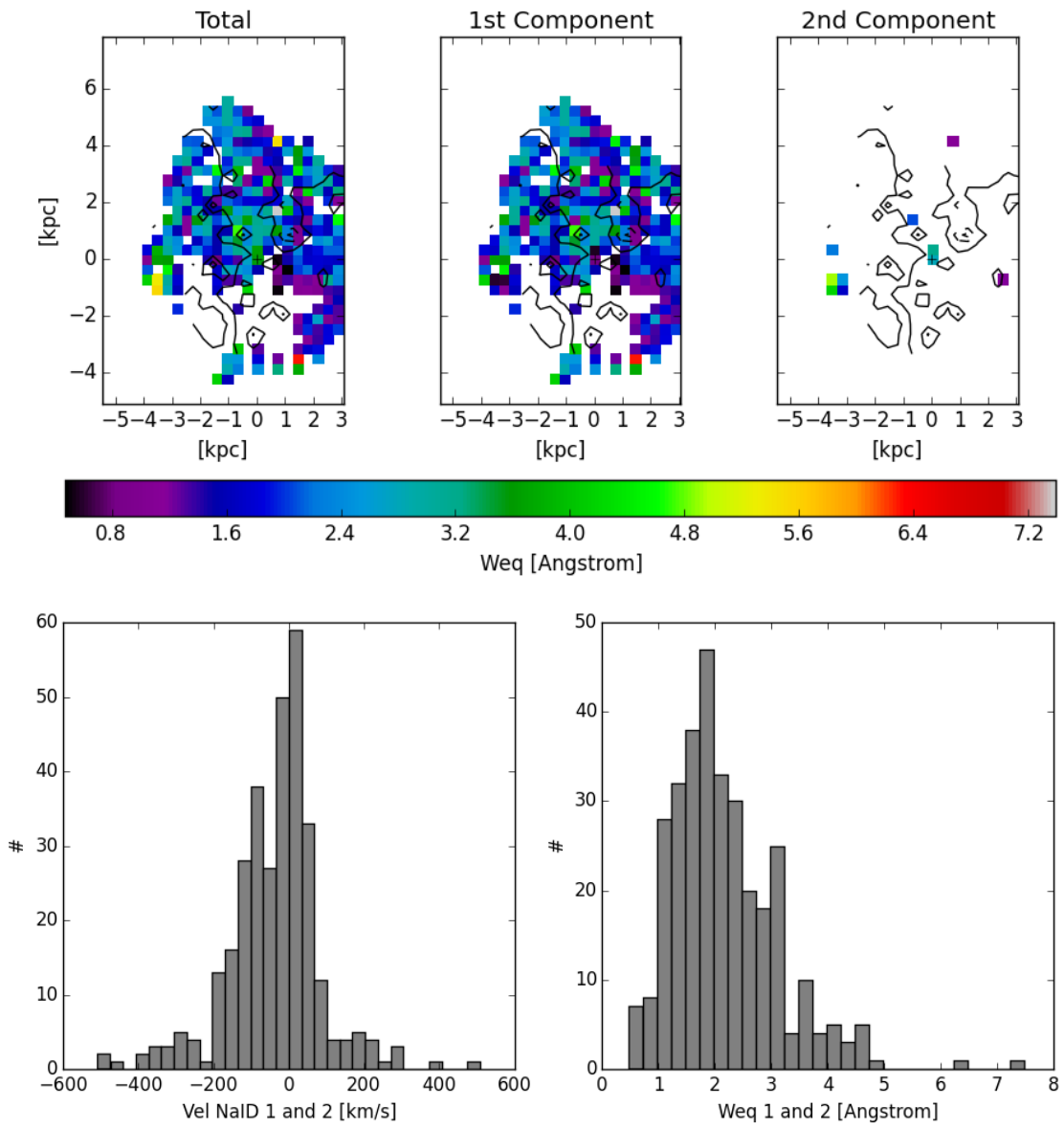

Figure C.41: IRAS F21453-3511 diagnostic plots continued. Top panels - Equivalent width, W_{eq}, values from fitting multiple components to NaI D absorption features. Left presents the total W_{eq} calculated at each spaxel, centre presents the W_{eq} of the first component and right presents the W_{eq} of the second component. The contours represent Gaussian smoothed ionised velocity where dashed contours represent negative velocities and solid contours represent positive velocities (inclusive of zero). Bottom panels - Left presents a histogram of the NaI D velocities in km/s. Right panels presents the histogram of the W_{eq} for each component.

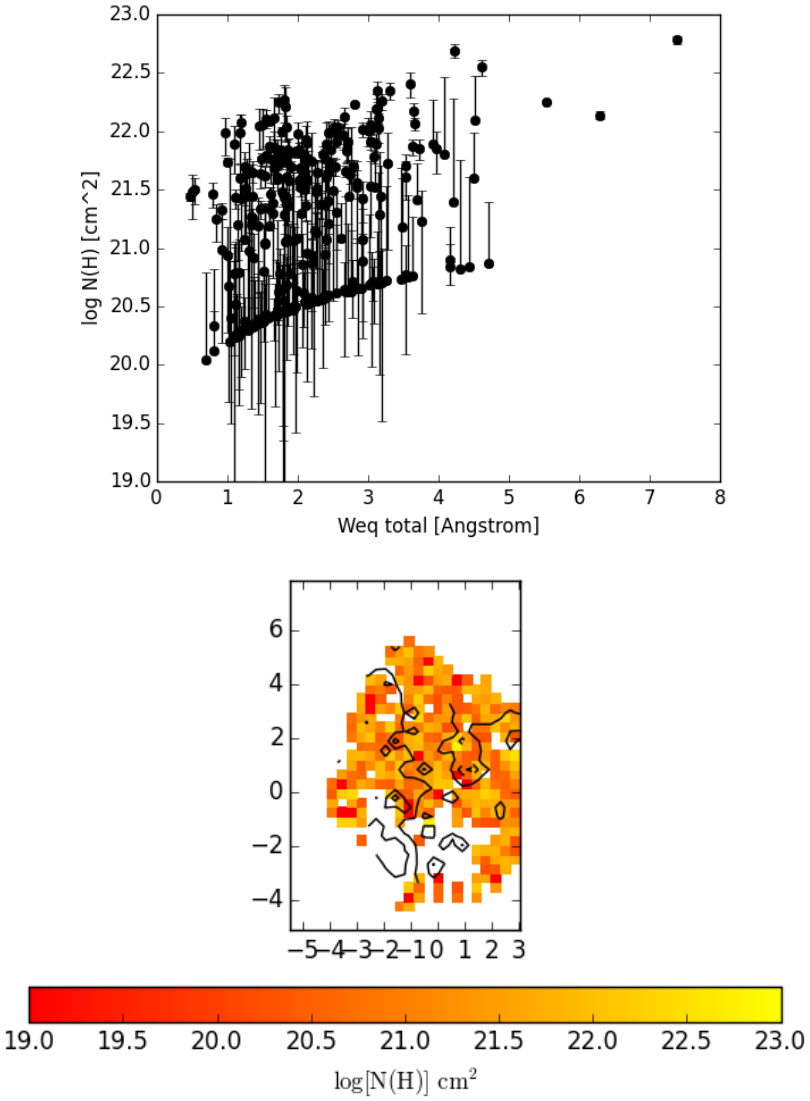

Figure C.42: IRAS F21453-3511 diagnostic plots continued. Top panel - Comparisons of Hydrogen column density to total W_{eq} of IRAS F21453-3511. Bottom panel - map of the calculated N(H).

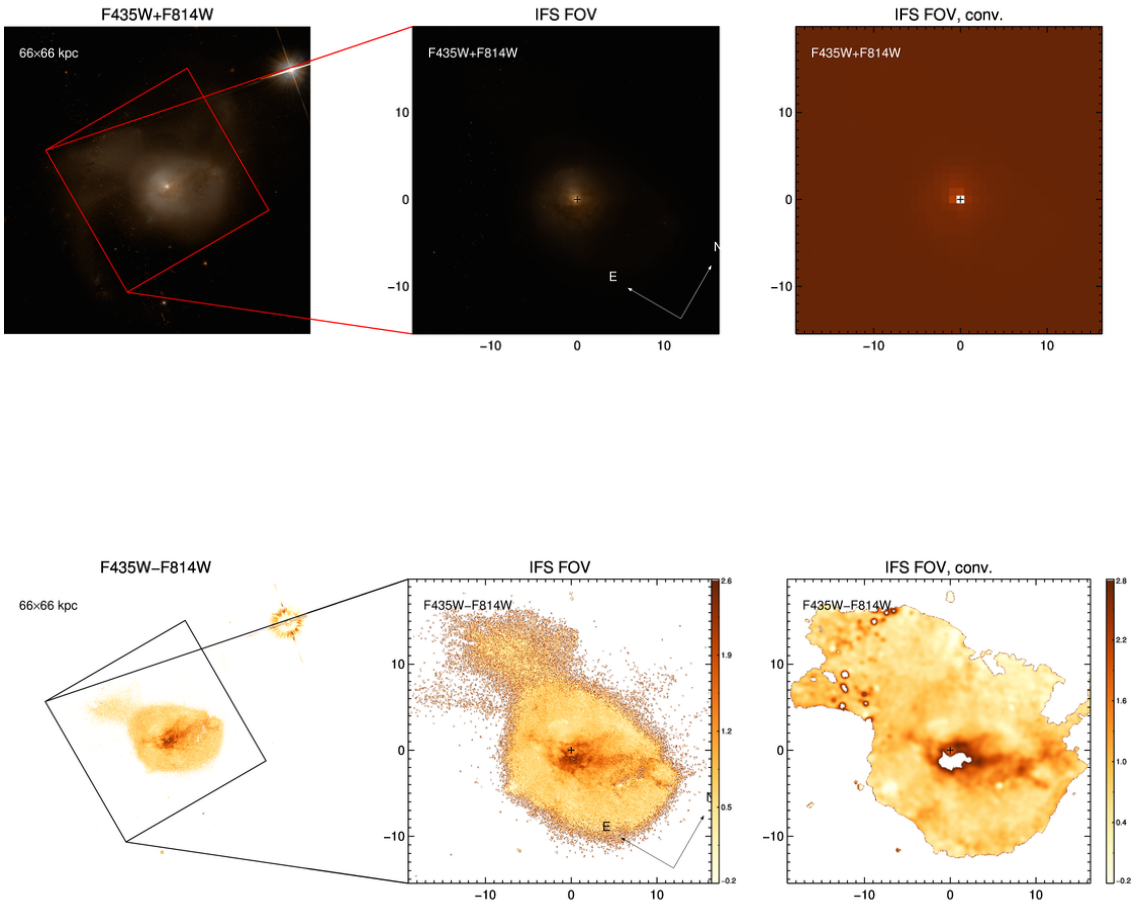

Figure C.43: IRAS F22467-4906 diagnostic plots. HST colour image of IRAS F22467-4906. Top right presents the HST image (F435W+F814W) with the FoV outlined in red. Top middle present the FoV of our WiFeS observations. Top right is the HST image convolved to the same pixel scale as the WiFeS instrument (1″/pix). Presented here are the HST images used to calculate the dust content in IRAS F22467-4906 through the calculation of F435W-F814W in the bottom panels. Bottom left presents the FoV of the WiFeS instrument overlaid on the HST image and bottom middle presents the cut out of the FoV orientated to the WiFeS observation. Bottom right presents the F435W-F814W image convolved to the same spatial scale as the WiFeS observation.

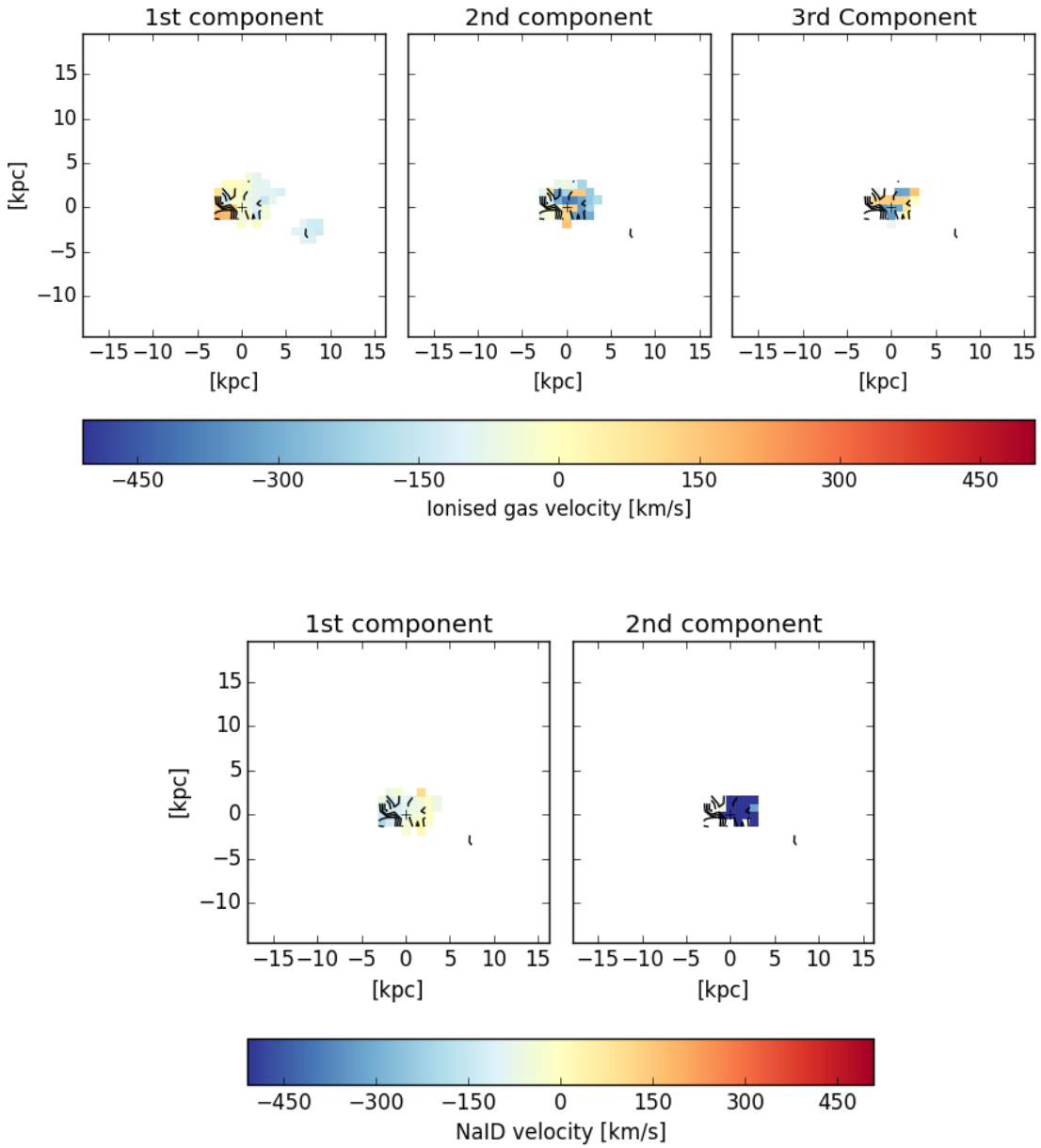

Figure C.44: IRAS F22467-4906 diagnostic plots continued. Top panels - The ionised gas velocity maps of IRAS F22467-4906 defined from emission line fitting are presented in the top panels. There are up to three Gaussian components needed to explain the emission lines observed in this galaxy. Bottom panels - The neutral gas velocity maps of IRAS F22467-4906 defined through fitting NaI D absorption features with multiple components are presented in the bottom panels. The contours represent Gaussian smoothed ionised velocity where dashed contours represent negative velocities and solid contours represent positive velocities (inclusive of zero).

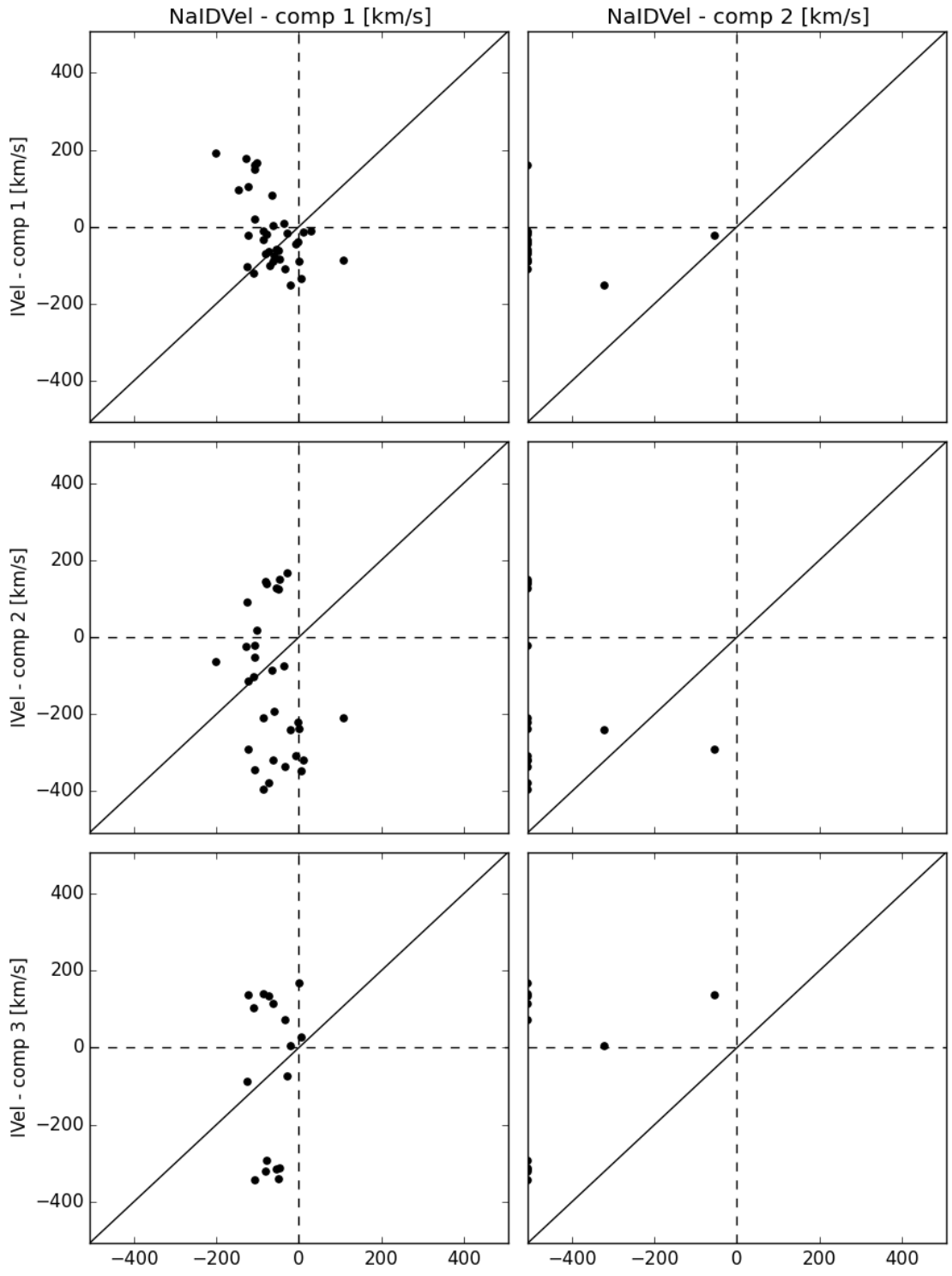

Figure C.45: IRAS F22467-4906 diagnostic plots continued. These panels show the comparison of the ionised (y-axis) and neutral (x-axis) gas velocities as defined through emission line analysis and the fitting of the NaI D absorption lines, respectively.

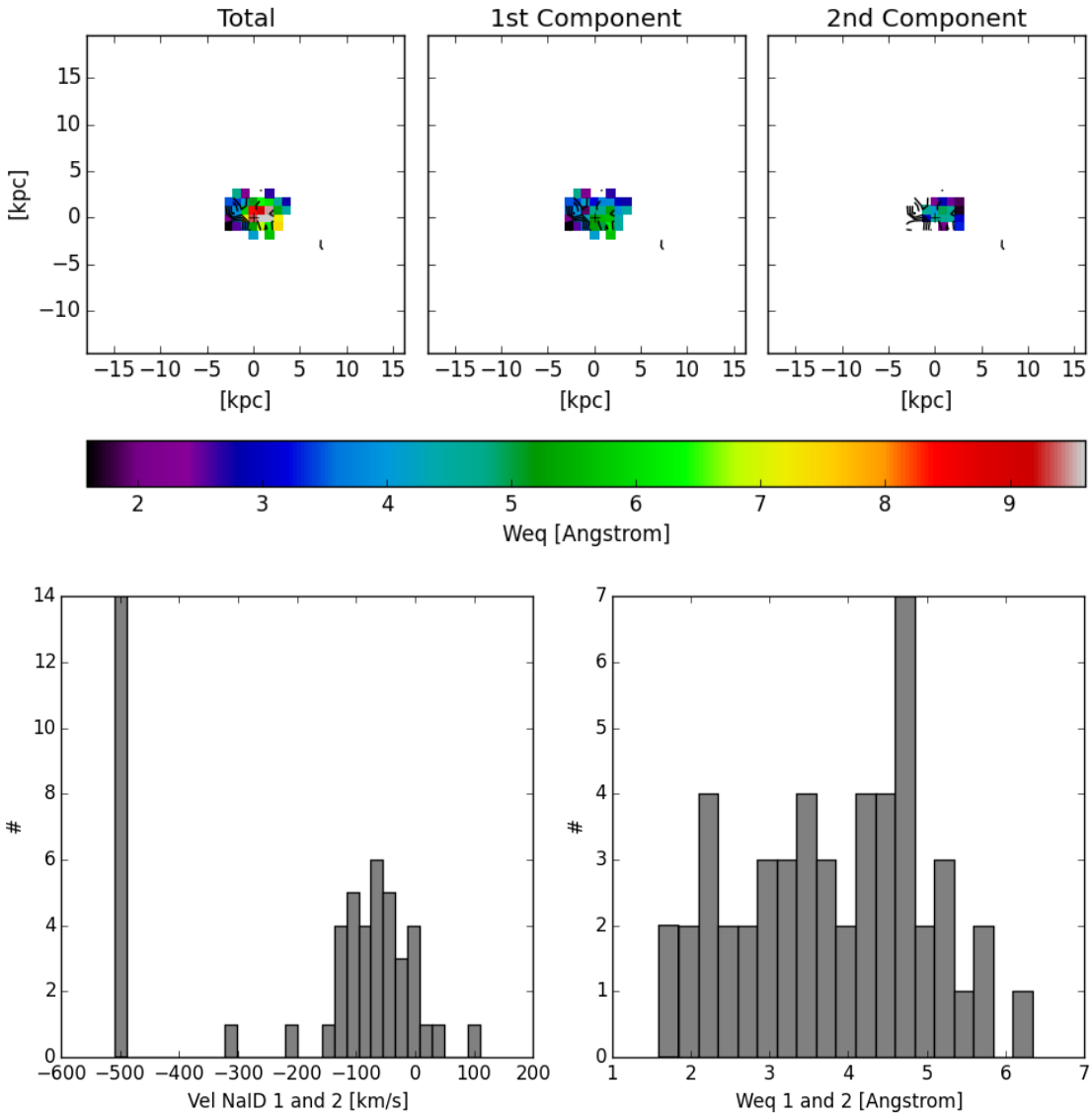

Figure C.46: IRAS F22467-4906 diagnostic plots continued. Top panels - Equivalent width, W_{eq}, values from fitting multiple components to NaI D absorption features. Left presents the total W_{eq} calculated at each spaxel, centre presents the W_{eq} of the first component and right presents the W_{eq} of the second component. The contours represent Gaussian smoothed ionised velocity where dashed contours represent negative velocities and solid contours represent positive velocities (inclusive of zero). Bottom panels - Left presents a histogram of the NaI D velocities in km/s. Right panels presents the histogram of the W_{eq} for each component.

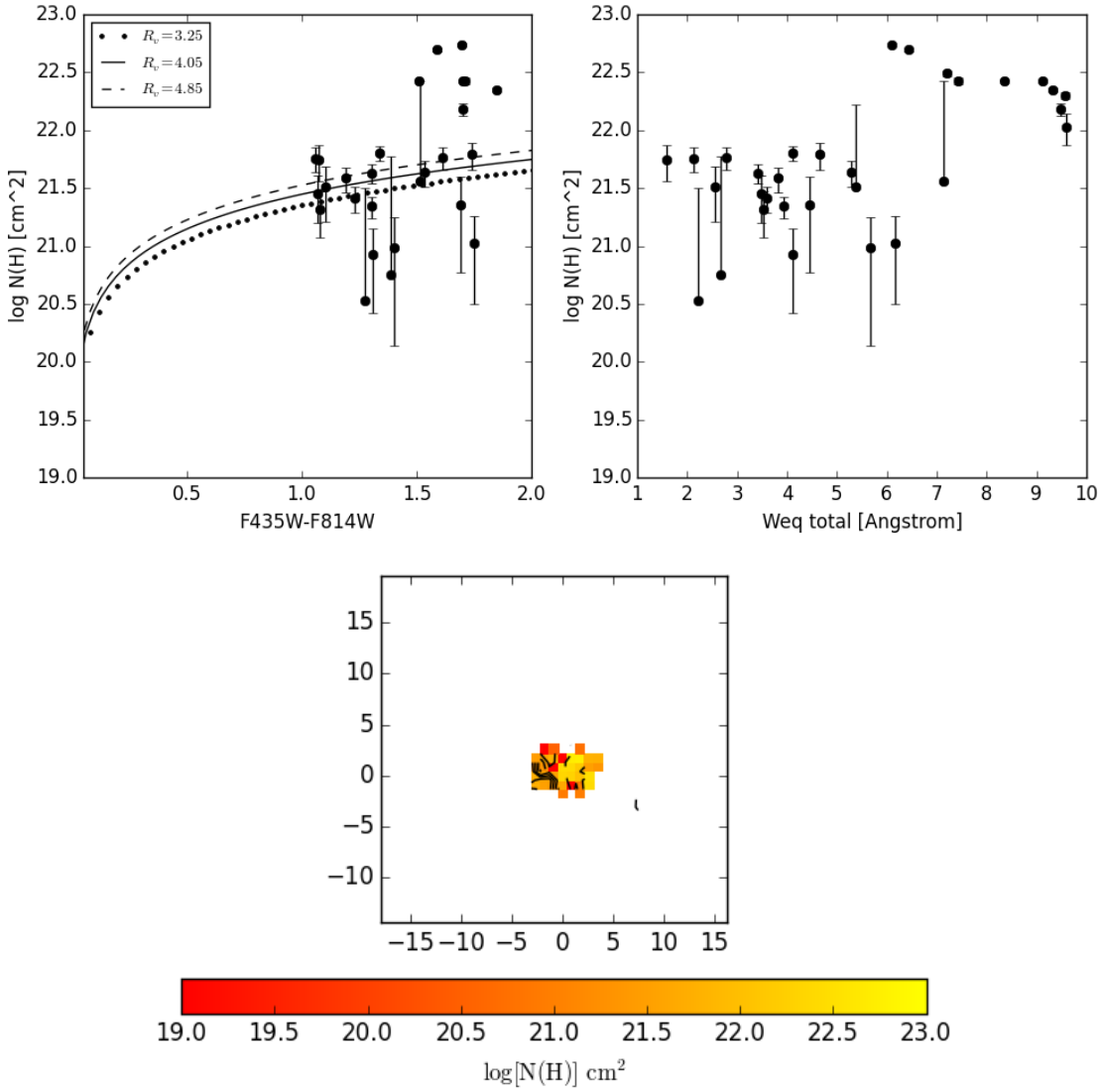

Figure C.47: IRAS F22467-4906 diagnostic plots continued. Top panels - Comparisons of Hydrogen column density to HST colour (left) and total W_{eq} of IRAS F22467-4906 (right). Bottom panel - map of the calculated N(H).

Bibliography

Allen J. T. et al., 2015a, MNRAS, 446, 1567

Allen J. T. et al., 2015b, VizieR Online Data Catalog, 744

Allen J. T. et al., 2015c, MNRAS, 451, 2780

Allen M. G. et al., 2008, ApJS, 178, 20

Alonso-Herrero A. et al., 2012, ApJ, 744, 2

Alonso-Herrero A. et al., 2006, ApJ, 650, 835

Alonso-Herrero A. et al., 2002, Astronomical Journal, 124, 166

Armus L., Heckman T. M., Miley G. K., 1989, ApJ, 347, 727

Armus L. et al., 2009, PASP, 121, 559

Arribas S. et al., 2004, AJ, 127, 2522

Arribas S., Colina L., 2003, ApJ, 591, 791

Arribas S. et al., 2014, A&A, 568, A14

Arribas S. et al., 2008, A&A, 479, 687

Bacon R. et al., 2010, in Proceeding of Science, Vol. 7735, Ground-based and Airborne Instrumentation for Astronomy III, p. 773508

Baldwin J. A., Phillips M. M., Terlevich R., 1981, PASP, 93, 5

Barnes J. E., Hernquist L., 1992, ARA&A, 30, 705

Barnes J. E., Hernquist L., 1996a, ApJ, 471, 115

Barnes J. E., Hernquist L., 1996b, ApJ, 471, 115

Barnes J. E., Hernquist L. E., 1991, ApJL, 370, L65

Belfiore F. et al., 2016, MNRAS, 461, 3111

Bellocchi E. et al., 2013, A&A, 557, A59

Binette L. et al., 1994, A&A, 292, 13

Bland-Hawthorn J. et al., 2011, Optics Express, 19, 2649

Bobra M. G., Couvidat S., 2015, ApJ, 798, 135

Boeker T. et al., 1997, PASP, 109, 827

Bryant J. J. et al., 2014, MNRAS, 438, 869

Bryant J. J. et al., 2011, MNRAS, 415, 2173

Bryant J. J. et al., 2015, MNRAS, 447, 2857

Bryant, J. J. J. J., Bland-Hawthorn J., 2016, ASPC

Bundy K. et al., 2015, ApJ, 798, 7

Calzetti D., 1997, in American Institute of Physics Conference Series, Vol. 408, American Institute of Physics Conference Series, Waller W. H., ed., pp. 403–412

Calzetti D. et al., 2000, ApJ, 533, 682

Cappellari M., Emsellem E., 2004, PASP, 116, 138

Cecil G. et al., 2016, MNRAS, 456, 1299

Cecil G. N. et al., 2015, in American Astronomical Society Meeting Abstracts, Vol. 225, American Astronomical Society Meeting Abstracts, p. 250.10

Cortese L. et al., 2016, MNRAS

Cortese L. et al., 2014, ApJL, 795, L37

Croom S. M. et al., 2012, MNRAS, 421, 872

Davies R. L. et al., 2016a, ApJ, 824, 50

Davies R. L. et al., 2016b, MNRAS, 462, 1616

Davies R. L. et al., 2014, MNRAS, 444, 3961

Di Matteo T., Springel V., Hernquist L., 2005, Nature, 433, 604

Díaz-Santos T. et al., 2008, ApJ, 685, 211

Doert M., Errando M., 2014, ApJ, 782, 41

Dopita M. et al., 2007, APSS, 310, 255

Dopita M. A. et al., 2002, ApJS, 143, 47

Dopita M. A. et al., 2014a, APSS, 350, 741

Dopita M. A. et al., 2014b, A&A, 566, A41

Dopita M. A. et al., 2015, ApJS, 217, 12

Driver S. P. et al., 2011, MNRAS, 413, 971

Elmegreen B. G., Elmegreen D. M., 2006, ApJ, 650, 644

Emonts B. H. C. et al., 2014, A&A, 572, A40

Farrah D. et al., 2007, ApJ, 667, 149

Fernandes I. F. et al., 2004, MNRAS, 355, 728

Filho M. E. et al., 2004, A&A, 418, 429

Fogarty L. M. R. et al., 2012, ApJ, 761, 169

Franceschini A. et al., 2003, MNRAS, 343, 1181

Genzel R. et al., 2001, ApJ, 563, 527

Grimes J. P. et al., 2005, ApJ, 628, 187

Haan S. et al., 2011, AJ, 141, 100

Hampton E. J. et al., 2017, MNRAS, 470, 3395

Hassan T. et al., 2013, MNRAS, 428, 220

Heckman T. M., Armus L., Miley G. K., 1990, ApJS, 74, 833

Heckman T. M. et al., 2004, ApJ, 613, 109

Heckman T. M. et al., 2000, ApJS, 129, 493

Ho I.-T. et al., 2014, MNRAS, 444, 3894

Ho I.-T. et al., 2015, MNRAS, 448, 2030

Ho I.-T. et al., 2016a, MNRAS, 457, 1257

Ho I.-T. et al., 2016b, APSS, 361, 280

Hopkins P. F. et al., 2012, MNRAS

Howell J. H. et al., 2010, ApJ, 715, 572

Husemann B. et al., 2013, A & A, 549, A87

Imanishi M. et al., 2010, ApJ, 721, 1233

Inami H. et al., 2013, ApJ, 777, 156

Ishida C. M., 2004, PhD thesis, UNIVERSITY OF HAWAI'I

Iwasawa K. et al., 2009, ApJL, 695, L103

Iwasawa K. et al., 2011, A&A, 529, A106

Kauffmann G. et al., 2003, MNRAS, 346, 1055

Keel W. C., 1983, ApJ, 269, 466

Kennicutt, Jr. R. C., Keel W. C., 1984, ApJL, 279, L5

Kewley L., Kobulnicky H. A., 2007, Astrophysics and Space Science Proceedings, 3, 435

Kewley L. J. et al., 2001a, ApJ, 556, 121

Kewley L. J. et al., 2001b, ApJ, 556, 121

Kewley L. J. et al., 2006, MNRAS, 372, 961

Kewley L. J. et al., 2001c, ApJS, 132, 37

Kim D.-C., Sanders D. B., 1998, ApJS, 119, 41

Kim D.-C. et al., 1995, ApJS, 98, 129

Kim D.-C., Veilleux S., Sanders D. B., 1998, ApJ, 508, 627

Kim D.-C., Veilleux S., Sanders D. B., 2002, ApJS, 143, 277

Kormendy J. et al., 2009, ApJS, 182, 216

Kovo O., Contini T., 1999, in IAU Symposium, Vol. 193, Wolf-Rayet Phenomena in Massive Stars and Starburst Galaxies, van der Hucht K. A., Koenigsberger G., Eenens P. R. J., eds., p. 604

Kuminski E. et al., 2014, PASP, 126, 959

Lehmer B. D. et al., 2015, ApJ, 806, 126

Leslie S. et al., 2015, in IAU Symposium, Vol. 309, Galaxies in 3D across the Universe, Ziegler B. L., Combes F., Dannerbauer H., Verdugo M., eds., pp. 324–324

Lípari S. et al., 2000, AJ, 120, 645

Lípari S. L. et al., 2004, MNRAS, 354, L1

Lira P. et al., 2008, MNRAS, 384, 316

Markwardt C. B., 2009, in Astronomical Society of the Pacific Conference Series, Vol. 411, Astronomical Data Analysis Software and Systems XVIII, Bohlender D. A., Durand D., Dowler P., eds., p. 251

Martin C. L., 2005, ApJ, 621, 227

Mast D. et al., 2014, A&A, 561, A129

McElroy R. et al., 2015, MNRAS, 446, 2186

Medling A. M. et al., 2015, MNRAS, 448, 2301

Mihos J. C., Hernquist L., 1994, ApJL, 437, L47

Mihos J. C., Hernquist L., 1996, ApJ, 464, 641

Momcheva I. G. et al., 2013, Astronomical Journal, 145, 47

Monreal-Ibero A. et al., 2010, A&A, 517, A28

Moran E. C., Halpern J. P., Helfand D. J., 1996, ApJS, 106, 341

Morton D. C., 1991, ApJS, 77, 119

Nardini E. et al., 2008, MNRAS, 385, L130

Neff S. G., Ulvestad J. S., Campion S. D., 2003, ApJ, 599, 1043

Osterbrock D. E., De Robertis M. M., 1985, PASP, 97, 1129

Panessa F. et al., 2005, ApJ, 631, 707

Pereira-Santaella M. et al., 2010, ApJ, 725, 2270

Petric A. et al., 2011, in IAU Symposium, Vol. 280, IAU Symposium, Cernicharo J., Bachiller R., eds., p. 298P

Poggianti B. M., Wu H., 2000, ApJ, 529, 157

Pounds K. A., 1979, Proceedings of the Royal Society of London Series A, 366, 375

Ptak A. et al., 2003, ApJ, 592, 782

Rich J. A. et al., 2010, ApJ, 721, 505

Rich J. A., Kewley L. J., Dopita M. A., 2011, ApJ, 734, 87

Rich J. A., Kewley L. J., Dopita M. A., 2014, ApJL, 781, L12

Rich J. A., Kewley L. J., Dopita M. A., 2015, ApJS, 221, 28

Rich J. A. et al., 2012, ApJ, 753, 5

Richards S. N. et al., 2016, MNRAS, 455, 2826

Richards S. N. et al., 2014, MNRAS, 445, 1104

Roth M. M. et al., 2005, PASP, 117, 620

Rothberg B., Fischer J., 2010, ApJ, 712, 318

Rothberg B., Joseph R. D., 2004, AJ, 128, 2098

Rothberg B., Joseph R. D., 2006, AJ, 131, 185

Rupke D. S., Veilleux S., Sanders D. B., 2002, ApJ, 570, 588

Rupke D. S., Veilleux S., Sanders D. B., 2005a, ApJ, 632, 751

Rupke D. S., Veilleux S., Sanders D. B., 2005b, ApJS, 160, 87

Rupke D. S., Veilleux S., Sanders D. B., 2005c, ApJS, 160, 115

Rupke D. S. N., 2014, Ifsfit: Spectral fitting for integral field spectroscopy. ASCL Code Record

Rupke D. S. N., Veilleux S., 2013, ApJL, 775, L15

Rupke D. S. N., Veilleux S., 2015, ApJ, 801, 126

Sakamoto K. et al., 2014, ApJ, 797, 90

Sakamoto K., Ho P. T. P., Peck A. B., 2006, ApJ, 644, 862

Sánchez S. F. et al., 2012, A&A, 538, A8

Sanders D. B. et al., 2003, Astronomical Journal, 126, 1607

Sanders D. B., Mirabel I. F., 1996, Annual Review of Astronomy and Astrophysics, 34, 749

Sanders D. B. et al., 1988, ApJL, 328, 35

Sani E. et al., 2008, ApJ, 675, 96

Sarzi M. et al., 2006, MNRAS, 366, 1151

Savage B. D., Sembach K. R., 1996, ARA&A, 34, 279

Scharwächter J. et al., 2016, in Astrophysics and Space Science Proceedings, Vol. 42, The Universe of Digital Sky Surveys, Napolitano N. R., Longo G., Marconi M., Paolillo M., Iodice E., eds., p. 263

Scharwächter J. et al., 2011, AJ, 142, 43

Scoville N. Z. et al., 2000, AJ, 119, 991

Sharp R. et al., 2015, MNRAS, 446, 1551

Sharp R. G., Bland-Hawthorn J., 2010, ApJ, 711, 818

Shih H.-Y., Rupke D. S. N., 2010, ApJ, 724, 1430

Shull J. M., McKee C. F., 1979, ApJ, 227, 131

Singh R. et al., 2013, A&A, 558, A43

Solomon P. M. et al., 1997, ApJ, 478, 144

Spitzer L., 1978, Physical processes in the interstellar medium

Springel V., Di Matteo T., Hernquist L., 2005, MNRAS, 361, 776

Stanghellini L., Renzini A., 2000, ApJ, 542, 308

Stierwalt S. et al., 2014, ApJ, 790, 124

Stierwalt S. et al., 2013, ApJS, 206, 1

Stierwalt S. et al., 2012, in American Astronomical Society Meeting Abstracts, Vol. 219, American Astronomical Society Meeting Abstracts 219, p. 411.05

Stokes G. M., 1978, ApJS, 36, 115

Sturch L., Madore B., 2012, in American Astronomical Society Meeting Abstracts, Vol. 219, American Astronomical Society Meeting Abstracts #219, p. 411.07

Tacconi L. J. et al., 2002, APJ, 580, 73

Trancho G. et al., 2007, ApJ, 658, 993

Tremaine S. et al., 2002, ApJ, 574, 740

Väisänen P. et al., 2008, MNRAS, 384, 886

Veilleux S., Kim D.-C., Sanders D. B., 2002, ApJS, 143, 315

Veilleux S. et al., 1995a, ApJS, 98, 171

Veilleux S. et al., 1995b, ApJS, 98, 171

Veilleux S., Osterbrock D. E., 1987, ApJS, 63, 295

Veilleux S., Rupke D. S., 2005, in Astronomical Society of the Pacific Conference Series, Vol. 331, Extra-Planar Gas, Braun R., ed., p. 313

Wang J. X. et al., 2004, ApJL, 612, L109

Wild V. et al., 2014, A&A, 567, A132

Wilkes B. J. et al., 2002, ApJL, 564, L65

York D. G. et al., 2000, The Astronomical Journal, 120, 1579

Yuan T.-T., Kewley L. J., Sanders D. B., 2010a, ApJ, 709, 884

Yuan T.-T., Kewley L. J., Sanders D. B., 2010b, ApJ, 709, 884

Zahid H. J., Kewley L. J., Bresolin F., 2011, ApJ, 730, 137